UNIVERSITY OF COPENHAGEN

Exploring a common solution to Dark Matter, Neutrino oscillations and Baryogenesis of the Universe

Displaced Heavy Neutral Lepton searches at the Large Hadron Collider

Edis Devin Tireli, Mads Mølbak Hyttel
Supervised by Oleg Ruchayskiy

January 3, 2023

Contents

1 Short introduction to the structure of the thesis **3**

I Theory, Phenomenology and Results **5**

2 The Standard Model **6**
2.1 Introduction . . . 6
2.2 Fermions . . . 7
2.3 Electroweak interactions . . . 9
2.4 Quantum Chromodynamics . . . 13
2.5 Open problems in the Standard Model . . . 20
2.6 Potential solutions to the BSM problems . . . 25

3 Heavy Neutral Leptons **26**
3.1 Mass terms allowable due to symmetry . . . 26
3.2 Mechanisms of neutrino mass generation . . . 27
3.3 Filling the gaps in the Standard Model . . . 31

4 Physical processes of interest **36**
4.1 Processes involving charged mesons . . . 38
4.2 Processes involving on-shell $W^{\pm}$-bosons . . . 41

5 Strategy of producing exclusion limits **43**
5.1 Number of detected events . . . 43
5.2 Defining confidence interval . . . 43
5.3 Signal acceptance . . . 44
5.4 DV trigger schemes . . . 45

6 Results **48**
6.1 Previous searches . . . 48
6.2 HNLs produced from $W^{\pm}$ bosons . . . 48
6.3 HNLs produced from heavy flavoured mesons . . . 53
6.4 Results for SND . . . 61
6.5 Consolidated results . . . 62
6.6 Stability of results with varying selection criteria . . . 65
6.7 Uncertainties . . . 68

II Methodology & Validation **70**

7 Collider physics - a very short primer **71**

7.1 Basic concepts . . . 71
7.2 Detectors . . . 74

8 Event generation **81**
8.1 Pythia . . . 81
8.2 MadGraph . . . 89
8.3 MadGraph models . . . 91

9 Data analysis and post-processing **98**
9.1 Post-processing architecture . . . 98
9.2 Event selection . . . 101
9.3 Event rate and efficiency landscapes . . . 113
9.4 Invariant mass . . . 117
9.5 Summary of trigger and cut parameters . . . 118

III Conclusions & Outlook **119**

10 Conclusion and outlook **120**
10.1 Conclusion . . . 120
10.2 Outlook . . . 121

A Appendices **124**
A.1 HNL Theory . . . 124
A.2 A Realistic choice of mixing angles . . . 125
A.3 QCD . . . 125
A.4 Geometry . . . 127
A.5 The Abelian & non-Abelian Higgs models . . . 130
A.6 Alternative rapidity cut computation . . . 132
A.7 $B_c^{\pm}$ meson sample validation . . . 134

B Notation & Conventions **135**
B.1 Convention . . . 135
B.2 Notation . . . 135

Abstract

What is Dark matter? Why is there an asymmetry between matter and anti-matter? How do neutrinos get mass? Despite its overwhelming success in describing the results of high-energy experiments at subatomic scales, the Standard Model of particle physics cannot answer these questions. Scientists seek therefore *extensions* of the Standard Model, that can play a pivotal role in our understanding of the universe at micro- and macro-scales.

Heavy neutral leptons (or *HNLs*) provide one such extension. These hypothetical particles are akin to the Standard Model neutrinos — neutral fermions, interacting with $W^{\pm}$, Z^0 and Higgs bosons. However, HNL phenomenology is distinct, owing to two facts: (1) their interaction strength is much weaker than that of neutrinos, and (2) they are much heavier. HNLs can be long-lived, traveling macroscopic distances before their decay. This determine possible strategies of their experimental tests.

This thesis focuses on HNL searches at the ATLAS experiment (part of the Large Hadron Collider at CERN). Our work differs from the previous searches in a number of ways. First, we consider HNL production not only from $W^{\pm}$ bosons, but also in decays of mesons containing charm or beauty quarks ($B^{\pm}, B_c^{\pm}, D^{\pm}$). The amount of such mesons is much larger than that of W-bosons, which boosts HNL production for masses below that of mesons. Second, unlike all the previous searches we focus on utilising the Muon Spectrometer of the ATLAS experiment. The overall instrumented volume of the Muon Spectrometer is several m^3 which allows us to probe for the existence of particles with the proper decay distance of the order of meters and even more. Specifically, we do not rely on tagging of prompt leptons or jets but rather limit our decay patterns to the processes with *displaced* $\mu^+\mu^-$ pair in the final state. We expect that as the quest for long-lived particles continues, it will become possible to have more advanced triggers for displaced muons and/or retain highly displaced muon events. We also investigate HNL-mediated processess with *three* muons in the final states, two of which are displaced. The displacement in excess of 2 cm is expected to reduce the background of Standard Model processes to a negligible level, making the proposed searches essentially background-free.

Our results demonstrate that such a displaced muons analysis can push the exclusion limits both to smaller mixing angles and to higher HNL masses. The main improvement comes in case of the HNLs produced in W decays where the limits can improve by as much as the order of magnitude with forthcoming LHC runs. For the heavy-flavour production channel, low transverse momenta of the resulting particles greatly impair the efficiency of event selection and the resulting searches are less sensitive than those with parent W-bosons.

In order to explore the data efficiently, we have developed a dedicated analysis pipeline that combines Monte Carlo generators (PYTHIA, MADGRAPH) and post-processing tools. Our pipeline provides a versatile interface for dissecting the data by quickly changing data selection criteria. A significant part of this thesis is devoted to the validation of this suite of tools.

As a demonstration of the power of our tool, we also perform the sensitivity estimates for HNLs with the proper distance in hundreds of meters that can potentially be detected by the new experiment SND@LHC. We confirm that such searches will not improve over the existing bounds owing to the small decay volume of the SND@LHC experiment.

This thesis should be regarded as *feasibility studies* for the HNL searches with the ATLAS Muon Spectrometer. Our results demonstrate potential in such searches in reaching deeply into otherwise unreachable part of the parameter space and therefore warrant further careful investigations, including proper detector response and background evaluation.

Acknowledgements

Edis:

I would first and foremost like to thank my supervisor, *Oleg*. My first introduction to you was in your course on elementary particle physics, which I loved. The contents of your lectures were incredibly fascinating, to-the-point, but also rich with references and further remarks, allowing ones curiosity to flourish. Working on the thesis with you has been an elongated version of this, and I could almost not call it work (almost). I very much enjoyed our conversations as they are filled with details and perspectives from which I have learned incredibly much of.

Secondly, I would like to thank the rest of the research group, *Inar* and *Kevin* for all the fruitful discussions on HNL theory, Cosmology and the Standard Model. Without you, the theory section would not have been as complete as it is, and I will miss the ability of walking by your office and asking you about a detail that only few in the world know. Thank you specifically to *Jean-Loup* and *Inar* once more for sharing their scripts.

Thirdly, I would like to thank *Jørgen*, for all your expertise with Pythia and details concerning the ATLAS detector. Your help has been invaluable, and your open-door policy, a great comfort. I would further like to thank my friends in the *seesaw-playground*: *Arnau*, *Jonathan*, *Katinka* and *Marie-Louise* for all the snacks, fun conversations and help with colour-palletes, histograms and general computer issues.

I would also, sincerely, like to thank my friends, *Natalia*, *Nicholas* and *Wojtek*, and my family; my parents, my brother, *Milas*, and my girlfriend, *Sara*, for all the love and support during this process, and for your belief in me.

Last, but certainly not least, I would like to thank my dear friend and colleague *Mads*. Your constant optimism, enthusiasm and intellectual sparring has been a great addition to my life in the previous year, and I could not imagine it without you.

Mads:

First of all I want to express my warmest and most sincere gratitude for the solid and inspiring supervision received from our main supervisor *Oleg Ruchayskiy*, without whose guidance we would not have made it through. Thanks for opening up the doors of HNLs and thanks for a year that will be remembered for a lifetime. You once mentioned that there are two kind of physicists, those who know the mass of the electron and those who do not. I might have started out as the latter, but after countless look-ups in the PDG database I now consider my self among the former.

Secondly I extended deep thanks for the help we got from the research staff from all round the Niels Bohr Institute M-building. Especially *Jørgen Beck Hansen* whose endless knowledge on anything computational and experimental we needed was a bigger help than he might have realised. From Pythia to triggers, you had the answers. In the same breath also thanks to *Inar Timiryasov*, and *Kevin Calderón* for sparring and sharing, I think you make us both feel like there is still so far for us to go, and that is appreciated. Though only formely in the building, also thanks to *Jean-Loup Tastet* (aswell as Inar, again) for providing their essential script needed for our work.

Also big thanks to the fellow students in Chambre de Bébé. Could not think of a lovelier atmosphere to be conducting ones studies in, and we owe many good discussions and helpful considerations to you guys. Thanks to all of you.

The current list would not be complete without mention my friends and family, look forward to reconnect now that we are on the other side of the deadline. Of friends, special thanks to *Jakob Wrigley* for lending his ear and contributing with valuable input on the programming front!

Of family especially deep thanks to my wife and kids for enduring my absence and allowing me to colonise the dining table with papers, laptop and notes. I look forward to make up for that; we have a lot of laughing and playing to do, and after that I must face my accumulated deficit of household chores. Special thanks to my son *Elvis* whom I had the joy of spending maternity leave with, while completing the thesis, sparing with you on HNL theory was invaluable. Equally invaluable was the help from my parents in once in a while taking care of you, freeing some days for much needed study. In the end I think we all found it to be a very precious time.

Finally thanks to my partner in crime *Edis Tireli*. We jumped into the joint thesis on a wildcard, but I think our cooperation and team-spirit have exceeded even the most generous upper bounds.We made not only physics but also friends during the last year. Look forward to build on that and do more fun physics together in the future!

Chapter 1

Short introduction to the structure of the thesis

This thesis addresses searches for new physics at Large Hadron Collider. It does not perform the analysis of actual data, rather – it performs computer modelling of the expected signal. For this purpose it uses Monte Carlo simulations. Any computational project necessarily involves a large technical part with both implementation and validation playing an important role. Therefore, we have chosen to organise the thesis in 3 major parts, to facilitate the reading of the thesis.

Part I lays out main theoretical scene (Standard Model and Beyond, Chapter 2 and the specific model under investigation, Chapter 3). After a brief sketch of the main physical processes, described by our simulation techniques (Chapter 4) we skip directly to the results, represented in the form of exclusion plots and histograms of relevant observables in Chapter 6. This is our main Chapter with all the other serving as either introduction to it or explanation of the way the results were obtained.

Part II (starting on page 71) describes our main methodology. There we start from the brief introduction to the collider experiments with the emphasis on the ATLAS experiment at CERN (Chapter 7). We then follow with the description of our Monte Carlo generators (and the corresponding models of new physics, used with them), Chapter 8. Finally, our data processing strategies and the structure of the data processing pipeline is reviewed in Chapter 9.

Part III (starts on page 120) contains our concluding remarks (Chapter 10) as well as various supplementary materials (Appendices).

Main abbreviations used in the text

ATLAS	A Toroidal LHC Apparatus
CL	Confidence limit
CMS	Compact Muon Solenoid
DV	Displaced vertex
HL-LHC	High-luminosity phase of the LHC
HNL	Heavy neutral lepton
ID	Inner Detector
IP	Interaction Point (referring to the point of beam collision)
L1	Level-1 hardware trigger of the ATLAS Experiment
LEP	Large Electron-Positron Collider
LHC	Large Hadron Collider
LLP	Long Lived Particle
MG	MadGraph
MS	Muon Spectrometer
PV	Primary vertex
PD	Pixel Detector
SCT	Semiconductor Tracker
SM	Standard Model
SND	Scattering and Neutrino Detector
$\mathbf{T}_1$	*Trigger*: Two muons of opposite charge sharing a single displaced vertex. Both muons are required to have $p_T > 5$ GeV.
$\mathbf{T}_2$	*Trigger*: Two muons, each with $p_T \geq 15$.
$\mathbf{T}_3$	*Trigger*: Two muons, one with $p_T \geq 9$ and one with $p_T \geq 23$.
TRT	Transition Radiation Tracker
vev	The vacuum expectation value of the Higgs field

Part I

Theory, Phenomenology and Results

Chapter 2

The Standard Model

This Chapter provides a brief introduction to the Standard Model of particle physics and problems beyond the Standard Model. The parts important in the subsequent Chapters are especially emphasised.

2.1 Introduction

The gauge group of the Standard Model (SM) is

$$\underbrace{SU(3)_C}_{\text{QCD}} \times \underbrace{SU(2)_L \times U(1)_Y}_{\text{electroweak}}, \tag{2.1.1}$$

the field contents of which will be reviewed in the following sections. The SM can be expressed compactly in terms of Lagrangians such that the full SM is the sum of the five Lagrangians that make up the gauge fields, their interactions and ghost fields,

$$\mathscr{L}_{\text{SM}} = \mathscr{L}_{\text{gauge}} + \mathscr{L}_{\text{f}} + \mathscr{L}_{\text{Yuk}} + \mathscr{L}_{\phi} + \mathscr{L}_{\text{ghosts}}. \tag{2.1.2}$$

We will return to this Lagrangian later in the chapter, but it proves important to start the discussion here with a brief consideration of the gauge term of the SM Lagrangian, $\mathscr{L}_{\text{gauge}}$. This term defines the structure of interactions and the strength of their self-interaction and is given [1] by,

$$\mathscr{L}_{\text{gauge}} = \tfrac{1}{4} G^{i\mu\nu} G^{i}_{\mu\nu} - \tfrac{1}{4} W^{j\mu\nu} W^{j}_{\mu\nu} - \tfrac{1}{4} B^{\mu\nu} B_{\mu\nu}, \tag{2.1.3}$$

with Einstein summation convention over $i \in \{1, 2, .., 8\}$ indexing the eight generators of the colour $SU(3)_C$ Lie group, $G^{i\mu\nu}$, and $j \in \{1, 2, 3\}$ indexing the three generators/gauge fields of the left chiral $SU(2)_L$ group, with the third gauge field, $B^{\mu\nu}$, representing the single generator of the $U(1)_Y$ hypercharge group, defined more closely as:

$$G^{i}_{\mu\nu} = \partial_{[\mu} G^{i}_{\nu]} - g_s f_{ijk} G^{j}_{\mu} G^{k}_{\nu} \tag{2.1.4}$$

$$W^{i}_{\mu\nu} = \partial_{[\mu} W^{i}_{\nu]} - g \varepsilon_{ijk} W^{j}_{\mu} W^{k}_{\nu} \tag{2.1.5}$$

$$B_{\mu\nu} = \partial_{[\mu} B_{\nu]} \tag{2.1.6}$$

with commuting index notation where e.g. $\partial_{[\mu} G^{i}_{\nu]}$ is defined in (B.2.1). The gauge fields of (2.1.4) and (2.1.5) are non-Abelian, and thus contain self-coupling terms governed by coupling constants g_s and g,

and structure constants f_{ijk} and ε_{ijk} respectively, to be elaborated upon in the upcoming sections. For the full set of our notations see Appendix B.

2.2 Fermions

We start with a brief mathematical introduction to fermions, as they are of central importance to the development of later sections. The starting point is the famous *Dirac equation*, presented below.

2.2.1 The *Dirac* equation

The Dirac Lagrangian for a free fermion field ψ is

$$\mathscr{L} = \bar{\psi}(i\partial\!\!\!/ - m)\psi, \tag{2.2.1}$$

where ψ is a four component spinor field, the *Dirac conjugated* of which, $\bar{\psi}$, is given by

$$\bar{\psi} = \psi^\dagger \gamma^0. \tag{2.2.2}$$

The Euler-Lagrange procedure leads to the equation of motion, known as the *Dirac equation*:

$$(i\partial\!\!\!/ - m)\psi = 0. \tag{2.2.3}$$

2.2.2 The *Weyl* equation

Fermions compose the matter content of the SM and modern gauge theories. In particular, massless fermions can be constructed from chiral, *left* and *right* handed fields [2]. They flow from the Dirac equation (2.2.3) where for a chiral fermionic field [3],

$$\psi = \begin{pmatrix} \chi_1 \\ \chi_2 \end{pmatrix} \tag{2.2.4}$$

then the Dirac equation, under the Dirac basis of the Gamma matrices[1], can be written as

$$\begin{pmatrix} (i\partial_0 - m)\mathbb{I} & -i\sigma^k\partial_k \\ i\sigma^k\partial_k & -(i\partial_0 + m)\mathbb{I} \end{pmatrix} \begin{pmatrix} \chi_1 \\ \chi_2 \end{pmatrix} = 0 \tag{2.2.5}$$

where $k \in \{1, 2, 3\}$ and σ^k are *Pauli matrices*. The above can be expanded explicitly to the following system of equations:

$$i(\partial_0\chi_1 - \sigma^k\partial_k\chi_2) = m\chi_1 \tag{2.2.6}$$
$$i(\partial_0\chi_2 - \sigma^k\partial_k\chi_1) = -m\chi_2 \tag{2.2.7}$$

which can also be written as

$$i(\partial_0 - \sigma^k\partial_k)(\chi_1 + \chi_2) = m(\chi_1 - \chi_2) \tag{2.2.8}$$
$$i(\partial_0 + \sigma^k\partial_k)(\chi_1 - \chi_2) = m(\chi_1 + \chi_2). \tag{2.2.9}$$

[1] The explicit form of which is placed in the Appendix B

Defining *left* and *right* chiral fermionic fields respectively as

$$\psi_L = \tfrac{1}{2}(\chi_1 - \chi_2) \quad \text{and} \quad \psi_R = \tfrac{1}{2}(\chi_1 + \chi_2), \tag{2.2.10}$$

the system of equations in (2.2.8) and (2.2.9) can be written in terms of the chiral fields, and further, defining $(\partial_0 - \sigma^k \partial_k) = \partial\!\!\!/$, yields

$$i\partial\!\!\!/\psi_R = m\psi_L \tag{2.2.11}$$
$$i\partial\!\!\!/\psi_L = m\psi_R \tag{2.2.12}$$

where the space-time evolution of the left and right fields are coupled via the mass m [3]. If the fermions are *massless*, equations (2.2.11) and (2.2.12) decouple and become two *Weyl equations*:

$$i\partial\!\!\!/\psi_R = 0 \tag{2.2.13}$$
$$i\partial\!\!\!/\psi_L = 0 \tag{2.2.14}$$

where ψ_L and ψ_R are known as *Weyl spinors* [2].

2.2.3 The *Majorana* equation

In the footsteps of Ettore Majorana [4], one can take the Hermitian conjugate of (2.2.11) and (2.2.12), using the property $\gamma^0 \gamma^{\mu^\dagger} \gamma^0 = \gamma^\mu$ to yield

$$-i\partial_\mu \bar{\psi}_R \gamma^\mu = m\bar{\psi}_L. \tag{2.2.15}$$

Taking the transpose of the fields and multiplying from the left with a *charge conjugation matrix*, $\mathcal{C}$, we get

$$i\gamma^\mu \partial_\mu \mathcal{C}\bar{\psi}_R^T = m\mathcal{C}\bar{\psi}_L^T, \tag{2.2.16}$$

where the anti-commuting property $\mathcal{C}(\gamma^\mu)^T\mathcal{C}^{-1} = -\gamma^\mu$ was used. Equation (2.2.16) now has the same form as (2.2.11) and (2.2.12), but are only identical under the following condition

$$\psi_R = \xi\mathcal{C}\bar{\psi}_L^T \tag{2.2.17}$$

where ξ is an arbitrary phase factor such that $\xi^2 = 1$. The condition of (2.2.17) is known as the *Majorana relation*, stating that the transpose of the Hermitian conjugated left handed field is equivalent to the right, under multiplication by the charge conjugation operator. Thus, under substitution into (2.2.12) one arrives at the *Majorana equation*:

$$i\partial\!\!\!/\psi_L = m\xi\mathcal{C}\bar{\psi}_L^T \tag{2.2.18}$$

where the phase factor ξ can be absorbed into a redefinition of the field

$$\psi_L \to \sqrt{\xi}\psi_L \tag{2.2.19}$$

such that (2.2.18) resolves to

$$i\partial\!\!\!/\psi_L = m\mathcal{C}\bar{\psi}_L^T. \tag{2.2.20}$$

One can further define $\psi_L^c = \mathcal{C}\bar{\psi}_L^T$ and introduce the Majorana field as

$$\psi = \psi_L + \psi_L^c \tag{2.2.21}$$

with the Majorana condition of (2.2.17) then written as $\psi = \psi^c$, implying equality between particle and anti-particle.

2.3 Electroweak interactions

We turn next to the electroweak interactions, appropriately labeled in (2.1.1). As it turns out, the theory of weak interactions is *chiral* and maximally *parity-violating*, i.e. the SU(2) gauge fields couple only to left-handed fermions [5]. In the Standard Model, the left-handed leptons $(e, \nu_e, \mu, \nu_\mu, \tau, \nu_\tau)$ as well as the left-handed quarks (u, d, s, c, b, t) can be paired up in doublets to transform under SU(2) in the fundamental representation. There are thus three generations of the SU(2) lepton doublets, L^α, and quark doublets, Q^α, defined:

$$L^\alpha = \begin{pmatrix} \nu_{eL} \\ e_L \end{pmatrix}, \begin{pmatrix} \nu_{\mu L} \\ \mu_L \end{pmatrix}, \begin{pmatrix} \nu_{\tau L} \\ \tau_L \end{pmatrix} \quad \text{and} \quad Q^\alpha = \begin{pmatrix} u_L \\ d_L \end{pmatrix}, \begin{pmatrix} c_L \\ s_L \end{pmatrix}, \begin{pmatrix} t_L \\ b_L \end{pmatrix}, \tag{2.3.1}$$

with $\alpha \in \{1, 2, 3\}$ indexing the three generations. These doublet pairs all transform as left-handed Weyl spinors, i.e. in the $(\frac{1}{2}, 0)$ representation of the Lorentz group. The right-handed fermions can be indexed as follows,

$$e_R^\alpha = \{e_R, \mu_R, \tau_R\}, \qquad \nu_R^\alpha = \{\nu_{1R}, \nu_{2R}, ..., \nu_{nR}\}, \tag{2.3.2}$$

$$u_R^\alpha = \{u_R, c_R, t_R\}, \qquad d_R^\alpha = \{d_R, s_R, b_R\}, \tag{2.3.3}$$

and are SU(2) singlets, thus being uncharged under weak interactions and transform as right-handed Weyl spinors, i.e. in the $(0, \frac{1}{2})$ representation of the Lorentz group.

The n right-handed neutrinos, ν_R^α, have as of yet *not* been observed. However, these hypothetical particles are the main focus of the current thesis and therefore we include them in the above prescription, allowing for $n \in \mathbb{N}$ generations (n not necessarily equal to 3).

The fermionic content of the Standard Model is described by the following Lagrangian (see *e.g.* [1]):

$$\mathscr{L}_f = \sum_{\alpha=1}^{3} \left(i f_\alpha^\dagger \bar{\sigma}^\mu D_\mu f_\alpha + i f_\alpha \sigma^\mu D_\mu f_\alpha^\dagger \right), \tag{2.3.4}$$

where $f_\alpha \in \{Q_\alpha, L_\alpha\}$ and $f_\alpha^\dagger \in \{e_{R\alpha}^\dagger, u_{R\alpha}^\dagger, d_{R\alpha}^\dagger\}$. Here we introduced notations

$$\sigma^\mu \equiv (\mathbb{I}, \sigma^i), \quad \bar{\sigma}^\mu \equiv (\mathbb{I}, \text{-}\sigma^i) \tag{2.3.5}$$

for the covariant Pauli matrices, and the covariant derivative defined as

$$D_\mu = \partial_\mu + \tfrac{i g_s}{2} \lambda^i G_\mu^i + \tfrac{ig}{2} \sigma^j W_\mu^j + i g_Y q_Y B_\mu, \tag{2.3.6}$$

with coupling constants g_s, g, g_Y belonging to the $SU(3)_c, SU(2)_L, U(1)_Y$ gauge theories respectively, indexed in the adjoint representation by i and j for $SU(3)_c$ and $SU(2)_L$ respectively, and finally q_Y is the hyper-charge.

2.3.1 Electroweak symmetry breaking in the Standard Model

Electroweak unification is based on the principle of the spontaneous symmetry breaking of $SU(2)_L \times U(1)_Y \to U(1)_{\rm EM}$ where the high energy *hypercharge* $U(1)_Y$ symmetry is not to be confused with the low energy $U(1)_{\rm EM}$ that we know as electromagnetism. The $SU(2)_L \times U(1)_Y$ gauge group is broken by the vacuum expectation value (vev) of a complex doublet, ϕ, with hypercharge $q_Y = \frac{1}{2}$ called the *Higgs multiplet* [5]. The following combined Lagrangian can be constructed for the EM and weak gauge fields in (2.1.5) and (2.1.6),

$$\mathscr{L}_{EW} = -\tfrac{1}{4}(W^a_{\mu\nu})^2 - \tfrac{1}{4}B^2_{\mu\nu} + (D_\mu\phi)^\dagger(D_\mu\phi) - V(\phi) \tag{2.3.7}$$

where the Higgs potential $V(\phi) = -m^2|\phi|^2 + \lambda|\phi|^4$ (with $m^2 < 0 < \lambda$) induces a vev, v, for ϕ such that

$$\phi = \frac{1}{\sqrt{2}} \exp\left(\frac{i\pi^a\sigma^a}{v}\right)\begin{pmatrix}0\\ v+h\end{pmatrix} \tag{2.3.8}$$

with $v = \frac{m}{\sqrt{\lambda}}$. Under the unitary gauge, π is set to zero so that (2.3.8) reduces to

$$\phi = \frac{1}{\sqrt{2}}\begin{pmatrix}0\\ v+h\end{pmatrix}. \tag{2.3.9}$$

Focusing only on the electroweak sector of the SM, putting $q_Y = \frac{1}{2}$ and ignoring QCD interactions[2] the gauge covariant derivative, D_μ, acting on the Higgs field, takes the following form

$$D_\mu = \partial_\mu + \tfrac{ig}{2}\sigma^i W^i_\mu + \tfrac{ig_Y}{2}B_\mu, \tag{2.3.10}$$

where then,

$$D_\mu\phi = \frac{1}{\sqrt{2}}\left(\partial_\mu \cdot \mathbb{I}_2 + \tfrac{ig}{2}\sigma^i W^i_\mu + \tfrac{ig_Y}{2}B_\mu \cdot \mathbb{I}_2\right)\begin{pmatrix}0\\ v+h\end{pmatrix}. \tag{2.3.11}$$

In components this can be written as:

$$D_\mu\phi = \frac{1}{\sqrt{2}}\begin{pmatrix}\frac{ig}{2}(W^1_\mu - iW^2_\mu)(v+h)\\ (\partial_\mu - \frac{ig}{2}W^3_\mu + \frac{ig_Y}{2}B_\mu)(v+h)\end{pmatrix} \tag{2.3.12}$$

The kinetic energy term can now be computed to give

$$\begin{aligned}|D_\mu\phi|^2 =& \frac{1}{2}\left(\tfrac{ig}{2}((W^1)^\mu + i(W^2)^\mu)(v+h)\ (\partial^\mu + \tfrac{ig}{2}(W^3)^\mu - \tfrac{ig_Y}{2}B^\mu)(v+h)\right)\begin{pmatrix}\frac{ig}{2}(W^1_\mu - iW^2_\mu)(v+h)\\ (\partial_\mu - \frac{ig}{2}W^3_\mu + \frac{ig_Y}{2}B_\mu)(v+h)\end{pmatrix}\\ =&(\partial^\mu + \tfrac{ig}{2}W^{3\mu} - \tfrac{ig_Y}{2}B^\mu)(v+h)(\partial_\mu - \tfrac{ig}{2}W^3_\mu + \tfrac{ig_Y}{2}B_\mu)(v+h)\\ &- \frac{1}{4}g^2(W^{1\mu} - iW^{2\mu})(v+h)(W^1_\mu + iW^2_\mu)(v+h)\end{aligned} \tag{2.3.13}$$

[2]The Higgs field is not charged with respect to strong interactions, *i.e.* one can put $\frac{ig_s}{2}\lambda^i G^i_\mu \to 0$

where four vector bosons can be defined as

$$W_\mu^\pm = \frac{1}{\sqrt{2}}\left(W_\mu^1 \mp iW_\mu^2\right) \tag{2.3.14}$$

$$Z_\mu^0 = \frac{1}{\sqrt{g^2+g'^2}}\left(gW_\mu^3 - g_Y B_\mu\right) \tag{2.3.15}$$

$$A_\mu = \frac{1}{\sqrt{g^2+g_Y^2}}\left(g_Y W_\mu^3 + gB_\mu\right). \tag{2.3.16}$$

and thus (2.3.13) can be written as follows (with the parameter $\xi = \frac{i\sqrt{g^2+g_Y^2}}{2}$, introduced for convenience):

$$\begin{aligned}
|D_\mu\phi|^2 =&(\partial^\mu + \xi(Z^0)^\mu)(h+v)(\partial_\mu - \xi(Z^0)_\mu)(h+v) - \frac{1}{2}g^2(W^-)^\mu(h+v)(W^+)_\mu(h+v)\\
=&(\partial^\mu h + \xi(Z^0)^\mu(h+v))(\partial_\mu h - \xi(Z^0)_\mu(h+v)) - \frac{1}{2}g^2(W^-)^\mu(h+v)(W^+)_\mu(h+v)\\
=&\,\partial^\mu h\partial_\mu h + \xi^2(Z^0)^\mu(h+v)(Z^0)_\mu(h+v) - \frac{1}{2}g^2(W^-)^\mu(h+v)(W^+)_\mu(h+v)
\end{aligned} \tag{2.3.17}$$

where one can expand (2.3.17) explicitly to arrive at

$$\begin{aligned}
|D_\mu\phi|^2 =&\partial^\mu h\partial_\mu h + \xi^2(Z^0)^\mu h(Z^0)_\mu h + 2v\xi^2(Z^0)^\mu h(Z^0)_\mu + \overbrace{v^2\xi^2(Z^0)^\mu(Z^0)_\mu}^{Z^0\text{-boson mass term}}\\
&- \frac{1}{2}g^2(W^-)^\mu h(W^+)_\mu h - vg^2(W^-)^\mu h(W^+)_\mu - \underbrace{\frac{v^2}{2}g^2(W^-)^\mu(W^+)_\mu}_{W^\pm\text{-boson mass term}}
\end{aligned} \tag{2.3.18}$$

Eqs. (2.3.18) lead to the mass terms for the Z^0 and $W^\pm$ bosons, as labeled, as well as three- and four-point interaction vertices, displayed in Figure 2.1. The A_μ field (2.3.16) does not couple to the h field or its vev, thus remaining massless, the physical interpretation of this field is of course the photon!

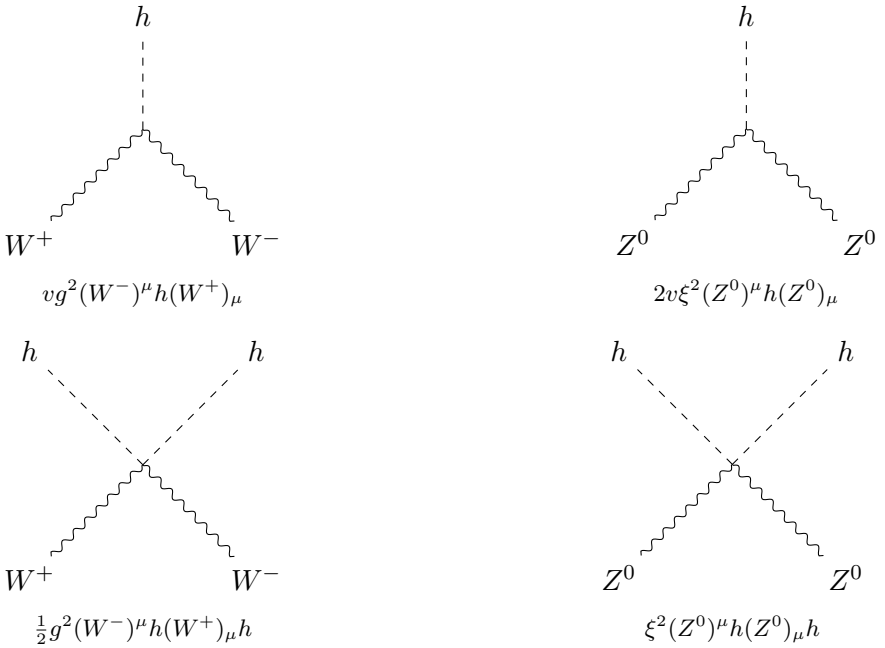

Figure 2.1: Interactions between the Higgs and intermediate vector bosons $W^\pm$ and Z^0.

2.3.2 Fermionic coupling

In QED, a contraction such as $\bar{e}_L e_R$ was connected by a Dirac mass term, however a term of this form would explicitly break $SU(2)$ invariance [6]. Therefore, for the generation of *fermionic* masses, the Higgs vev must couple to the fermion fields in some way that is invariant under $SU(2)$, such that after spontaneous symmetry breaking it will lead to the appearance of fermionic mass terms. Thus, under *Yukawa* coupling between a Higgs doublet of the form (2.3.9) and the left handed fermionic doublets of the form (2.3.1) one can write,

$$\mathscr{L}_{\text{Yuk}} = - Y^u_{\alpha\beta}(Q^\dagger_{L\alpha} \cdot \tilde{\phi}) u^\dagger_{R\beta} - Y^e_{\alpha\beta}(L^\dagger_{L\alpha} \cdot \phi) e^\dagger_{R\beta} + \text{h.c.} \tag{2.3.19}$$

After the spontaneous symmetry breaking (SSB), the Higgs will gain a vev and (2.3.19) will generate mass terms [6, 1],

$$\mathscr{L}_{\text{Yuk}} \xrightarrow{\text{SSB}} (m^u_{\alpha\beta} \bar{u}_{L\alpha} u_{R\beta} + m^e_{\alpha\beta} \bar{e}_{L\alpha} e_{R\beta}) + \text{h.c.} + \mathcal{O}(h) \tag{2.3.20}$$

with Dirac mass matrices $m^\rho_{\alpha\beta} = \frac{v}{\sqrt{2}} Y^\rho_{\alpha\beta}$, with $\rho \in \{e, u\}$, the conjugated Higgs field $\tilde{\phi} = i\sigma_2 \phi^*$, thus generating the fermionic masses. In the same Lagrangian as (2.3.19), the fermionic fields couple to the Higgs, h, as well, thus yielding the following three point amplitudes [7]

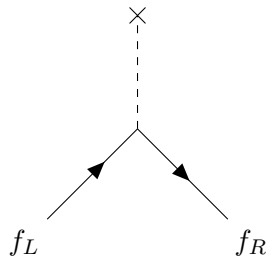

(a) Dirac mass term: interaction of left- and right-chiral components of a fermion with the non-zero Higgs vev (dashed line with the cross).

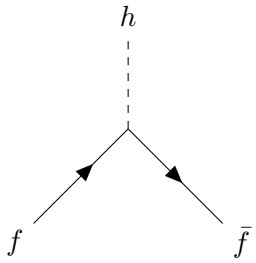

(b) $hf\bar{f}$ vertex. The interaction strength is proportional to the fermion's mass.

Figure 2.2: Yukawa couplings in the Standard Model generate both the Dirac mass terms (a) *and* Higgs-fermion interactions (b).

The Standard Model Lagrangian can thus be fully expressed as:

$$\mathscr{L}_{\text{SM}} = \mathscr{L}_{\text{gauge}} + \mathscr{L}_{\text{f}} + \mathscr{L}_{\text{Yuk}} + \mathscr{L}_{\phi} + \mathscr{L}_{\text{ghosts}} \tag{2.3.21}$$

with the Yukawa Lagrangian leading after the electroweak symmetry breaking to the generation of masses to all fermions. The extra ghost term, $\mathscr{L}_{\text{ghosts}}$, shows extra interactions with the fiducial (ghost) fields due to the Faddeev-Poppov procedure as a consequence of the non-Abelian gauge symmetry.[3]

2.3.3 Charged-current and Neutral-current Interactions

The electroweak couplings between fermions and the bosons are of importance to the thesis, with special emphasis on the *charged current* interactions between quarks and fermions (i.e. quark and lepton coupling to $W^\pm$) and *neutral current* coupling with leptons (i.e. lepton coupling to Z^0 or A_μ). To

[3] If a non-Abelian field theory admits a local gauge symmetry, gauge freedom leads to auxiliary, non-dynamical, quantum fields that under the Fadeev-Poppov procedure are anti-commuting scalar fields [6].

derive an expression where this coupling becomes obvious, one can expand the fermionic $\mathscr{L}_f$ of (2.3.4) in terms of the covariant derivative defined in (2.3.10), as in the above analysis, to find

$$\mathscr{L}_f = \sum_{\alpha=1}^{3} i f_\alpha^\dagger \bar{\sigma}^\mu (\partial_\mu + \tfrac{ig}{2}\sigma^i W_\mu^i + \tfrac{ig_Y}{2} B_\mu) f_\alpha + \text{h.c.} \tag{2.3.22}$$

Following the treatment of [6], the Lagrangian resolves to

$$\mathcal{L} = \bar{L}_L(i\partial\!\!\!/)L_L + \bar{e}_R(i\partial\!\!\!/)e_R + \bar{Q}_L(i\partial\!\!\!/)Q_L + \bar{u}_R(i\partial\!\!\!/)u_R + \bar{d}_R(i\partial\!\!\!/)d_R \tag{2.3.23}$$

$$+g\left(W_\mu^+ J_W^{\mu+} + W_\mu^- J_W^{\mu-} + Z_\mu^0 J_Z^\mu\right) + eA_\mu J_{EM}^\mu \tag{2.3.24}$$

with the fermionic currents being defined as

$$J_W^{\mu+} = \tfrac{1}{\sqrt{2}}\left(\bar{\nu}_L\gamma^\mu e_L + \bar{u}_L\gamma^\mu d_L\right) \tag{2.3.25}$$

$$J_W^{\mu-} = \tfrac{1}{\sqrt{2}}\left(\bar{e}_L\gamma^\mu \nu_L + \bar{d}_L\gamma^\mu u_L\right) \tag{2.3.26}$$

$$\begin{aligned} J_Z^\mu = \tfrac{1}{\cos\theta_w}\Big[&\bar{\nu}_L\gamma^\mu\left(\tfrac{1}{2}\right)\nu_L + \bar{e}_L\gamma^\mu\left(-\tfrac{1}{2}+\sin^2\theta_w\right)e_L + \bar{e}_R\gamma^\mu\left(\sin^2\theta_w\right)e_R \\ &+\bar{u}_L\gamma^\mu\left(\tfrac{1}{2}-\tfrac{2}{3}\sin^2\theta_w\right)u_L + \bar{u}_R\gamma^\mu\left(-\tfrac{2}{3}\sin^2\theta_w\right)u_R \\ &+\bar{d}_L\gamma^\mu\left(-\tfrac{1}{2}+\tfrac{1}{3}\sin^2\theta_w\right)d_L + \bar{d}_R\gamma^\mu\left(\tfrac{1}{3}\sin^2\theta_w\right)d_R\Big] \end{aligned} \tag{2.3.27}$$

$$J_{EM}^\mu = \bar{e}\gamma^\mu(-1)e + \bar{u}\gamma^\mu\left(+\tfrac{2}{3}\right)u + \bar{d}\gamma^\mu\left(-\tfrac{1}{3}\right)d. \tag{2.3.28}$$

The aforementioned *charged-current* interactions are those of mediated by the $W^\pm$-bosons, while *neutral-current* interactions are mediated by Z^0 such as the ones shown below in Fig. 2.3

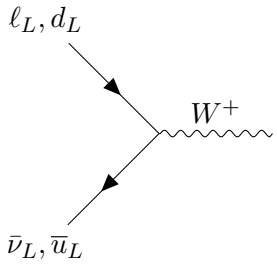

(a) A charged-current mediated three-point vertex from the $\frac{g}{\sqrt{2}}W_\mu^+(\bar{\nu}_L\gamma^\mu e_L + \bar{u}_L\gamma^\mu d_L)$ term

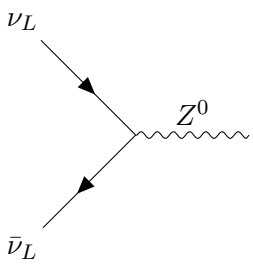

(b) A neutral-current mediated three-point vertex from the $\frac{g}{2\cos\theta_w}Z^0(\bar{\nu}_L\gamma^\mu\nu_L)$ term.

Figure 2.3: Examples of processes mediated by the Charged Current (CC, left diagram) and Neutral Current (NC, right diagram) interactions.

2.4 Quantum Chromodynamics

We now consider the dynamics of non-Abelian gauge fields (2.1.4) – $SU(3)$ Yang-Mills theory known as *Quantum Chromodynamics* (QCD).

2.4.1 A brief phenomenological introduction

QCD is the theory of strong interactions, namely between that of quarks and gluons: the $SU(3)_C$ part of the SM gauge group. The *chromo* in chromodynamics comes from the Greek word for colour ($\chi\rho\acute{\omega}\mu\alpha$ or *chroma*), namely due to the colour charge that is ascribed to the field quanta that appear in the Lagrangian. In a similar to how electrons and positrons carry electric charge in quantum electrodynamics (QED), in QCD, quarks carry *colour* charge. This is where the similarities stop, because wherein QED

there exists only a single kind of charge, in QCD, colour charge appears in three types; red, green, blue as well as their respective associated anti-colors: anti-red, anti-blue, anti-green [8].

Further, the gauge field in charge of force mediation in QED, the photon, is electrically neutral. In QCD however, the gauge field, the gluon, is *not* colour neutral and in fact carries both colour and anti-colour charge. One can use the isometries of the non-Abelian Lie group SU(N), knowing there are N^2-1 such generators of the isometries to compute the number of generators of the group for a non-Abelian, Yang Mills (YM), gauge theory. QCD is an example of one such important YM, where, as stated earlier, the associated gauge group is SU(3) and therefore there are $3^2-1=8$ such generators, $G^{i\mu\nu}\ \forall\ i\in\{1,2,..,8\}$, with following colour basis:

$$\begin{aligned}
&\tfrac{1}{\sqrt{2}}(r\bar{b}+b\bar{r}) && -i\tfrac{1}{\sqrt{2}}(r\bar{b}-b\bar{r})\\
&\tfrac{1}{\sqrt{2}}(r\bar{g}+g\bar{r}) && -i\tfrac{1}{\sqrt{2}}(r\bar{g}-g\bar{r})\\
&\tfrac{1}{\sqrt{2}}(b\bar{g}+g\bar{b}) && -i\tfrac{1}{\sqrt{2}}(b\bar{g}-g\bar{b})\\
&\tfrac{1}{\sqrt{2}}(r\bar{r}-b\bar{b}) && \tfrac{1}{\sqrt{6}}(r\bar{r}+b\bar{b}-2g\bar{g})
\end{aligned}$$

A third difference between the two is in the couplings. In QED, the coupling approaches zero for small momenta, however in QCD, due to asymptotic freedom, the opposite is the case.

2.4.2 The QCD Lagrangian

The theory, as stated earlier, is non-Abelian and can therefore be described by the Yang-Mills Lagrangian. Starting from a definition of the gauge covariant derivative such that

$$D_\mu = \partial_\mu - ig_s t^a G^a_\mu \tag{2.4.1}$$

with $t^a=\frac{1}{2}\lambda^a$ [5, 8], λ^a being the eight Gell-Mann matrices, defined in Appendix B. The above covariant derivative can be seen to follow from (2.3.6) in the regime where G^μ is the only relevant gauge field such that the $\frac{ig}{2}\sigma^j W^j_\mu + ig_Y q_Y B_\mu$ is zero. The gluon field strength $G_{\mu\nu}$ can further be expressed in terms of a commutator

$$G_{\mu\nu} = t^a G^a_{\mu\nu} = \frac{i}{g_s}\left[D_\mu, D_\nu\right] \tag{2.4.2}$$

so that the QCD Lagrangian can be expressed, compactly, as [5, 6]

$$\mathscr{L}_{\text{QCD}} = \sum_{f=1}^{3} \overline{\psi}^a_f(x)\left[i\not{D} - m_f\right]_{ab}\psi^f_b(x) - \tfrac{1}{4}G^a_{\mu\nu}G^{a\mu\nu}, \tag{2.4.3}$$

where $\not{D}=\gamma^\mu D_\mu$. This Lagrangian, $\mathscr{L}_{\text{QCD}}$, is manifest in Eq. 2.3.4 for $f_\alpha, f^\dagger_\alpha$ being quark fields. There are 6 quark flavours ($f=\{u,d,s,c,b,t\}$) over which we sum explicitly below:

$$\mathscr{L}_{\text{QCD}} = \underbrace{\sum_{f=1}^{6}\bar{\psi}^a_f(x)(i\not{\partial}\delta_{ab}-m_f)\psi^f_b(x)}_{\text{free Lagrangian}} - \underbrace{\sum_{f=1}^{6}\bar{\psi}^a_f(x)g_s\gamma^\mu t^a G^a_\mu\psi^f_b(x)}_{\text{quark-gluon}} - \underbrace{\tfrac{1}{4}G^a_{\mu\nu}G^{a\mu\nu}}_{\text{gluon-gluon}} \tag{2.4.4}$$

The Lagrangian (2.4.4) splits into 3 distinct parts: the free (quadratic) Lagrangian $\mathcal{L}_0$, quark-gluon $\mathscr{L}_{\text{qg}}$, and gluon-gluon interactions respectively, $\mathscr{L}_{\text{gg}}$ the last two of which will be elaborated upon piece by piece in the next subsection.

2.4.2.1 QCD interactions

The quark-gluon term $\mathscr{L}_{\mathrm{qg}}$ gives rise to the following vertex

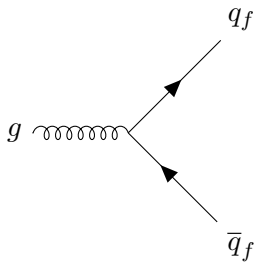

Figure 2.4: Three point $\bar{q}gq$ vertex. Notice that the flavour $f = \{u, d, s, c, b, t\}$ of the quark and anti-quark are always the same at the quark-gluon vertex. This means that the quark flavour is a *conserved quantum number* within the QCD framework.

An important property of the quark sector of the Lagrangian (2.4.4) is that it is *diagonal* in the quark flavours. This means, that quark cannot change its flavour by interacting with a gluon and new flavours can only be created in a quark-antiquark pair. The quark flavour thus becomes a conserved quantum number. As a result, the lightest particle, carrying a given quark flavour, is stable *within a framework of QCD*! It is important to stress, that weak interactions do change flavours of the quarks and therefore decays of such particles are possible (see below in the Section 2.4.4).

Finally, the purely gluonic part, $\mathscr{L}_{\mathrm{gg}}$

$$\mathscr{L}_{\mathrm{gg}} = -\tfrac{1}{4} G_a^{\mu\nu} G^{\mu\nu a} \tag{2.4.5}$$

leads to the following gluon-gluon interactions:

$$\mathscr{L}_{\mathrm{gg}} = -\underbrace{g_s f^{abc} (\partial_\kappa G^a_\lambda) G^{\kappa b} G^{\lambda c}}_{ggg \text{ term}} - \underbrace{\tfrac{1}{4} g_s^2 (f^{eab} G^a_\kappa G^b_\lambda)(f^{ecd} G^c_\kappa G^d_\lambda)}_{gggg \text{ term}}. \tag{2.4.6}$$

These terms, derived from the non-Abelian structure of the su(N) algebra, illustrate the fundamental difference between QED and QCD: gluons are self-coupled, giving rise to the following vertices:[4].

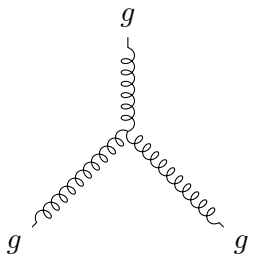

(a) Three point ggg vertex

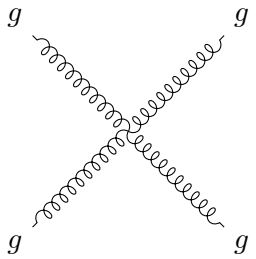

(b) Four point $gggg$ vertex

Figure 2.5: Gluon self-interaction terms.

The important consequence of this interaction is an unavoidable complexity of any QCD process. While the vertex in Fig. 2.4 is similar to the QED one, the processes in Fig. 2.5 lead to "avalanche" creation of gluons ("gluon splitting"), followed by more splittings, quark-antiquark pair creation, gluon bremsstrahlung, and so. The resulting multitude of quarks later *hadronizes*, which we will sketch below.

[4]The three-point amplitude is suppressed by a factor g_s, while the four-point is suppressed by a factor g_s^2.

We stress already at this stage that treating of such QCD processes are essentially non-analytic and require special numerical tools, such as, *e.g.* Monte Carlo generators (see Chapter 8 below).

2.4.3 Colour confinement and Hadrons

The effective quark-antiquark potential in QCD has the following form:

$$V_{\text{QCD}} = \underbrace{-\frac{4}{3}\frac{\alpha_s}{r}}_{\text{short range}} + \underbrace{\kappa r.}_{\text{long range}} \tag{2.4.7}$$

It contains a short-ranged, Coulomb like potential term, and a long-ranged linear term that grows with separation, r, at a rate of change defined by $\kappa \approx 1$ GeV/fm. It is due to the form of this potential that the energy stored per unit length of the field is approximately constant as $V(r) \propto r$. Thus, quark interactions at small distances (high energies) is relatively weak, however at large distances (lower energy scales) it becomes asymptotically stronger. This property is called *confinement*, and it is due to this property that *bare* or *unconfined* quarks have not been observed as this would require infinite energies [7].

Consequently, colour confinement implies that the asymptotic states of quarks are colour neutral. The bound states can therefore be organized into colour multiplets called *hadrons*. There are two kinds of hadrons. *Mesons* are composed of a quark anti-quark pair and with respect to the SU(3) gauge group form a colour singlet with a wavefunction of the form [7]

$$\Psi_{\text{meson}}(q\bar{q}) = \tfrac{1}{\sqrt{3}}(r\bar{r} + g\bar{g} + b\bar{b}). \tag{2.4.8}$$

Baryons are constructed from combinations of three quarks, so that their wavefunctions has following form:

$$\Psi_{\text{baryon}}(qqq) = \tfrac{1}{\sqrt{6}}(rgb - rbg + gbr - grb + brg - bgr). \tag{2.4.9}$$

Figure 2.6 below shows how quarks combine into hadrons – the process called *hadronisation*. (i) a quark anti-quark pair is produced with momenta pointing in opposite directions. As the pair separates (ii) the colour field is restricted to a tube with energy density κ as introduced above. As they continue to separate, the field stores enough energy to form a new $q\bar{q}$ pair, (iii) the tube *breaks* into two smaller *strings* as they are energetically favorable. The process continues, breaking several more times with further $q\bar{q}$ pairs forming (iv) until all the pairs have reached low enough energies to form colourless hadrons (v). This process results in two *jets* of hadrons, one following each initial quark direction [7].

2.4.4 Heavy flavoured mesons

An important concept for the current study is on *heavy mesons*. A heavy flavoured meson contains *heavy* quarks (c and/or b). As already mentioned above, the lightest carrier of the *beauty* or *charm* quark quantum number cannot decay via QCD processes. They do decay, however, via charged-current interactions, mediated by W-bosons (see Figure 2.7).[5]

[5]It should be mentioned that W bosons can mix up- and down-quarks of different generations due to a non-diagonal CKM matrix, see *e.g.* [7].

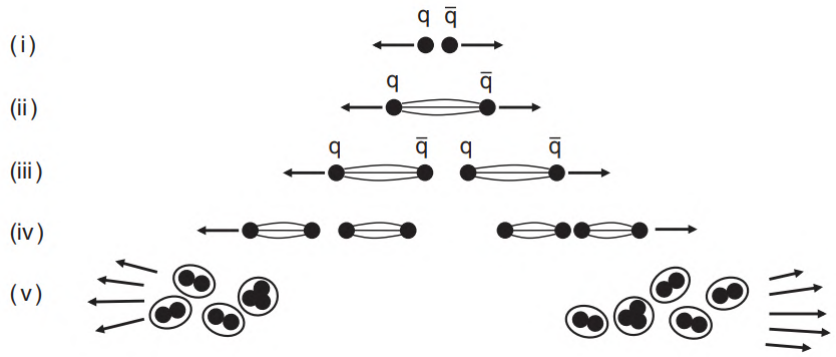

Figure 2.6: A schematic representation of the process of hadronisation and quark confinement [7]

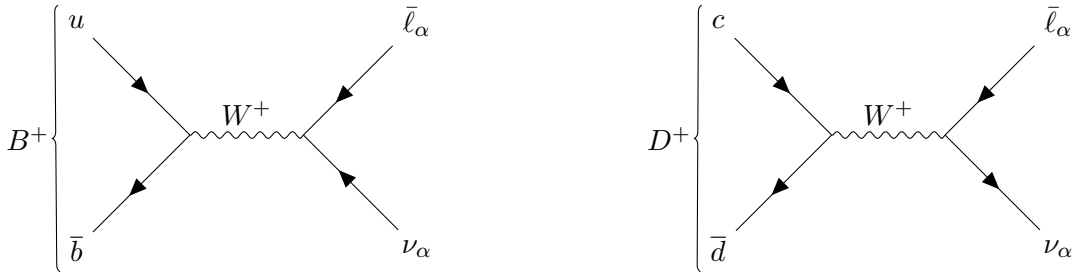

Figure 2.7: Fully leptonic decays of heavy mesons, B^+ (left), and D^+ (right), to a neutrino, ν and anti-lepton, ℓ^+ pair. Both processes are mediated by the charge current interactions.

As a result, these mesons are sufficiently long-lived (with a typical lifetime of order of 10^{-12} sec) while their counterparts – mesons like D^* or B^* have lifetimes $\sim 10^{-23}$ sec to 10^{-20} sec, see [9]).

Table 2.1 shows few selected purely leptonic decay channels of $B^\pm$ and $D^\pm$ mesons that will be important for our studies. Notice that owing to parity-violating nature of weak interactions, the branching ratio of $B^\pm$ or $D^\pm$ mesons to a lepton plus anti-neutrino is proportional to the lepton's mass. We will come to this point again in Chapter 4 when discussing heavy meson decays, producing new particles (heavy neutral leptons, see below);

Decay channel	Branching ratio
$D^+ \to e^+\nu_e$	$< 8.8 \times 10^{-6}$
$D^+ \to \mu^+\nu_\mu)$	$(3.74 \pm 0.17) \times 10^{-4}$
$D^+ \to \tau^+\nu_\tau)$	$(1.20 \pm 0.27) \times 10^{-3}$
$B^+ \to e^+\nu_e$	$< 9.8 \times 10^{-7}$
$B^+ \to \mu^+\nu_\mu$	$< 1.0 \times 10^{-6}$
$B^+ \to \tau^+\nu_\tau$	$(1.09 \pm 0.24) \times 10^{-4}$

Table 2.1: Branching ratios of the leptonic decay channels of the $B^\pm$ and $D^\pm$ mesons [9].

Owing to the complexity of QCD interactions, the exact process of hadronisation, and even the distribution of quarks and gluons within hadrons is still poorly understood, and must be modelled from the data. One such successful model is the Parton model discussed below.

2.4.5 The Parton Model

Originally introduced by Feynman, the parton model is based on the assumption that within the proton, objects, called *partons*, are essentially free [5]. These partons refer to not only quarks and

B mesons			
type	Quark content	mass [GeV]	lifetime [s]
B^+	$u\bar{b}$	5.27925	$(1.638 \pm 0.004) \times 10^{-12}$
B^0	$d\bar{b}$	5.27965	$(1.519 \pm 0.004) \times 10^{-12}$
B_s	$s\bar{b}$	5.36688	$(1.515 \pm 0.004) \times 10^{-12}$
B_c	$c\bar{b}$	6.2749	$(0.510 \pm 0.009) \times 10^{-12}$
D mesons			
type	Quark content	mass [GeV]	lifetime [s]
D^+	$c\bar{d}$	1.86958	$(1.040 \pm 0.007) \times 10^{-12}$
D^0	$c\bar{u}$	1.86484	$(4.101 \pm 0.015) \times 10^{-13}$
D_s	$c\bar{s}$	1.96847	$(5.00 \pm 0.07) \times 10^{-13}$

Table 2.2: Basic information about mesons, containing b or c quark (heavy mesons) relevant for the present analysis. The mesons are *long-lived* as compared to the particles, decaying via strong interactions, where a typical lifetime is $\mathcal{O}(10^{-23}\,\text{sec})$. The information is taken from [9].

anti-quarks, but gluons as well and their existence within a hadron. The quark and gluon within the proton will interact, the dynamics of which will result in a distribution of the quark momenta within the proton, from which one can develop functions to approximate this distribution [10]: *Parton Distribution Functions* (PDFs). Different choices of PDFs will lead to different asymptotic states, and in general, different physics.[6] A further treatment of the parton model is given in Appendix B for deep inelastic scattering processes.

2.4.6 Different ways of treating QCD interactions

In non-Abelian gauge theories, due to the many contractions in each vertex, complete analytic solutions for any process becomes computationally exhaustive. For example, for the $gg \to ggg$ process, there are around 10 *thousand* terms contributing *only* at tree level [8, 5]. Therefore, there have been developed many different approaches to solving QCD processes up to specified order, a few of them will be presented here.

2.4.6.1 Lattice QCD (LQCD)

Lattice QCD is established on the basis of discretizing ones spacetime into a four-dimensional lattice with some lattice spacing χ. One can hereby consider that the gluon fields *live* on the links connecting lattice points, if the quark fields then *live* on the sites [11] as presented in Fig. 2.8 . One can compute the values of the quark/gluon fields at all the vertices of the geometry (nodes) and solve the relevant Feynman path integrals numerically, and then extrapolating the results into the continuum limit. This approach proves very useful in precision tests of the SM and at low energy regimes, in e.g. the determination of the values of the CKM matrix, however at the high energy regime of the proton-proton collisions at the LHC, where center-of-mass energies reach 14 TeV, one needs a lattice spacing of $\chi \approx 10^{-5}$ fm to resolve all the processes that occur. At this limit, one would need 10^{34} nodes upon which one must calculate Feynman path integrals numerically [8].

Therefore, although LQCD can be extremely useful in its precision and is still a rich and developing field, at the high energy regime of the LHC the method proves computationally exhaustive, and thus other alternatives have proven more successful.

[6] A short discussion on which PDF has been chosen and why is elaborated in Sec. 8.1.0.1

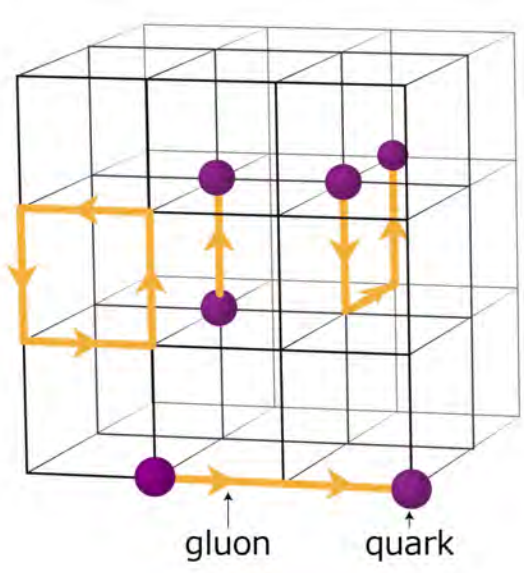

Figure 2.8: Lattice QCD discretization illustration. Quark fields lie on the grid points, and gluon are represented by links connecting two points [12].

2.4.6.2 AdS_5/CFT_4 and holographic QCD

It has been postulated that certain correlators in a super-conformal YM theory ($\mathcal{N} = 4$ super Yang-Mills) can be computed as classical observables in a theory of gravity, living in the $AdS_5 \times S^5$ space, see *e.g.* [13] for a review. It was proposed that one can extend this approach to the case of ordinary, non-supersymmetric QCD [14, 15] by choosing suitable geometry of the gravity dual. The so-called *AdS/QCD* correspondence (see *e.g.* [16] for an overview) uses extra-dimensional models of QCD motivated by the AdS/CFT correspondence that allow to reproduce low-energy hadronic data like meson masses, decay constants, and coefficients of the chiral Lagrangian.

2.4.6.3 Perturbative QCD (pQCD)

One of the difficulties with QCD is that it does not contain a small dimensionless quantity that would allow for perturbative calculations of low-energy observables, in contrast to QED, which contains a small parameter, named the *low-energy fine structure constant* $\alpha \approx \frac{1}{137}$, which determines the relative size of the terms that appear in the perturbative expansion [17].

Perturbation theory in QCD is therefore only valid in the high energy, or short distance, regime. At long distances, QCD becomes strongly interacting, and perturbation theory breaks down [17], as the coupling constant becomes of order 1 [18]. Therefore, for most scattering processes in high energy hadron colliders, like at the Large Hadron Collider (LHC) at CERN, the processes can effectively be *factorized* into the two regimes; a *hard* process, involving large momentum transfer Q^2 where the dynamics of the processes are weakly coupled, and thus perturbation theory may be used to, most commonly, LO and NLO precision, and *soft* processes which require detailed non-perturbative information e.g. as to how hadrons are composed [19, 20].

First developed by Drell and Yan, it was realized that the parton model[7] developed originally for deep inelastic scattering events, could be used in the description of hadron-hadron collisions, namely, in the Drell-Yan process in which massive leptons are produced by a quark-anti-quark pair: $q\bar{q} \to \ell^+\ell^- + X$. It was postulated that the hadronic cross-section, $\sigma(q\bar{q} \to \ell^+\ell^- + X)$ could be derived by weighting the

[7] More details in Appendix B

subprocess cross-section $\hat{\sigma}$ for $q\overline{q} \to \ell^+\ell^-$ with the parton distribution functions extracted from deep inelastic scattering [20]:

$$\sigma = \int \mathrm{d}x_q \mathrm{d}x_{\overline{q}} f_{q/A}(x_q) f_{\overline{q}/B}(x_{\overline{q}}) \hat{\sigma}_{q\overline{q}\to\ell\overline{\ell}}. \tag{2.4.10}$$

This method proved good agreement between theoretical predictions and measured cross sections, however large logarithmic divergences were soon discovered when the method was extended to compute perturbative corrections in processes where collinear gluons were emitted. The very same divergent terms appeared in deep inelastic scattering events, to which the Dokshitzer–Gribov–Lipatov–Altarelli–Parisi (DGLAP) evolution equations were used to absorb these divergences into the definitions of parton distribution functions. In this way, all logarithmic divergences appearing in Drell-Yan processes could be factorized into *renormalized* parton distribution functions. Therefore, using these renormalized functions, one can modify (2.4.10) into

$$\sigma = \int \mathrm{d}x_q \mathrm{d}x_{\overline{q}} f_{q/A}(x_q, Q^2) f_{\overline{q}/B}(x_{\overline{q}}, Q^2) \hat{\sigma}_{q\overline{q}\to\ell\overline{\ell}}, \tag{2.4.11}$$

to correct for the leading logarithmic divergences. Further, perturbative corrections to order $\mathcal{O}(\alpha_s^n)$ must be considered for the above processes, as the leading logarithmic corrections are not sufficient in absorbing all divergences, thus, one can write

$$\sigma = \int \mathrm{d}x_q \mathrm{d}x_{\overline{q}} f_{q/A}(x_q, \mu_F^2) f_{\overline{q}/B}(x_{\overline{q}}, \mu_F^2) \left(\hat{\sigma}_0 + \alpha_s(\mu_R^2)\hat{\sigma}_1 + ...\right)_{q\overline{q}\to\ell\overline{\ell}} \tag{2.4.12}$$

where μ_F is the *factorization scale*, a scale that separates the long- and short-distance physics, and μ_R is the renormalization scale for the QCD running coupling, $\alpha_s(\mu_R^2)$ [20]. In order to determine the correct value of the coupling in the above perturbative expansion of a scale invariant quantity, the renormalization scale μ_R must be set. The uncertainty in this scale is one of the largest uncertainties in making precise predictions in QCD [21].

This method is implemented in Monte Carlo generators, the details of which are further elaborated upon in Chapter 4.

2.5 Open problems in the Standard Model

The Standard Model is not a theoretically derived equation, it is a man-made construction representing physical phenomenology observed from experiments in particle physics. Thus, it is not unnatural that this model may contain *gaps* in areas yet untouched by experiment, or unexplained by theory. In this section, we present three of the largest issues present in physics yet unexplained by the Standard Model, as motivation for seeking beyond it.

2.5.1 Neutrino masses

One of the most critical observational shortcomings of the Standard Model lies in the fact that neutrinos are massive and oscillate between flavour states, despite their theoretical constructions demanding otherwise[8]. The origin of this idea comes from the observational discrepancy between the predicted solar neutrino flux, and the observed, coined the *solar neutrino problem.*

[8]The Higgs-Yukawa Lagrangian from (2.3.19) *cannot* include neutrino couplings as no *right-handed* neutrinos exist within the SM, excluding subsequent couplings with the Higgs.

The problem started in the 1970's with the Homestake experiment lead by Ray Davis Jr. in which 100,000 gallons of dry cleaning fluid (perchloroethylene) was used to detect neutrinos. However, only *a third* of the expected solar neutrino flux arrived. In 1989, the Kamiokande experiment in Japan added to this confusion. The pure water detector found *more* neutrinos than Davis' experiment, however still about only *half* the expected [2].

As measurements of the sun improved and the solar model was validated, researchers looked more and more to new physics beyond the Standard Model to explain the neutrino deficit. The breakthrough came with data from two newer experiments. Super-Kamiokande, an improved version of the Kamiokande experiment, which began observations in 1996, and the Sudbury Neutrino Observatory in Canada, which joined in 1999. Leaders of these two projects would go on to receive the 2015 Nobel Prize in physics for discovering the solution to the solar neutrino problem, a problem that took nearly four decades to solve: *neutrino oscillations*. The neutrinos produced from reactions in the Sun's core, ν_e, oscillate between two other flavours, ν_μ and ν_τ, giving rise to precisely the originally predicted neutrino flux.

Turning to the mathematics of neutrino oscillations, a phenomena that occurs due to mixing between mass and flavour eigenstates, neutrinos can thus be represented using either eigenstate basis as

$$|\nu_\alpha\rangle = \overbrace{\sum_{i\in\{1,2,3\}} U^*_{\alpha i}|\nu_i\rangle}^{\text{mass basis}} \quad \text{and} \quad |\nu_i\rangle = \overbrace{\sum_{\alpha\in\{e,\mu,\tau\}} U_{\alpha i}|\nu_\alpha\rangle}^{\text{flavor basis}} \tag{2.5.1}$$

As a consequence of flavour oscillation, the neutrino of a given flavour that couples via a charged current interaction is not given in terms of a mass eigenstate, but rather as a coherent superposition of mass eigenstates,

$$\mathscr{L}_{\text{CC}} = \frac{g}{\sqrt{2}} W^-_\mu \sum_{\alpha=e,\mu,\tau} \bar{\ell}_{L\alpha}\gamma^\mu \nu_{L\alpha} + \text{ h.c. } = \frac{g}{\sqrt{2}} W^-_\mu \sum_{\alpha=e,\mu,\tau} \bar{\ell}_{L\alpha}\gamma^\mu \sum_{i=1,2,3} U_{\alpha i}\nu_i + \text{ h.c. } . \tag{2.5.2}$$

The unitary transformation relating the flavour to the mass eigenstate left-handed neutrino fields is the lepton mixing matrix, known as the PMNS (*Pontecorvo-Maki-Nakagawa-Sakata*) matrix and can be parameterised as a product of three plane-rotation matrices R_{12}, R_{13}, R_{23} through the angles $\theta_{12}, \theta_{13}, \theta_{23}$, and formally, *six* phases. These phases however are not all physical, and thus under rephasing of ones left-handed lepton fields one, one can reduce this number down to three physical phases. In the case of Diracian neutrinos, one can further rephase the left-handed neutrino fields as well, reducing the number of physical phases down to only *one*, the CP violating phase, δ_{CP} known as the *Dirac phase*. If ones neutrino fields are Majorana in nature however, one cannot rephase the neutrino fields as this would neccessarily lead to complex masses, thus the number of physical fields can maximally be reduced to *three*: two Majorana phases ϕ_2, ϕ_3 and the Dirac phase, δ_{CP} [22]. Thus, the PMNS matrix can be parametrized as follows:

$$\begin{aligned} U &= \overbrace{\begin{pmatrix} 1 & 0 & 0 \\ 0 & c_{23} & s_{23} \\ 0 & -s_{23} & c_{23} \end{pmatrix}}^{R_{23}} \overbrace{\begin{pmatrix} c_{13} & 0 & s_{13}e^{-i\delta_{\text{CP}}} \\ 0 & 1 & 0 \\ -s_{13}e^{i\delta_{\text{CP}}} & 0 & c_{13} \end{pmatrix}}^{R_{13}} \overbrace{\begin{pmatrix} c_{12} & s_{12} & 0 \\ -s_{12} & c_{12} & 0 \\ 0 & 0 & 1 \end{pmatrix}}^{R_{12}} P \\ &= \begin{pmatrix} c_{12}c_{13} & s_{12}c_{13} & s_{13}e^{-i\delta_{\text{CP}}} \\ -s_{12}c_{23} - c_{12}s_{13}s_{23}e^{i\delta_{\text{CP}}} & c_{12}c_{23} - s_{12}s_{13}s_{23}e^{i\delta_{\text{CP}}} & c_{13}s_{23} \\ s_{12}s_{23} - c_{12}s_{13}c_{23}e^{i\delta_{\text{CP}}} & -c_{12}s_{23} - s_{12}s_{13}c_{23}e^{i\delta_{\text{CP}}} & c_{13}c_{23} \end{pmatrix} P. \end{aligned} \tag{2.5.3}$$

where $s_{ij} = \sin(\theta_{ij})$ and $c_{ij} = \cos(\theta_{ij})$ with $\theta_{ij} \in [0, 2\frac{\pi}{2}$ and $\delta_{\text{CP}} \in [0, 2\pi[$. In the case of Dirac neutrinos, $P \to \mathbb{I}$, and in the case of Majorana neutrinos, P resolves to a diagonal matrix containing the two phases associated with the Majorana neutrinos and the Dirac phase, such that

$$P_{\text{Majorana}} = \begin{pmatrix} 1 & 0 & 0 \\ 0 & e^{i\phi_2} & 0 \\ 0 & 0 & e^{i(\phi_3+\delta_{\text{CP}})} \end{pmatrix}. \tag{2.5.4}$$

One can hereby consider neutrino oscillations in vacuum by defining the coherent superposition of mass eigenstated defined in (2.5.1) as the state at $t = 0$, and thus under operation of time-evolution, the time-evolved state can be written, ignoring handedness and using latin indices $i, j \in \{1, 2, 3\}$ to run over mass indices, as

$$|\nu(t)\rangle = \sum_{i=1,2,3} U^*_{\alpha i} e^{iE_i t} |\tilde{\nu}_i\rangle = \sum_{i=1,2,3} U^*_{\alpha i} e^{iE_i t} \sum_{\beta=e,\mu,\tau} U_{\beta i} |\nu_\beta\rangle \tag{2.5.5}$$

where each mass eigenstate evolves with its own phase factor $e^{-E_i t}$ for $E_i = \sqrt{p^2 + m_i^2}$. The probability amplitude for a neutrino with flavour α oscillating to a flavour β is thus

$$P(\nu_\alpha \to \nu_\beta) = |\langle \nu_\alpha | \nu(t) \rangle|^2 = \left| \sum_{i=1,2,3} U_{\alpha i} U^*_{\beta i} e^{-iE_i t} \right|^2. \tag{2.5.6}$$

Expanding in $E_i = \sqrt{p^2 + m_i^2} \simeq p + \frac{1}{2E} m_i^2$, (2.5.6) resolves to

$$P(\nu_\alpha \to \nu_\beta) = \delta_{\alpha\beta} - 4 \sum_{i<j} \Re \left[U_{\alpha i} U^*_{\beta i} U^*_{\alpha j} U_{\beta j} \right] \sin^2 \left(\frac{\Delta m^2_{ji} L}{4E} \right) \tag{2.5.7}$$

$$+ 2 \sum_{i<j} \Im \left[U_{\alpha i} U^*_{\beta i} U^*_{\alpha j} U_{\beta j} \right] \sin \left(\frac{\Delta m^2_{ji} L}{2E} \right), \tag{2.5.8}$$

where $\Delta m^2_{ij} = m_j^2 - m_i^2$ and the distance traveled by the neutrinos is $L \sim c\tau$. Oscillations therefore require neutrinos to have non-degenerate mass such that $\Delta_{ij} \neq 0$ and non-trivial mixing $U \neq 1$. In more sophisticated models, the probabilities are computed for oscillations within a matter density (MSW), and thus from computations of oscillation probabilities, the phenomena of neutrino oscillations of solar and atmospheric neutrinos has been verified analytically [22].

For three flavour oscillations, Δm^2_{sol} is identified with the squared-mass splitting between ν_1 and ν_2 and labelled such that $m_2 > m_1$, i.e. $\Delta m^2_{21} = \Delta m^2_{\text{sol}} > 0$. Then Δm^2_{atm} is identified as $|\Delta m^2_{31}|$ or $|\Delta m^2_{32}|$, and lastly, as $\Delta m^2_{\text{sol}} \ll \Delta m^2_{\text{atm}}$, one can write

$$\Delta m^2_{\text{sol}} = \Delta m^2_{21} \ll |\Delta m^2_{31}| \simeq |\Delta m^2_{32}| \simeq \Delta m^2_{\text{atm}} \tag{2.5.9}$$

There are thus two possibilities for the mass spectrum: either $m_1 < m_2 < m_3$, referred to as the *normal mass ordering* or *normal hierarchy*, with $\Delta m^2_{31} > 0$, or $m_3 < m_1 < m_2$, which is known as the *inverted mass ordering* or *inverted hierarchy*, characterized by $\Delta m^2_{31} < 0$ [22].

2.5.2 Baryon asymmetry of the Universe

The existence of anti-matter is a consequence of finding negative energy (or time) solutions to the Dirac equation [23]: a unification of quantum mechanics and the special theory of relativity. At the time, anti-matter was understood to be an exact mirror image of ordinary matter and as such was invariant

under conjugation of parity (P), charge (C), and time reversal (T). It was only after the theoretical developments of the Big Bang theory, the observational discovery of cosmic microwave background radiation and cosmic inflation, that it became clear the universe was exceedingly hot at early times. When the temperature of the universe fell to a point when particle energies in the cooling plasma was too low for pair production, particles and anti-particles annihilated each other. By symmetry arguments, no excess to this annihilation must remain, however, this is obviously not the case.

One of the largest cosmological questions is on this excess of matter (in the form of baryons) over anti-matter in the Universe. If, before the Big Bang, there was equal amounts of matter and anti-matter, why then have we not observed anti-stars, anti-galaxies? Why has anti-matter not annihilated equal amounts of matter? This problem is known as the *Baryon asymmetry of the Universe* (BAU) and can be quantified [24] by a dimensionless number, η as the ratio between baryon number density, N_B, over photon number density, N_γ,

$$\eta = \frac{N_B - N_{\bar{B}}}{N_\gamma} \sim 6 \times 10^{-10} \tag{2.5.10}$$

The observed violations of P, C and CP in nature provides hints that the matter-antimatter discrepancy may be created dynamically by *baryogenesis* from a matter-antimatter symmetric initial state. First formulated by Sakharov, there are three necessary conditions for baryogenesis to occur [24]:

- *Baryon number violation*: Intuitively, without baryon number violation, it is not possible for any system to evolve from a state with baryon number $B = 0$ to one with $B \neq 0$. Formally, the baryon number, B, is non-conserved in the Standard Model with *sphaleron* processes [25]

- *C and CP violation*: If these symmetries were upheld for each process that generates a matter-antimatter asymmetry, there would be a C (or CP) conjugate process that generates an asymmetry with the opposite sign, occurring with the same probability.

- *A deviation from thermal equilibrium*: Thermal equilibrium is a time translation invariant state in which the expectation values of all observables are constant, thus it requires deviation to evolve from a $B = 0$ to $B \neq 0$ state.

These three conditions are enough to ensure baryogensis, but still do not give arguments for why total symmetric annihilation of matter with anti-matter doesn't occur.

2.5.3 Dark matter

It is evident when studying cosmic phenomena, such as supernovae, spiral galaxies, galactic clusters and from the anisotropies in the Cosmic Microwave Background (CMB) that *something* is unaccounted for [26]. First discovered in the 1970's by Ford and Rubin, the problem is, that spiral galaxies, especially the outermost tips of the tentacles are rotating with a velocities much higher than theoretical predictions allow. In the case of galaxies and clusters, the rotation curves of spiral galaxies, most notably of which NGC 6503, require some form of dark matter structure or mechanism to explain the observed phenomena, shown in diagram (a) above.

Further evidence comes from exaggerated gravitational lensing, a phenomena of which is a consequence of Einstein's theory on General Relativity as detailed in the figure below. The problem here is that the light sent from galaxies and clusters are being lensed to a degree not matching what the content of

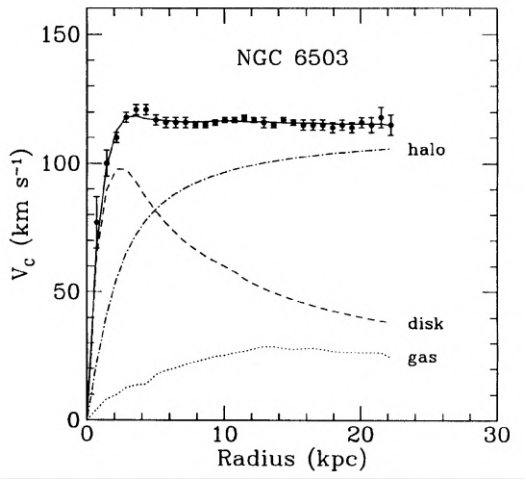

(a) Galactic rotation curve for NGC 6503 showing disk, gas and dark matter halo contribution required to match the observed data. Figure taken from [26].

(b) The dwarf spiral galaxy, NGC 6503, taken from the Hubble telescope.

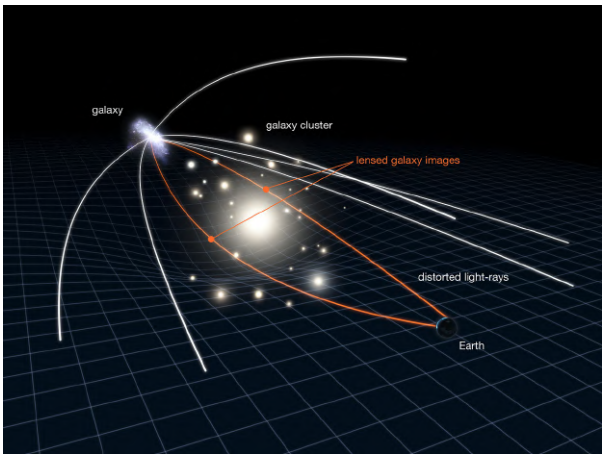

(a) Schematic diagram describing strong gravitational lensing. Credit: NASA and ESA.

(b) Image of galaxy cluster SMACS 0723 4 billion light years from Earth, taken by the James Webb space telescope depicting gravitationally distorted stellar objects. Credits: NASA, ESA, CSA, and STScI

observable stellar bodies allow for. The lensing effect can be easily quantified using the angular radius of the Einstein circle given by [27] where

$$\theta_E = \frac{2}{c}\sqrt{\frac{GM(D_S - D_L)}{D_S D_L}} \tag{2.5.11}$$

where M is the mass of the lens, D_L and D_S is the distance to the lens and the source respectively. The gravitational lensing method is used to approximate the mass of galactic sources, whereby numerous studies are consistent in demonstrating that the visible mass present represents only $10 - 20\%$ of the total [28].

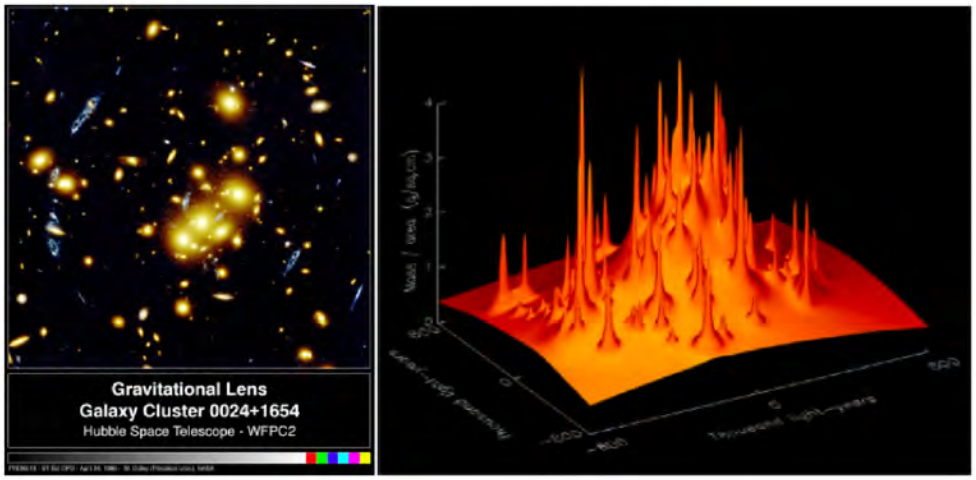

Figure 2.11: Left: The foreground cluster of galaxies gravitationally lensing the background galaxy (in blue) into multiple images. Right: A computer generated reconstruction of the lensing effect shows a smooth background component not accounted for by the masses of the luminous objects. Figure taken from [26].

From Fig. 2.11 above, it is clear that a smooth surface *gluing* the luminous masses is required to reconcile the observed lensing effect with theoretical predictions. The idea here is that dark matter is contained in clusters between the galaxies.

There are further examples, for that we refer to the reviews by [26, 28]. It is however clear, that there is an unexplained excess requiring extension of either the Standard Model of particle physics, or Cosmology.

2.6 Potential solutions to the BSM problems

It is clear from the elaborations above, that the Standard Model is incomplete. However the point of debate is around the question of which theory is the most suitable to extend the model. Some believe supersymmetric string theories may provide the answers, while others turn to Grand Unified theories such as E_6 [29] or $SO(10)$ [30]. For a long time the common consensus was that new physics at electroweak scale (such as *e.g.* supersymmetry [31], extra dimensions [32] or technicolor [33]) would be discovered at the LHC together with the Higgs boson, see [34, 35, 36, 37].

Chapter 3

Heavy Neutral Leptons

In this Chapter we present a new model that can cover three of the biggest gaps of the Standard Model while sharing all its success at accelerator level. It does so by adding several new neutrino-like states to the Standard Model.

3.1 Mass terms allowable due to symmetry

3.1.1 Dirac neutrino mass terms

It is in fact possible to write down a mass term for Dirac neutrinos allowable in the SM. For simplicity, one can consider a single generation of neutrino,

$$\mathscr{L}^D_{\text{mass}} = -m\bar{\nu}\nu \tag{3.1.1}$$

where one can define the neutrino field as

$$\nu = \nu_L + \nu_R \tag{3.1.2}$$

such that (3.1.1) can be expanded to

$$\mathscr{L}^D_{\text{mass}} = -m(\bar{\nu}_L\nu_R + \bar{\nu}_R\nu_L) \tag{3.1.3}$$

where the terms of $\bar{\nu}_L\nu_L$ and $\bar{\nu}_R\nu_R$ necessarily drop out due to parity:

$$\bar{\nu}_L\nu_L = \nu_L^\dagger\gamma^0\nu_L = \nu_L^\dagger\gamma^0 P_L\nu_L = \nu_L^\dagger P_R\gamma^0\nu_L = (P_R\nu_L^\dagger)\gamma^0\nu_L \stackrel{!}{=} 0. \tag{3.1.4}$$

Under introduction of $\alpha, \beta \in \{1, 2, ..., \mathcal{N}\}$ such right-handed neutrinos and $\dot{\alpha}, \dot{\beta} \in \{1, 2, ..., \mathcal{N}\}$ such left-handed neutrinos[1] (3.1.1) expands to

$$\mathscr{L}^D_{\text{mass}} = -M^D_{\alpha\beta}(\bar{\nu}_{\dot{\alpha}}\nu_\beta + \bar{\nu}_\alpha\nu_{\dot{\beta}}), \tag{3.1.5}$$

with $-M^D_{\alpha\beta}$ a mass matrix. It should be noted here that the dotted indices are used *only* to indicate left-handed states, the index is still summed over the same index as the right-handed, which is why $M^D_{\alpha\beta}$ only expresses right-handed indices.

[1] Taking inspiration from the standard spinor-helicity formalism

3.1.2 Majorana neutrino mass terms

Under Majorana representation, one can write right-handed neutrino fields as

$$\nu_\alpha = \nu_{\dot{\alpha}}^c = \mathcal{C}\bar{\nu}_{\dot{\alpha}}^T \tag{3.1.6}$$

and thus (3.1.5) can be written simply as

$$\mathscr{L}_{\text{mass}}^M = -\tfrac{1}{2} M_{\alpha\beta}^M (\bar{\nu}_{\dot{\alpha}} \nu_{\dot{\beta}}^c + \bar{\nu}_{\dot{\alpha}}^c \nu_{\dot{\beta}}). \tag{3.1.7}$$

3.2 Mechanisms of neutrino mass generation

3.2.1 Dirac neutrino mass

By introducing the right-handed neutrino singlets of (2.3.2)

$$\nu_\alpha = \{\nu_1, \nu_2, ..., \nu_n\},$$

where $n \in \mathbb{N}$, the fermionic sector of the Standard Model can be extended with a kinetic term for the right-handed neutrinos,

$$\mathscr{L}_f^\nu = -i\nu_\alpha \sigma^\mu D_\mu \nu_\alpha^\dagger \tag{3.2.1}$$

with D_μ and σ^μ defined in Sec. 2.3. However under the assumption that the right-handed neutrino does not couple to any of the gauge fields already in the SM gauge group, the covariant derivative reduces to a partial derivative, i.e. $D_\mu \to \partial_\mu$ such that (3.2.1) reduces to

$$\mathscr{L}_f^\nu = -i\nu_\alpha \sigma^\mu \partial_\mu \nu_\alpha^\dagger. \tag{3.2.2}$$

Under the further assumption that the neutrino is massive, the corresponding mass term must be generated by Yukawa coupling. To include Yukawa coupling with ν^α one can simply extend the Yukawa Lagrangian to couple with the right-handed neutrino singlet, ν_β, such that

$$\mathscr{L}_{\text{Yuk}}^\nu = -Y_{\alpha\beta}^\nu (L_{\dot{\alpha}} \cdot \tilde{\phi}) \nu_\beta - (Y_{\alpha\beta}^\nu)^* (L_{\dot{\alpha}} \cdot \tilde{\phi}) \nu_\beta \tag{3.2.3}$$

so that under electroweak symmetry breaking, one generates the following Dirac mass term of the form in (3.1.5)

$$\mathscr{L}_{\text{mass}}^D = -M_{\alpha\beta}^D (\bar{\nu}_{\dot{\alpha}} \nu_\beta + \bar{\nu}_\alpha \nu_{\dot{\beta}}). \tag{3.2.4}$$

where $M_{\alpha\beta}^D = \frac{\nu}{\sqrt{2}} (Y_{\alpha\beta}^\nu)^*$ and the conjugate $(M_{\alpha\beta}^D)^* = \frac{\nu}{\sqrt{2}} (Y_{\alpha\beta}^\nu)$. The Dirac mass matrix, $M_{\alpha\beta}^D$ is a complex $3 \times n$ matrix, where the associated sterile fields are singlets under the SM gauge group of $SU(3)_c \times SU(2)_L \times U(1)_Y$ and thus are non-interacting with any known forces and effect neither gauge invariance, renormalization or introduce any anomalies [38].

3.2.2 Lepton number

Taking a closer look at the Majorana mass term of (3.1.7), under a global $U(1)$ gauge transformation,

$$\nu_{\dot{\alpha}} \to e^{i\theta} \nu_{\dot{\alpha}} \tag{3.2.5}$$

the mass term transforms to

$$\mathscr{L}^M_{\text{mass}} \to -\tfrac{1}{2} M^M_{\alpha\beta}(e^{2i\theta}\bar{\nu}_{\dot{\alpha}}\nu^c_{\dot{\beta}} + e^{-2i\theta}\bar{\nu}^c_{\dot{\alpha}}\nu_{\dot{\beta}}). \tag{3.2.6}$$

which is not the same as (3.1.7), demonstrating a breaking of global $U(1)$ invariance: the term is not invariant under the transformation. If, instead of the transformation acting only on the left chiral field, it acted on the Majorana field such that

$$\nu \to e^{i\theta}\nu \tag{3.2.7}$$

then, the mass term would remain invariant under the transformation, however, in violation of the Majorana condition because

$$\nu^c_\alpha \to e^{-i\theta}\nu^c_\alpha \quad \text{and} \quad \nu^c_{\dot{\alpha}} \to e^{-i\theta}\nu^c_{\dot{\alpha}}. \tag{3.2.8}$$

It seems therefore, that lepton number *cannot* be conserved.

3.2.3 Majorana neutrino mass

Imposing the lepton number conservation [5, 39] one necessarily arrives at a theory with right-handed Dirac neutrinos in the above form. If one does not to impose a lepton number conserving symmetry (i.e. a global $U(1)$ symmetry), a *Majorana* mass term of the following form *can* be added to the Lagrangian [5, 38]

$$\mathscr{L}^M_{\text{mass}} = -\tfrac{1}{2} M^M_{\alpha\beta}(\bar{\nu}_{\dot{\alpha}}\nu^c_{\dot{\beta}} + \bar{\nu}^c_{\dot{\alpha}}\nu_{\dot{\beta}}). \tag{3.2.9}$$

There is however no *natural* way for this mass term to appear without further extension of the Standard Model from renormalizable terms. Considering terms that are non-renormalizable however, such as the dimension five *Weinberg operator* given [5, 40]

$$\mathscr{L}_{\text{dim-5}} = \tilde{M}^M_{\alpha\beta}(\bar{L}^\alpha \cdot \phi)(\tilde{\phi} \cdot L^\beta). \tag{3.2.10}$$

generating a mass terms of the form in (3.2.9), where $\tilde{M}^M_{\alpha\beta}$ must have dimension mass^{-1}. The dim-5 Lagrangian is not a suitable term as non-renormalizable terms are unacceptable in the SM. However, one must note here that the SM is not a final theory of everything, but instead an effective low-energy theory as a product of spontaneous symmetry breaking at high energies. It is therefore plausible that there are effective low-energy Lagrangian terms which respect the symmetries of the Standard Model but are non-renormalizable and is comparable to the effective non-renormalizable Fermi theory of weak interactions [2].

The effective Weinberg operator can manifest itself at tree level in many different ways:

- Type-I seesaw: New $SU(2)$ singlets, the right-handed neutrinos, ν_R, are assumed to exist carrying zero hypercharge. They are entirely sterile under the Standard Model gauge group and obtain mass terms from the previously elaborated Yukawa-Dirac coupling with the Higgs boson.
- Type-II seesaw: A new scalar triplet of the $SU(2)_L$ gauge group, $\Delta_L = (\Delta^{++}_L, \Delta^{+}_L, \Delta^0_L)$ is assumed, carrying hypercharge 2. They obtain their mass from direct Yukawa coupling with the lepton doublet, $Y^\nu L_L L_L \Delta_L$ (here suppressing the index α, β to do with lepton generation) and direct coupling to a Higgs doublet $\mu\phi\phi\Delta^*_L$.
- Type-III seesaw: Here it is assumed that a fermionic triplet of the $SU(2)_L$ may exist, $\Sigma = (\Sigma^+, \Sigma^0, \Sigma^-)$ carrying zero hypercharge and obtaining it's mass similarly to the Type I model.

Assuming a type-I seesaw mechanism, one can construct a Lagrangian under the extension of $I = 1...\mathcal{N}$ Majorana neutrinos, ν_I, with associated mass matrix M_I,

$$\begin{aligned}\mathscr{L}^{\nu}_{\text{Type-I seesaw}} =& \mathscr{L}^{\nu}_{f} + \mathscr{L}^{\nu}_{\text{Yuk}} + \mathscr{L}^{M}_{\text{mass}} \\ =& - i\bar{\nu}_I \partial\!\!\!/ \nu_I - Y_{\nu}^{\alpha I} \bar{L}_{\dot{\alpha}} \tilde{\phi} \nu_I - \tfrac{1}{2} M_I \bar{\nu}_I \nu_I^c + \text{h.c.}\end{aligned} \tag{3.2.11}$$

where Y_ν is the complex Yukawa matrix and M_I is a complex symmetric Majorana mass matrix. After electroweak symmetry breaking, the Lagrangian generates Dirac mass matrices as previously demonstrated, resulting in a non-diagonal, complex, symmetric Dirac-Majorana mass matrix

$$\mathscr{L}^{\nu}_{\text{mass}} = -\frac{1}{2}(\bar{\nu}^c_{\dot{\alpha}}, \bar{\nu}_\beta) \underbrace{\begin{pmatrix} M_L & (M^D)^T \\ M^D & M_R \end{pmatrix}}_{M^{\text{DM}}} \begin{pmatrix} \nu^c_{\dot{\alpha}} \\ \nu_\beta \end{pmatrix} \tag{3.2.12}$$

with $M_R = \text{diag}(M_I...)$ while SM gauge invariance imposes the condition[2] that $M_L \overset{!}{=} 0$. In the pure Dirac limit, where neutrinos are purely Dirac in nature, a further condition is imposed such that $M_R = 0$, and in the pseudo-Dirac limit, M_R must be small with respect to M^D. Further, unless explicitly specified, the $\alpha\beta$ indices on the mass matrices will be suppressed for pedagogical reasons.

If the eigenvalues of M_R^M are greater than those of M^D, the mass matrix M^{DM} can be block diagonalized, up to corrections of the order $(M_R)^{-1} M^D$ with

$$V^T M^{\text{DM}} V \simeq \begin{pmatrix} M_{\text{light}} & 0 \\ 0 & M_{\text{heavy}} \end{pmatrix}, \tag{3.2.13}$$

where

$$V \simeq \begin{pmatrix} 1 - \frac{1}{2}(M^D)^\dagger (M_R M_R^\dagger)^{-1} M^D & \left(M_R^{-1} M^D\right)^\dagger \\ -M_R^{-1} M^D & 1 - \frac{1}{2} M_R^{-1} M^D M^{D\dagger} M_R^{-1\dagger} \end{pmatrix}. \tag{3.2.14}$$

This leads to the following mass sub-matrices,

$$M_{\text{light}} \simeq -\frac{(M^D)^T M^D}{M_R} \quad \text{and} \quad M_{\text{heavy}} \simeq M_R, \tag{3.2.15}$$

and the following mass eigenstates $\nu = (n_1, n_2, n_3)$ and $N = (n_4, n_5, ..., n_{\mathcal{N}+3})$. The relation between M_{light} and M_{heavy} in the first part of (3.2.15) is known as the *see-saw* mechanism and provides a natural reason as to why neutrino masses are small: because they are suppressed by a large mass, M_{heavy}. The masses, M_R, are not constrained by gauge symmetry, and thus can be arbitrarily large as $M_R \gg Y_\nu v$. As M^D likely has order $\simeq Y_\nu v$, one finds that the active neutrino masses, $m_\nu \ll m_{e,u,d}$ as per [41].

The mass eigenstates mix with the flavour eigenstates $\nu_{\dot{\alpha}}$ and ν_I as

$$\nu_I \simeq N_I \tag{3.2.16}$$

$$\nu_{\dot{\alpha}} \simeq U^{\text{PMNS}}_{\alpha i} \nu_i + \Theta_{\alpha I} N_I \tag{3.2.17}$$

$$\Theta_{\alpha I} \simeq \frac{M^D_{\alpha I}}{M_I} \tag{3.2.18}$$

where U^{PMNS} is the PMNS matrix, the mixing angle $\Theta_{\alpha I}$ represents mixing strength between N_I HNLs and *active* flavour states $\nu_{\dot{\alpha}}$: heavy neutral leptons mix with the *active* SM neutrinos!

[2] This mass term may however come from a Weinberg dim-5 operator [38]

Taking the Yukawa coupling to be uncorrelated and $\mathcal{O}(1)$ then (3.2.15) leads to neutrino masses of order $\frac{v^2}{|M_R|}$ with $M_R \sim 10^{15}$ being around some GUT scale, leading to neutrino masses of the order $|M_{\text{light}} \leq 10^{-1}$ eV. One could also take M_R to be around the electroweak scale (100-1000 GeV) where the smallness of the light neutrino masses is attributed to small Yukawa coupling $Y_{\alpha I} \sim \frac{1}{v}\sqrt{|M_{\text{light}} M_{\text{heavy}}}$.

In the flavour basis, one can draw Feynman diagrams representing their phenomenology. As they are introduced to the fermionic sector as neutrinos, they behave in much the same way as the active neutrinos, by couplings in the electroweak and fermionic sectors, which can be seen from the following Lagrangian terms given in [42, 43]:

$$\begin{aligned}\mathcal{L}_{\text{EW}} =& \frac{m_W}{v} W_\mu^+ \overline{N^c}_I U^*_{\alpha I} \gamma^\mu (1-\gamma_5)\, \ell^-_{\dot{\alpha}} + \frac{m_Z}{\sqrt{2}v} Z_\mu \overline{N^c}_I U^*_{\alpha I} \gamma^\mu (1-\gamma_5)\, \nu_{\dot{\alpha}} \\ &+ \frac{M_N}{v} h \bar{\nu}_{\dot{\alpha}} U^*_{\alpha I} \gamma^\mu (1-\gamma_5)\, N_I + \text{ h.c.}\end{aligned} \tag{3.2.19}$$

In the following figures, the electroweak couplings are presented for processes with $W^\pm$ coupling (a), Z^0 coupling (b) and h coupling (c).

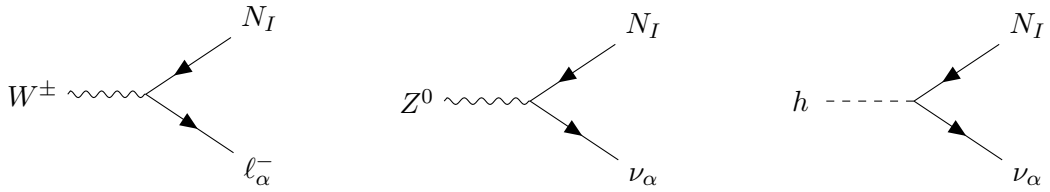

(a_1) (b_1) (c_1)

Figure 3.1: Phenomenology of N interactions with electroweak sector of SM where (a) is charged-current interaction, (b) is neutral-current and (c) is with the Higgs boson. The interactions above are suppressed by a factor $|\Theta_{\alpha I}|^2$ for $\alpha \in \{e, \mu, \tau\}$ and $I \in \{1, 2, ..., \mathcal{N}\}$.

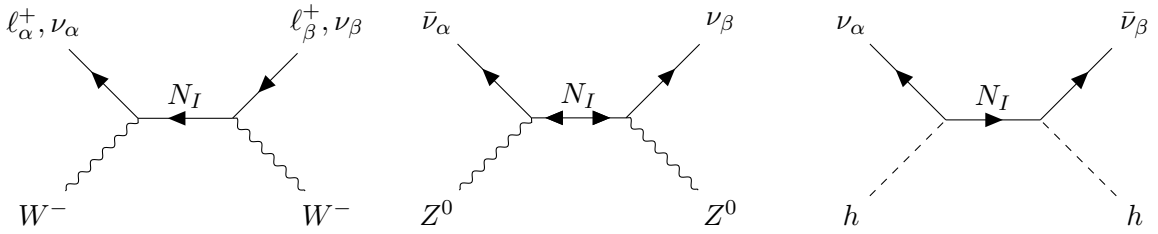

(a_2) (b_2) (c_2)

Figure 3.2: In the case of an *off-shell* HNL, all diagrams are suppressed by a factor $|\Theta_{\alpha I}|^2 |\Theta_{\beta I}|^2 \sim \Theta^4$. However, in the case of the HNL being *on-shell* the diagrams are suppressed by a factor $|\Theta_{\alpha I}| \cdot |\Theta_{\beta I}| \sim \Theta^2$ because the matrix element contains a factor $\frac{1}{\Gamma} \sim \frac{1}{\Theta^2}$. These processes can be lepton number and lepton flavour violating.

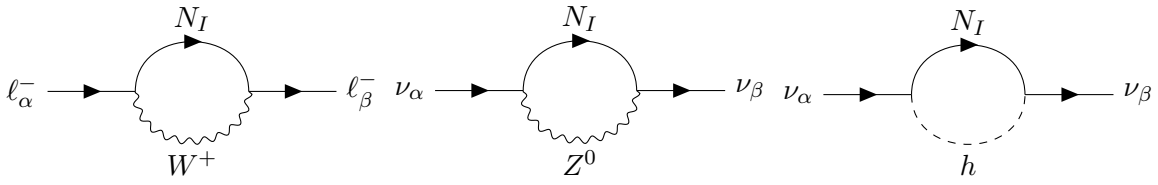

(a_3) (b_3) (c_3)

Figure 3.3: Examples of loop mediated lepton flavour violating processes in line with the above processes.

A further point of interest of the phenomenology lies in the process known as *neutrinoless double-beta decay* $(0\nu\beta\beta)$ first proposed in [44] with Feynman diagram shown below in Fig. 3.4.

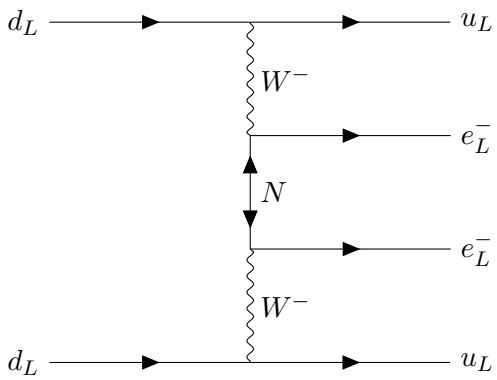

Figure 3.4: A neutrinoless double-beta decay process first proposed by [44]

which can only occur if the HNL is found to exist, thus providing a falsifiable claim to either prove or disprove it's existence. There exist however supersymmetric models with scalar neutrinos that would also lead to $0\nu\beta\beta$ processes (see e.g. [45]).[3]

The HNLs can decay leptonically, and thus, for a single species of N with associated mixing matrices $\Theta_e, \Theta_\mu, \Theta_\tau$, the inverse lifetime is defined given [42]:

$$\tau^{-1} = \Gamma_N(M_N, \Theta_e, \Theta_\mu, \Theta_\tau) = \sum_{\rho=e,\mu,\tau} |\Theta|^2 \times \hat{\Gamma}_\rho(M_N) \tag{3.2.20}$$

with $\hat{\Gamma}_\rho(M_N) = \Gamma_N(M_N, \delta_{\rho e}, \delta_{\rho\mu}, \delta_{\rho\tau})$ being the total decay width after setting $\Theta_\rho = 1$ and the two other mixing matrices to zero. The relevant decay modes will be presented at a later point in Sec. 4.

3.3 Filling the gaps in the Standard Model

In this Section we sketch briefly how HNLs can fill the gaps in the Standard Model, discussed in Chapter 2, specifically in Section 2.5.

3.3.1 HNLs and neutrino masses

As we have just seen, neutrino masses can be generated very naturally from the seesaw mechanism, and thus the idea of the active neutrinos being massive, as well as oscillating between flavour states is well defined within this framework.

3.3.2 HNLs and baryogenesis

The introduction of heavy neutral leptons to the SM Lagrangian is required to reconcile two of the Sakharov conditions: CP violation and a deviation from thermal equilibrium [47].

The Lagrangian for the νMSM, with eigenvalues of M_N far above the electroweak scale, is a possible solution to generating cosmological baryon number [48] without resorting to Grand Unified theories. In this model, a lepton number excess, originating from Majorana mass terms, may transform into a baryon number excess through unsuppressed baryon-number violations of electroweak processes at high temperatures: a thermal leptogenesis in which the CP-asymmetry responsible for the BAU is generated during the *freezout* and decay of right handed neutrinos [24].

[3] Further exotic diagrams such as *HNL Penguins* also exist, see *e.g.* [46]

Under the introduction of heavy neutral leptons, the Yukawa sector describing the coupling between N and the higgs field can be written as [49], where again we reiterate that $I \in \{1, 2, ..., \mathcal{N}\}$,

$$\mathscr{L}_Y = h_{\alpha I} \left(\bar{\nu}_{\dot{\alpha}} \ \bar{\ell} \right) \begin{pmatrix} -\chi^- \\ (H - i\chi^0)/\sqrt{2} \end{pmatrix} N_I + \text{h.c.} \tag{3.3.1}$$

where H is the CP-even Higgs field, χ^0 is the CP-odd Higgs scalar and $\chi^\pm$ the charged Higgs scalars[4]. The Lagrangian in (3.3.1) leads to the following tree level diagrams for the decay modes of N,

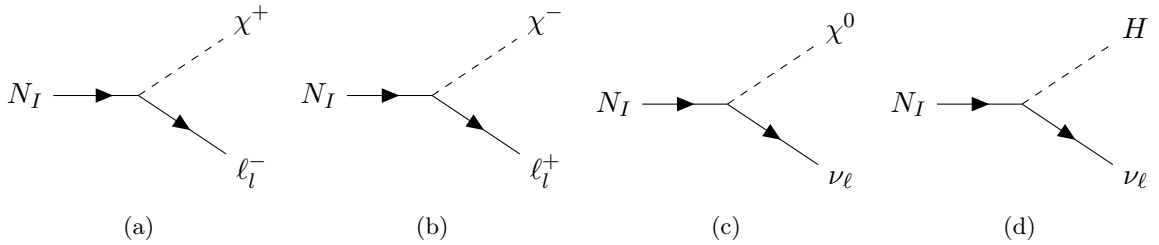

(a) (b) (c) (d)

Figure 3.5: Tree level diagrams of the semi-leptonic decay modes of N.

The decay widths occur with differing probabilities if CP is violated, which can occur through one-loop corrections of diagrams (a)-(d), such as the following two for process (a):

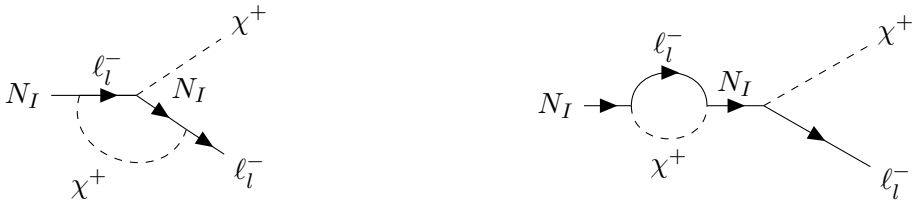

(a_1) (a_2)

Figure 3.6: Loop corrections to the semi-leptonic decay mode of N pictured in (a).

There is an inherent *decay asymmetry* [47] coming from the interference of the loop-contributions which can lead to a *resonant enhacement*. This effect eventually leads to leptogenesis.

Leptogenesis can however also be caused by HNL oscillations, where the decay asymmetry of the type discussed earlier is not the driver, but rather here leptogenesis occurs as a consequence of HNLs oscillating through CP violating phases [47].

Leptogenesis through HNL oscillations necessitate GeV scale neutrinos, while in the resonant leptogenesis model, TeV scale HNLs are required.

3.3.3 HNLs and dark matter

For HNL masses, $M_N < 2m_e$, the dominating decay channel of the HNL is the *invisible*, i.e. $N_I \to \nu_{\dot{\alpha}} \nu_{\dot{\beta}} \bar{\nu}_{\dot{\beta}}$ with total decay width given [50]:

$$\Gamma(N \to \nu_{\dot{\alpha}} \nu_{\dot{\beta}} \bar{\nu}_{\dot{\beta}}) = \frac{G_F^2 M_N^5}{96\pi^3} \sum_{\alpha=e,\mu,\tau} |\Theta_\alpha|^2 \approx \frac{1}{1.5 \times 10^{14} \text{ sec}} \left(\frac{M_N}{10 \text{ keV}} \right)^5 |\Theta|^2 \tag{3.3.2}$$

[4] As we are considering physics before electroweak symmetry breaking, the fields are all massless, however as the Universe expands, and the temperature, $T \to 0$ such that symmetry breaking may occur. At this point, H is understood to be the massive SM Higgs boson, with $\chi^0, \chi^\pm$ being the Goldstone bosons eaten by the longitudinal degrees of freedom of the $Z^0, W^\pm$ gauge bosons respectively [49].

with $\Theta^2 = \sum_{\alpha=e,\mu,\tau} |\Theta_\alpha|^2$. Considering that DM is still abundant, one can constrain (3.3.2) by imposing the condition that the lifetime, corresponding to the process in (3.3.2), be greater than the age of the Universe $\sim 4.4 \times 10^{17}$ sec. Then, one can solve for the sum of the mixing angles, Θ^2 such that

$$\Theta^2 < 3.3 \times 10^{-4} \left(\frac{10 \text{ keV}}{M_N} \right)^5 . \tag{3.3.3}$$

This condition implies that the DM neutrino may only contribute very weakly to the active neutrino masses, with $\delta m_\nu \sim M_N \Theta^2$ being smaller than the solar neutrino mass difference, thus, at least two more HNLs are required to explain the observed mass differences and also give rise to neutrino masses [50].

The loop mediated radiative decay of $N_I \to \gamma \nu_{\dot{\alpha}}$ presented in Fig. 3.7 below,

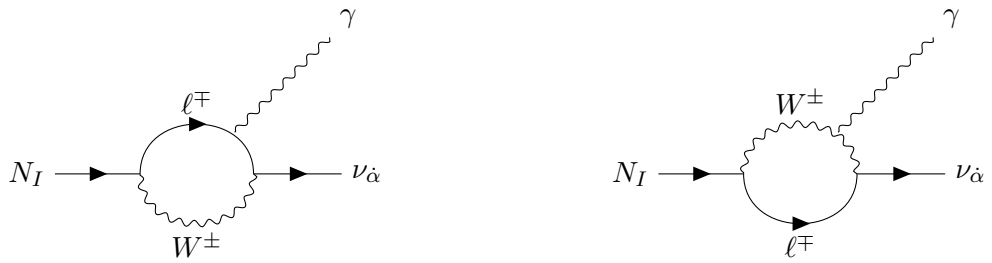

Figure 3.7: Feynman diagram of radiative decay of an HNL $N_I \to \gamma + \nu_{\dot{\alpha}}$ strongly inspired by [50].

given by following decay width [50],

$$\Gamma(N_I \to \gamma \nu_{\dot{\alpha}}) = \frac{9 \alpha G_F^2}{256 \pi^4} \Theta^2 M_N^5 = 5.5 \times 10^{-22} \Theta^2 \left(\frac{M_N}{1 \text{ keV}} \right)^5 \text{ sec}^{-1}, \tag{3.3.4}$$

produces a photon with energy $E = \frac{1}{2} M_N$! A monochromatic photon in the X-ray region produced by such a process could then potentially be detectable from Earth as astrophysical sources of DM overdensities.

With respect to recent developments of the field, an unidentified monochromatic 3.5 keV line has been detected from galactic clusters, the Andromeda and Milky Way galaxies, the signal of which can be interpreted as a photon in a radiative decay process, as the one presented in fig. 3.7, of an HNL of mass ~ 7 keV with $\sin^2 2\theta \sim 10^{-10}$.

3.3.4 The Neutrino Minimal Standard Model

Being *a priori* agnostic about *how* a Majorana mass term may arise, under inclusion of heavy neutral leptons from the Type-I seesaw Lagrangian, and a certain arrangement of ones theoretical parameters, the above gaps in the SM can be filled with a coherent mechanism [51, 52]. The approach received a name *Neutrino Minimial Standard Model* (or νMSM for short), see *e.g.* [53].

One can assume an extension of the SM with *three* HNLs (for $I \in \{1, 2, 3\}$), where the lightest HNL, N_1, can have a mass of between $1 - 50$ keV with mixing between $10^{-7} - 10^{-13}$ leading to a lifetime of $\tau_{N_1} \gg \tau_{\text{Universe}}$ so that this particle may be a Dark Matter candidates. Two other particles, N_2 and N_3, can explain the origin of neutrino masses and phenomenon of oscillations. If they are also to explain the generation of baryon asymmetry of the Universe, their masses should be above 100 MeV range and

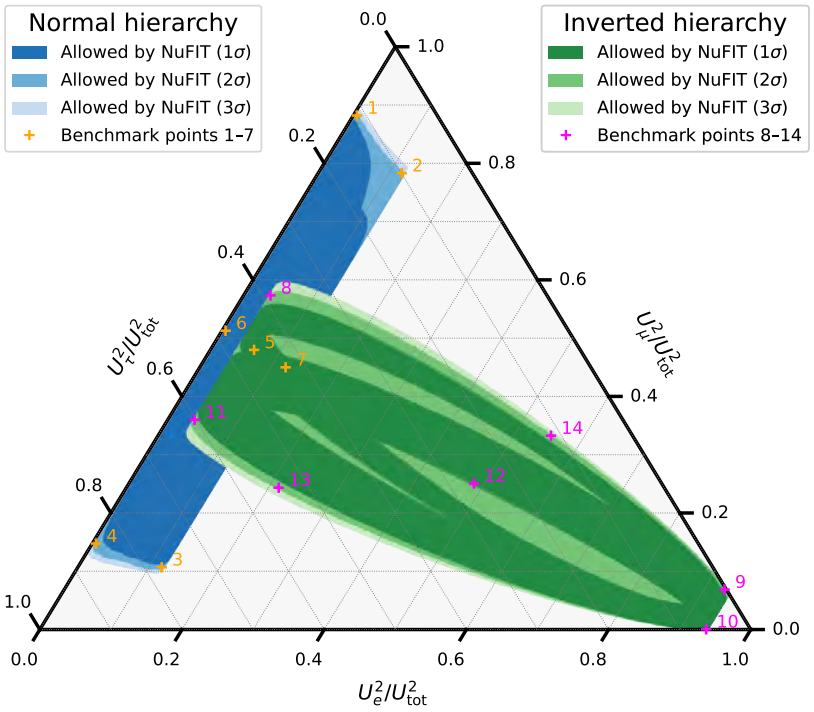

Figure 3.8: Ternary plot depicting the experimental constraints obtained from NuFIT 5.0 neutrino oscillation data[55]. $|\Theta_I|^2$ is defined as $\sum_{\alpha=e,\mu,\tau}$ and $I = 2$ or 3. Figure from [1].

be degenerate, $|M_2 - M_3| \ll M_2, M_3$. Thus, it is convenient to their masses, M_2 and M_3 in terms of a central mass and a physical mass splitting such that

$$M_2 = M - \frac{\delta_M}{2} \quad \text{and} \quad M_3 = M + \frac{\delta_M}{2}. \tag{3.3.5}$$

The mass splitting, δ_M, must give rise to the observed neutrino masses[5]. Under the Casas-Ibarra parametrization, the HNL mixing angles, $\Theta_{\alpha I}$, can be related to their masses, $\hat{M}_N = \text{diag}(M - \frac{\delta_M}{2}, M + \frac{\delta_M}{2})$, the PMNS matrix U_{PMNS} (including one Majorana phase η) and the light neutrino masses $\hat{M}_\nu = \text{diag}(m_1, m_2, m_3)$, in accordance with [1, 54], by:

$$\Theta = i U_{\text{PMNS}} \hat{M}_\nu^{-\frac{1}{2}} \Omega \hat{M}_N^{-\frac{1}{2}} \tag{3.3.6}$$

where Θ is a matrix composed of mixing angles $\Theta_{I\alpha}$, and Ω is a 3×2 matrix in which an arbitrary 2×2 complex orthogonal matrix depending on complex angle ω and parity $\xi \in \pm 1$, is embedded such that $\Omega^T \Omega = \mathbb{1}$. The exact form of which will depend on the neutrino hierarchy, see *e.g.* [1]. The number of free parameters then reduces to one complex parameter, ω, and three real ones, HNL mass, M_N, and their mass splittings δ_M and the Majorana phase η. The remaining parameters have to do with mixing angles, which can be obtained and constrained from data. Shown in 3.8 is an estimate from neutrino oscillation data by NuFIT [55] showing the experimental constraints on the HNL mixing angles $\Theta_{\alpha I}$.

The plot was obtained by scanning over the remaining free parameters of the Cassas-Ibarra parameterization of (3.3.6). It is useful to indicate that for experimental sensitivities to be compared irrespective of choice of parameterization, the convention for *single-flavour mixing* is to necessarily set the mixing of the only relevant mixing angle to one, and the rest to zero. This corresponds to points on Fig. 3.8 that are inconsistent with neutrino oscillation data, namely, the three corners of the ternary plot.

[5] in the regime of massless neutrinos, the mass splitting is necessarily $\delta_M = 0$ and the cancellation is exact [1].

Under these considerations, the theoretical basis for the current study is setting the parameters of N_1 in accordance with being a Dark matter candidate, elaborated above, with low enough mixing to cause it to decouple, and further restricting the masses of N_2 and N_3 to the GeV scale necessarily above 100 MeV, and degenerate. The parameter space will be probed between a mass range of $0.5 \geq M_N \leq 20$ GeV and a total mixing angle in the range of $1 \times 10^{-10} \geq \Theta^2 \leq 1$. [6]

[6]However, under a physically reasonable choice of mixing angles, consistent with *both* the inverted and normal hierarchy, one can chose model parameters such that $\Theta_\mu = \Theta_\tau = 0.5$ with $\Theta_e = 0$ such that for the process of $pp \to W^\pm \to N\mu^\pm, N \to \mu^+\mu^-\nu_\mu$ an exclusion region for the parameter space plot is presented in Sec. A.2

Chapter 4

Physical processes of interest

In this Chapter we summarise main physical processes related to production and decay of heavy neutral leptons.

Naively, HNLs cannot be observed directly, being *sterile* with respect to all gauge interactions of the SM.[1] These sterile states are, however, the *flavour eigenstates*, not having well-defined propagation equations of motion. The corresponding *mass eigenstates* do carry weak-like interactions, suppressed as compared to the neutrino interactions by a factor $\Theta_{\alpha I}$ (see Eq. 3.2.16 in Chap. 3). The mixing angle is necessarily small, $|\Theta_{\alpha I}| \ll 1$. HNL properties dictate the following "experimental wishlist" :

1. Due to the weakness in their interactions, one would require high-intensity experiments to be able to *produce* such particles.

2. Owing to their macroscopic decay length, detect its decay products, experiments with large *decay volume* are needed.

3. Finally, given that the HNL mass is not constrained from above, their parent particles should be as heavy as possible to probe a wide mass range.

To wit, the Large Hadron Collider proves to be one of the optimal hosts of experiments for the purpose. As the LHC produces large amounts of hadrons (not surprising, given its name), it proves interesting at the very least to consider HNLs decaying from mesons or gauge bosons.[2]

Much of the low-hanging fruit of HNL searches has been gathered in the form of prompt searches, see ref [57] summarising the recent searches. However one increasing area of interest and importance is the search for Long Lived Particles (LLPs) [58]. Roughly speaking these are particles with proper distance $c\tau \gtrsim 1\,\text{cm}$ [59]. If such particles can be produced copiously, their substantial decay has very distinct experimental signatures, as they can travel macroscopic distances from their *production vertex*[3] (PV) to their *decay vertex* (DV), see fig.4.1 on the facing page.

[1] We remind that the Yukawa interactions of right-handed neutrinos, ν_R with the Higgs and left-handed lepton doublets imply that HNLs carry no charges under the SM gauge group.

[2] Other potentially interesting experiments are those of *Intensity Frontier*, see *e.g.* [56].

[3] The *production vertex* is the point of production for the particle in question, and the *decay vertex* is the point of decay.

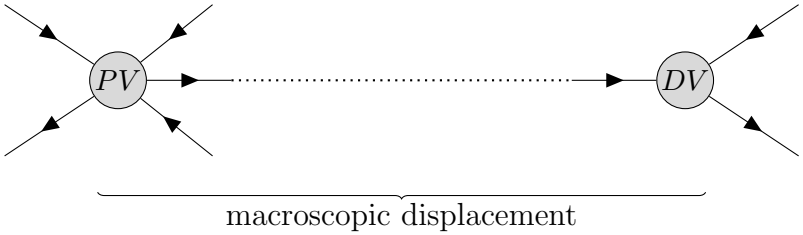

Figure 4.1: Schematic representation of a process with a displaced vertex. PV stands for *production vertex* (a point in space-time where the primary interaction took place) and DV is the *decay vertex*, located some macroscopic distance away from PV. The lines are only illustrative and the figure should not be interpreted as a literal Feynman diagram.

A fundamental component in displaced vertex searches is the so called *decay volume*, which is the volume in which the specific search scheme accepts the displaced vertices to happen. The size and placement of the decay volume are important factors when it comes to which part of the LLPs parameter space an experiment can probe. Generally speaking, the bigger decay volume, the more effective the search will be. This comes down to the laws of exponential decay, which tells us that the probability to decay between a distance ℓ_{min} and a distance ℓ_{max} is given by

$$P_{\text{dec}} = e^{-\ell_{\text{min}}/v\tau\gamma} - e^{-\ell_{\text{max}}/v\tau\gamma}, \tag{4.0.1}$$

where τ is the proper lifetime of the particle, γ is its associated Lorentz factor and v is the speed of the particle, related to the speed of light c via $v = c\sqrt{1 - \frac{1}{\gamma^2}}$.[4]

LLP searches at the LHC are ongoing endeavour [58], including long-lived HNL searches [60, 61, 62]. The work in this thesis is aimed at probing the prospects of expanding the search for LLPs at LHC to include:

(i) Decay processes of heavy-flavoured mesons (see Sec. 2.4.4)

(ii) Decay processes of $W^{\pm}$ bosons.

The prospects of searches for processes in category (i) will be done for both ATLAS and SND experiments and the processes in category (ii) only for the ATLAS experiment. Both of these experiments will receive a proper introduction below. The following section discusses two such process types in which indirect detection of an HNL may be possible from considerations of displaced vertices.

4.0.1 Factorisation of the full process

In complete generality, one has two consider the process $pp \to f$ where f are all possible final states (involving two muons, neutrinos, jets, etc). However, owing to the fact that many of the intermediate particles are sufficiently long-lived, we can split this complex process into a set of subprocesses:

S_0: pp collision produces parent particle χ $\sigma(pp \to \chi)$;

S_1: The parent particle χ decays to HNL plus leptons $\chi \to N + \ell_\alpha$;

S_2: After traveling some (macroscopic) distance, HNL decays to a pair of muons and neutrino, $N \to \mu^+\mu^-\nu_\alpha$.

[4] For most of the work considered in this thesis the particles are ultra-relativistic ($\gamma \gg 1$) and therefore $v \simeq c$.

4.1 Processes involving charged mesons

Charged heavy flavour mesons, discussed in Section 2.4.4 on page 16, possess purely leptonic decay channels: $M^{\pm} \to \ell^{\pm}_{\alpha}\nu_{\alpha}$, for $\alpha \in \{e, \mu, \tau\}$. The same process can give rise to an HNL instead of the neutrino in the final state, $M^{\pm} \to \ell^{\pm}_{\alpha}N$. This process is however suppressed by a factor $|\Theta_{\alpha I}|^2$, and by a factor dependent on the available phase-space. These meson processes put limits on the HNL mass, as the HNL mass must be smaller or equal to the difference of the meson and lepton mass: $m_N \leq m_M - m_\ell$. With this consideration, it becomes favorable to consider heavy mesons, such as B or D mesons, as this extends the possible search boundary of the heavy neutral lepton as compared to the decay of light mesons, such as pions, π, or kaons, K.

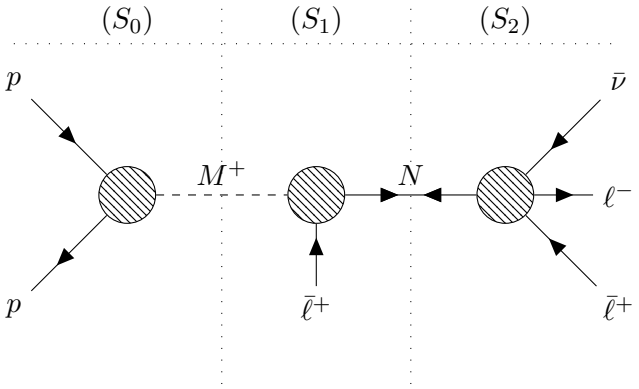

Figure 4.2: Schematic diagram of relevant sub-processes S_0, S_1, S_2 for the decay of charged heavy mesons $M^{\pm}$. The sub-processes $S_{0,1,2}$ are defined as in Section 4.0.1.

Looking closer at sub-process S_1 and S_2 in which a charged meson, $M^{\pm}$, produced from proton-proton collisions, decays leptonically into a heavy neutral lepton (HNL) and a *prompt*-lepton[5]. This decay is mediated by an *off-shell* $W^{\pm}$-boson. In sub-process S_2, the HNL, N, decays tri-leptonically, into $N \to \ell\ell\nu$.

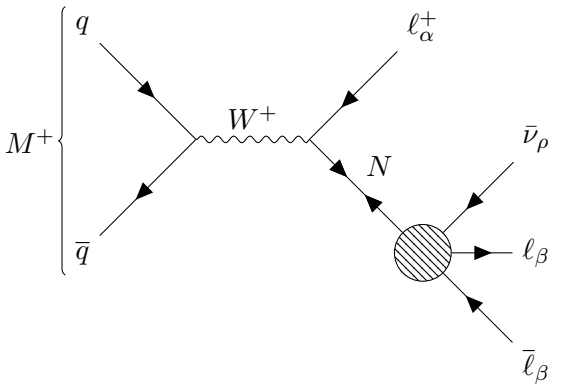

Figure 4.3: Purely leptonic decay mode of a charged meson, M^+, produced from proton-proton collisions, into an HNL, N, and prompt lepton, ℓ, with further di-leptonic decay mode of HNL.

These two processes are shown in more detail above in Fig. 4.3. The effective vertex shown above is to be understood as the sum of all charged-current and neutral current mediated decays.

[5]We will henceforth refer to the lepton produced *together* with the HNL as the *prompt*-lepton, and all other leptons produced subsequently from the HNL as *displaced*-leptons.

In the current section, the indices, $\alpha, \beta, \rho \in \{e, \mu, \tau\}$, are used to indicate lepton flavour. Setting $\alpha = \rho$ requires only a single mixing angle of the HNl to be determined, as e.g. in the process below in Fig. 4.4:

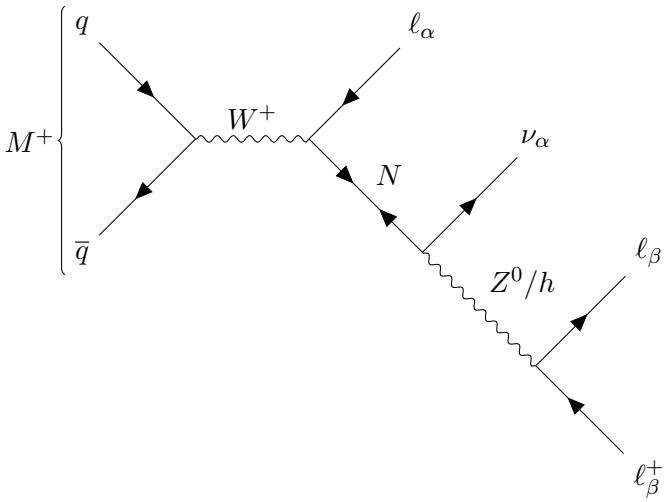

Figure 4.4: Purely leptonic decay mode of a charged meson, produced from proton-proton collisions, into an HNL, N, and prompt lepton, ℓ, with further di-leptonic decay mode of HNL.

where the only relevant mixing angle for the HNL that appears in the computation of the Feynman diagram, is Θ_α. It is useful to note that in this case, where $\alpha = \rho \neq \beta$, the contributing diagrams will only be neutral-current mediated by either the Z^0 or h boson. A charged-current mediated process will then occur only for single flavoured processes, i.e. when $\alpha = \beta = \rho$ and namely only for lepton number conserving processes, shown below in Fig. 4.5.

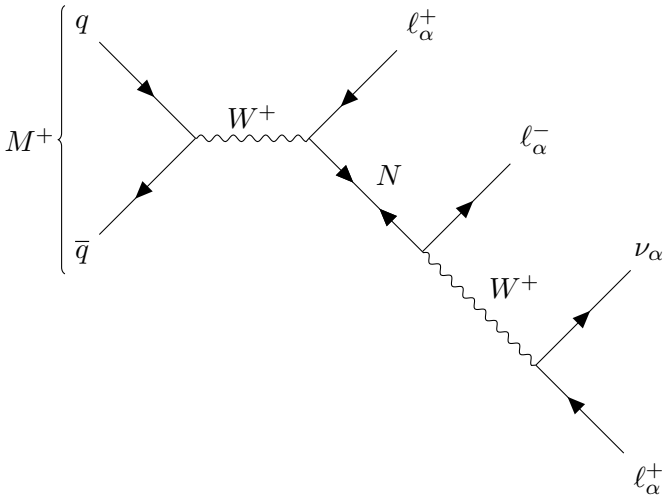

Figure 4.5: Purely leptonic decay mode of a charged meson, produced from proton-proton collisions, into an HNL, N, and prompt lepton, ℓ, with further di-leptonic decay mode of HNL.

Considering the MS can only detect displaced leptons of the μ flavour, i.e. the case where the displaced-leptons is a *di*-muon pair produced from the decay of an HNL in the S_2 sub-processes. Returning to Fig. 4.3, and under the assumption that the HNL is *on-shell*, the process can effectively be *factorized* into the following two sub-processes:

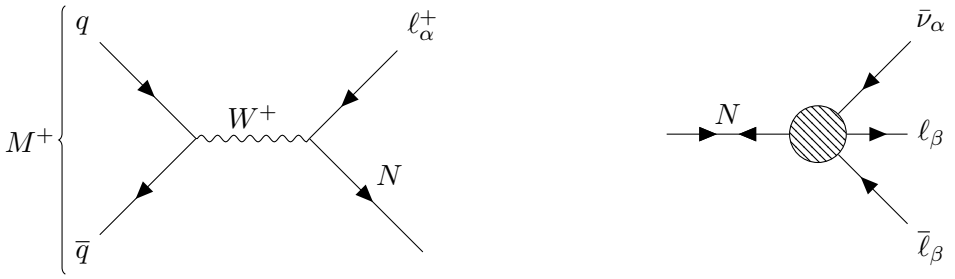

Sub-process S_1 Sub-process S_2

Figure 4.6: Charged current mediated interaction of the charged meson process

where sub-process S_2 is the sum of the following charged and neutral current mediated decay Feynman diagrams:

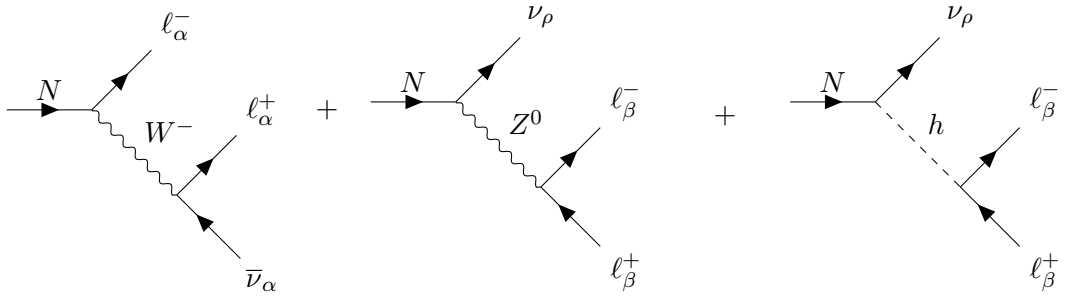

Charged-current decay Neutral-current decay Higgs-mediated decay

Figure 4.7: The three relevant Feynman diagrams contributing to the $N \to \ell\ell\nu$ decay width, where charge-conjugated diagrams have been omitted.

The decay width depicted in sub-process S_1 is a fully leptonic decay of a charged meson, $M^\pm$, to an HNL, N, and prompt lepton, $\ell^\pm$, and can be computed following [42] as,

$$\Gamma\left(h \to \ell_\alpha N\right) = \frac{G_F^2 f_h^2 m_h^3}{8\pi} \left|V_{UD}\right|^2 \left|U_\alpha\right|^2 \left[y_N^2 + y_\ell^2 - \left(y_N^2 - y_\ell^2\right)^2\right] \sqrt{\lambda\left(1, y_N^2, y_\ell^2\right)}, \tag{4.1.1}$$

where $y_\ell = m_\ell / m_h, y_N = M_N / m_h$ and λ is the Källén function defined [63]

$$\lambda(a,b,c) = a^2 + b^2 + c^2 - 2ab - 2ac - 2bc. \tag{4.1.2}$$

The decay width depicted in sub-process S_2, namely for the process of $N \to \nu_\alpha \ell_\beta \overline{\ell}_\beta$ as a sum of the contributing charged and neutral current diagrams can be written[42] as

$$\begin{aligned}\Gamma(N \to \nu_\alpha \ell_\beta \overline{\ell}_\beta) = \frac{G_F^2 M_N^5 |U_\alpha|^2}{192\pi^3} \big[& C_1 \left(1 - 14x^2 - 2x^4 - 12x^6\right)\zeta + 12x^4(x^4 - 1)L(x)\big) \\ & + 4C_2 \left(x^2(2 + 10x^2 - 12x^4)\zeta + 6x^2(1 - 2x^2 + 2x^4)L(x)\right)\big],\end{aligned} \tag{4.1.3}$$

where $x = \frac{m_\ell}{M_N}$, $L(x) = \log\left[\frac{1 - 3x^2 - (1-x^2)\zeta}{x^2(1+\zeta)}\right]$ and $\zeta = \sqrt{1 - 4x^2}$. The values of C_1 and C_2 depend on whether the process is charged-current mediated, in the case of $\alpha = \beta$, or neutral-current mediated, in the case of $\alpha \neq \beta$: The reason for splitting the process into the previously elaborated two sub-processes

f	C_1	C_2
$\alpha = \beta$	$\frac{1}{4}\left(1 + 4\sin^2\theta_W + 8\sin^4\theta_W\right)$	$\frac{1}{2}\sin^2\theta_W\left(2\sin^2\theta_W + 1\right)$
$\alpha \neq \beta$	$\frac{1}{4}\left(1 - 4\sin^2\theta_W + 8\sin^4\theta_W\right)$	$\frac{1}{2}\sin^2\theta_W\left(2\sin^2\theta_W - 1\right)$

Table 4.1: Coefficients C_1 and C_2 for the charged and neutral mediated decay

is partly technical. In simulating decays of this type, one can use Monte Carlo generators of the types elaborated upon in chapter 4, namely, PYTHIA for the generation of a meson sample, $M^{\pm}$ of sub-process S_0, and MADGRAPH for the subsequent decays described in S_1 and S_2.

If one considers the rest frame decay of the charged mesons, one can utilize a low energy effective field theory to simulate the decay to an *on-shell* heavy neutral lepton. In this regime, one can use the EFFECTIVE_HEAVYN model with MADGRAPH which proves most appropriate[64]. Thereafter, one can use the SM_HEAVYN model [65] for the purely leptonic decay mode of the heavy neutral lepton.

4.2 Processes involving on-shell $W^{\pm}$-bosons

The W-process can also be split into sub-processes as well, however this is superfluous as the entire process can be simulated in the SM_HEAVYN model, as no low energy effective field theoretical model is required for computation of meson dynamics. The process is shown below in Fig. 4.8 The contributing

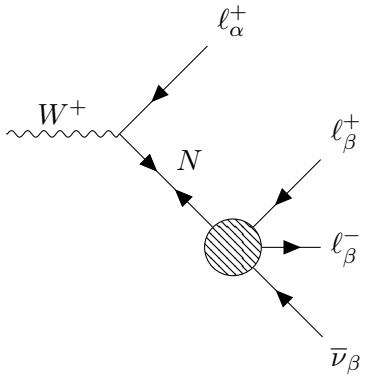

Figure 4.8: Purely leptonic decay mode of *on-shell* W-boson, produced from proton-proton collisions, into an HNL, N, and prompt lepton, ℓ, with further di-leptonic decay mode of HNL.

diagrams to the purely leptonic decay mode of the heavy neutral lepton is the same as for the charged meson process, and thus one should refer to the previous treatment for further details, and considering the same arguments as for the charged-meson process, we restrict ourselves to muon flavoured *displaced* leptons (or di-muons) for this as well.

The leptonic decay mode of $W^+ \to \ell^+\nu$ can be computed analytically, and approximated to follow the same factorisation method as for the charged meson process such that

$$\sigma(pp \to W^{\pm} \to \ell^{\pm}N, N \to \mu^+\mu^-\nu) \simeq \underbrace{\sigma(pp \to W^{\pm})}_{S_0} \cdot \underbrace{\mathrm{Br}(W^{\pm} \to \ell^{\pm}N)}_{S_1} \cdot \underbrace{\mathrm{Br}(N \to \mu^+\mu^-\nu)}_{S_2} \tag{4.2.1}$$

where the leptonic decay channel of the $W^{\pm}$ boson, $\Gamma(W^{\pm} \to \ell^{\pm}\nu_\ell)$ to leading order in the perturbative expansion of the coupling constant g is given by [66], and under approximate modification of $m_\nu \to M_N$ and inclusion of a $U^2_{\alpha\xi}$ term, the hypothetical decay width of $\Gamma(W^{\pm} \to \ell_\alpha N_\xi)$ can be approximated as

$$\begin{aligned}\Gamma(W^{\pm} \to \ell_\alpha N_\xi) =& \frac{g^2 M_W}{48\pi}\sqrt{\left[1-\left(\frac{m_\ell + M_N}{M_W}\right)^2\right]\left[1-\left(\frac{m_\ell - M_N}{M_W}\right)^2\right]} \\ &\times \left[1 - \frac{\left(m_\ell^2 + M_N^2\right)}{2M_W^2} - \frac{\left(m_\ell^2 - M_N^2\right)^2}{2M_W^4}\right].\end{aligned} \tag{4.2.2}$$

The decay width of $N \to \mu^+\mu^-\nu$ can be computed by use of (4.1.3) and further the branching fractions of $\mathrm{Br}(W^{\pm} \to \ell^{\pm}N)$ and $\mathrm{Br}(N \to \mu^+\mu^-\nu)$ can be computed by simply multiplying the partial decay widths by their respective lifetimes. In the case of the $W^{\pm}$-boson, the lifetime is measured and listed in [9]. For the HNL, the lifetime must be computed in accordance with (3.2.20).

Chapter 5

Strategy of producing exclusion limits

In the current chapter, we sketch our main strategy of producing exclusion limits based on the Monte Carlo data described in the Part II of this thesis. The main emphasis is put into the considerations of signal acceptance.

5.1 Number of detected events

The main results of the project take the form of exclusion regions of the parameter space of the hypothesis, computed in a unified way, as follows. We determine the number of detected events following *e.g.* [67]:

$$N_{\text{events}} = \mathcal{L}_{\text{int}} \cdot \sigma(pp \to \chi \to \ell N, N \to \mu^+ \mu^- \nu) \cdot \mathcal{S}_\Gamma \cdot \mathcal{S}_\Theta \cdot \epsilon_{\text{acc}} \tag{5.1.1}$$

Our notations in Eq. (5.1.1) are as follows. The symbol $\mathcal{L}_{\text{int}}$ denotes the integrated luminosity of the experiment, adopted in our case to be either $300\,\text{fb}^{-1}$ (LHC Runs 3 & 4) or $\mathcal{L}_{\text{int}} = 3000\,\text{fb}^{-1}$ (end of high-luminosity LHC phase). $\chi \in \{B^\pm, B_c^\pm, D^\pm, W^\pm\}$ denotes parent particles for HNL production. $\mathcal{S}_\Gamma$ is the rescaling factor due to the *narrow width approximation* (if applicable, see Appendix A.1.1) and $\mathcal{S}_\Theta$ is the rescaling factor for the mixing angle relevant for the process. Finally, the *signal acceptance* is labeled ϵ_{acc}. Calculation of the geometric acceptance is one of the main emphasis of this work. It is discussed in details in Section 9.2 on page 101. Below we simply sketch the main aspects of it.

5.2 Defining confidence interval

Having found N_{events} as a function of HNL parameters (mass, Θ_α) the projected sensitivity of discovery is defined as the solution to the equation $N_{\text{events}} = 3$. This defines a 95% confidence interval, assuming no background *i.e.* under the null hypothesis $N_{\text{events}} = 0$. This assumption is motivated by a minimal distance where the displaced vertex cut is assumed to discard the majority of SM background. Given that N_{events} is discrete and and events occur independently of each other, it is reasonable to model its probability distribution as Poisson, such that

$$\text{P}(N_{\text{events}} = k) = \frac{\lambda^k e^{-\lambda}}{k!}, \tag{5.2.1}$$

where λ is the mean number of events. If our confidence interval is 2σ we tolerate a $\leq 5\%$ chance of getting the same result as if the the null hypothesis was true. The Poisson distribution with $\lambda = 3$ it what comes closest to this with $\mathrm{P}(0; \lambda = 3) \approx 0.0498$, and thus the event sensitivity for the exclusion region of the parameter space was set to 3. An exclusion plot is then produced on the basis of valuating (5.1.1) for different values of Θ and M_N.

5.3 Signal acceptance

This work performs a deliberately simplified analysis, not simulating the detector's response and ignoring many of the highly relevant subtleties. For example, we assume 100% trigger efficiencies, event reconstruction efficiencies, confusion factors, energy resolution, etc. However, even when not simulating the detector fully, we still take into account its basic geometry and key details. Namely, not every lepton can be detected or recorded. The Muon Spectrometer does not cover a full 4π solid angle, not all muons have the sufficient kinematic properties needed for triggering and the decay volume is bounded; consequentially some of the relevant final states cannot be detected. To account for this and determine the acceptance of our signal, we impose the following cuts:

1. Pseudo-rapidity cuts $|\eta| < 2.4$ for ATLAS. The quoted pseudorapidity range for SND is $7.2 < \eta < 8.6$, however further non-trivial geometric considerations were taken into consideration, detailed in Sec. 7.2.2.
2. Transverse momenta (p_T) cuts (that we vary, as specified in the captions of the corresponding exclusion plots)
3. Displacement cuts

5.3.1 Displaced vertices (DV) cuts

The main signature of our long-lived HNLs is a di-muon pair displaced from the interaction point by macroscopic distance. Therefore, along with the kinematic cuts, described above, we retain only those events, whose displaced vertex (DV) has the following properties:

1. DV is located *outside* the sphere with radius 1 cm (2 cm for the $W^{\pm}$ processes)[1] around the primary vertex (interaction point). This kills most of the SM background.
2. Furthermore, DV is located within a *cylinder* with the radius $R_{\mathrm{MS}} = 5\,\mathrm{m}$ and the length along the beam line $L_{\mathrm{MS}} = 7\,\mathrm{m}$ (to each side of the primary vertex).

It should further be stressed that the cuts enumerated above are approximate. In actual ATLAS data analysis, different displacement requirements are placed on the longitudinal and the transverse impact parameters of particles, polar and azimuthal angles at particle trajectory's perigee, etc. (see *e.g.* [68, 69, 70, 71, 72]). However, as we will see below, the sensitivity reach is dominated by the largest sizes of the ATLAS detector. Therefore, these subtleties can be largely ignored for the preliminary analysis we are doing here.

Heavy neutral leptons, as elaborated earlier, can be long lived depending on their mass and mixing angles, such that $l_{\mathrm{dec}} \equiv v\tau\gamma \gg l_{\mathrm{max}}$ where l_{max} is the maximal length of the ATLAS decay volume.

[1] The $W^{\pm}$ processes proved to be quite robust with respect to strengthening the criteria on the minimal DV distance, and thus to be generous, the DV min distance was increased to 2 cm for them. This consolidates the justification of the assumption that true DVs from SM background is negligible. Combinatorial background with fake DVs may still be present i.e. intersecting muon paths that resembles a di-muon production vertex.

In this limit is possible to Taylor expand (4.0.1) describing the decay probability within an isotropic volume defined by l_{min} and l_{max}, such that

$$P_{\text{dec}} = \frac{l_{max} - l_{min}}{v\tau\gamma} + \mathcal{O}\left(\left(\frac{1}{v\tau\gamma}\right)^2\right). \tag{5.3.1}$$

For a large decay volume i.e. $l_{max} \gg l_{min}$ we can neglect the contribution from l_{min} and thus enter a linear regime where

$$P_{\text{dec}} \approx \frac{l_{max}}{v\tau\gamma}. \tag{5.3.2}$$

In this region the number of decays within the volume is proportional to l_{max}, giving ATLAS an advantage in DV searches in the $l_{\text{dec}} \gg l_{\text{max}}$ due to its comparatively large l_{max}.

Following this reasoning DV searches at ATLAS with the MS falls into three regions

- $l_{\text{dec}} \ll l_{\text{min}}$ for which we see en exponential sharp decline in P_{dec};
- $l_{\text{min}} < l_{\text{dec}} < l_{\text{max}}$ flat region for which P_{dec} is approximately constant and close to 1;
- $l_{\text{dec}} \gg l_{\text{max}}$ linear region where $P_{\text{dec}} \approx l_{\text{dec}}/l_{\text{max}}$.

For an overview of the regions, see Fig. 5.1.

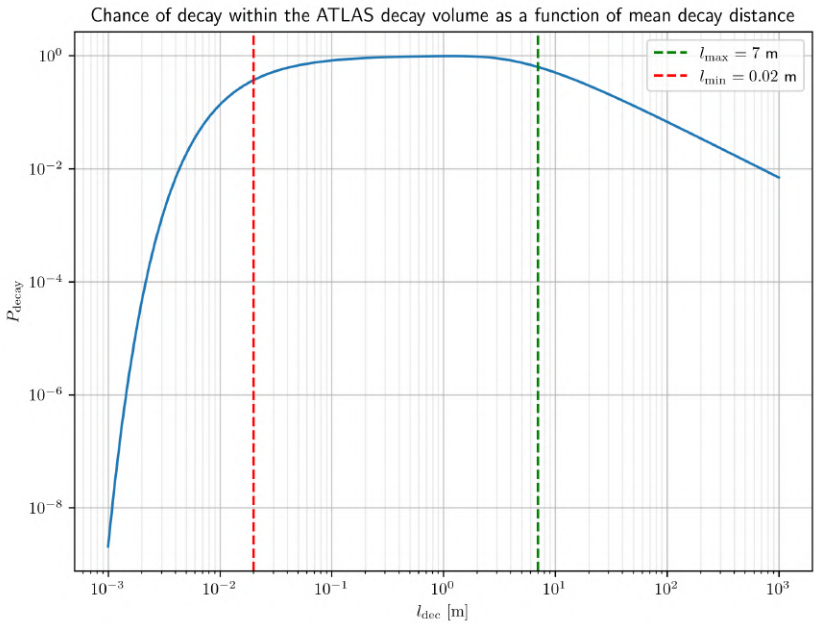

Figure 5.1: Overview of relevant $l_{\text{dec}} = v\tau\gamma$ regions for DV searches at the ATLAS MS. For simplicity the MS is here modeled as a sphere of radius 7 m and all particles are assumed to travel at same speed, v. The dashed lines indicates the decay volume. Note the linear region for $l_{\text{dec}} \gg l_{\text{min}}$ where $P_{\text{dec}} \approx l_{\text{dec}}/l_{\text{max}}$ and the flat region for $l_{\text{min}} < l_{\text{dec}} < l_{\text{max}}$.

5.4 DV trigger schemes

The results of the present study can be divided in two categories; DV search scheme 1 and 2, distinguished by the triggers they rely on. The two categories are presented below, along with a brief discussion of each.

5.4.1 DV search scheme 1

Our original research goal was to create the necessary programming tools needed to evaluate the prospects of a dedicated di-muon DV trigger, triggering on muons of opposite charge whose reconstructed trajectories originated from a single DV, solely relying on the ATLAS Muon Spectrometer (MS). Furthermore a p_T cut of minimum 5 GeV is required for each of the displaced muons. This p_T condition should largely remove combinatorial background coming from two SM muons, produced by different heavy flavour mesons, coincidentally crossing tracks and thereby creating a fake DV (see e.g. [59]). Such a trigger is currently not available at ATLAS, hence results for this trigger scheme are totally depended on the development of such a dedicated di-muon DV trigger at ATLAS. Triggers in the same vein are described in e.g. [73] and [74]. DV searches based on this trigger will be referred to as DV search scheme 1.

5.4.2 DV search scheme 2

Having achieved the main research goal just mentioned by constructing a program automating the generation of results based on e.g. cut-parameters, we expanded our scientific focus to include *currently available* triggers. Specifically we selected two promising triggers from the 2018 ATLAS trigger menu [75]. Results based on these triggers comprises the second category of results which shall be refereed to as DV search scheme 2.

Note that DV search scheme 2 does not rely on the DV for triggering, but will instead use it to sort events after they were retained by the triggers already existing triggers. Reconstructing the DV after the events were recorded then allows for events without a relevant DV to be discarded, so that a dataset consisting solely of events living up to the DV criteria can be created.

The following enumeration explicitly summarise and label the relevant triggers used in the present study:

(T_1) Two muons of opposite charge sharing a single displaced vertex. Both muons are required to have $p_T > 5$ GeV.

(T_2) Two muons (no requirement with respect to charge or displacement), each with $p_T > 15$ GeV or one with $p_T > 9$ GeV and one with $p_T > 23$.

(T_3) Three muons (no requirement with respect to charge or displacement), each with $p_T > 7$ GeV. *Only relevant for tri-muon processes.*

To reiterate; the currently unavailable DV trigger scheme relying on a novel dedicated DV trigger is associated with T_1 from the above enumeration, and labeled DV search scheme 1. The DV trigger scheme based on currently available triggers T_2 and T_3 is labelled DV search scheme 2. These search schemes are displayed in Table 9.2.

For the tri-muon processes specifically, one would ideally *pool* all three muons (one prompt + two displaced) and apply T_2 and T_3[2]. However, for the presents study T_2 was always *only* imposed on the displaced di-muons (excluding the prompt muon from triggering). Furthermore T_2 and T_3 were never applied in concert but always *only* individually. For the two preceding reasons, results for T_2 and T_3 are actually lower bounds, though correlation between events that pass either cut may cause their combined result to show only modest improvement. Finally, for the meson results specifically, potential muons

[2] *Pool* in the sense of group them together and indiscriminately apply the cuts.

created from the b/c-quark[3] that did not give rise to an HNL could also be included in the T_2 and T_3 triggers. By considering such SM leptonic decay channels of the secondary meson and pooling its muon contribution along with the ones already considered, significant improvement of results could be expected!

It should be emphasized that the Level-1 trigger[4] (L1) have hard-wired criteria with respect to impact parameter, requiring all muons (including displaced!) to have trajectories pointing back to the beam collision point. Throughout the present study it is assumed that the displaced muons fulfills this requirement, making them eligible for triggering at the L1 level. The relatively high $E_{\text{tot}}/E_{\text{kin}}$ ratio of the HNLs studied, justifies that the angular separation of the displaced muons could allow for such assumption. For a more detailed discussion see Section 7.2.1.1.

Though the T_2 and T_3 triggers are currently available and will be retained by the L1 trigger system, the High-Level trigger system (HLT) of ATLAS rejects muon tracks whose impact parameter is away from the interaction point by more than ~ 20 cm or whose trajectory cannot be associated with a track in the Inner Detector (ID). Since the tracks of the displaced di-muons certainly do not show up in the ID for $v\tau\gamma \gtrsim 0.5$ m (which is the region of interest for the current study) this poses a challenge for the proposed DV trigger schemes. However, as T_2 and T_3 are presently retained at L1 hardware level, the development of specialised stand-alone Muon Spectrometer DV trigger algorithms for the HLT could realise the prospects these two triggers entail, some of which we present in the present work.

As the signal from T_2 and T_3 is already retained at the hardware L1 trigger, we expect no hardware upgrade to be required if such a trigger algorithm was available. This opens up the possibility that our results could already be applicable to within LHC Run3. Further hope could be held that upgrades made during the Long Shutdown 3 phase, in preparation for HL-LHC, will also contribute to bridge the gap by offering hardware capabilities enabling further DV trigger improvement. In this light our study serves as motivation for developing ameliorated triggering tools for conducting DV searches at ATLAS, by presenting the prospects of such embodied by trigger scheme 1.

[3]Due to conservation of color charge quarks come in pairs. Eventually the quarks would end up in mesons, possibly via a baryon. Thus is can be assumed that for every e.g. B, B_c or D meson, an associated partner meson is also present in the event.

[4]For an introduction to triggers and the ATLAS trigger system in particular see Chapter 7. Suffice it to say here that the ATLAS trigger system is composed of two layers. Events need to pass both; first the gross but quick *hardware based* Level-1 trigger, and then the more detailed but slower *software based* High-Level trigger.

Chapter 6

Results

This Chapter presents our main results in the form of exclusion regions of the HNL parameter space. First results of the individual processes (with uncertainties) are compared with exclusion regions of previous searches. Then stability plots with variations of cut parameters are shown, along with summary plots combining results from across all processes and mixing schemes (without uncertainties).

6.1 Previous searches

Before presenting our results, let us briefly review previous searches and the parameter space for the HNLs in the mass range 1 GeV to 80 GeV. HNL searches have been actively pursued by major particle physics experiments, see [76, 57] and refs. therein. Here we only list the most important experiments in this mass region. For HNLs lighter than light flavoured mesons (π, K) the beam dump experiments provide the best sensitivities owing to extremely large number of mesons produced in collisions of the beam with the target. In the region of interest ($M_N \gtrsim 1\,\text{GeV}$) the most relevant experiments are CERN's CHARM [77] and Fermilab's NuTeV [78]. They are mostly sensitive to electron- and muon mixings of HNLs, much less so for HNLs with $M_N > 1\,\text{GeV}$, mixing with the τ flavour (see, however, [79]). Another major experiment of the past was LEP (Large Electron-Positron collider), operating at CERN between 1989 and 2000. One of the LEP's experiments – DELPHI – produced HNL exclusion limits for masses $\sim 2\,\text{GeV}$ to $90\,\text{GeV}$, universal for all three couplings [80], that remain a *de facto* benchmark against which all the current searches compare. In the most part of the mass region these limits are $|\Theta_\alpha|^2 \sim 10^{-5}$. These limits are shown in Figs. 6.1–6.17.

Finally, Figures 6.1–6.17 also show the results of the recent by the ATLAS and CMS collaborations [81, 82, 60, 61]. The purple line marked "CMS" represents the CMS dilepton + jets searches [81] and tri-lepton prompt searches [82]. The dashed blue line shows ATLAS tri-lepton prompt search [60]; the shaded blue area is the first-ever ATLAS displaced HNL searches [60]. Finally, the dotted blue line is the most recent ATLAS tri-lepton displaced vertex searches [61].

6.2 HNLs produced from $W^\pm$ bosons

In this Section we summarise sensitivity of searches for HNLs, produced from the W-bosons. We present both di-muon searches (without triggering and/or using of the prompt lepton). The results are presented for integrated luminosities $300\,\text{fb}^{-1}$ and $3000\,\text{fb}^{-1}$ (black and red crosses correspondingly).

6.2.0.1 Di-muon results

In Figs. 6.1–6.2 we present our sensitivity estimates based solely on the displaced di-muon searches. We assume that HNLs have been produced in decays of $W^{\pm}$-boson. We impose a cut of $p_T > 5\,\text{GeV}$ on the displaced di-muons. The required positions of the displaced vertices are described in Section 5.3.1.

Our p_T criteria does not correspond to any of the currently existing muon triggers. In order to see how our results depend on this selection criterion, we repeat the exercise for the case of the displaced muon pair, passing current ATLAS di-muon trigger criteria [73].[1] Relevant kinematic criteria are listed in Table 9.2 on page 118 and in the caption of Figs. 6.3 and 6.4 which shows the corresponding bounds.

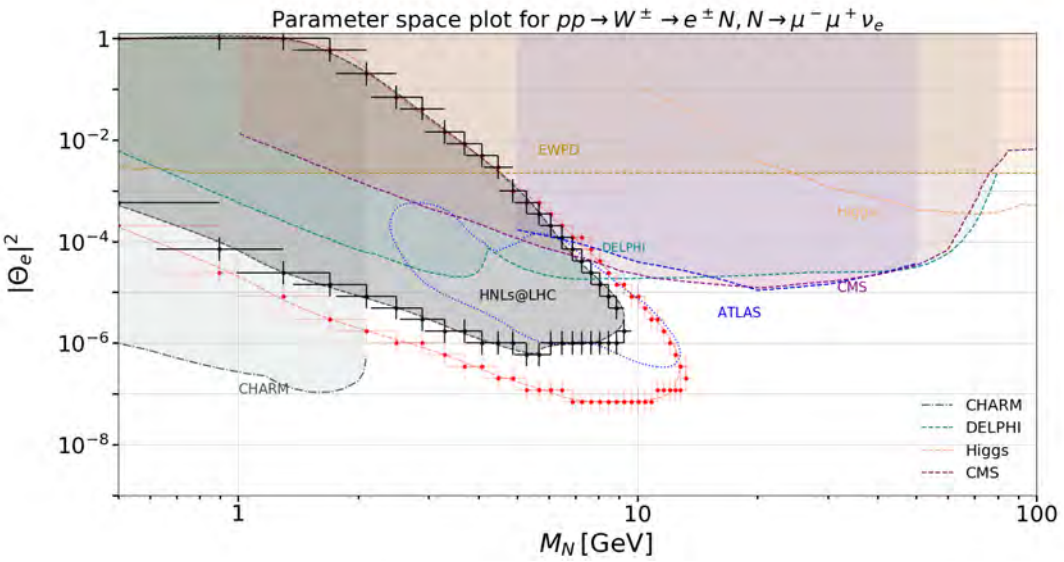

Figure 6.1: Projected 95% CL exclusion region for HNLs with $\Theta_e \neq 0, \Theta_\mu = \Theta_\tau = 0$ for integrated luminosities $300\,\text{fb}^{-1}$ (black crosses) and $3000\,\text{fb}^{-1}$ (red crosses). The top label shows the analysed process. Both muons pass transverse momentum cut $p_T > 5\,\text{GeV}$ and are in the pseudo-rapidity range $|\eta| < 2.4$, while the prompt electron is not included into analysis. The DV cuts are described in the Section 5.3.1. Exclusions from the previous experiments are discussed in Section 6.1.

[1] Currently the ATLAS trigger system rejects the muon tracks whose impact parameter is away from the interaction point by more than few centimeters, as elaborated in Sec. 5.3.1. We expect, however, that with the development of displaced muon triggers, such criteria will be modified.

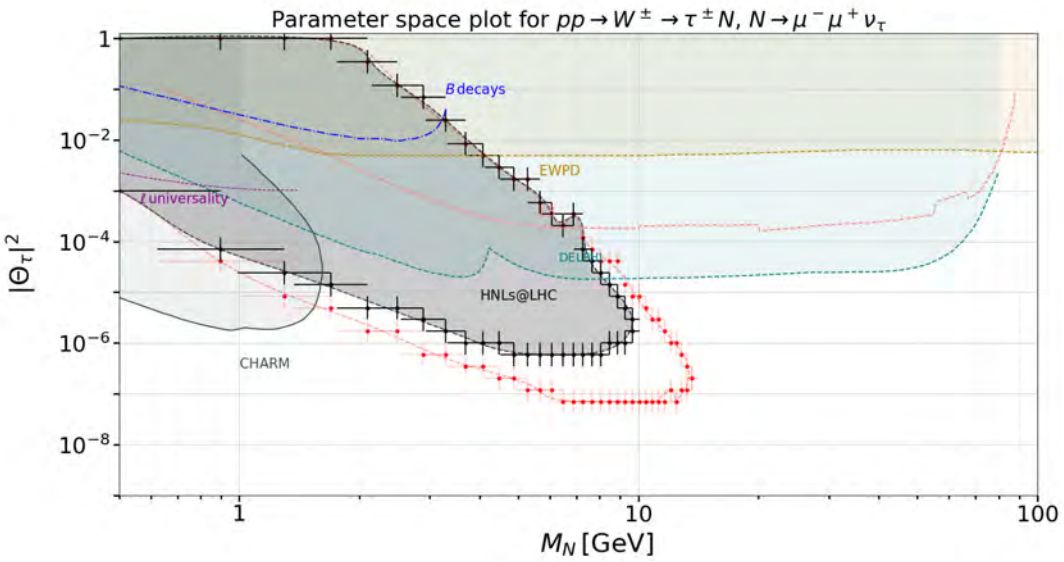

Figure 6.2: Projected 95% **CL exclusion region for HNLs with** $\Theta_\tau \neq 0, \Theta_e = \Theta_\mu = 0$ for integrated luminosities $300\,\text{fb}^{-1}$ (black crosses) and $3000\,\text{fb}^{-1}$ (red crosses). The top label shows the analysed process. Both muons pass transverse momentum cut $p_T > 5\,\text{GeV}$ and are in the pseudo-rapidity range $|\eta| < 2.4$, while the prompt *tau*-lepton is not included into analysis. The DV cuts are described in the Section 5.3.1. Exclusions from the previous experiments are discussed in Section 6.1.

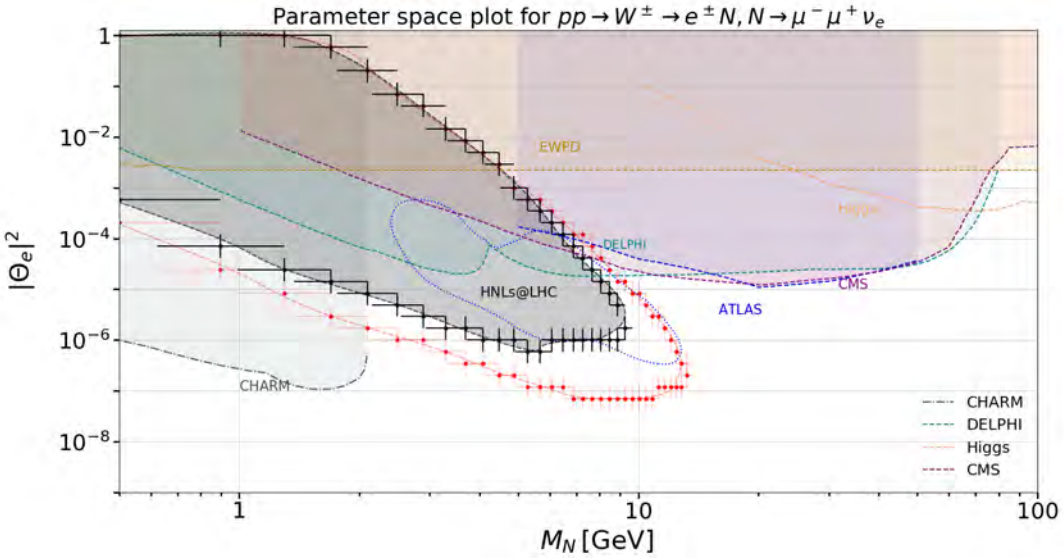

Figure 6.3: Projected 95% **CL exclusion region for HNLs with** $\Theta_e \neq 0, \Theta_\mu = \Theta_\tau = 0$ **for integrated luminosities** $300\,\text{fb}^{-1}$ **(black crosses) and** $3000\,\text{fb}^{-1}$ **(red crosses).** The top label shows the analysed process. The displaced muon pair passes *either* of the two p_T cuts: *(i)* $p_T > 23$ and 9 GeV or *(ii)* both $p_T > 15\,\text{GeV}$ and are in the pseudo-rapidity range $|\eta| < 2.4$. The DV cuts are described in the Section 5.3.1. Exclusions from the previous experiments are discussed in Section 6.1.

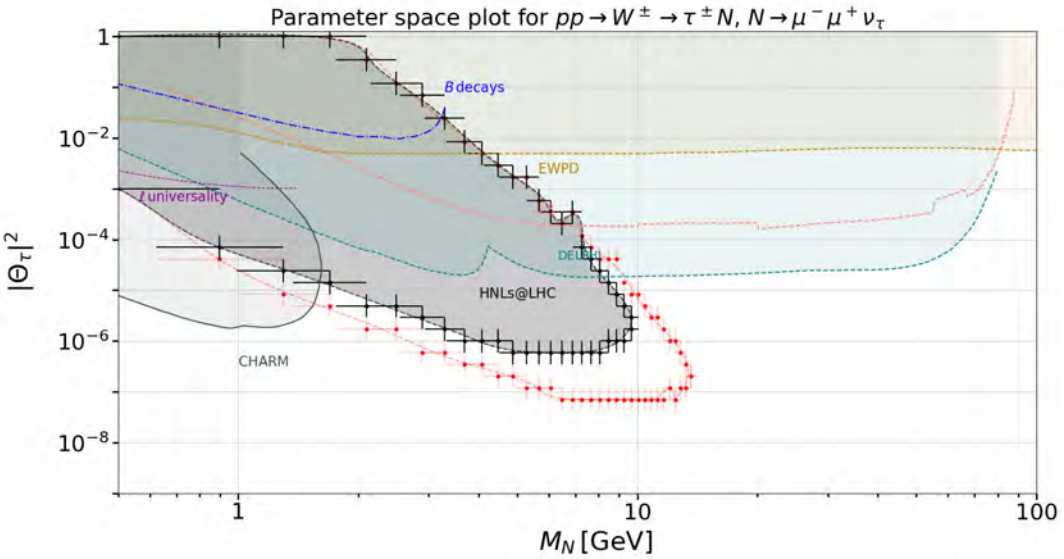

Figure 6.4: Projected 95% CL exclusion region for HNLs with $\Theta_\tau \neq 0, \Theta_e = \Theta_\tau = 0$ for integrated luminosities $300\,\text{fb}^{-1}$ (black crosses) and $3000\,\text{fb}^{-1}$ (red crosses). The top label shows the analysed process. The displaced muon pair passes *either* of the two p_T cuts: *(i)* $p_T > 23$ and 9 GeV or *(ii)* both $p_T > 15\,\text{GeV}$ and are in the pseudo-rapidity range $|\eta| < 2.4$. The DV cuts are described in the Section 5.3.1. Exclusions from the previous experiments are discussed in Section 6.1.

6.2.0.2 Tri-muon results

In Figs. 6.5–6.7 we present our sensitivity estimates based on the *tri*-muon processes for HNLs produced the process of $pp \to W^{\pm} \to \mu^{\pm} N, N \to \mu^{\pm}\mu^{\mp}\nu_{\mu}$. Here we explore the effect of different trigger requirements, starting, in the same vein as for the di-muon results, by imposing a cut of $p_T > 5\,\text{GeV}$ on the displaced leptons (which should largely remove combinatorial background[2] with the results placed in Fig. 6.5. This search scheme, under all aforementioned experimental assumptions, will beat all other previous search schemes for the relevant mass range, most notably [61].

We start by considering a cut on *all* muons (both prompt and displaced) of $p_T > 7\,\text{GeV}$, the results of which is placed in Fig. 6.6. This also removes a large portion of the combinatorial background[3], as well as ensuring the L1 hardware trigger is satisfied[4].

Finally, we present the result in Fig. 6.7 of imposing no selection criteria on the prompt lepton, but an even stronger requirement on the displaced muons to satisfy *either* of the two p_T cuts: *(i)* $p_T > 23$ and 9 GeV or *(ii)* both $p_T > 15\,\text{GeV}$, in line with a currently available hardware trigger per the trigger menu referenced by [75]. This search strategy (for Run-3) does provide a greater sensitivity for HNL masses in the range $2 \leq M_N \leq 10$ GeV, however is overshadowed by [61] in the range $10 \leq M_N \leq 15$ GeV. The HL-LHC phase will however provide greater sensitivity by up to an order of magnitude in comparison to [61].

Further, when comparing Figs. 6.1 and 6.2 with Fig. 6.5 one may notice that the latter searches are sensitive for the smaller mixing angles (reaching all the way to $|\Theta_\mu|^2 \simeq 10^{-8}$. This difference comes

[2]The combinatorial background of two SM muons is produced by the leptonic decay modes of different heavy flavour mesons with accidentally crossing tracks, see e.g. [59]

[3]There will however still be cavern background present in the MS, leading to the appearance of *fake* muons. This will be discussed in Ch. 10

[4]To reiterate, it is assumed that all muons are *pointing*, as the trigger requires reconstructed tracks in the MS to originate from the ID, and thus for non-pointing displaced muons in the MS, the trigger criteria is not satisfied.

solely from the larger branching ratio of the process $N \to \mu\mu\nu_\mu$, mediated by both charged and neutral current interactions as compared to the $N \to \mu\mu\nu_e$ or $N \to \mu\mu\nu_\tau$, mediated by the neutral current interaction alone.

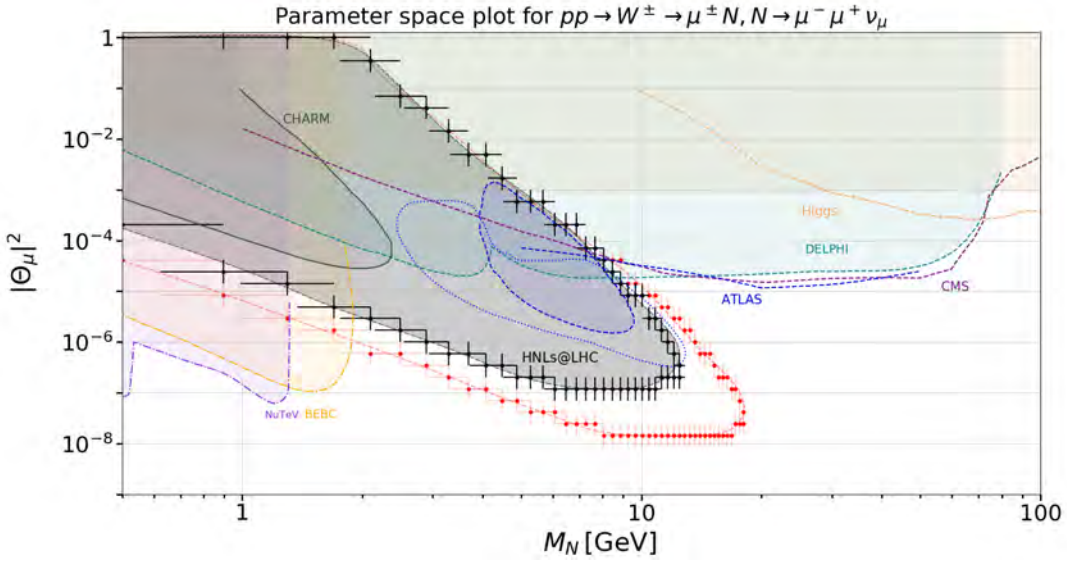

Figure 6.5: Projected 95% **CL exclusion region for HNLs with** $\Theta_\mu \neq 0, \Theta_e = \Theta_\tau = 0$ for integrated luminosities $300\,\text{fb}^{-1}$ (black crosses) and $3000\,\text{fb}^{-1}$ (red crosses). The top label shows the analysed process. Both muons pass transverse momentum cut $p_T > 5\,\text{GeV}$ and are in the pseudo-rapidity range $|\eta| < 2.4$, while the prompt muon is not included into analysis. The DV cuts are described in the Section 5.3.1. Exclusions from the previous experiments are discussed in Section 6.1.

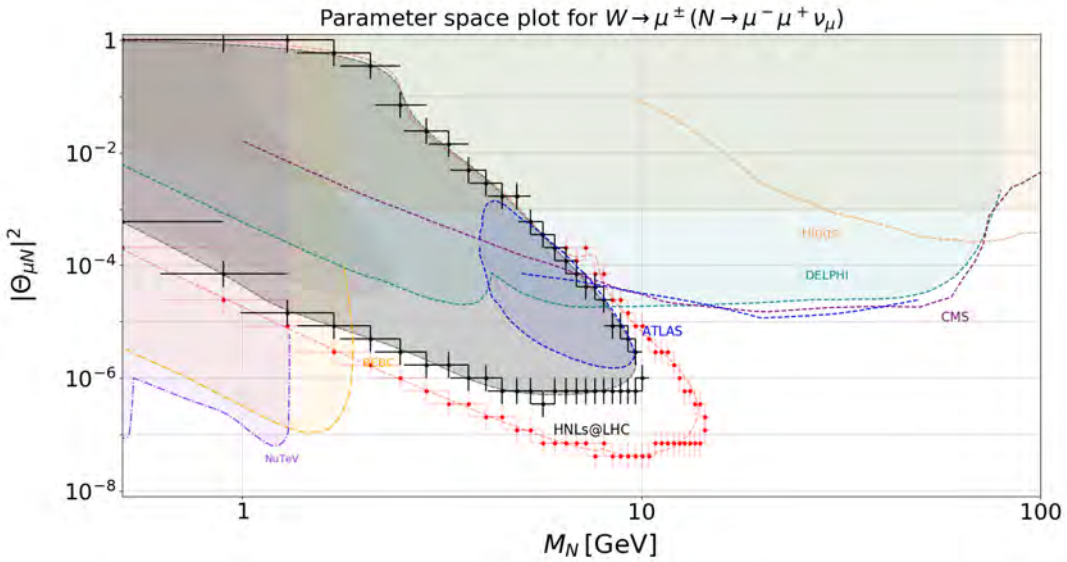

Figure 6.6: Projected 95% **CL exclusion region for HNLs with** $\Theta_\mu \neq 0, \Theta_e = \Theta_\tau = 0$ **for integrated luminosities** $300\,\text{fb}^{-1}$ **(black crosses) and** $3000\,\text{fb}^{-1}$ **(red crosses).** The top label shows the analysed process. All 3 muons pass transverse momentum cut of $p_T > 7\,\text{GeV}$ according to the tri-muon trigger [73] and are in the pseudo-rapidity range $|\eta| < 2.4$. The DV cuts are described in the Section 5.3.1. Exclusions from the previous experiments are discussed in Section 6.1.

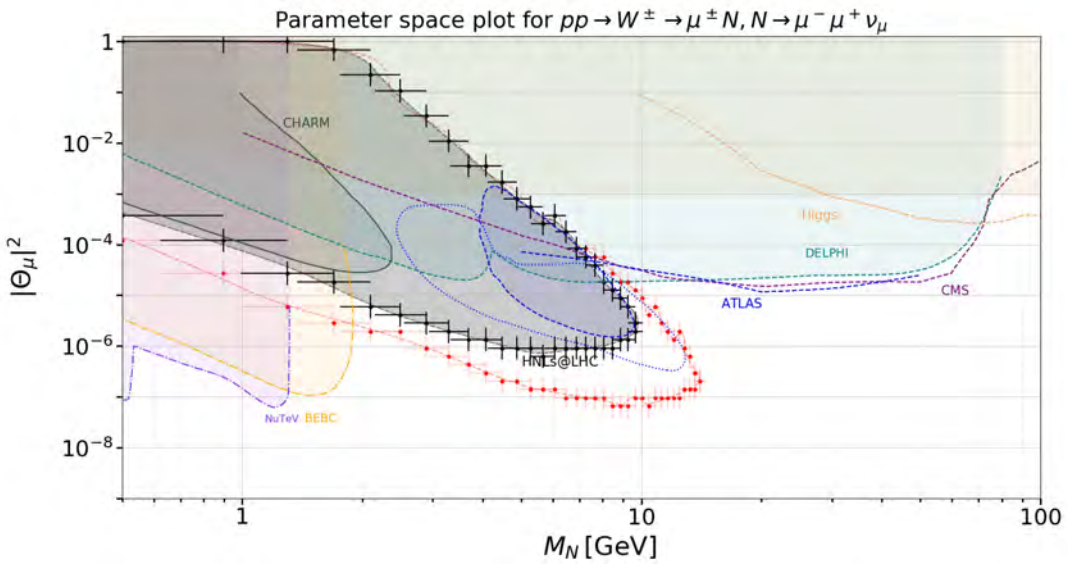

Figure 6.7: Projected 95% CL exclusion region for HNLs with $\Theta_\mu \neq 0, \Theta_e = \Theta_\tau = 0$ for integrated luminosities $300\,\text{fb}^{-1}$ (black crosses) and $3000\,\text{fb}^{-1}$ (red crosses). The top label shows the analysed process. The displaced muon pair passes *either* of the two p_T cuts: *(i)* $p_T > 23$ and 9 GeV or *(ii)* both $p_T > 15\,\text{GeV}$ and are in the pseudo-rapidity range $|\eta| < 2.4$. The DV cuts are described in the Section 5.3.1. Exclusions from the previous experiments are discussed in Section 6.1.

6.3 HNLs produced from heavy flavoured mesons

In this Section we summarise sensitivity of searches for HNLs, produced from heavy flavoured charged mesons ($B^{\pm}$, $B_c^{\pm}$, $D^{\pm}$). We present both di-muon and tri-muon searches, similarly to the case of W-bosons presented above (Section 6.2). HNLs produced from mesons tend to have much lower p_T than those, produced from the W-bosons. This loss of high-p_T displaced muons turns out to be more severe than the gain due to the much larger number of B/D mesons produced (as compared to the W-bosons). Finally, it should be noticed that in this thesis we did not consider production of HNLs from neutral mesons (D^0, B^0, B_s). These mesons generally posses a semi-leptonic decay channels producing HNLs but are usually subdominant to the purely leptonic production channels [42]. As before, the results are presented for integrated luminosities $300\,\text{fb}^{-1}$ and $3000\,\text{fb}^{-1}$ (black and red crosses correspondingly).

6.3.1 General trends for the meson processes

Comparing results across processes, a clear pattern appears. Most notably it can be seen that tri-muon processes leads to lower exclusion limits (i.e. gives better results) than di-muon processes. This trend is caused by the larger branching ratio of the process $N \to \mu\mu\nu_\mu$, mediated by both charged and neutral current interactions as compared to the $N \to \mu\mu\nu_e$ or $N \to \mu\mu\nu_\tau$, mediated by the neutral current interaction alone. The same mechanism was seen in the results for the W-processes.

To a lesser degree it is also noticeable that among the di-muon processes, the exclusion limits for τ flavoured processes surpass those of e in the range $M_N \lesssim 3$ GeV. The reason for this being the branching ratio, which slightly favors τ over e as seen in Fig. 8.12, due to spin effects [83, 84]. The branching ratios become equal at $M_N \approx 3$ GeV.

6.3.2 HNLs from $B^{\pm}$ mesons.

6.3.2.1 Di-muon results

In Figs. 6.8–6.9 we present our sensitivity estimates based solely on the displaced di-muon searches and impose a p_T cut of $p_T > 5\,\text{GeV}$ on the displaced di-muons, in line with the T_1 trigger mentioned in Section 5.4. The criteria for the positions of the displaced vertices are described in Section 5.3.1. None of the exclusion bounds reach previously unsearched regions, and the search scheme, *DV Search Scheme 1*, is therefore not competitive for this process. The displaced muons are *too* soft to survive the p_T cut significantly. For HNLs with masses above 3 GeV, the efficiency of the minimal distance DV-cut is low enough to have non-trivial effect, as can be seen in the lower right corner of the exclusion bound of Fig. 6.8. The lighter HNLs will in general travel a greater distance, surpassing the minimum DV-cut criteria, up until masses of 3 GeV, after which the criteria becomes more difficult to fulfil, and thus a clear upward trend on the exclusion region appears. This is not the case for Fig. 6.9 as, due to the heavy mass of the τ-lepton, HNLs of masses greater than 3 GeV will violate energy conservation, and thus cannot be produced from the decay of the meson.

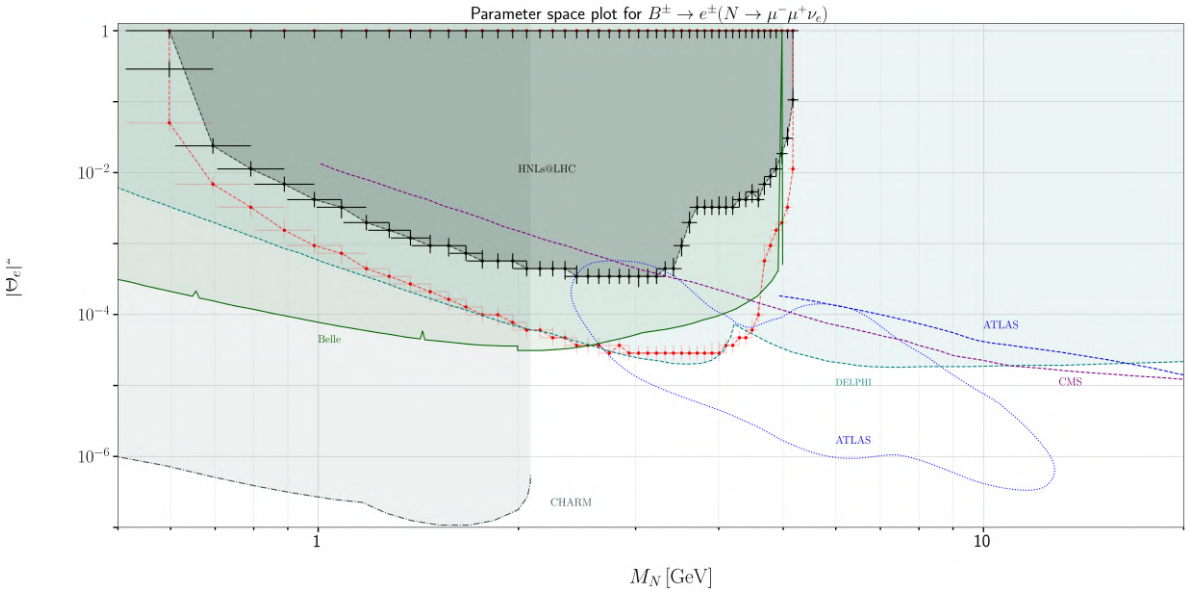

Figure 6.8: Projected 95% **CL exclusion region for HNLs with** $\Theta_e \neq 0, \Theta_\mu = \Theta_\tau = 0$ for integrated luminosities $300\,\text{fb}^{-1}$ (black crosses) and $3000\,\text{fb}^{-1}$ (red crosses). The top label shows the analysed process. Both muons pass transverse momentum cut $p_T > 5\,\text{GeV}$ and are in the pseudo-rapidity range $|\eta| < 2.4$, while the prompt electron is not included into analysis. In addition, the meson pass transverse momentum cut of $p_T > 10\,\text{GeV}$ for tagging. The DV cuts are described in the Section 5.3.1. Exclusions from the previous experiments are discussed in Section 6.1.

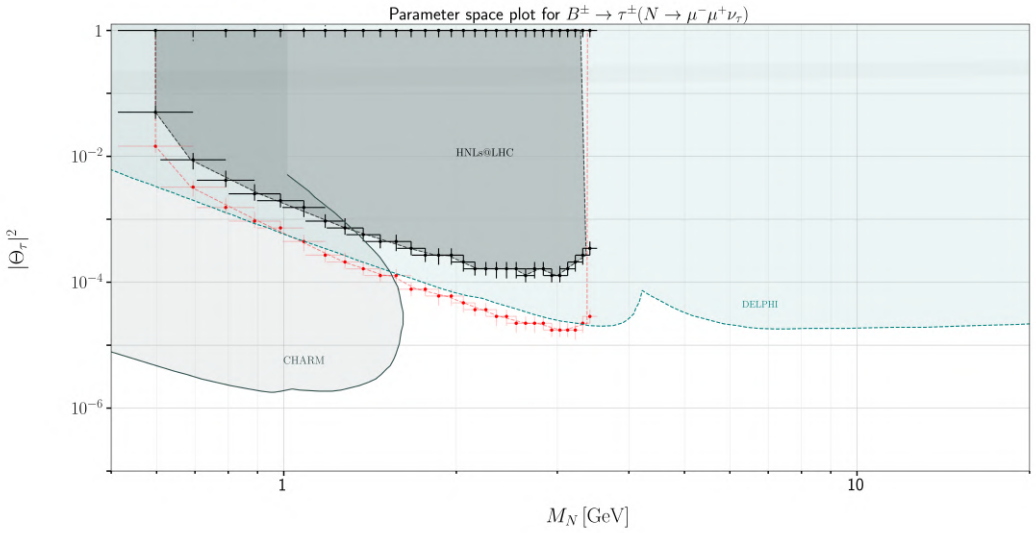

Figure 6.9: Projected 95% **CL exclusion region for HNLs with** $\Theta_\tau \neq 0, \Theta_e = \Theta_\mu = 0$ for integrated luminosities $300\,\text{fb}^{-1}$ (black crosses) and $3000\,\text{fb}^{-1}$ (red crosses). The top label shows the analysed process. Both muons pass transverse momentum cut $p_T > 5\,\text{GeV}$ and are in the pseudo-rapidity range $|\eta| < 2.4$, while the prompt *tau*-lepton is not included into analysis. In addition, the meson pass transverse momentum cut of $p_T > 10\,\text{GeV}$ for tagging. The DV cuts are described in the Section 5.3.1. Exclusions from the previous experiments are discussed in Section 6.1.

6.3.2.2 Tri-muon results

In Fig. 6.10-6.11 we present our sensitivity estimate based on the *tri*-muon processes for HNLs produced the process of $pp \to B^{\pm} \to \mu^{\pm} N, N \to \mu^{\pm}\mu^{\mp}\nu_{\mu}$. In addition to the $p_T > 5\,\text{GeV}$ cut emulating the T_1 trigger we here also impose a cut of $p_T > 7\,\text{GeV}$ on *all* charged leptons emulating the T_3 trigger. Both results perform approximately equally, their stability has been considered in Fig. 6.24, where both search schemes provide sensitivity bounds to $\Theta_\mu \simeq 10^{-5}$ for Run-3 luminosity, and $\Theta_\mu \simeq 10^{-6}$ for the luminosities of HL-LHC . For Run-3 luminosity, HNL masses below 4 GeV, Search Scheme 1 predicts the greatest sensitivity in comparison to previous searches, and the T_3 trigger of Search Scheme 2 predicts the greatest sensitivity for HNL masses under 3 GeV, after which both schemes will be overshadowed by [61].

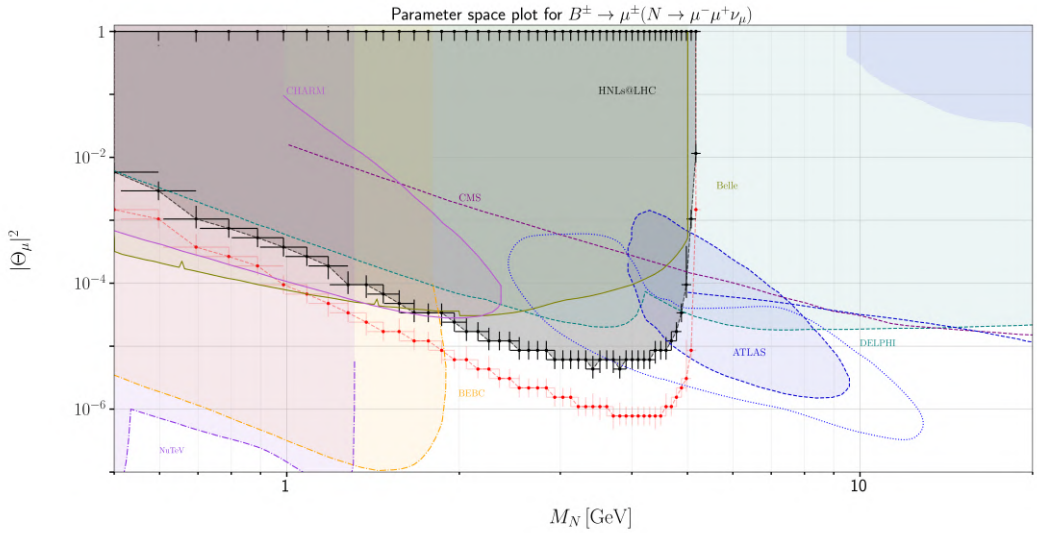

Figure 6.10: Projected 95% **CL exclusion region for HNLs with** $\Theta_\mu \neq 0, \Theta_e = \Theta_\tau = 0$ for integrated luminosities $300\,\text{fb}^{-1}$ (black crosses) and $3000\,\text{fb}^{-1}$ (red crosses). The top label shows the analysed process. Both displaced muons pass transverse momentum cut $p_T > 5\,\text{GeV}$ and are in the pseudo-rapidity range $|\eta| < 2.4$, while the prompt muon is not included into analysis. In addition, the meson pass transverse momentum cut of $p_T > 10\,\text{GeV}$ for tagging. The DV cuts are described in the Section 5.3.1. Exclusions from the previous experiments are discussed in Section 6.1.

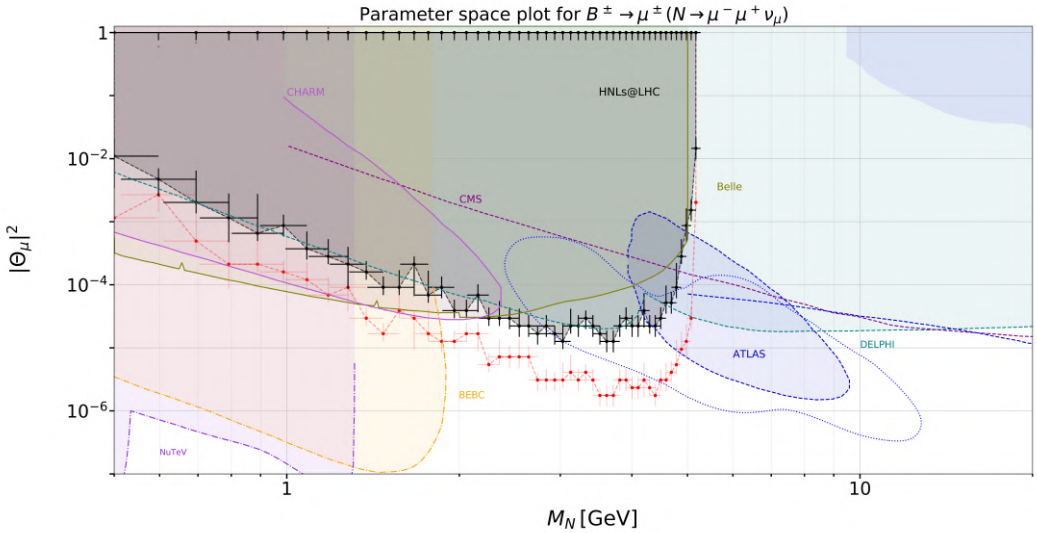

Figure 6.11: Projected 95% **CL exclusion region for HNLs with** $\Theta_\mu \neq 0, \Theta_e = \Theta_\tau = 0$ for integrated luminosities $300\,\text{fb}^{-1}$ (black crosses) and $3000\,\text{fb}^{-1}$ (red crosses). The top label shows the analysed process. All three muons pass transverse momentum cut $p_T > 7\,\text{GeV}$ and are in the pseudo-rapidity range $|\eta| < 2.4$. The DV cuts are described in the Section 5.3.1. Exclusions from the previous experiments are discussed in Section 6.1.

6.3.3 $D^{\pm}$ mesons processes

Due to the light mass of the $D^{\pm}$-meson, the τ channel is excluded, and thus the only two channels are therefore presented. Fig. 6.12 represents the e-flavoured process, and Fig. 6.13 represents the μ-flavoured process.

Neither of the two processes contribute with competitive bounds on HNL sensitivity. The results of Fig. 6.12, the exclusion region is overshadowed entirely by the CHARM experiment, and the results of Fig. 6.13 are overshadowed by the BEBC beamdump experiment.

The μ process is the more sensitive of the two, in line with the expected behavior described in 6.3.1. It can be noted that the relatively small mass of the $D^{\pm}$-meson (∼1.9 GeV), as compared to the other mesons included in the current study, limits the HNL mass range sensitivity. Although the lightness of its mass implies enhancement of production (e.g. ∼5 times greater than $B^{\pm}$)[5] and branching from $D^{\pm}$ to HNL is favorable (e.g. peaking at ∼2 orders of magnitude more than $B^{\pm}$), the p_T cut and DV cut kills the majority of the signal by raising the exclusion limit with more than 2 and 1 orders of magnitude respectively for the tri-muon process.

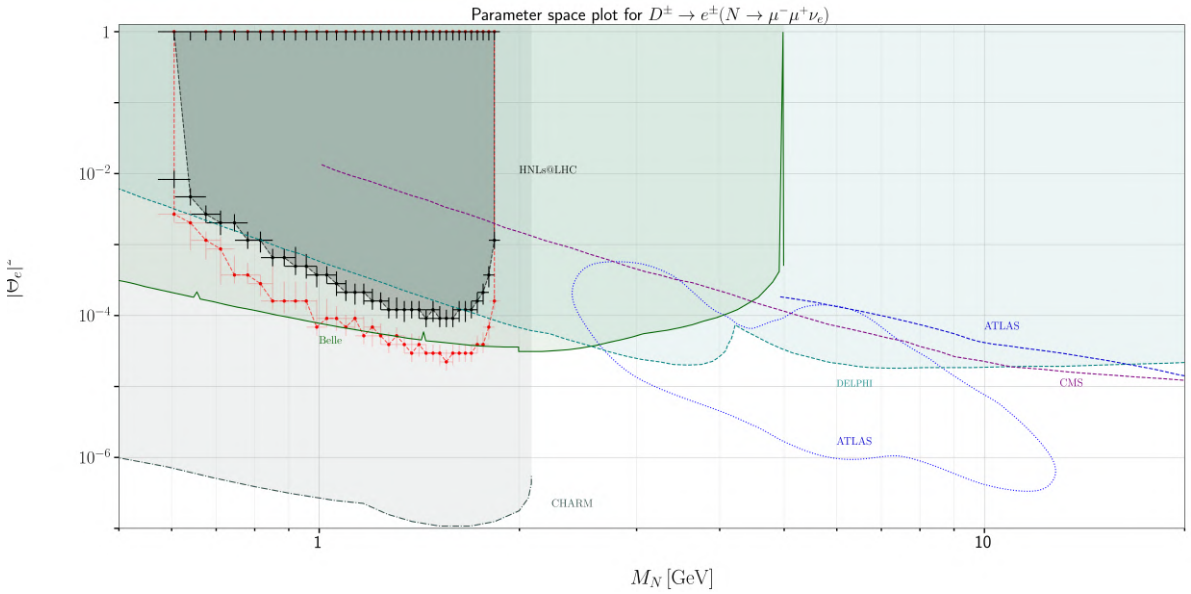

Figure 6.12: Projected 95% **CL exclusion region for HNLs with** $\Theta_e \neq 0, \Theta_\mu = \Theta_\tau = 0$ for integrated luminosities 300 fb^{-1} (black crosses) and 3000 fb^{-1} (red crosses). The top label shows the analysed process. Both muons pass transverse momentum cut $p_T > 5\,\text{GeV}$ and are in the pseudo-rapidity range $|\eta| < 2.4$, while the prompt electron is not included into analysis. In addition, the meson pass transverse momentum cut of $p_T > 10\,\text{GeV}$ for tagging. The DV cuts are described in the Section 5.3.1. Exclusions from the previous experiments are discussed in Section 6.1.

6.3.4 $B_c^{\pm}$ mesons processes

Mesons, containing b and c quarks — $B_c^{\pm}$ mesons — are the heaviest of the family of heavy flavour mesons. As such they offer the largest reach of HNL masses, up to $m_{B_c} \simeq 6.3\,\text{GeV}$. The production of these mesons are suppressed due to phase-space, due to their mass. However the branching ratio of the $B_c^{\pm}$-meson is enhanced due to its CKM matrix element $V_{\text{cb}} \simeq 0.04$ in comparison to $V_{\text{ud}} \simeq 0.003$ for the $B^{\pm}$-meson. Therefore, although the production is suppressed due to the extra heavy quark, as shown in

[5] For an overview of the production of different heavy mesons, see Fig. 8.3. The comparison is based on simulated data, but nevertheless gives a good impression (the simulation was validated).

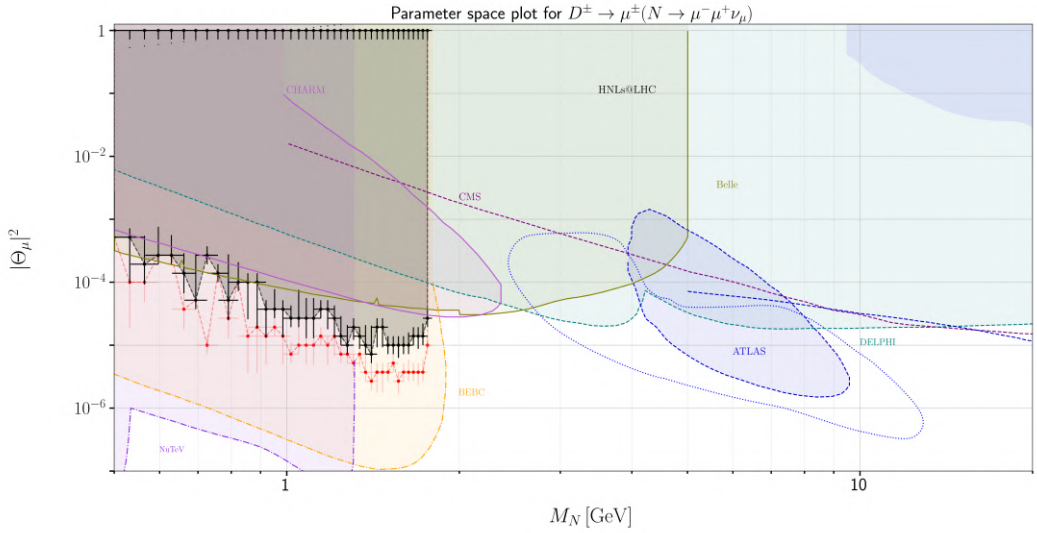

Figure 6.13: Projected 95% **CL exclusion region for HNLs with** $\Theta_\mu \neq 0, \Theta_e = \Theta_\tau = 0$ for integrated luminosities $300\,\text{fb}^{-1}$ (black crosses) and $3000\,\text{fb}^{-1}$ (red crosses). The top label shows the analysed process. Both muons pass transverse momentum cut $p_T > 5\,\text{GeV}$ and are in the pseudo-rapidity range $|\eta| < 2.4$, while the prompt muon is not included into analysis. In addition, the meson pass transverse momentum cut of $p_T > 10\,\text{GeV}$ for tagging. The DV cuts are described in the Section 5.3.1. Exclusions from the previous experiments are discussed in Section 6.1.

Fig. 8.16, the enhancement due to the CKM matrix element leads to the greatest sensitivity of any of the heavy meson processes.

6.3.4.1 Di-muon DV searches

In Figs. 6.14–6.15 we present our sensitivity estimates based solely on the displaced di-muon searches and impose a cut of $p_T > 5\,\text{GeV}$ on the displaced di-muons, in line with the T_1 trigger of DV search scheme 1. The required positions of the displaced vertices are described in Section 5.3.1. The upward tendency of the lower right corner of the exclusion region of Fig. 6.14 falls in line with the expected behavior, explained earlier, due to the emergence of non-trivial minimal distance DV-cuts.

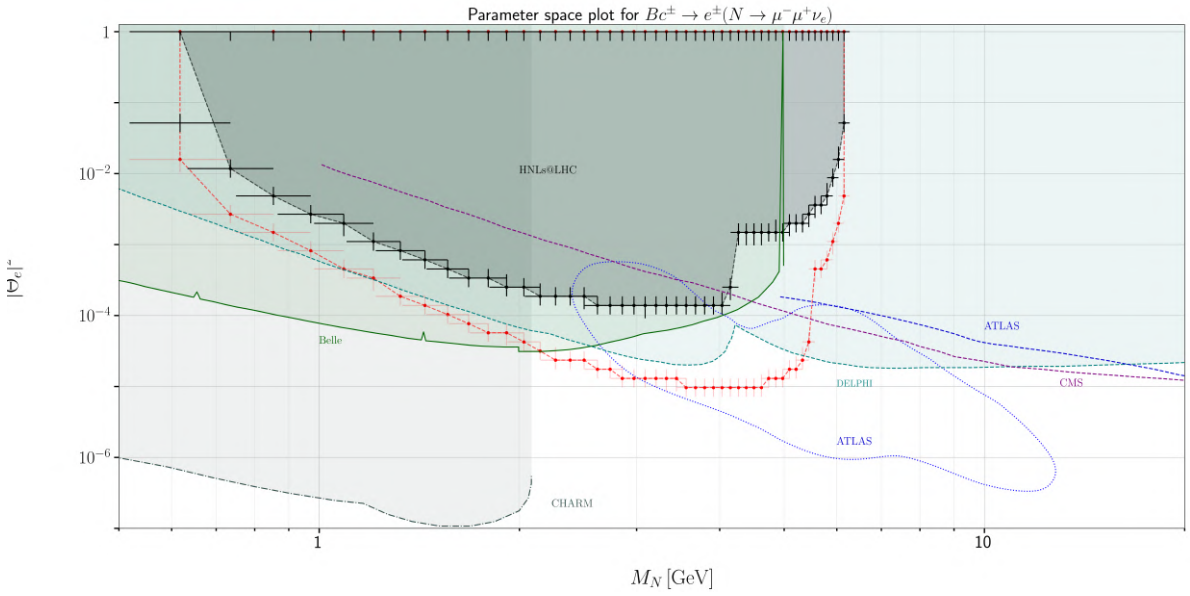

Figure 6.14: Projected 95% **CL exclusion region for HNLs with** $\Theta_e \neq 0, \Theta_\mu = \Theta_\tau = 0$ for integrated luminosities $300\,\text{fb}^{-1}$ (black crosses) and $3000\,\text{fb}^{-1}$ (red crosses). The top label shows the analysed process. Both muons pass transverse momentum cut $p_T > 5\,\text{GeV}$ and are in the pseudo-rapidity range $|\eta| < 2.4$, while the prompt electron is not included into analysis. In addition, the meson pass transverse momentum cut of $p_T > 10\,\text{GeV}$ for tagging. The DV cuts are described in the Section 5.3.1. Exclusions from the previous experiments are discussed in Section 6.1.

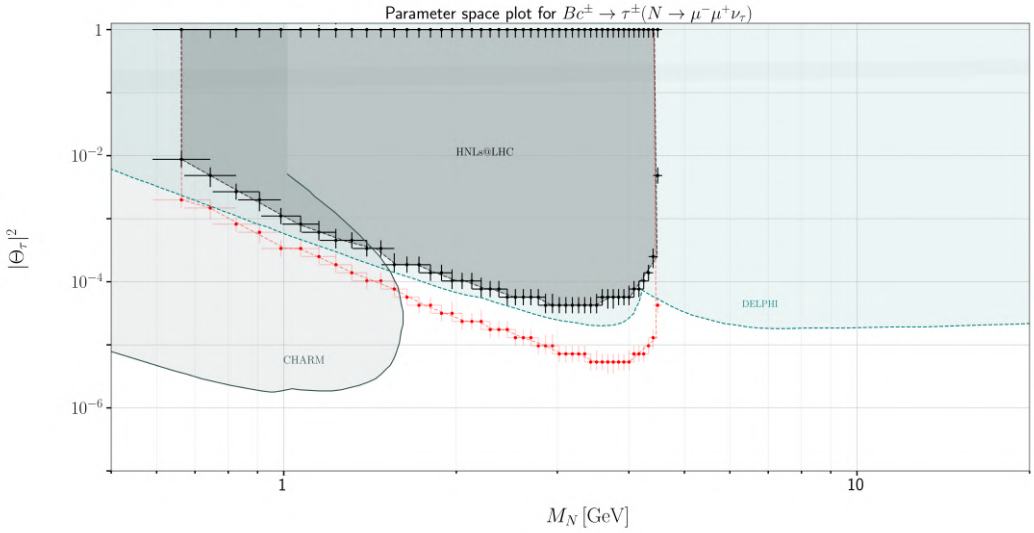

Figure 6.15: Projected 95% **CL exclusion region for HNLs with** $\Theta_\tau \neq 0, \Theta_\mu = \Theta_e = 0$ for integrated luminosities $300\,\text{fb}^{-1}$ (black crosses) and $3000\,\text{fb}^{-1}$ (red crosses). The top label shows the analysed process. Both muons pass transverse momentum cut $p_T > 5\,\text{GeV}$ and are in the pseudo-rapidity range $|\eta| < 2.4$, while the prompt *tau*-lepton is not included into analysis. In addition, the meson pass transverse momentum cut of $p_T > 10\,\text{GeV}$ for tagging. The DV cuts are described in the Section 5.3.1. Exclusions from the previous experiments are discussed in Section 6.1.

6.3.4.2 Tri-muon DV searches

In Figs. 6.16–6.17 we present our sensitivity estimates based on the *tri*-muon processes for HNLs produced in the $pp \to B_c^{\pm} \to \mu^{\pm} N, N \to \mu^{\pm}\mu^{\mp}\nu_{\mu}$ process. Here we explore the effect of different trigger requirements, starting, in the same vein as for the di-muon results, by imposing a cut of $p_T > 5\,\text{GeV}$ on the displaced leptons, with the results placed in Fig. 6.16. This exclusion region provides the greatest sensitivity of all heavy meson processes, and is only met by the region of [61] for HNL masses $M_N \lesssim 6$ GeV, as well as the beamdump experiments.

Then, the exclusion region formed by selection criteria of the T_3 trigger is placed in Fig. 6.17. This result is slightly weaker than for the T_1 trigger, as there are greater criteria of p_T, the stability between these results are placed in Fig. 6.24.

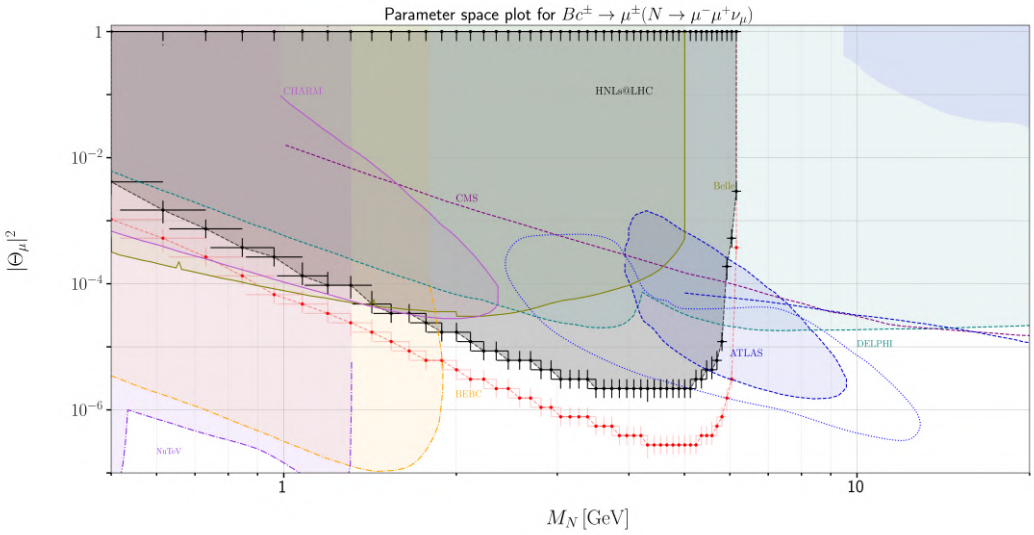

Figure 6.16: Projected 95% CL exclusion region for HNLs with $\Theta_\mu \neq 0, \Theta_e = \Theta_\tau = 0$ for integrated luminosities $300\,\text{fb}^{-1}$ (black crosses) and $3000\,\text{fb}^{-1}$ (red crosses). The top label shows the analysed process. Both muons pass transverse momentum cut $p_T > 5\,\text{GeV}$ and are in the pseudo-rapidity range $|\eta| < 2.4$, while the prompt muon is not included into analysis. In addition, the meson pass transverse momentum cut of $p_T > 10\,\text{GeV}$ for tagging. The DV cuts are described in the Section 5.3.1. Exclusions from the previous experiments are discussed in Section 6.1.

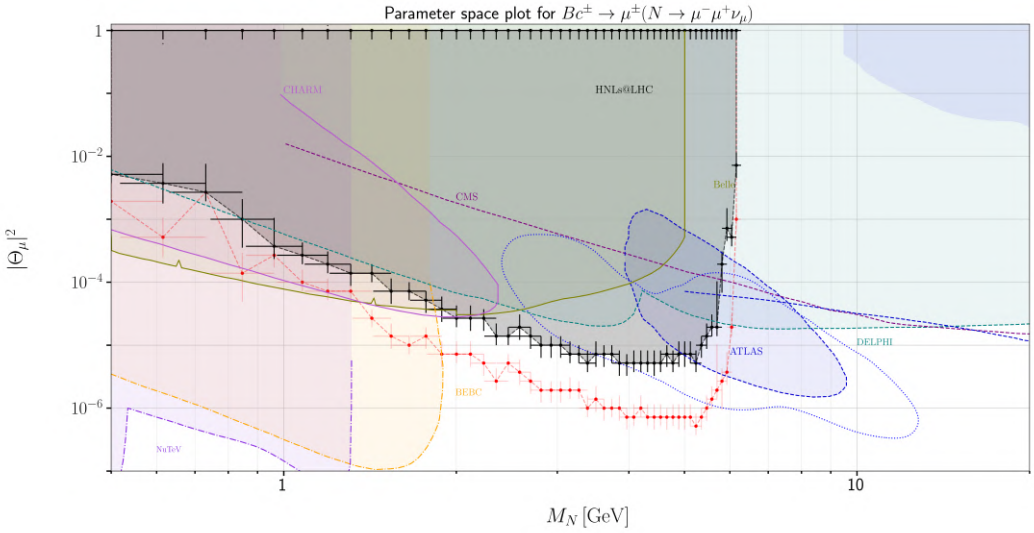

Figure 6.17: Projected 95% **CL exclusion region for HNLs with** $\Theta_\mu \neq 0, \Theta_e = \Theta_\tau = 0$ for integrated luminosities $300\,\text{fb}^{-1}$ (black crosses) and $3000\,\text{fb}^{-1}$ (red crosses). The top label shows the analysed process. All three muons pass transverse momentum cut $p_T > 7\,\text{GeV}$ and are in the pseudo-rapidity range $|\eta| < 2.4$. The DV cuts are described in the Section 5.3.1. Exclusions from the previous experiments are discussed in Section 6.1.

6.4 Results for SND

The results of HNL searches sourced by $B^{\pm}, B_c^{\pm}$ and $D^{\pm}$ mesons using the SND experiment can be summarised quite briefly, since *no signal survives* the stringent η and DV cuts the geometry of the experiment requires. This is true for all three mesons, for all three mixing schemes (the three variations of "one non-zero mixing angle"). The process that performs "best" is $D^{\pm} \to \mu^{\pm}N, N \to \mu^{+}\mu^{-}\nu_{\mu}$ which, as also seen for other results, benefits from being mediated by both charged and neutral currents unlike the di-muon processes.

A parameter space cut-flow plot showing the cumulative effect on the exclusion region when applying successive cuts emulating the SND detector, can be found in Fig. 6.18. From said figure it can be seen that it is the DV cut, requiring decay within a cuboid in the range of 480 m to 482.4 m to one side of the center of ATLAS along the collision axis, that kills the signal. The transversal area of the cuboid is a mere 0.16 m^2, and despite its placement very close to the collision axis increases its DV efficiency, it is still a very strong requirement to demand decay within its volume.

As can be seen in Fig. 6.18, some signal survives the η cut. For for the SND experiment the η cut was defined to require the displaced muon trajectories to intersect the transverse area of the SND detectors rear end. Fig. 6.18 was based on 60.000 events (double of the number of events used to generate the results for ATLAS), but still shows sign of lacking sample size by its ragged slope. During the study a sample size of 100.000 was reached (still no signal survived the DV cut), beyond which the analysis was found to be computationally prohibitive given the hardware we had available.

The SND experiment favors forward physics and requires no minimal p_T, whereas ATLAS favors high p_T events. With respect to p_T a big factor for the good performance of the $D^{\pm}$ meson can be the absence of any p_T cut at SND, which was the dominant cause of its loss in efficiency at ATLAS, in combination with its abundant production.

Hope could be held that some of the lighter mesons could perform so well with respect to the SNDs η and DV cut, as to actually retain some signal. The computational machinery developed for the present study is readily adapted include lighter mesons, and thus this could be an avenue for future exploration.

Unfortunately, a lower meson unavoidably comes with an even lower upper limit on the mass range of the HNL searches possible.

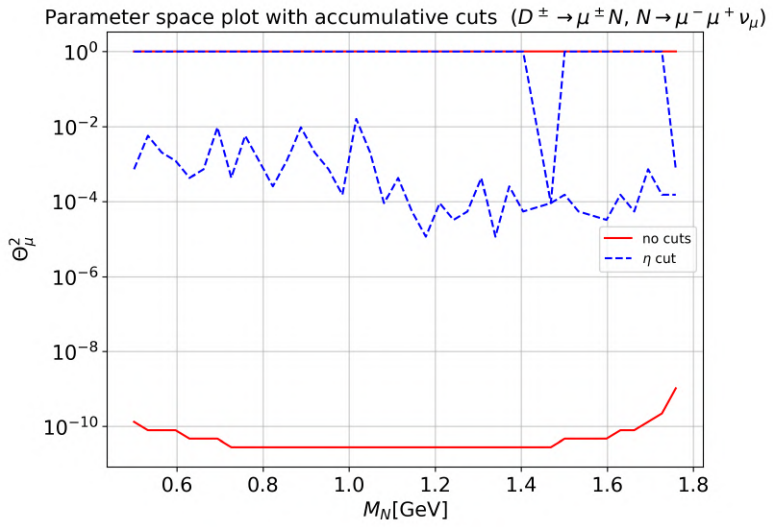

Figure 6.18: Parameter space cut-flow for SND, showing the effect on the exclusion region when applying the η cut. The process shown is $D^\pm \to \mu^\pm N, N \to \mu^+\mu^-\nu_\mu$ and the plot is based on 60.000 events (smoother curves could be achieved by increasing events but was found to be computationally prohibitive). Note that *no signal survives the DV cut*, although it can be seen that some signal is retained if only η cut is imposed (SND requires no p_T cut).

6.5 Consolidated results

For overview of the results presented above, all processes has been organised into three categories pertaining to their single non-zero mixing angle. The three resulting plots are presented below in figures 6.19-6.21.

Furthermore, since HL-LHC is scheduled to commence around same time that the SHiP experiment is also expected to be operational, a comparative plot between the two is also included here, comparing best results across flavors in a single comparative plot seen in Fig. 6.22. Exclusion regions pertaining to the two experiments are found to be complementary, which proves promising for HNL searches in the 0.5 GeV $< M_N <$ 16 GeV range, possibly bringing the exclusion bounds down by around 2-3 orders of magnitude across the range for all flavors. Exiting times ahead!

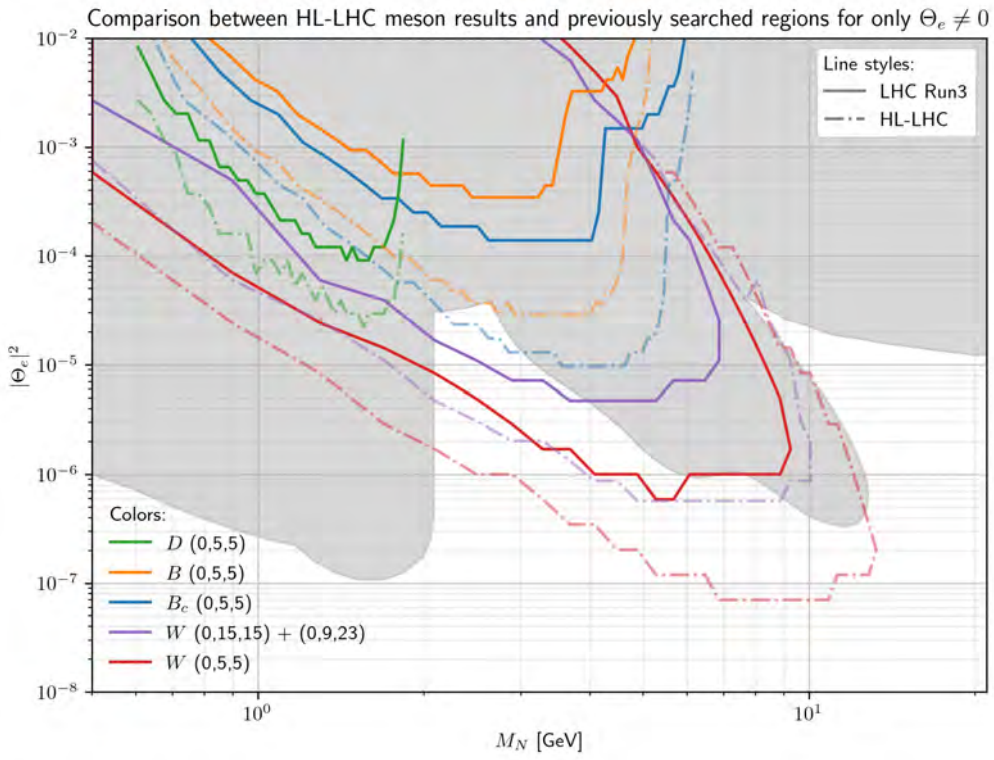

Figure 6.19: Summary plot of the results for the considered processes with $\Theta_e \neq 0$. Run3 predictions marked with solid lines, HL-LHC marked with lighter "dashdottet" lines. The shaded area indicates the previously searched region.

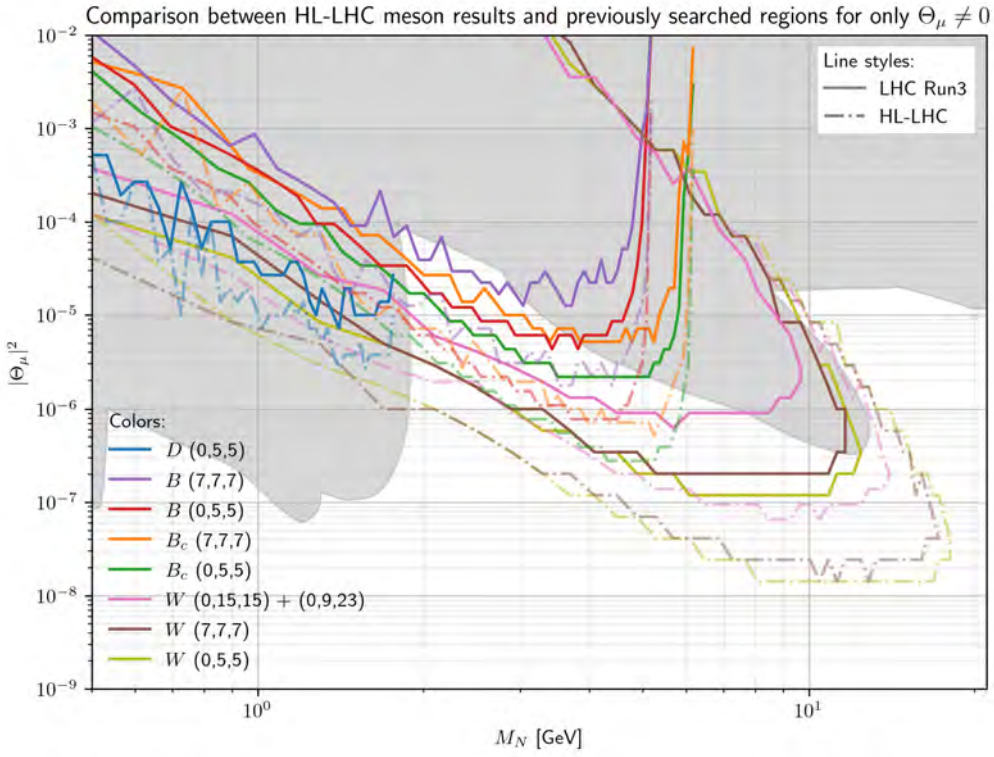

Figure 6.20: Summary plot of the results for the considered processes with $\Theta_\mu \neq 0$. Run3 predictions marked with solid lines, HL-LHC marked with lighter "dashdottet" lines. The shaded area indicates the previously searched region.

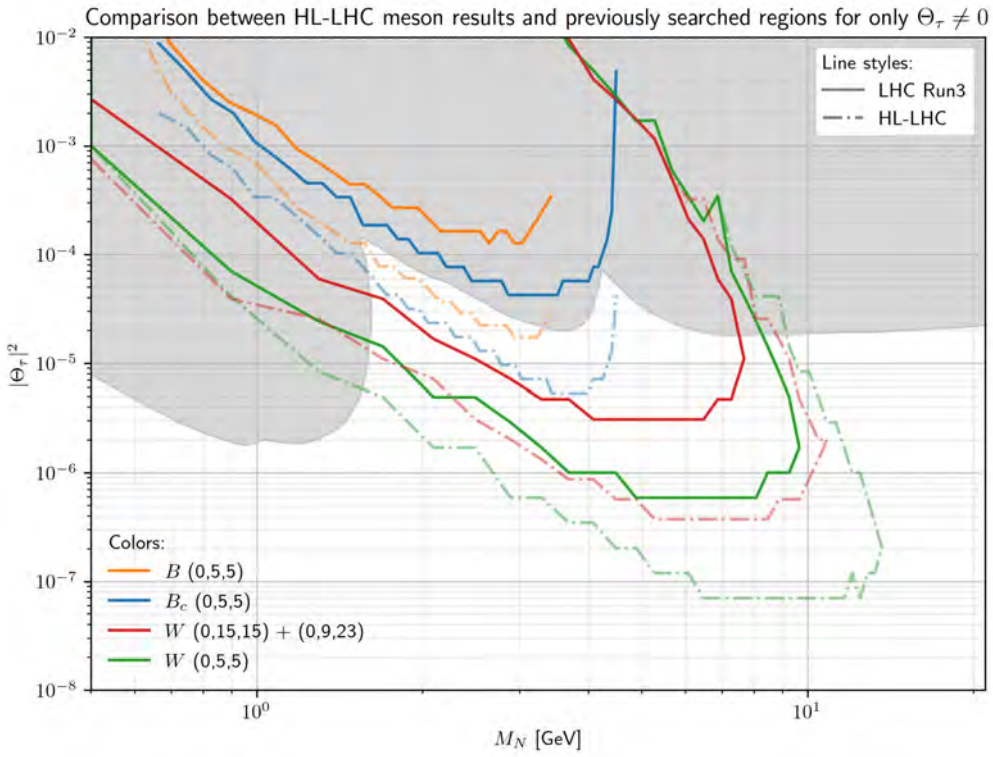

Figure 6.21: Summary plot of the results for the considered processes with $\Theta_\tau \neq 0$. Run3 predictions marked with solid lines, HL-LHC marked with lighter "dashdottet" lines. The shaded area indicates the previously searched region.

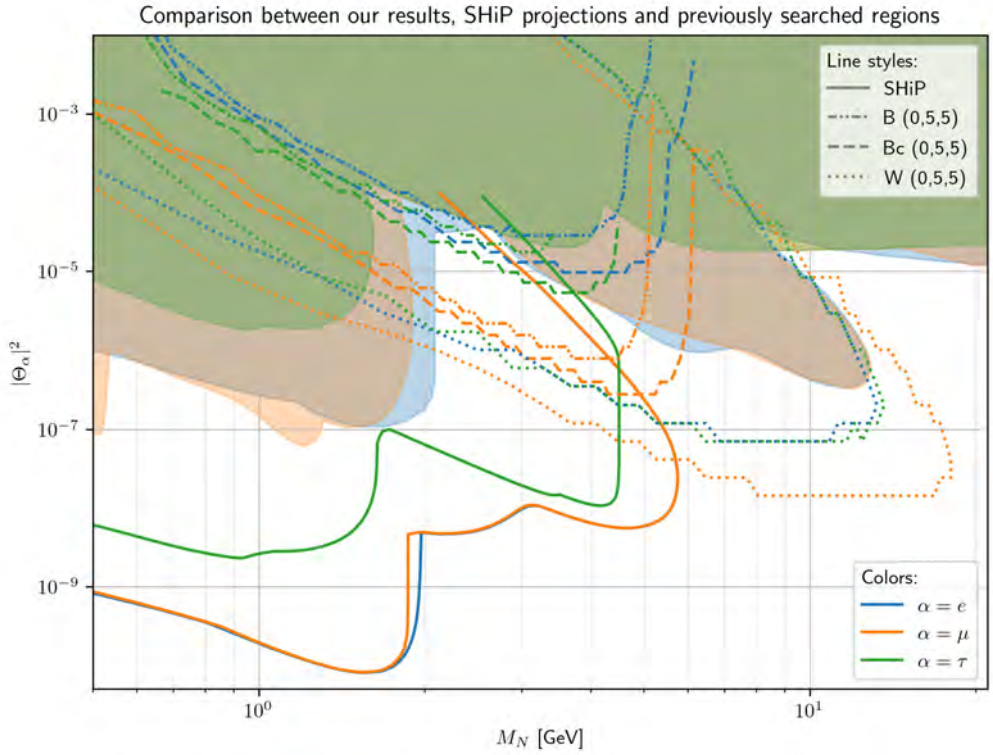

Figure 6.22: Comparative summary plot with projected exclusion region expected from the SHiP experiment and the HL-LHC results of the present work. Colors represent which mixing angle Θ_α is assumed non-zero. Dashed lines represent SHiP projections, "dashed dotted" lines represent our results and the shaded area indicates the previously searched region.

6.6 Stability of results with varying selection criteria

One can ask, how *stable* are the results for the previously presented parameter space exclusion regions with respect to changing event selection criteria. For the $W^{\pm}$-processes, the three exclusion regions for the parameter space of the tri-muon channels are shown below in Fig. 6.23.

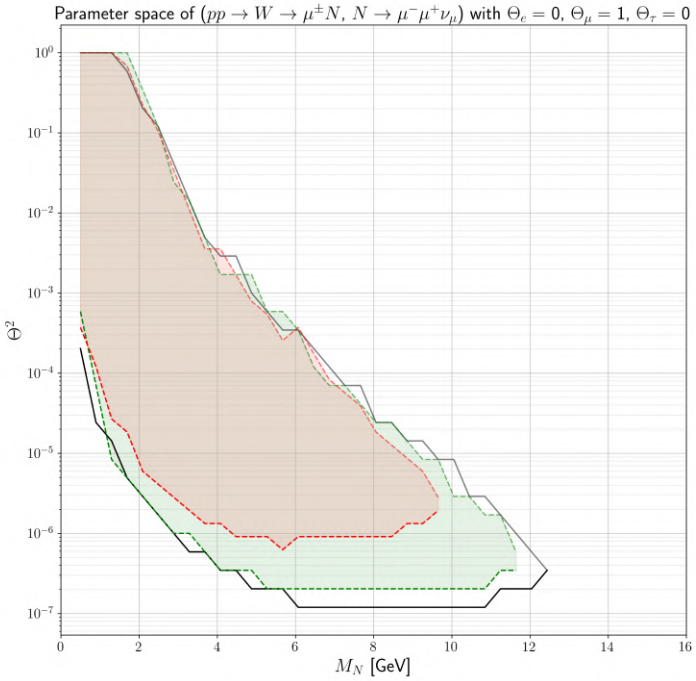

Figure 6.23: The exclusion region of the parameter space for the tri-muon process $pp \to W^{\pm} \to \mu^{\pm}N, N \to \mu^{+}\mu^{-}\nu_{\mu}$ for the three event selection criteria. The notation for the cuts is written in terms of three coordinates (a,b,c) where a refers to the p_T cut applied to the prompt lepton, and b,c refer to the p_T cut applied onto the displaced muons. The + symbol is used to indicate the presence of dual cuts, i.e. either (a, b, c) or (d, e, f) as described in Table 9.1.

Using the notation defined in Fig. 6.23, it is clear that there is not much deviation between the $(0, 5, 5)$ and $(7, 7, 7)$ cuts corresponding to the T_1 and T_3 triggers, in contrast to the third (in red). The third cut type (in red) is more extreme, corresponding to the T_2 trigger, and thus it is no surprise that there is deviation of a more significant magnitude as compared with the two others. Thus, it can be stated that the results are *relatively* stable with respect to choice of cut type.

For the meson processes, a single representative sample has been selected for the stability plot, namely the tri-muon process of $B^{\pm}$, placed in Fig. 6.24, to gauge an idea of the general effect on the B-mesons. Its is notable to mention, that the exclusion region is most sensitive to p_T cuts on the muons, whereas it is relatively stable with respect to p_T cuts on the constituent quarks, taking into consideration that the cross-section decreases with around two orders of magnitude when applying b-tagging with > 25 GeV. This can be explained by an increase in efficiency of the remaining cuts, since mesons with higher p_T are more likely to produce signal that survive these cuts. It can also be noted how the characteristic "cigar shape" common to displaced vertex searches (see Fig. 9.13) appears when the criteria for the minimal displacement of the displaced vertex is tightened to 5 cm.

It is of particular interest to see a well performing result when requiring $p_T \geq 6\,\text{GeV}$ for both displaced muons (represented by green in Fig. 6.24) since this p_T cut is compatible to a *currently available* dedicated b-physics low p_T muon trigger [75]. Said trigger accepts events with two muons, each with $p_T \geq 6$ GeV, and with combined invariant mass, $m(\mu_1, \mu_2)$, in the range of either $2.5 \leq m(\mu_1, \mu_2) \leq 4.0$ GeV or $4.7 \leq m(\mu_1, \mu_2) \leq 5.9$ GeV. Under the assumption that both displaced muons are not discarded due to their impact parameter (see discussion on *pointing* muons in Section 7.2.1.1), the dedicated b-physics trigger is applicable to HNLs within the prescribed mass range[6].

The results for the three B_c processes (the best performing meson results), with p_T cut corresponding to the dedicated b-physics trigger discussed above, are shown in Fig. 6.25. In said figure the invariant mass ranges associated with the dedicated b-physics trigger are demarcated in grey, indicating the ranges of the parameter space where it can be applied.

Interestingly, the aforementioned dedicated b-physics trigger can be used as a trigger on the leptons coming *not* strictly from the HNL mediated process in question, but rather from a consideration of the final state leptons produced in the event as a whole as further elaborated in Sec. 7.1.2. Concretely this would mean there would be extra prompt leptons available to trigger on, which was not taken into account in the current study.

For the reason above, the exclusion limits shown in Fig. 6.25 effectively acts as a *lower bound*[7] for heavy meson HNL searches using the dedicated b-physics trigger. A significant improvement could be expected when including prompt muons produced by the b/c-quarks, for which the trigger is originally intended. Though this avenue of exploration is not pursued further in the present work, it certainly looks very promising for future studies. To show the potential for improvement, a parameter space cut-flow plot showing the cumulative effect on the exclusion region, when applying successive cuts is shown in Fig. 6.26.

The difference between the lower exclusion limit before and after p_T cut defines the room for possible improvement in p_T cut efficiency. In this light is noteworthy that the p_T cut dominates and is responsible for raising the lower exclusion limit with up to two orders of magnitude, hinting at significant potential for lowering the exclusion limit with a more inclusive p_T cut.

[6] Ignoring the momentum escaping via the SM neutrino produced by the weak current (see Fig 4.3). The momentum contribution from the escaping SM neutrino is not negligible, however, as the dedicated b-physics trigger is not the main focus for the present work, including it into the analysis is left for future work at this exploratory stage. Thus the prospects of the dedicated b-physics trigger for HNL searches is just regarded as an auxiliary result to the main body of work presented in the present study.

[7] Ignoring an escaping SM neutrino as earlier described

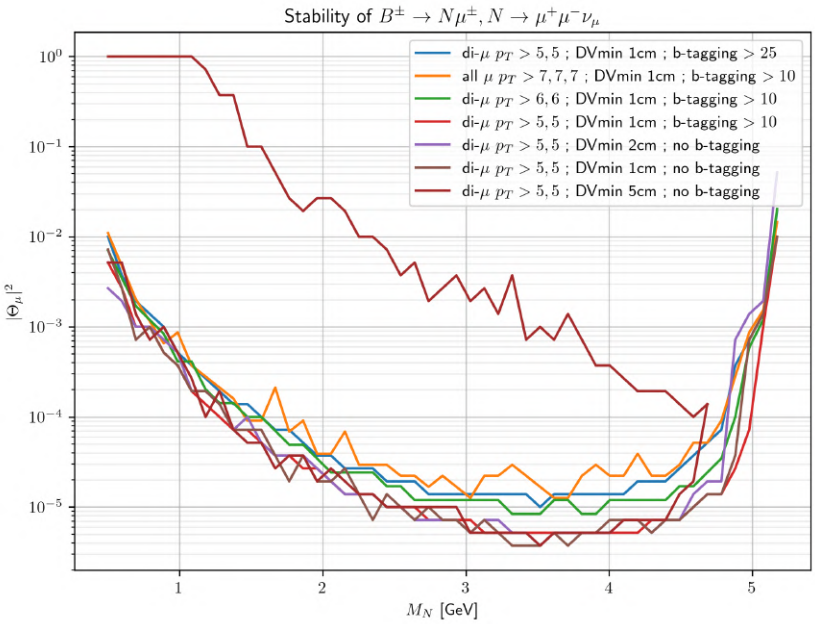

Figure 6.24: Stability plot of the tri-muon $B^{\pm}$ process, for varying p_T and minimal displacement event selection criteria.

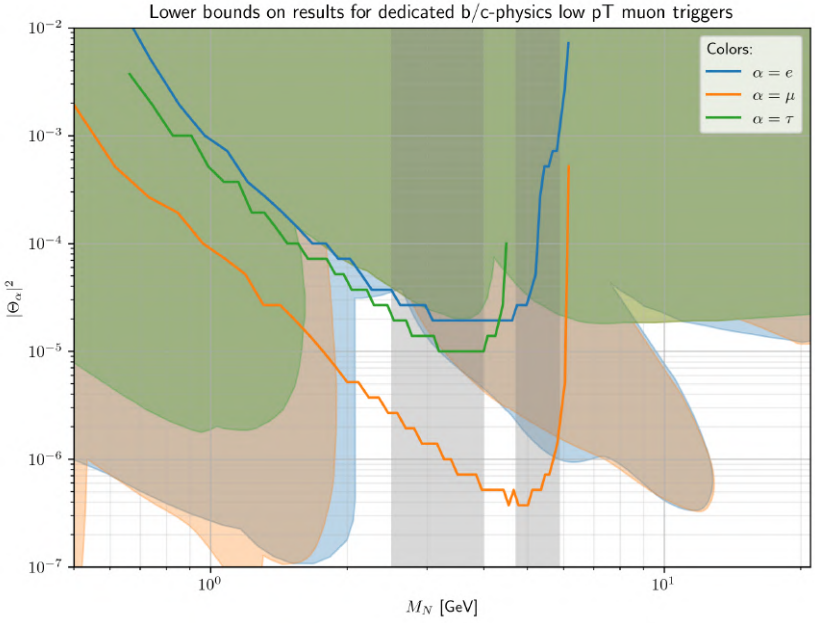

Figure 6.25: Parameter space plot of the *lower bound** for heavy meson HNL searches using the dedicated ATLAS b-physics trigger requiring two muons with $p_T > 6$ GeV and invariant mass in the ranges 2.5 - 4 GeV or 4.7 - 5.9 GeV. These invariant mass ranges are marked by grey vertical bands and are directly applicable to the parameter space plot since only displaced di-muons originating from HNLs are considered for the trigger i.e. inheriting the entire invariant mass from the HNL (neglecting an escaping SM neutrino). The bounds are based on the B_c process (see Fig. 4.3), giving the lowest bounds of all the heavy mesons process considered. **Ignoring momentum escaping in form of an SM neutrino.*

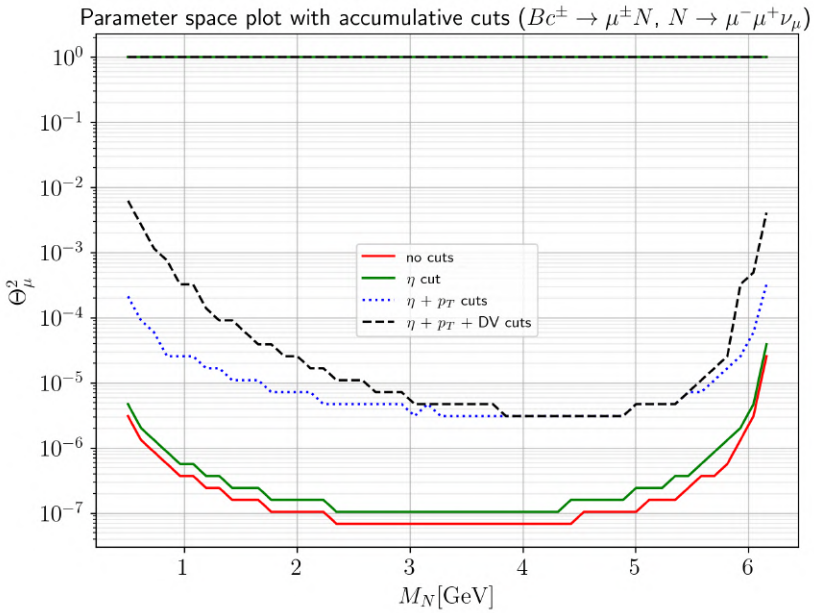

Figure 6.26: Parameter space cut-flow plot showing the cumulative effect on the exclusion region, when applying successive cuts. The process shown is $B_c^{\pm} \to \mu^{\pm} N, N \to \mu^{+}\mu^{-}\nu_{\mu}$ with p_T cut (0,6,6) on the muons. Specifically, it is noteworthy that the p_T cut dominates and is responsible for raising the lower exclusion limit with up to two orders of magnitude. This is significant since a more inclusive p_T cut than the one applied is actually feasible for triggering.

6.7 Uncertainties

The uncertainties present in the computation are three-fold:

- systematic, arising from the *granularity* of the parameter space plot
- statistical, arising from the random sampling of the exponential distribution related to the decay of HNLs
- statistical, arising from the Gaussian distributions related to the random sampling inherent in Monte Carlo simulations, as reported by PYTHIA and MADGRAPH

In the following subsections, these errors are elaborated, and further discussed in mathematical detail.

6.7.1 Systematic uncertainties

The exclusion bounds presented in the results chapter are not continuous, but rather granular with a certain height and width. The parameter space plots have been divided into *pixels* each with height $\Delta\Theta^2$ and width ΔM_N and have been accounted for in the error bars.

6.7.2 Statistical uncertainties

The uncertainties were computed using standard error propagation, such that for a function, $f = ABC$, the standard deviation, S_f, is defined as

$$S_f \simeq |f| \sqrt{\left(\frac{S_A}{A}\right)^2 + \left(\frac{S_B}{B}\right)^2 + \left(\frac{S_C}{C}\right)^2} \tag{6.7.1}$$

under the assumption that A, B and C are uncorrelated. Thus, for (5.1.1) one can write a simple expression as a function of the variables of the hypothesis such that

$$f(\Theta, M_N) = \mathcal{L} \cdot \sigma \cdot \mathcal{S}_\Gamma \cdot \mathcal{S}_\Theta \cdot \epsilon_{\text{detector}} \tag{6.7.2}$$

the standard deviation can then be computed as

$$\mathrm{S}_f = |f| \sqrt{\left(\frac{\mathrm{S}_\mathcal{L}}{\mathcal{L}}\right)^2 + \left(\frac{\mathrm{S}_\sigma}{\sigma}\right)^2 + \left(\frac{\mathrm{S}_\epsilon}{\epsilon}\right)^2} \tag{6.7.3}$$

since $\mathcal{S}_\Gamma$ was not subject to uncertainties $\mathcal{S}_\Theta$. The error on the efficiency estimated as

$$\mathrm{S}_\epsilon = \frac{\sqrt{n_{\text{survive}}}}{n_{\text{total}}} \tag{6.7.4}$$

, where n_{survive} is the number of events surviving all cuts out of the total ensemble of n_{total}. Ideally S_ϵ would be found be analysing the correlated contributions from ϵ_{p_T}, ϵ_η and ϵ_{DV}, where the exponential distribution enters the last two through our external HNL decay handling. Such statistical analysis was deemed beyond the scope of this thesis and the added precision it would bring was assumed insignificant. Further accuracy of the estimated error could be reached by e.g. bootstrapping (see [85]), but this proves computationally prohibitive for the current study.

Part II

Methodology & Validation

Chapter 7

Collider physics - a very short primer

Previous chapters established the theoretical underpinning and the specific processes we are investigating in this work. This chapter serves to introduce the collider physics concepts needed for our analysis and to introduce the two detectors which we will estimate the HNL signal for, namely ATLAS and SND.

7.1 Basic concepts

Here we will briefly introduce the relevant experimental considerations of the current work.

7.1.1 Units and accelerators

In collider physics the preferred unit for measuring cross-sections is the *barn* (b) defined as $1\text{b} = 10^{28}\,\text{m}^2$. It originates in the study of nuclear reactors and is fixed such that the cross-section of neutron-uranium (^{235}U) scattering is roughly equivalent to 1 b.[1] Due to the wide range of scales in the physics involved, both mili- and femto-barns, ($1\,\text{mb} = 10^{-3}\,\text{b}$ and $1\,\text{fb} = 10^{-15}\,\text{b}$) respectively, will be used. In the natural units ($c = \hbar = 1$) the barn to GeV conversion factor is $1\text{ b} = 2568\text{ GeV}^{-2}$ [87].

Two of the most fundamental parameters of a collider experiment is the *center-of-mass energy* and *luminosity* of the experiment. Furthermore, in collider experiments involving hadrons their constituent quarks and gluons (partons) interact [7]. They may do so with a non-zero net momentum with respect to the lab-frame. To be explicit and to set up conventions for later use, we can define the momentum of two colliding particles A and B as

$$p_A = (E, 0, 0, E) \quad \text{and} \quad p_B = (E, 0, 0, -E). \tag{7.1.1}$$

It is custom to let the axis of the relative motion of the colliding particles coincide with the z-axis. In this case, the z-axis is refereed to as the *beam-axis*. In Fig. 7.2 a 3D diagram depicts a cylindrical detector with with an inlaid coordinate system which is defines the convention adopted throughout the thesis. The center of mass energy $E_{\text{cm}} = 2E$ is then often expressed as the square-root of the Mandelstam variable $s = (p_A + p_A)^2 = E_{\text{cm}}^2$. Along with particle masses, E_{cm}, sets the energy scale for the processes that can be probed and determines the amount of particles produced in collisions through

[1] It is said that the peculiar name of the unit derives from Enrico Fermi, who purportedly remarked that neutrons in atomic reactors would hit Uranium targets as easily as hitting the broad side of a barn [86].

Einsteins fundamental mass-energy relation. To reach the high energies needed for exotic sub-atomic particles to be created at collision experiments they are fitted with an accelerator, which loads the particles with kinetic energy prior to collision.

Since the cross-section of individual processes can be relatively low, it is not enough to secure that they can happen. One must also ensure that they do so at a rate that allows for a statistically relevant signal. For such considerations it is necessary to consider the *luminosity* of the accelerator. The luminosity comes in two varieties; *integrated* and *instantaneous*. The instantaneous luminosity, $\mathcal{L}_{\text{inst}}$, is defined as the number of events per second per unit cross section [88], and the integrated luminosity, $\mathcal{L}_{\text{inst}}$, is simply the instantaneous luminosity integrated over time e.g. the duration of a specific run of a collider experiment (which may be years!). Since the time dimension is integrated out, the integrated luminosity is in units of events pr. unit cross-section, therefore the simple relation

$$N_{\text{ events}} = \mathcal{L}_{\text{int}}\sigma_X = \int_{t_0}^{t_1} \mathcal{L}_{\text{inst}}\sigma_X \, dt, \tag{7.1.2}$$

gives the number of collisions resulting in the process X, with cross-section σ_X during the time interval from t_0 to t_1. From the above equation it is obvious that the amount of events one would expect depends linearly with $\mathcal{L}_{\text{int}}$ and σ_X so increasing the integrated luminosity will allow one to probe the physics of increasingly rare events. The quantity $\mathcal{L}_{\text{inst}}$ together with the center-of-mass energy contains all the information about the accelerator needed to analyze the experiment [87].

7.1.2 Trigger system

Once sufficiently large luminosities are reached, another problem arises, namely that of large data. Due to the extraordinary amounts of data produced in the LHC it is not possible to process it all in detail, therefore a mechanism to pick out relevant events for further analysis needs to be put in place. This mechanism is called a *trigger system*, and it selects events based on a number of different physical signatures such as transverse momentum, hadron jets, missing transverse energy and so on. Currently around 1500 [89] such conditions are defined at the LHC. They can further be combined to reflect the specifics of the process, balancing the need to reduce data size while retraining the relevant events.

To give an impression of the actual numbers we can estimate the rate and total amount of proton-proton collisions during Run 3 of the Large Hadron Collider (LHC) at the European Organization for Nuclear Research (CERN). To this end we need the luminosities for Run 3 which are $\mathcal{L}_{\text{inst}} = 30\text{Hz} \cdot \text{nb}^{-1}$ [86] with expected integrated luminosity $\mathcal{L}_{\text{int}} = 300\,\text{fb}^{-1}$. The total cross-section for the proton-proton collisions (the LHC is colliding protons), σ_{pp}, at the center-of-mass energy of $\sqrt{s} = 13\,\text{TeV}$ [90], which is approximately 30 mb. [91]. From the definitions of the luminosities, it follows that

$$\text{Number of events pr. second in Run 3:} \quad \mathcal{L}_{\text{inst}} \cdot \sigma_{\text{pp}} = 30\,\frac{\text{Hz}}{\text{nb}} \cdot 30 \cdot 10^6\ \text{nb} = 0.9\ \text{GHz} \tag{7.1.3}$$

$$\text{Total number of events in Run 3:} \quad \mathcal{L}_{\text{int}} \cdot \sigma_{\text{pp}} = 300\frac{1}{\text{fb}} \cdot 30 \cdot 10^{12}\ \text{fb} = 9 \cdot 10^{15}. \tag{7.1.4}$$

Considering that current CPUs run at GHz scale, meaning they can perform roughly 10^9 operations a second, and that each event contains around 1 MB of data, it is not possible to write all events to the storage each second[2] [86]. Further more one would need $9 \cdot 10^{15} \cdot 1\ \text{MB} \approx 10^{10}$ TB of storage to save the complete data of Run 3, which is also not feasible. For these reasons e.g. the ATLAS experiment

[2] Assuming 64 bit processor one would need it to run at at least $8 \cdot 1\ \text{MB} \cdot 0.9\ \text{GHz}/64\ \text{bit} \approx 10^5$ GHz to save the data, although the real bottleneck would probably the hard drive which typically operates at MHz scale for reading and writing.

at LHC is limited to a data acquisition rate of ~ 1 kHz [92] , meaning that the trigger system only accepts about one in a million events, emphasizing its importance to the experiment as a whole. With the High-Luminosity LHC upgrade prospected to be operational around 2026 the integrated luminosity will reach 3000 fb^{-1} [93] and with that the need for the trigger system is further accentuated.

Finally it can be mentioned that, the trigger system tackles the copious data rates by implementing a two step filtering process whereby events are first run through a hardware based trigger system named the Level-1 trigger, reducing the rate to less than 100 kHz. This level only receives coarse information from the detector, but if the event survives the complete data read-out is passed on the to a software based trigger system named the High-Level trigger, which handles the final reduction down to 1 kHz [92].

7.1.3 Kinematics

As mentioned above, the center-of-mass frame of interacting partons is not generally the same as the lab-frame since the two may have some relative motion along the beam-axis. Therefore the Lorentz transformation relating the two frames may distort angles when transforming between the two frames. This motivates the desire to define some quantities which are boost invariant with respect to boosts along the beam-axis [86]. Since a general such boost only mixes the energy and z-component of the boosted four-vector, such that

$$E \longrightarrow E\cosh\beta + p_z\sinh\beta \tag{7.1.5}$$
$$p_x \longrightarrow p_x \tag{7.1.6}$$
$$p_y \longrightarrow p_y \tag{7.1.7}$$
$$p_z \longrightarrow p_z\cosh\beta + E\sinh\beta, \tag{7.1.8}$$

we see that the x and y components are left invariant. Therefor the transverse momentum, p_T, given by

$$\vec{p}_T = (p_x, p_y), \quad p_T = |\vec{p}_T| = \sqrt{p_x^2 + p_y^2}, \tag{7.1.9}$$

is one of the boost-along-beam-axis invariant quantities we sought for. This quantity will prove to be of utmost importance, so to emphasize, this simple concept has been granted its own figure, see Fig. 7.1.

Because diffractive scattering, where protons glance off each other, is the dominant interaction of the proton beams at LHC and similar colliders, most of the forward physics (i.e. outgoing particles with trajectories close to the beam-line) results from interactions with low momentum transfer. If we are interested in the rare hard processes with large momentum transfer, the place to look is thus off the beam-line, where these signals do not drown in soft background events. This further motivates the interest in transverse momentum, p_T, since it points to hard-collisions at the proton level.

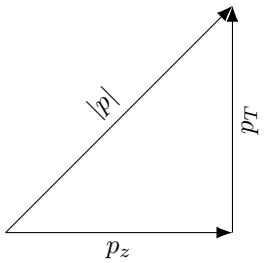

Figure 7.1: Illustration of the longitudinal p_z and transverse p_T components of a general momentum-vector, in accordance with Fig. 7.2 **(a)**.

Also of significant importance for the present thesis is the semi-conserved quantity, y, called *rapidity* (not to be confused with

the y-axis, it is simply the conventional notation). It is defined,
and transforms under boost along the beam-axis, as

$$y = \frac{1}{2}\ln\frac{E+p_z}{E-p_z} \longrightarrow y + \ln(\cosh\beta + \sinh\beta), \tag{7.1.10}$$

where β is the relativistic β-factor (see Eq. (9.1.4 on page 99) for definition). Though y itself is not invariant under such a boost, the difference between two rapidities y_1 and y_2 is. In the case of massless particles, the rapidity has a very special form which motivates the definition of its off-spring, η, called *pseudo-rapidity*, defined as

$$\eta \equiv \ln\cot\frac{\theta}{2} = y, \tag{7.1.11}$$

where the last equality is only true for massless particles! The angle θ is defined as in Fig. 7.1 (it can also be found in Fig. 7.2 (a)) and can be determined by simple trigonometry through

$$\tan\theta = \frac{p_T}{p_z}. \tag{7.1.12}$$

From its definition it is clear that η is a rephrasing of θ and thus quantifies angle with respect to beam-axis, as seen in Fig. 7.2 (a). In this sense η is used to specify a detectors angular coverage with respect to the interaction point. For particles produced in a displaced vertex, the situation is slightly less simple since the angular coverage can not be measured from the beam interaction point.

There are other invariant quantities such as e.g. the azimuth angle ϕ (see Fig. 7.2), parameterising rotations in the transverse plane, but these will not be relevant for the analysis in this thesis.

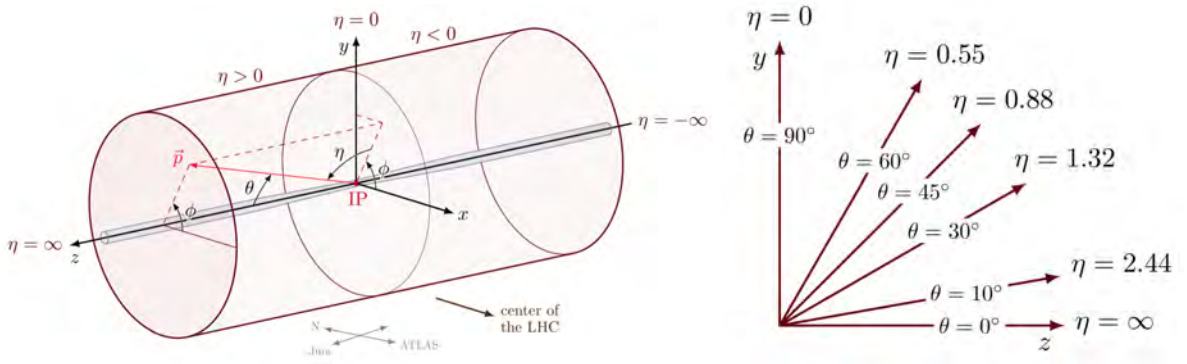

(a) **(b)**

Figure 7.2: **(a)** Depiction of cylindrical coordinate system with beam-pipe along the z-axis, arbitrary momentum vector $\vec{p}$ and interaction point of the beams at IP [94]. **(b)** Examples of angles with corresponding pseudorapidites [95].

7.2 Detectors

The LHC is the largest accelerator in the European Organization for Nuclear Research (CERN) complex. It is a circular accelerator with a circumference of 27 km and operates at a depth of 175 m, to e.g. shield the detectors from cosmic ray contamination. After a recently completed upgrade the accelerator has now begun its Run-3 phase, during which it will collide particle beams with center-of-mass energies of up to ~ 14 TeV [90], by the end of which it will have achieved an integrated luminosity of 300 fb^{-1}.

After Run-3, yet another upgrade is planned; the High-Luminosity LHC (HL-LHC), to be operational in ∼2029, with a prospective integrated luminosity up by an order of magnitude to 3000 fb^{-1} [93].

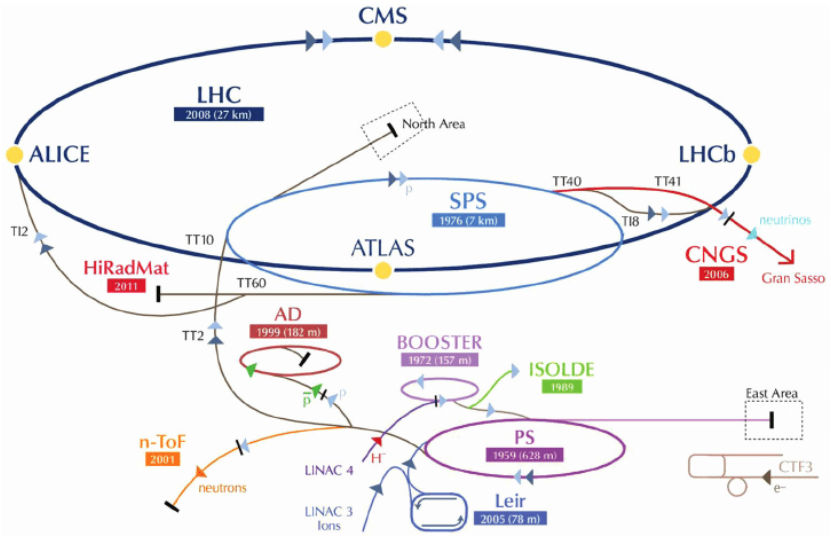

Figure 7.3: Schematic representation of the CERN accelerator complex depicting the various experiments. ATLAS is found at the bottom of the dark blue ring representing the LHC [96].

7.2.1 ATLAS

Weighing in at a whooping 7,000 tonnes and with a cylindrical construction of 46 m in length and 25 m in diameter, the ATLAS (A Toroidal LHC Apparatus) experiment is not only the largest detector at the LHC, but also has the world-record of being the largest volume detector ever built for a particle collider [97]. Situated 100 m underground it is one of two general purpose detectors at LHC, designed for experiments involving proton-proton collisions as well as lead-lead and proton-lead [98].

The detector is symmetric (along the beam-line) and consists of three main sub-detector types, namely; trackers, calorimeters and muon chambers, all centred around the interaction point [99]. The innermost detector is composed of a Pixel Detector[3] (PD) in the innermost layer, the Semiconductor tracker (SCT), the middlemost, and the Transition Radiation Tracker (TRT) composing the outer shell of the Inner Detector[4]. It is designed to measure the direction, momentum, and charge of electrically-charged particles produced by the collision and to reconstruct the decays vertices of said particles [100]. Then comes a thin superconducting solenoid providing a 2 T axial magnetic field, and again is enclosed by an *electromagnetic* and a *hadronic* calorimeters designed to measure particle energy by sampling the particle showers they induce [101]. Finally, and most importantly for the current case, the *Muon Spectrometer* (MS) encapsulates all the other detector systems. Due to the properties of muons, they will pass through the inner layers of the detectors and reveal themselves in the outer layer of ATLAS. For a graphic representation of the full splendor, see Fig. 7.4.

Pairs of muons play an important role in the processes described in chapter 4 and will be used as the trigger for this analysis to be elaborated upon later. The MS is composed of the *barrel region*, where its detector plates are placed horizontally along the beam-axis starting at a radius of 5 m, and the *end-caps*, placed in the transverse plane with respect the beam-axis starting at ±7m with respect to the IP. The MS trigger system is based on the resistive plate chambers (RPC) and the thin gap chambers (TGC)

[3]The Pixel Detector is composed of four layer of pixels, with each pixel smaller than *a single grain of sand*.

[4]It should be stated here, for use at a later point, that *no* part of the ID can be used for Level-1 (L1) hardware triggering for Run-2 and Run-3, however the trigger system is being upgraded for the high-luminosity phase of the LHC, and thus the L1 trigger may include the ID for the high-luminosity phase.

for the barrel and end-cap regions respectively. For noise reduction in both the barrel and end-caps, layers of monitored drift tube (MDT) are relied on, which reduce the two main culprits: 1) Fake muons emanating from between the first and second layer (counted from the center of ATLAS) of the end-cap due to slow moving protons mimicking the muon signal and 2) contamination from low p_T muons below the trigger threshold. To get an overview of the design see Fig. 7.5, which also includes the η-ranges of the various MS detector systems mentioned above. From the figure it can be seen that the geometry seals off cylindrical regions, with an open uncovered section of $|\eta| > 2.4$ (for the RPC trigger), where the beam-pipe exits the detector. This is of importance because the MS trigger must fire for the events of interest to be recorded.

As the biggest detector at the LHC, ATLAS, and specifically its MS, is advantageous for DV searches. As described above the MS is the last layer of detection systems in ATLAS and thus provide a significant decay volume, increasing it by a factor of > 10 [59, 42] compared to previous searches at the LHC (as of 2019). For the purpose of this study, we restrict the maximum allowable decay volume to 5m in the transverse direction and 7m in the longitudinal, effectively requiring all muon tracks to traverse the entire MS. This is in accordance with two noise reduction mechanisms mentioned above, and secures optimal possibility for track reconstruction. [5]

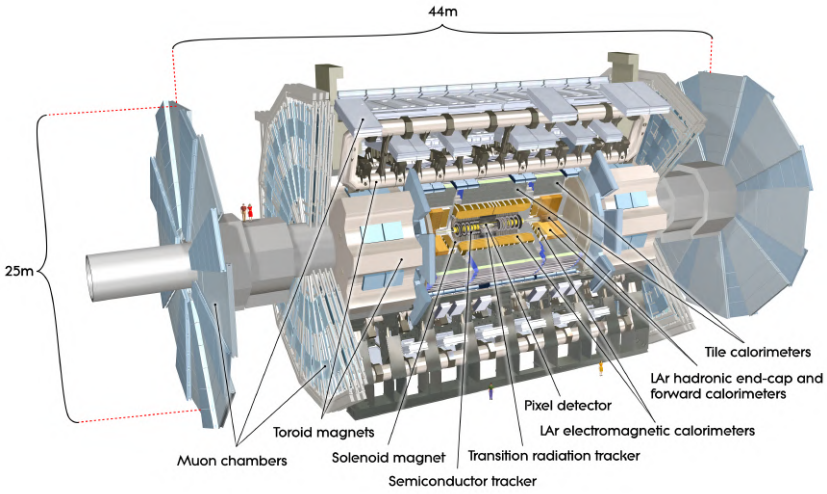

Figure 7.4: Graphic representation of the ATLAS detector. [102]

7.2.1.1 The stand-alone MS DV search scheme and the ATLAS trigger system

The search schemes proposed for ATLAS is *incompatible* with the current trigger system in place for one critical reason: Non-pointing muons in the MS. A non-pointing muon, in the MS of ATLAS, is categorized as having a direction pointing elsewhere than the approximate point in which the initial bunch-crossing occurred. For displaced muons, it is unlikely that they point towards this point, and thus cannot be triggered (at least, as a Level-1 hardware trigger) upon with the current algorithm.

There are some interesting ideas to circumvent the MS algorithm for the high-luminosity phase for e.g. the long-lived dark photon decaying into a di-muon pair [103], where, due to the relatively light mass of the dark photon, the angular separation of the di-muons are approximately *collinear*. Approximate enough that the track reconstruction algorithm in the MS can allow for this type of displaced muon trigger. The mass of the dark photon, γ_d, lies between the range of $0.4\,\text{GeV} \leq m_{\gamma_d} \leq 10\,\text{GeV}$ and

[5] The full detector volume could be expanded to 10m in the transverse, and 21 m in the longitudinal as in [43], however the ability to reconstruct the displaced tracks become much more difficult, and is thus excluded for the sake of this study.

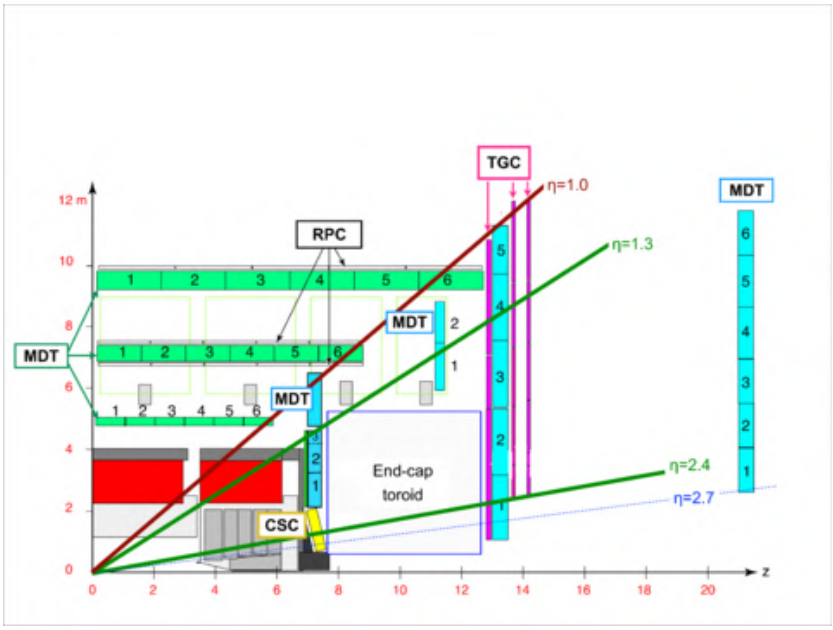

Figure 7.5: Outline of the ATLAS Muon Spectrometer with inlaid η-ranges of the monitored drift tubes (MDT) in the barrel region (green) and end-caps (blue/turquoise), along with the thin gap chambers (TGC, purple) for triggering [**?**].

comparable to the mass range of the HNLs within the proposed charged meson search scheme, thus a similar procedure is not unreasonable.

Therefore, the search scheme proposed assumes the highly optimistic case where *every* displaced muon is *pointing*, but with an opening angle big enough to be identified as *two distinct* muon tracks, and with a *pre-scaling*[6] factor of 1. Under this assumption, the L1 trigger requirement of two μ's with $p_T \geq 6$ GeV will be satisfied. This is mostly optimistic for the charged-meson processes, where, for the W-boson processes, the assumption is that the prompt lepton will have transverse momentum greater than $p_T \geq 27$ GeV, necessarily satisfying a L1 trigger of a single muon, to be saved for later analysis.

As quarks are produced in pairs, one can assume, that for heavy flavoured mesons, each event will contain *two* mesons of opposite charge. Thus for a single HNL mediated decay of a charged meson, one can assume that there will be a corresponding charge-conjugated leptonic meson decay process, not necessarily mediated by an HNL, that occurs simultaneously. Therefore, one can use the previously mentioned two μ trigger of $p_T \geq 6$ (or a generalised two-lepton trigger such as the T_2 trigger) to satisfy the L1 trigger requirements on the prompt leptons, instead of the displaced leptons. As the mesons decay relatively quickly, under a good approximation, each prompt lepton will be *pointing* back to the ID, and will in general have significantly larger transverse momentum than the displaced leptons, thus this trigger is more suited for the prompt leptons, however under the assumption that a secondary meson will be produced, and decay leptonically.

Therefore, although triggering on displaced muons is not currently possible, in the case where the muons are *non-pointing*. However, the increasing interest in long-lived particles are driving the need to develop coherent displaced lepton triggers[58]. The analysis performed in the thesis show the potential of implementing such triggers, and furthermore, the tool developed for this study allow for changes in the cuts (p_T, η, DV) and detector geometry $(rectangular, spherical, cylindrical)$ for both forward/asymmetrical physics, symmetrical physics, heavy-ion collisions, with or without heavy mesons,

[6] The pre-scaling factor is a scale factor that is used to reduce the rate of data storage.

with extensions to all currently available Feynrule models, allowing for any number of BSM models to be probed within innumerable detector and initial state configurations.

Although the results presented here are within or beyond competitive bounds, as described above and displayed in ch. 6, the true power lies in the tools ability to reconfigure quickly to a given detector geometry, DV scheme and triggers.

Another difficulty in searching for long-lived particles experimentally, is in the timings of bunch crossings, and the subsequent ability of the track reconstruction algorithms. For sufficiently slow LLPs, (i.e. the *time of flight* is greater than the time between one bunch crossing ~ 25 ns, called a *bunch spacing*) - the ability to reconstruct a process across multiple bunch-crossing events is improbable, and if no notable event occurred in the subsequent crossing, the probability of the algorithm to reconstruct the track is zero.

However, for sufficiently relativistic HNLs ($v \geq 0.7c$), the decay will occur before the subsequent crossing. In our analysis, we found that the HNLs are sufficiently relativistic in both the charged meson and W-boson processes for this not to be relevant.

Further, background noise in the form of *cavern background*, plays a large role in the muon system. This is a type of background noise produced from a combination of particles from recent proton collisions and long-lived particles accumulated from previous collisions, both before and after the collision of interest. Low energy neutrons scatter multiple times in the detector, effectively forming a long lived neutron gas in the detector cavern, and can excite atoms within the detector and cavern. The excited atoms then emit a photon upon returning to their ground state, which then interact with the detector and give rise to *fake* signals, such as fake muons. The *hit* rate is estimated to be at 5kHz in the barrel region, and 14kHz in the forward region, for 7TeV + 7TeV pp-collision [104].

7.2.2 The Scattering and Neutrino Detector

The Scattering and Neutrino Detector (SND) is a stand-alone fixed-target experiment complimentary to other experiments at the LHC. It feeds of the collisions happening in the ATLAS experiment by virtue of its location in an auxiliary tunnel 480 m downstream of the beam-line with respect to the ATLAS interaction point (IP) as seen in Fig. 7.6.

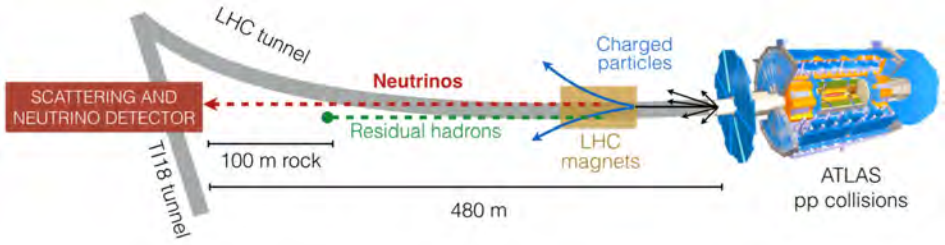

Figure 7.6: Bird's-eye view of the location of the SND detector relative to the ATLAS detector[105]

Since the LHC beam pipe is out of the way, the SND can detect particles with trajectories having very small angels with respect to the beam-axis at the IP. Specifically it is designed to perform measurements with neutrinos produced in the LHC in the previously unexplored η-range of $7.2 < \eta < 8.6$, opening a unique opportunity to study heavy-flavor production [**?**]. In this sense it is part of the forward physics program at the LHC, aiming at detecting low p_T particles which constitute the majority of the particles produced at the LHC [106]. Due to the shielding its long displacement from the IP in ATLAS, the SND experiment is not only capable of probing neutrino physics, but also possible new physics involving feebly interacting particles in general. It is in this context it is a relevant detector candidate for DV searches probing the HNL parameter-space.

The experiment consists from front to back (with front being closes to ATLAS) of the following three main components (see Fig. 7.7 for overview):

- A muon identification system, which also serves as a hadronic calorimeter
- A target region consisting of successive layers of tungsten acting as fixed-target. Between these, emulsion plates for photographic imaging of collisions between incoming particles and the target are placed.
- A veto plate that flags events with charged particles entering from the direction of the ATLAS IP.

As seen in Fig. 7.7 the SND detector is positioned slightly off-center with respect to the beam-axis in the transversal plane, which needs consideration when modelling the detector to accurately represent this asymmetry.

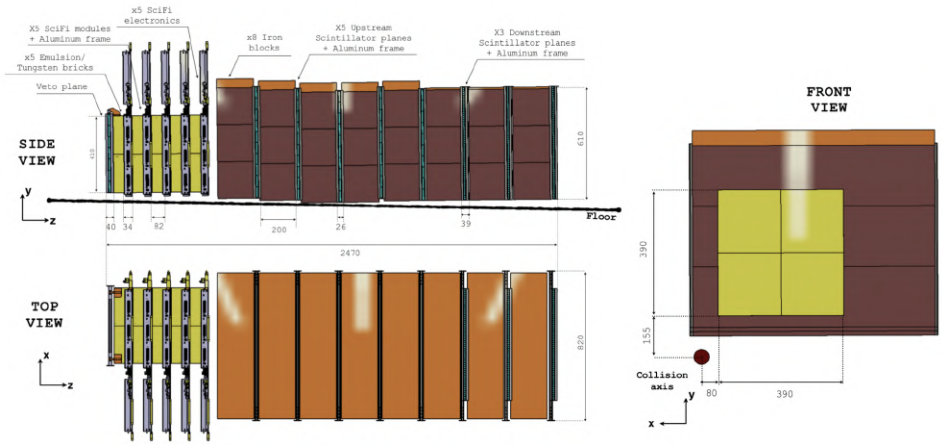

Figure 7.7: Schematic planar overview of the SND detector along its three axes. Particles from the ATLAS interaction point travel from right to left with respect to the side and top view. Beam/collision-axis is depicted in the front view[107].

The work presented in the current thesis *does* take this asymmetry into account. Further, the placement and geometry of SND places very stringent requirements on the DV of the events considered. As done for ATLAS in Section 5.3.1, we can estimate the chance of decaying within the SND decay volume by multiplying equation (4.0.1) by a factor $\frac{1}{2}$ to account for $\pm z$ asymmetry and a factor $\frac{1}{4}$ to account for the fact that SND lies within a single quadrant.

This gives a very crude upper bound, which likely will be quite generous, and is presented in Fig. 7.8. As compared to ATLAS one observes very low probabilities of survival, at best, suppressed by about four orders of magnitudes as compared with ATLAS's almost 100% efficiency in the $l_{\text{min}} < l_{\text{dec}} < l_{\text{max}}$ region. On the other hand the distribution is comparably quite flat i.e. less sensitive to variations in l_{dec}.

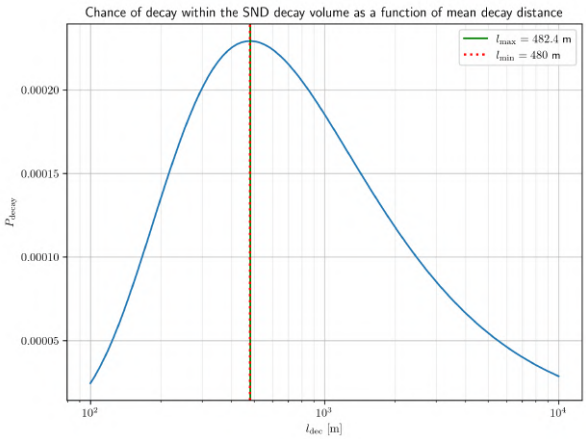

Figure 7.8: Probability of HNL decay within the SND decay volume as a function of $l_{\text{dec}} \equiv v\tau\gamma$, giving a generously estimated upper bound.

Chapter 8

Event generation

This Chapter describes our pipeline of Monte Carlo signal generation.

To estimate a signal corresponding to a detection of an HNL, a simulation of the proton-proton collisions at the the LHC must be performed. To this end one can make use of simulation software, namely, Pythia and MadGraph, designed for general purpose simulations of particle collisions and decays. Such programs are called *event generators* because they generate (simulate) the events (collisions) on which a signal estimation analysis is based, such as the work presented in this thesis. These programs use approximations and the data they produce is but a simulation, and as such it need to be exposed to solid validation in order to be trusted for further analysis. In this chapter the two event generators used for this thesis are introduced, along with the validation of their simulated data.

The two event generators used in this analysis are Monte Carlo[1] (MC) based, and such event generators are a popular a tool used by both experimentalists and theoreticians to make predictions on the results of collider experiments [108]. For experimentalists, the tool provides an easily accessible and scalable platform to generate simulated data on demand. For theorists, it allows for the unification of Beyond the Standard Model (BSM) processes and collider experiments by the simulation of hypothetical processes in a detector environment. Event generators are therefore crucial for predictions of collider results and possible explanations of unexplained SM phenomena.

One of the greatest achievements of 21st century particle physics is the discovery of the Higgs boson to which the importance of MC based event generators cannot be understated. They were relied upon extensively to set limits on the parameter space regions of the Higgses and it's discovery. The same tool can be used to set limits on the parameter space region of the heavy neutral lepton as well for a feat similar in comparison to the discovery of the Higgs [108].

8.1 Pythia

Pythia[2] is used for the generation of *high-energy* collisions within particle physics. The program admits a coherent set of physics models prepared for the generation of even complex multi-particle final states

[1] Meaning that each time the process is simulated, it is done so independently of previous or future simulations...just as the spin of the roulette wheel in a casino, hence the name. This is relevant when generating samples based on multiple successive runs of the same process, which is the standard method of obtaining any predictive accuracy.

[2] The specific version used in this thesis is Pythia8

evolved from few-body hard-scattering process with parts developed partly on theoretical estimates derived from perturbative quantum chromo-dynamics (QCD), and partly on phenomenological models with parameters derived from data [109].

The area of focus is specifically in proton-proton collisions with $\sqrt{s} \geq 50\,\text{GeV}$, below which one enters the hadronic resonance region, where the approximations of PYTHIA break down.

Further, PYTHIA's modus operandi is defined by solving a very specific problem, namely, the fact that high-energy collisions between elementary particles typically give rise to complex final states with large multiplicities of hadrons, leptons, photons and neutrinos. The relation between these final states and the underlying physics description proves quite complex and problematic. The problem at hand is multifold: firstly, there lacks a complete basis of theoretical understanding, and secondly, the presence of large multiplicities makes any analytical approach obsolete due to the complexity inherent in the system. The solution put forward with PYTHIA is to generate complete events using Monte Carlo methods and further enhanced by subdivision of the full process into separate tasks wherein all main phenomena, such as initial/final state radiation, fragmentation, decays, hadronisation and hard-process selection are included in the final computation [109].

8.1.0.1 PYTHIA *settings and operation*

The settings were chosen on the basis of close realistic representation of physical processes. Only generating the above mentioned two-quark processes rather than five-quark processes, such as for $pp \to q\bar{q}$ with $q \in \{u, d, s, b, c\}$ may not seem so, but the meson sample produced in both processes agree in their relative distributions, however in the five-quark process, due to the abundance of light quarks, more light mesons, such as pions and kaons, will be produced which is irrelevant for the current study. The cross-section in the five-quark case is a factor ~ 4 greater than in the two-quark case, however the amount of heavy mesons generated suffers a factor ~ 4 suppression. The heavy meson distribution in both cases are identical, and thus it is under this approximation that the study is restricted to two-quark processes to limit the computational run time.

The sample was generated on the basis of 10 million $pp \to \xi\bar{\xi}$ events, with $\xi \in \{b, c\}$ representing the two heavy quark flavours and under the following HardQCD settings, chosen on the basis of close realistic representation of physical processes. The following figures displayed below are the tree level amplitudes, corresponding to the LO contributions that Pythia uses, and the respective setting that allows for the process to occur:

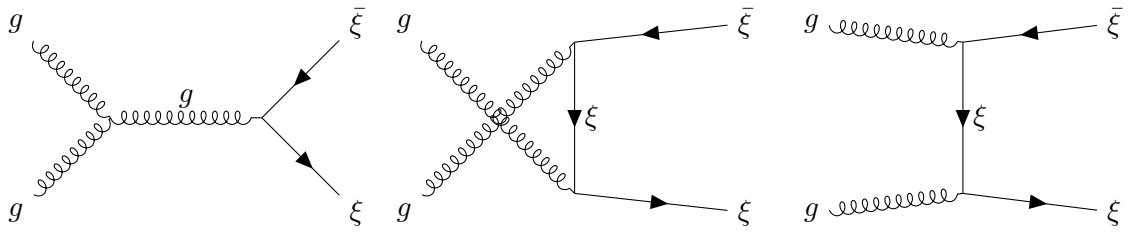

Figure 8.1: Some leading order QCD processes $gg \to \xi\bar{\xi}$ for $\xi \in \{b, c\}$ as used by PYTHIA8.

The full list of settings used with PYTHIA is enumerated and described below.

- `HardQCD:hardccbar=on` and `HardQCD:hardbbbar=on` switches on only the hard QCD processes $pp \to \xi\bar{\xi}$, with $\xi \in \{b, c\}$. The tree level amplitudes, corresponding to the LO contributions that Pythia uses can be seen in figure Fig. 8.1.
- `PartonLevel:ISR=on` and `PartonLevel:FSR=on` switches on initial and final state radiation respectively, shown in Fig. 8.2.

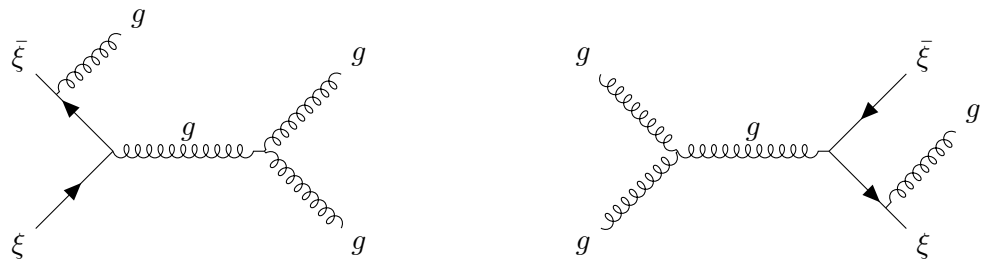

Figure 8.2: Feynman diagrams showing initial state radiation (left) and final state radiation (right) corresponding respectively to the ISR and FSR settings in PYTHIA.

- `PartonLevel:MPI=on` switch for multiparton interactions, allowed in our case
- `Beams_idA` and `Beams_idB` controls which particles each of the colliding beams will consist of. In this case protons with PDG code 2212 (see table 8.3)
- `Beams:eCM=14000` sets the center of mass energy, in this case 14 TeV.
- `PhaseSpace:pTHatMin=0` and `PhaseSpace:pTHatMax=-1` sets the minimum and maximum invariant p_T, `-1` is interpreted as infinite.
- `PhaseSpace:mHatMin=0` and `PhaseSpace:mHatMax=0` sets the minimum and maximum invariant masses.
- `PDF:pSet=9` sets the parton density function[3] (PDF). The PDF used was CTEQ66 [110], which was chosen over the Pythia default NNPDF3.1 [111] due to CTEQ66's reliability with heavy quark physics.
- X`:mayDecay=no` forces pythia to not decay particle X, where for the current study, the heavy mesons are the particles in question with their PDG ID listen in 8.3. Their subsequent decay was handled outside of PYTHIA and thus the decays were disabled within it.
- `Main:numberOfEvents=10000000` sets the desired number of simulated collisions, in the case of the meson sample elaborated below in section 8.1.1 this number was 10 million.

The main script to generate this sample in PYTHIA is written in C++ which provides great flexibility with respect to speed, operating directly above the assembly language. This is an important fact to avoid reaching a computationally prohibitive limit. The C++ script merges C++'s in-built functionalities and PYTHIA's vast catalogue of functions that are used to extract information from the generated data. Most importantly we tailored our script to harvest the four-momentum and production vertices of the generated mesons and save them in convenient data structures[4], with checks also made on the decay chains using statues codes.

8.1.1 Meson sample

The meson sample generated from the settings mention above in section 8.1.0.1 is presented in Fig. 8.3 and Fig. 8.4 below, showing the relative abundance and transverse momentum spectra of the different mesons, respectively.

[3]The PDF has set $\alpha_s = 0.1180$ and is predictive up to NLO.
[4]With double-level precision up to 10 significant figures.

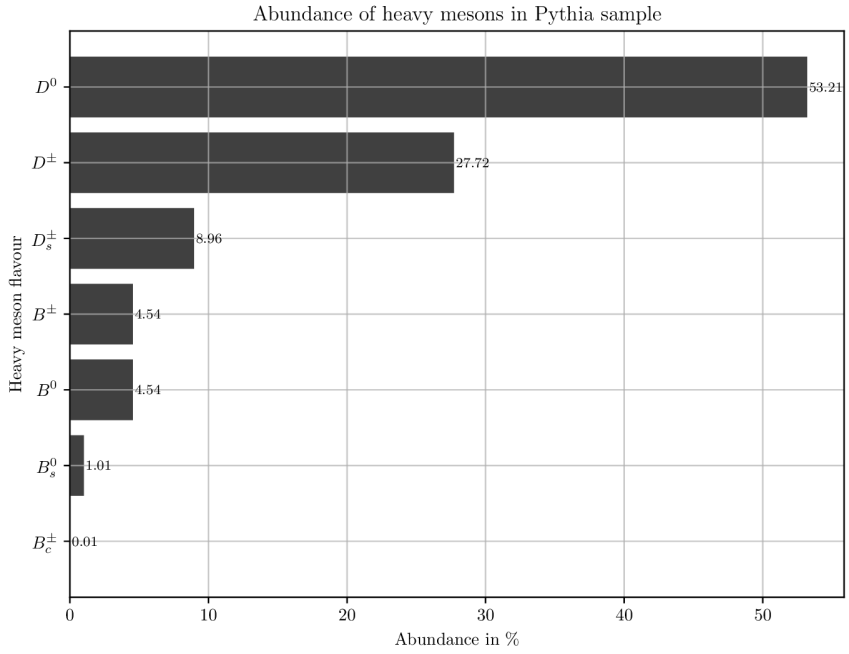

Figure 8.3: Relative abundance of light heavy flavour mesons generated in PYTHIA

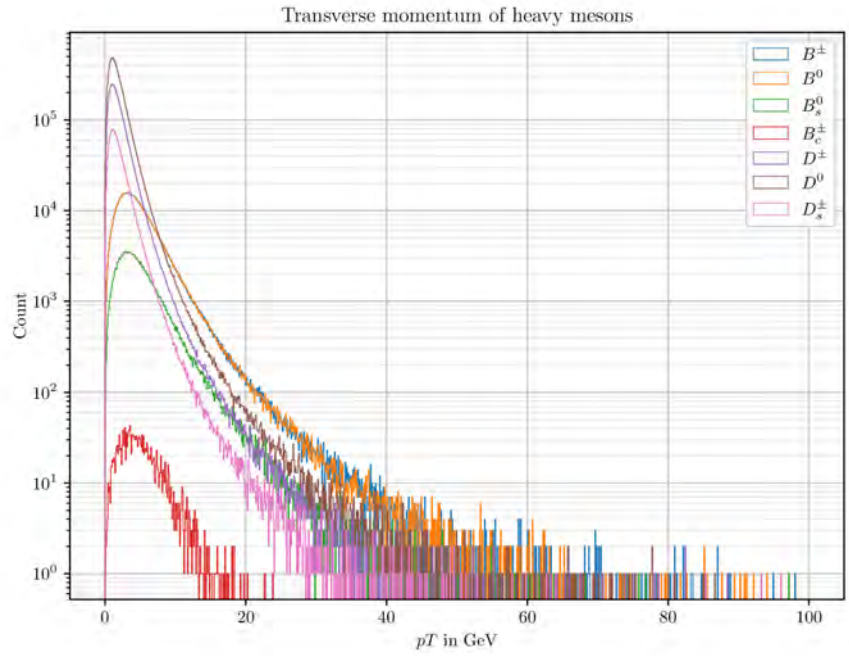

Figure 8.4: Transverse momentum of the heavy mesons generated in PYTHIA with the settings as described in section 8.1.0.1.

8.1.1.1 Validation of Meson sample

To verify that the chosen settings in PYTHIA, used to generate the meson samples, correspond to physically reasonable results, one can compare the sample to data and theoretical analysis. The comparison with data is straight forward, as the ATLAS collaboration has published data [112] on

the differential cross-section with respect to transverse momentum, $\frac{d\sigma}{dp_T}$, for $B^{\pm}$-mesons produced at a center-of-mass energy of $\sqrt{s} \sim 7$ TeV.

The theoretical side of things is slightly more complex, we have chosen to compare the sample with a model taking a Fixed Order in the perturbative expansion of the Next-To-Leading Logarithm (FONLL) [113]. The model provides good agreement with ATLAS data[112] and allows for flexibility with respect to energy scale, a feature that is incredibly important in the validation of physics beyond the current technological bounds.

8.1.1.2 $B^{\pm}$-meson sample

A three-point comparison is thus made between the differential cross-section of a $B^{\pm}$-meson sample generated in PYTHIA under the aforementioned settings, in FONLL and from data collected from the ATLAS collaboration shown in Fig. 8.5.

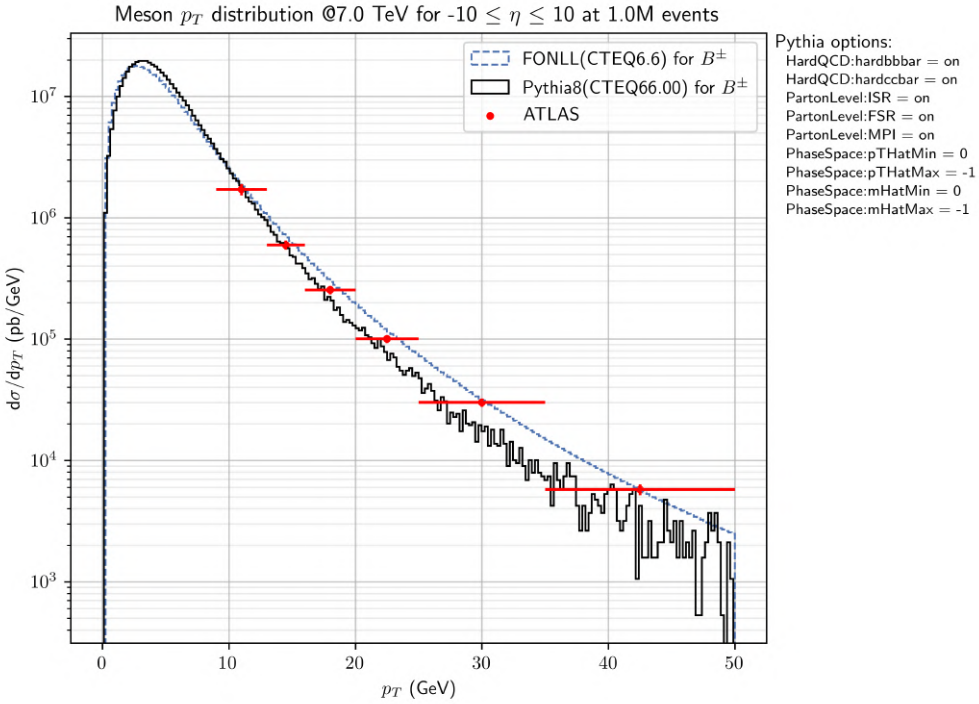

Figure 8.5: A comparison between ATLAS data, FONLL and the simulated data from PYTHIA for $B^{\pm}$-mesons. The figure includes statistical and systematic errors in ATLAS data [112], the same uncertainties for Pythia are negligible in comparison and have thus been suppressed. The uncertainties of FONLL is also neglected.

The (pseudo) rapidity distributions can also be compared with FONLL for the same center-of-mass as before in Fig. 8.5.

The meson sample generated from PYTHIA has good agreement with both FONLL and ATLAS data, and thus the choice of settings correspond to physically reasonable results, at least, for $\sqrt{s} \sim 7$ TeV. FONLL allows for comparisons up to 14 TeV and with up to *five* different PDF's, thus it is a useful step in validation to see the relationship scale to this regime, and under different choices of PDF's. In the following plots, this exact relationship is probed for the $B^{\pm}$-meson, the result of which further strengthens the idea that the meson sample is in good agreement at higher energy regimes as well. The simulated data for both the $B^{\pm}$-mesons agree best with FONLL in the transverse momentum range

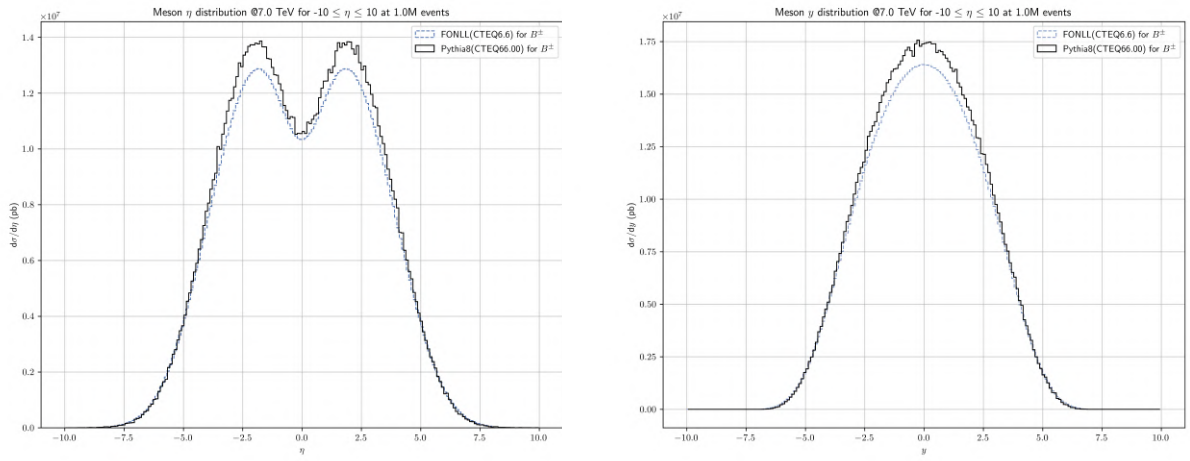

Figure 8.6: A comparison between FONLL and PYTHIA under the aforementioned choice of settings

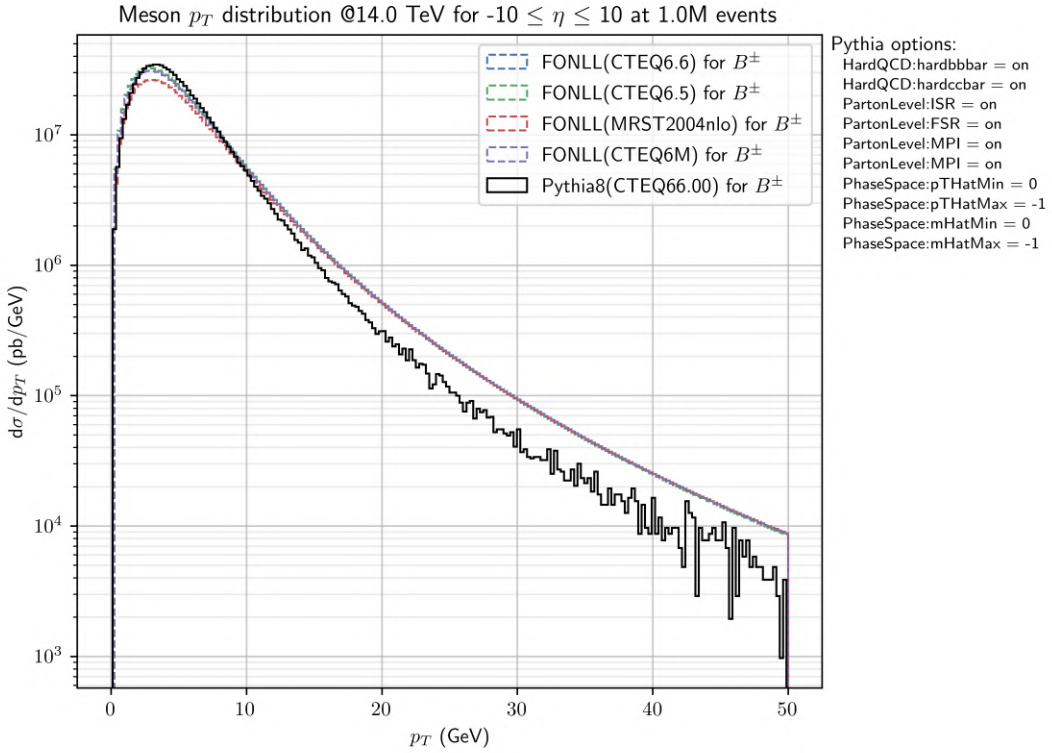

Figure 8.7: A comparison between FONLL and the simulated data from PYTHIA for $B^{\pm}$-mesons at $\sqrt{s} \sim 7$TeV. The figure includes statistical and systematic errors in ATLAS data [114]. The same uncertainties for Pythia are negligible in comparison and have thus been suppressed. The uncertainties of FONLL is also neglected.

of $0 \leq pT \leq 15$ GeV, after which one can argue that perturbative effects, which are *not* accounted for in PYTHIA's hadronisation engine, take effect, leading to the divergence at higher energies. These next-to-leading (NLO) corrections prove important, as they bridge the gap to aligning with ATLAS data as seen in Fig. 8.5, however one can thus claim that up to leading order in the perturbative expansion, the meson samples hold reasonable agreement with FONLL.

8.1.1.3 $D^{\pm}$-meson sample

The three-point comparison between FONLL, ATLAS data [114] and the simulated data from PYTHIA can also be done for the $D^{\pm}$ meson in exactly the same treatment as before. The (pseudo) rapidity

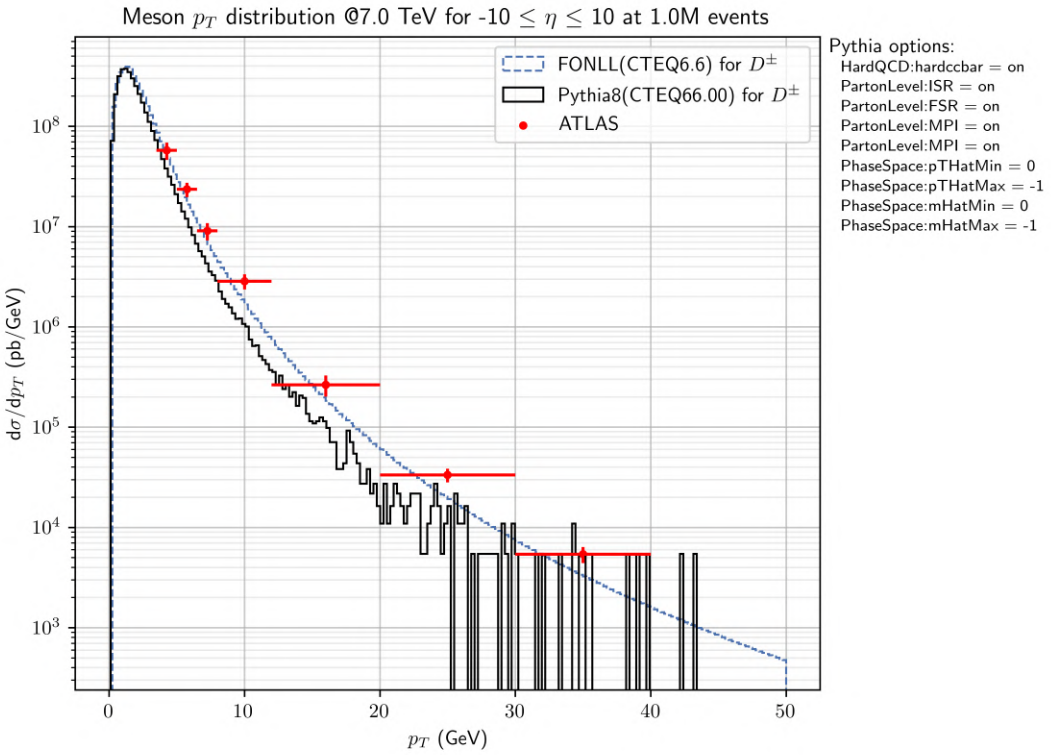

Figure 8.8: A comparison between ATLAS data, FONLL and the simulated data from PYTHIA for $D^{\pm}$-mesons at $\sqrt{s} \sim 7$ TeV. The figure includes statistical and systematic errors in ATLAS data [114], the same uncertainties for PYTHIA are negligible in comparison and have thus been surpressed and are otherwise not reported by FONLL.

distributions can also be compared with FONLL for the same center-of-mass as before in Fig. 8.8. The

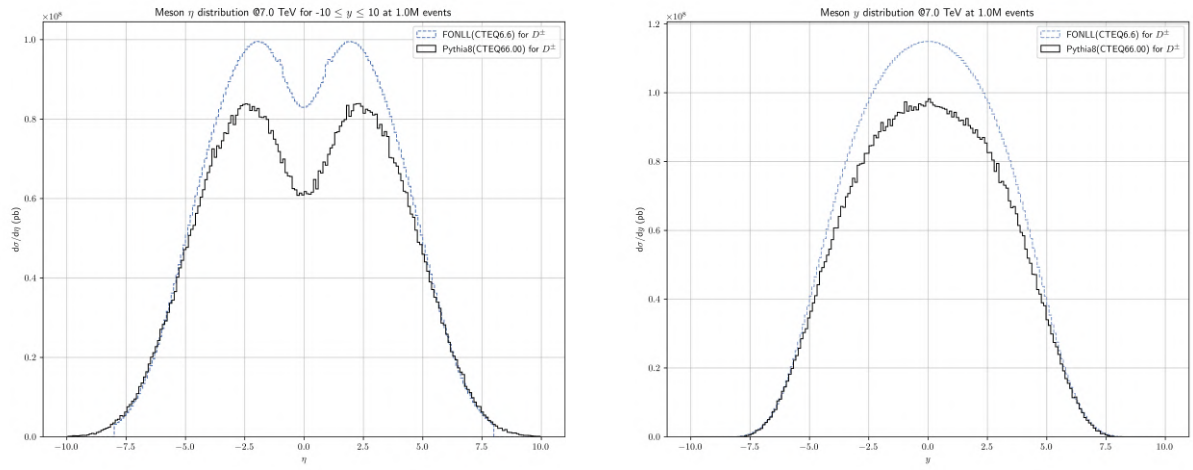

Figure 8.9: A comparison between FONLL and PYTHIA under the aforementioned choice of settings

comparison between FONLL at $\sqrt{s} \sim 14$ TeV is also done for the $D^{\pm}$-meson, the results of which are given in Fig. 8.10

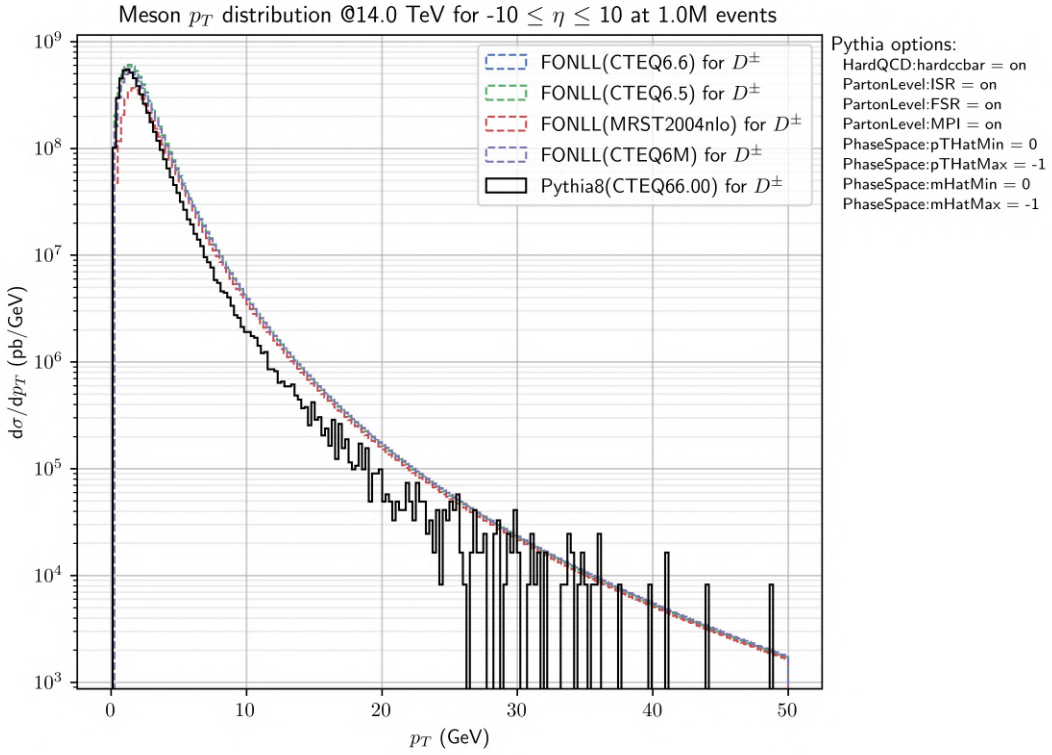

Figure 8.10: A comparison between ATLAS data, FONLL and the $D^{\pm}$-meson sample generated in PYTHIA

The simulated data for the $D^{\pm}$-mesons agree with both FONLL and ATLAS data in Fig. 8.8, even in the higher pT regions where the $B^{\pm}$ mesons previously had weaker correlation. The rapidities are less in agreement however, as evident in Fig. 8.9, however it must be noted here that the y-axis is *not* logarithmic, in contrast to the transverse momentum plot. In totality however, it can be argued that the $D^{\pm}$ meson sample shows good agreement with both FONLL and ATLAS data.

8.1.1.4 PYTHIA *cross-section estimates of* $\sigma(pp \to q\bar{q})$

PYTHIA estimates of the $q\bar{q}$ cross-section $\sigma_{pp\to q\bar{q}}$ for $q \in \{b, c\}$ based on the simulation of one million pp-collisions can be seen in table 8.1, and were used when calculating event rates.

Multiplying $\sigma_{pp\to q\bar{q}}$ with two times the meson fragmentation fraction, $f(q/\bar{q} \to M^{+})$, gives the $M^{\pm}$ cross-section $\sigma_{pp\to M^{\pm}}$[5], where M is B and D mesons in our case. This procedure applied to obtain the PYTHIA estimate of $\sigma_{pp\to M^{\pm}}$, using the fragmentation fractions found in Table 8.2.

[5]We multiply by two to account for M^{-}

Cross-section	pT-cut	Pythia estimate
$\sigma_{pp\to b\bar{b}}$	none	$(2.481 \pm 0.001) \times 10^{-1}$ mb
	$b, \bar{b}$ $p_T > 10$ GeV	$(2.095 \pm 0.001) \times 10^{-2}$ mb
	$b, \bar{b}$ $p_T > 25$ GeV	$(1.208 \pm 0.006) \times 10^{-3}$ mb
$\sigma_{pp\to c\bar{c}}$	none	2.048 ± 0.001 mb
	$c, \bar{c}$ $p_T > 10$ GeV	$(2.561 \pm 0.001) \times 10^{-2}$ mb
$\sigma_{pp\to b\bar{b},c\bar{c}}$	none	2.254 ± 0.001 mb
	$c, \bar{c}$ $p_T > 10$ GeV	$(\pm 0.001) \times 10^{-2}$ mb

Table 8.1: Cross-sections for proton-proton to $b\bar{b}$ and $c\bar{c}$ quarks respectively. Pythia estimates are based on 1 million pp-collisions

meson	$f(q \to M)$	meson	$f(q \to M)$
D^+	0.207	B^+	0.417
D^0	0.632	B^0	0.418
D_s	0.088	B_c^+	2.6 $\times 10^{-3}$

Table 8.2: Fragmentation fractions for a selection of heavy mesons [42] [115]

8.2 MadGraph

MadGraph5_aMC@NLO [116] (henceforth MG) is a general purpose Monte Carlo-based open source[6] simulation tool used for the generation of collisions and decays of particle physics within and beyond the Standard Model. It offers NLO precision across the board in standard model calculations as well as in some beyond standard model packages. Furthermore, various analytical tools to study the output are also available within the MG framework in its MadAnalysis package. As input MG takes *a)* a model (defined by a Lagrangian) , *b)* a *parameter card* setting the parameters of the model and *c)* a *run card* giving MG general setting such as e.g. the centre-of-mass energy and which type of particles to collide. The parameter and run cards are just simple `.dat` files, and easily be modified to tailor the parameter and run settings to the users needs once the user is familiar with usage of MG.

MG is compatible with the Mathematica based program FeynRules [117], which can compute the Feynman rules of any quantum field theory directly from the Lagrangian of the model (provided it is expressed in four-dimensional space-time). In the case of heavy neutral leptons, one can therefore supply MG with a FeynRules package of the Type-I seesaw Lagrangian of (3.2.11) for $\mathcal{N}$ Majorana neutrinos to thereafter simulate it's phenomenology within the framework. This is indeed the case for the SM_HeavyN_NLO model, which extends the SM Lagrangian with *three* HNLs.

MG outputs its simulated data in the Les Houches Event [118] file format (LHE), of which an example can be seen in Fig. 8.11. This common format allows seamless integration with other event generator such that e.g. MG can be set to automatically call Pythia for parton showering; a commonly used procedure. To label particles numerical in the output file, the Particle Data Group (PDG) numbering scheme has been adopted, which uniquely identifies each particle with a number (a few honorable mentions are given in table 8.3).

[6] Source code and download available at: https://launchpad.net/mg5amcnlo

Quarks		Leptons		misc.	
particle	PDG ID	particle	PDG ID	particle	PDG ID
d	1	e^-	11	Z^0	23
u	2	ν_e	12	W^+	24
s	3	μ	13	D^+	411
c	4	ν_μ	14	B^0	511
b	5	τ	15	B^+	521
t	6	ν_τ	16	p	2212

Table 8.3: A selection of particles and their associated Particle Data Group numbering scheme IDs. The ID of an anti-particle is the negative of the associated particle's ID e.g. e^+ has ID -11.

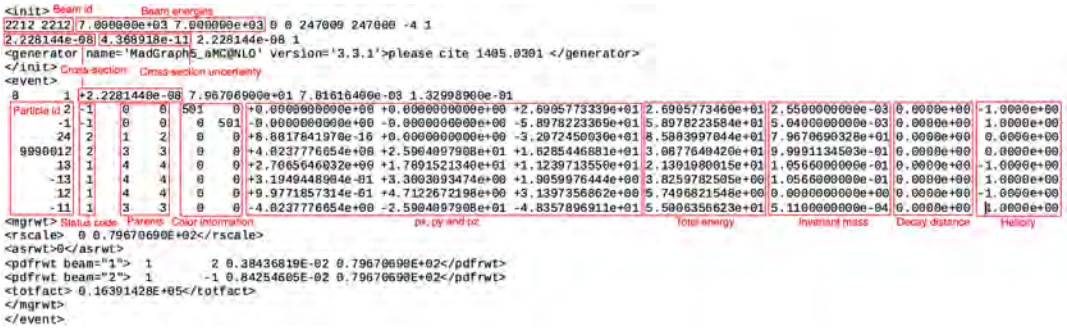

Figure 8.11: Example of the first event in an LHE file belonging to the W-process described in section 4, with a prompt electron and di-muons [119].

An example of an event recorded in the LHE file format is presented in Fig. 8.11. Each row pertains to an individual particle and contains all data about that particle stored in the file. From left to right the columns contain:

- PDG IDs of the various particles involved in the process
- The so called *status code* indicating whether the particle is an incoming initial state particle, or if they are outgoing final state particles, labeled by -1 and +1 respectively. In Fig. 8.11 the incoming particles can be seen to be an up quark (2) and an anti-down quark (-1), in accordance with a proton-protons collision. Status codes +2 and -2 indicates intermediate resonances with preserved masses, and space-like resonances, respectively.
- Information about the ancestry of the particle in terms of its first and last mother, respectively. The values indicate the row index of the parent particles, such that e.g. the W^+particle (24) in Fig. 8.11, can be seen to have been created directly from the two colliding quarks in row 1 and 2. In the case of a decay with only one mother, the second mother column may either be 0 or equal to the first mother column. More than two mothers are also possible, but rarely happens in practice.
- Information on the color flow of the process. Then comes columns containing four-vector elements p_x, p_y, p_z and E respectively, all measured in units of GeV and with respect to lab-frame.
- Invariant mass, i.e. $\sqrt{p^2}$ which may be different from the nominal mass.
- $v\tau$ in mm, the distance (as experienced by the particle) traveled from the production vertex to the possible decay vertex of the particle. This functionality seems to be disabled in the example given in Fig. 8.11 and was calculated externally by ourselves for the analysis.
- Helicity information in the form of cosine of the angle between the spin-vector of the particle and its three-momentum, calculated in the lab frame[119]

Every column, except the one containing colour data, was used to validate the coherence of the event generation, e.g. that final state particles had the correct status codes, and that decay chains were correct. The ancestry information was also used to separate prompt muons from displaced ones when loading in the data from the LHE files, which was important for the data-analysis.

8.3 MadGraph models

To study the processes described in Section 4, the following two MG models were used: SM_HeavyN_NLO and Effective_HeavyN. In accordance with simulating processes with "only one non-zero mixing" scheme, two of the three mixing angles were set to zero.

8.3.1 The SM_HeavyN_NLO model

This model allows for three HNLs, with the following mixing matrices

$$\Theta_{eN} = \begin{pmatrix} \text{VeN1} \\ \text{VeN2} \\ \text{VeN3} \end{pmatrix}, \qquad \Theta_{\mu N} = \begin{pmatrix} \text{VmuN1} \\ \text{VmuN2} \\ \text{VmuN3} \end{pmatrix}, \qquad \Theta_{\tau N} = \begin{pmatrix} \text{VtauN1} \\ \text{VtauN2} \\ \text{VtauN3} \end{pmatrix}.$$

Finally, the model defines the three HNL masses as mn1,mn2 and mn3, with the decay widths as being, respectively: wn1, wn2 and wn3.

8.3.2 The Effective_HeavyN model

The SM_HeavyN_NLO model describes QCD sector of the Standard Model at quark/gluon level. Therefore, it does not allow, for example, to describe production of HNLs from B or D mesons. In order to achieve this, the Effective_HeavyN model was constructed in [120]. The model introduces new low energy degrees of freedom (mesons) and describes HNL interaction with them.

This model allows a single HNL, $N4$, whose mass parameter is named MN4. The effective model accommodates the possibility of imaginary mixing angles, such that

$$\Theta_N = \begin{pmatrix} \text{modthetae} \cdot e^{i\text{argthetae}} \\ \text{modthetamu} \cdot e^{i\text{argthetamu}} \\ \text{modthetatau} \cdot e^{i\text{argthetatau}} \end{pmatrix}.$$

Imposing the condition of purely real mixing angles, the above arguments of the mixing angles should be to zero, in which case

$$\Theta_N = \begin{pmatrix} \text{modthetae} \\ \text{modthetamu} \\ \text{modthetatau} \end{pmatrix}.$$

8.3.3 Model parameters for the charged meson process

The two sub-processes S_1 and S_2 of the charged meson processes can be generated in MadGraph with the following commands, in their respective models:

Physical process	Effective_HeavyN (S_1)	SM_HeavyN_NLO (S_2)	α
$B^\pm \to e^\pm(N \to \mu^\pm\mu^\mp\nu_e)$	`B > e n4`	`n1 > mu mu ve`	e
$B^\pm \to \mu^\pm(N \to \mu^\pm\mu^\mp\nu_\mu)$	`B > mu n4`	`n2 > mu mu vmu`	μ
$B^\pm \to \tau^\pm(N \to \mu^\pm\mu^\mp\nu_\tau)$	`B > tau n4`	`n3 > mu mu vt`	τ
$D^\pm \to e^\pm(N \to \mu^\pm\mu^\mp\nu_e)$	`D > e n4`	`n1 > mu mu ve`	e
$D^\pm \to \mu^\pm(N \to \mu^\pm\mu^\mp\nu_\mu)$	`D > mu n4`	`n2 > mu mu vmu`	μ
$D^\pm \to \tau^\pm(N \to \mu^\pm\mu^\mp\nu_\tau)$	`D > tau n4`	`n3 > mu mu vt`	τ

Table 8.4: Commands for the generation of the charged meson processes in MadGraph related to the sub-processes S_1 and S_2 for di-muon events, where $\beta = \mu$ is kept fixed.

In the purely muonic channel of table 8.4 the final neutrino, $\nu = \nu_e + \nu_\mu + \nu_\tau$, is defined as a *multi-particle* so that MadGraph takes the sum of all contributing processes: this effectively means that one takes into account the charged-current and two contributing neutral-current mediated processes. The leptons are also defined as multi-particles, so that $\ell = \ell^+ + \ell^-$, allowing for charge-conjugated processes to be summed over as well.

8.3.4 Model parameters for the $W^\pm$-boson process

The $W^\pm$-processes can be generated in MadGraph with the commands found in table 8.5, however, as no mesons are present in these processes, they can be simulated in entirety within SM_HeavyN_NLO:

Physical process	SM_HeavyN_NLO (S_2)	α
$pp \to W^\pm \to e^\pm(N \to \mu^\pm\mu^\mp\nu_e)$	`p p > W, W > e n4, n4 > mu mu ve`	e
$pp \to W^\pm \to \mu^\pm(N \to \mu^\pm\mu^\mp\nu_\mu)$	`p p > W, W > mu n4, n4 > mu mu vm`	μ
$pp \to W^\pm \to \tau^\pm(N \to \mu^\pm\mu^\mp\nu_\tau)$	`p p > W, W > tau n4, n4 > mu mu vt`	τ

Table 8.5: Commands for the generation of the $W^\pm$-processes in MadGraph for di-muon events, where $\beta = \mu$ is kept fixed.

In table 8.5, W, e, μ, τ are defined as *multi-particles* so that MadGraph understands these as variables as containing both charge conjugated forms, such that $W, e, \mu, \tau = W^\pm, e^\pm, \mu^\pm, \tau^\pm$.

To determine the physical cross-section for our model, the same model parameters must be set: the HNL mass, M_N, it's decay width, Γ_N, and it's mixing angles, Θ_e, Θ_μ, Θ_τ. One can utilize the scaling properties of the cross-section of the previously elaborated processes to compute many-fold the cross-sections required by only generating very few processes in MadGraph, allowing for otherwise computationally prohibitive event generation to be replaced by pseudo-analytic solutions.

8.3.5 Narrow-Width approximation

Returning to the case at hand, one must first supply MadGraph with the desired model parameters, so that the generated cross-section remains consistent with our theory. However, one can use the *narrow width approximation*[7], and thus choose reference parameters as follows, where the decay width is set to $\Gamma_N^{\text{ref}} = 10^{-5}$ and the relevant mixing angles set to $\Theta_\chi^{\text{ref}} = 1$, for $\chi \in \{e, \mu, \tau\}$.

[7] Elaborated upon in Appendix A.

As the Feynman diagram of the process contains two mixing angles, we use the indices α and β to distinguish between them. Further, it is worth noting that the cross-section for the processes are proportional to

$$\frac{|\Theta_\alpha|^2|\Theta_\beta|^2}{\Gamma_N}$$

one can re-scale the reference cross-section, σ^{ref}, determined from the reference parameters, to the physical cross-section, σ, as follows

$$\sigma(M_N, \Theta_e, \Theta_\mu, \Theta_\tau) = \sigma^{\text{ref}} \times \frac{|\Theta_\alpha|^2|\Theta_\beta|^2}{|\Theta_\alpha^{\text{ref}}|^2|\Theta_\beta^{\text{ref}}|^2} \times \frac{\Gamma_N^{\text{ref}}}{\Gamma_N(M_N, \Theta_e, \Theta_\mu, \Theta_\tau)} \tag{8.3.1}$$

setting $\Theta_\chi^{\text{ref}} = 1$, the above can be reduced to the following expression,

$$\sigma(M_N, \Theta_e, \Theta_\mu, \Theta_\tau) = \frac{|\Theta_\alpha|^2|\Theta_\beta|^2\Gamma_N^{\text{ref}}\sigma^{\text{ref}}}{\Gamma_N(M_N, \Theta_e, \Theta_\mu, \Theta_\tau)}. \tag{8.3.2}$$

The above expression, (8.3.2) requires the total decay width to be determined analytically, which was done in the same way as in [1], namely in noting that the total decay width is equal to the sum of partial widths into a given decay channel, ξ and the corresponding mixing angle, $\Theta_{\xi(\alpha)}$:

$$\tau_N^{-1} = \Gamma_N(M_N, \Theta_e, \Theta_\mu, \Theta_\tau) = \sum_{\alpha=e,\mu,\tau} |\Theta_\alpha|^2 \times \hat{\Gamma}_\alpha(M_N) \tag{8.3.3}$$

where $\hat{\Gamma}_\alpha(M_N) = \hat{\Gamma}_\alpha(M_N, \delta_{\alpha e}, \delta_{\alpha\mu}, \delta_{\alpha\tau})$ is the total decay width obtained by setting the relevant mixing angle, $\Theta_\alpha = 1$, and the other two to zero. This value can be computed in MadGraph by generating the $n1 >$ all all all process.

8.3.6 Unified model parameters

From the considerations of the section above, as well as appendix B[8], it proves effective to set $\Theta_{\text{ref}} = 1$ and $\Gamma_N^{\text{ref}} = 1 \times 10^{-5}$, which for the two relevant models, translates to the following model parameters, where the decay width, Γ_N^{ref}, must be set *only* in the SM_HeavyN_NLO model, as the HNL decay

Physical process	Effective_HeavyN (S_1)	SM_HeavyN_NLO (S_2)
$\Theta_e^{\text{ref}} = 1$	`modthetae=1`	`VeN2=1`
$\Theta_\mu^{\text{ref}} = 1$	`modthetamu=1`	`VmuN2=1`
$\Theta_\tau^{\text{ref}} = 1$	`modthetatau=1`	`VtauN2=1`

Table 8.6: MadGraph model parameters

occurs only in the S_2 sub-process, handled by the aforementioned MadGraph model, thus translating to setting WN2=1e-5. The importance of unifying these parameters across models and processes is to maintain a coherent picture of the physical situations they represent and to be able to compare final results without implementing different scaling parameters for each process.

8.3.6.1 Validation of Effective_HeavyN

The model was validated by comparing simulated results of SM processes with literature results from [9], shown below in Table 8.7 and 8.8 respectively

[8] The narrow-width approximation can be used in this case as $\Gamma_N^{\text{ref}} \ll M_N$

Channel	Literature	Madgraph
$\mathrm{Br}(D^+ \to e^+\nu_e)$	$< 8.8 \times 10^{-6}$	9.549751×10^{-9}
$\mathrm{Br}(D^+ \to \mu^+\nu_\mu)$	$(3.74 \pm 0.17) \times 10^{-4}$	4.057538×10^{-4}
$\mathrm{Br}(D^+ \to \tau^+\nu_\tau)$	$(1.20 \pm 0.27) \times 10^{-3}$	1.064946×10^{-3}
$\mathrm{Br}(D^+ \to \pi^0 e^+\nu_e)$	$(3.72 \pm 0.17) \times 10^{-3}$	5.173045×10^{-20}
$\mathrm{Br}(D^+ \to \pi^0 \mu^+\nu_\mu)$	$(3.50 \pm 0.15) \times 10^{-3}$	9.739355×10^{-21}
$\mathrm{Br}(D^+ \to \eta e^+\nu_e)$	$(1.11 \pm 0.07) \times 10^{-3}$	4.476248×10^{-21}
$\mathrm{Br}(D^+ \to \rho^0 e^+\nu_e)$	$(2.18 \pm 0.25) \times 10^{-3}$	1.720662×10^{-23}
$\mathrm{Br}(D+ \to \omega \ell^+\nu_\ell)$	$(1.19 \pm 0.09) \times 10^{-4}$	$7.0133032 \times 10^{-20}$
$\mathrm{Br}(D_s^+ \to \mu^+\nu_\mu)$	$(5.49 \pm 0.16) \times 10^{-3}$	5.329×10^{-3}
$\mathrm{Br}(D_s^+ \to \tau^+\nu_\tau)$	$(5.48 \pm 0.23)\%$	5.185%
$\mathrm{Br}(D^+ \to \overline{K}^0 e^+\nu_e)$	0.089	0.1599
$\mathrm{Br}(D^+ \to \overline{K}^0 \mu^+\nu_\mu)$	0.093	0.1537

Table 8.7: Branching ratios for various decay channels (left column) of B mesons. Literature values in middle column, simulated values in right column. Green indicates the simulated value lays within the uncertainty, i.e. within 1σ , yellow is within 2σ and red is otherwise.

Channel	Literature	Madgraph
$\mathrm{Br}(B^+ \to e^+\nu_e)$	$< 9.8 \times 10^{-7}$	8.249577×10^{-12}
$\mathrm{Br}(B^+ \to \mu^+\nu_\mu)$	$< 1.0 \times 10^{-6}$	3.5238011×10^{-7}
$\mathrm{Br}(B^+ \to \tau^+\nu_\tau)$	$(1.09 \pm 0.24) \times 10^{-4}$	7.843941×10^{-5}
$\mathrm{Br}(B^+ \to \overline{D}^0 \tau^+\nu_\tau)$	$(7.7 \pm 2.5) \times 10^{-3}$	1.0295173×10^{-2}
$\mathrm{Br}(B^+ \to \pi^0 \ell^+\nu_\ell)$	$(7.80 \pm 0.27) \times 10^{-5}$	8.463592×10^{-5}
$\mathrm{Br}(B^+ \to \overline{D}^0 \ell^+\nu_\ell)$	$(2.35 \pm 0.09) \times 10^{-12}$	8.485990×10^{-12}
$\mathrm{Br}(B^+ \to \rho^0 e^+\nu_e)$	$(1.58 \pm 0.11) \times 10^{-14}$	$3.7602143 \times 10^{-25}$
$\mathrm{Br}(B^+ \to D^-\pi^+\ell^+\nu_\ell)$	$(4.4 \pm 0.4) \times 10^{-3}$	$1.4388855 \times 10^{-33}$
$\mathrm{Br}(B^+ \to \omega \ell^+\nu_\ell)$	$(3.90 \pm 0.5) \times 10^{-5}$	7.013303×10^{-20}

Table 8.8: Branching ratios for various decay channels (left column) of D mesons. Literature values in middle column, simulated values in right column. Green indicates the simulated value lays within the uncertainty, yellow is within 1σ and red is otherwise.

It is clear, that for purely leptonic processes of both charged meson decays, the model performs within an uncertainty of 1σ *from literature. Semi-leptonic decays are apparently not implemented correctly.* One can therefore rely on the model for purely leptonic decay modes of particles within the SM. The results of [42] show that these processes dominate production of HNLs from heavy flavour and therefore are sufficient for our purposes.

However the current study is interested in the decay to the BSM particle, the heavy neutral lepton, N, and thus a proper validation of the behaviour of MadGraph with respect to this particle is still needed. On this front, one can approximate the BSM decay width of

$$\Gamma(M^\pm \to \ell^\pm_\alpha N) \propto \Gamma(M^\pm \to \ell^\pm_\alpha \nu_\alpha)|\Theta_\alpha|^2. \tag{8.3.4}$$

however, this approximation does not take into account important details such as phase-space suppression due to HNL mass. A closer treatment can therefore be conducted analytically following the procedure of [42] where the decay widths can be computed using (4.1.1). The decay widths perform as expected, and in good agreement with [42, 121]

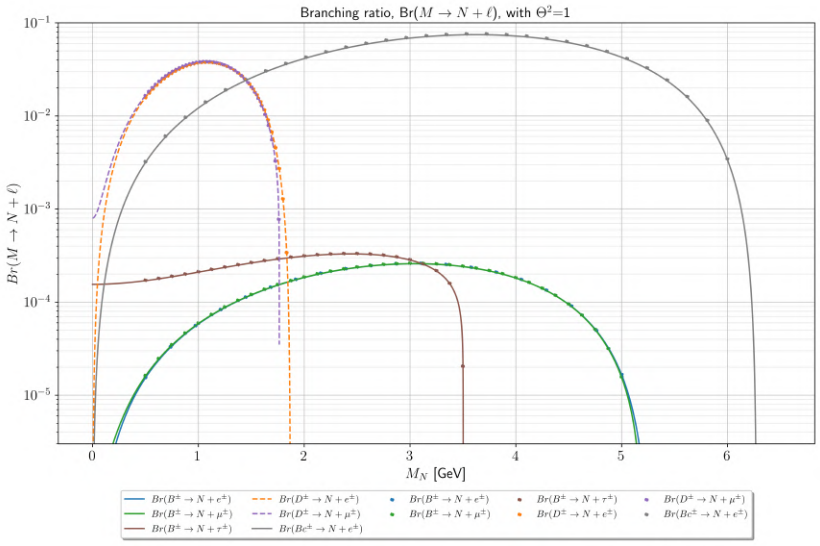

Figure 8.12: The analytic behaviour of the branching fractions of charged mesons with respect to HNL mass, M_N, with $|\Theta|^2 = 1$. Simulated data from MadGraph is represented as dotted points, and the analytic functions are represented as continuous lines. The analytic results were normalized to match the values from MG, there is a slight discrepancy due to differences in HNL lifetime between MG and analysis, which is neglected for the purpose of the current comparison. The shape of the analytic decay functions from [42] are thus in very good agreement with data supplied by MG.

To validate that Effective_HeavyN handled leptonic decays channels involving HNLs correctly, a kinematic check was also done by plotting the distribution of the spherical coordinates of the decay products. One such plot can be seen in Fig. 8.13 and represents the conclusion that Effective_HeavyN decays the mesons isotropically as it should. This conclusion was further consolidated by examining three dimensional HNL momentum space histograms such as those shown in Fig. 8.14, where again clear isotropy can was found.

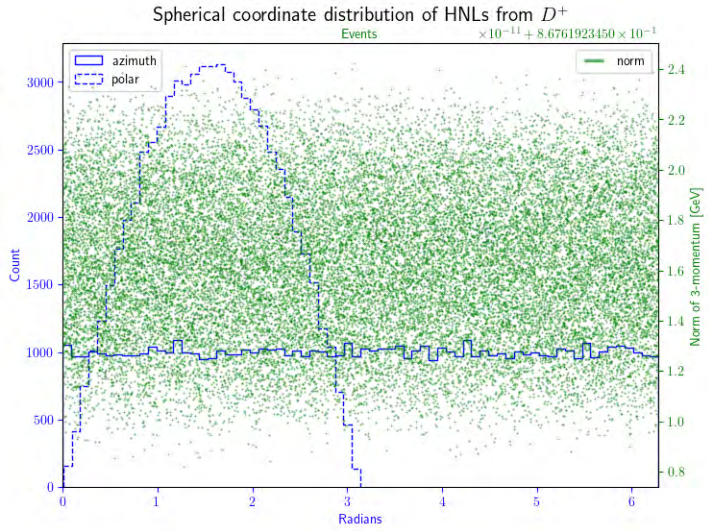

Figure 8.13: Distribution of spherical coordinates of HNLs produced from a $B^{\pm}$ decay by Effective_HeavyN. Based on a sample of 30.000 decays.

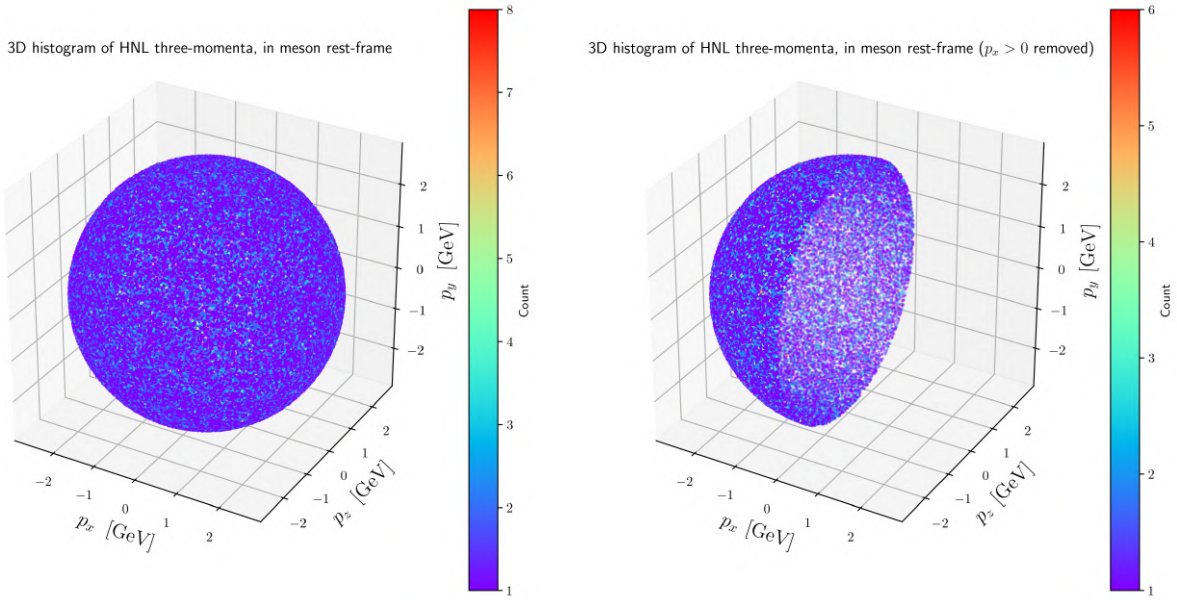

(a) Full momentum space **(b)** Momentum space with $p_x > 0$ removed

Figure 8.14: Three dimensional momentum space histogram based on 100.000 EFFECTIVE_HEAVYN simulated HNL momenta, colorbar represents count. The specific decay shown is $B_c^{\pm} \to N\tau$. Clear isotropy is seen with slight traces of moiré patterns resulting from the binning. **(a)** Histogram of full HNL momentum space, **(b)** Histogram of HNL momentum space with $p_x > 0$ removed.

Furthermore, the decay width of the muon, computed from it's Breit-Wigner distribution was also compared with literature [9] and had good agreement (see Fig. 8.15). One can estimate the lifetime of the muon to be $\sim 3.3 \times 10^{-6}$ sec. The literature value of it's lifetime is $\sim 2.2 \times 10^{-6}$ sec. [9].

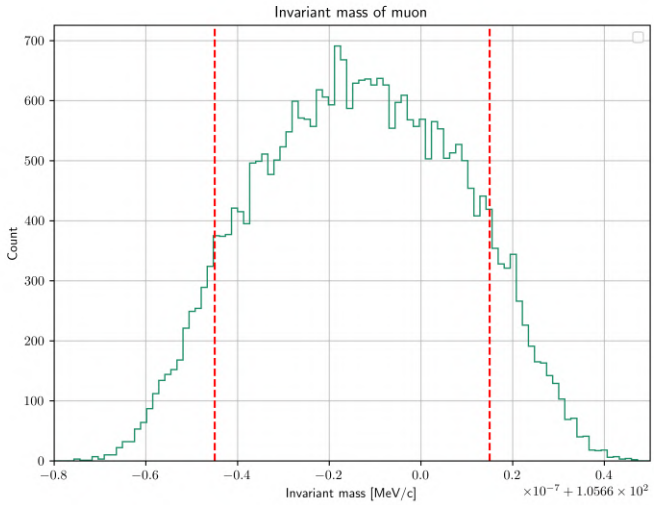

Figure 8.15: Validation of muon decay width by inspection of its invariant mass distribution, based on an ensemble produced by EFFECTIVE_HEAVYN. Full width half height is indicated by the dotted red lines.

8.3.6.2 Validation of SM_HEAVYN_NLO

The SM_HEAVYN_NLO model is used in this thesis to generate the purely leptonic decay modes of the HNL. These decay modes have not been observed as of yet, thus a comparison to literature is

not possible in the same way it was for the leptonic decay modes of the heavy mesons. However, by using the analytic result for the leptonic decay width of the HNL given in (4.1.3), one can compare the models performance with the expected results from analysis: It is clear that (4.1.3) is in very good

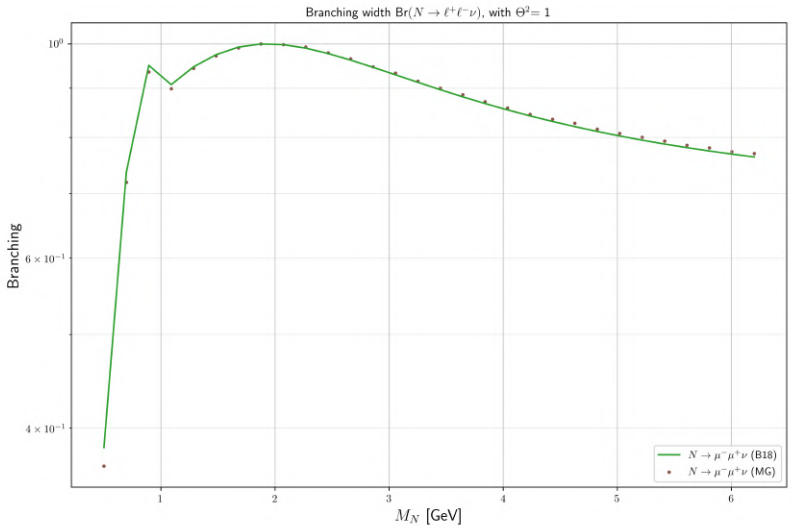

Figure 8.16: The analytic behaviour of the branching fraction of the leptonic mode of the HNL with respect to HNL mass, M_N, with $|\Theta|^2 = 1$ and $\Theta_\alpha = 1$ for $\alpha \in \{e, \mu, \tau\}$. The analytic results were normalized to match the values from MG, there is a slight discrepancy due to differences in HNL lifetime between MG and analysis, which is neglected for the purpose of the current comparison. The shape of the analytic decay functions from [42] are thus in very good agreement with data supplied by MG.

agreement with [42]. Further, a comparison between the analytic estimation of the $W^\pm$-process given in 4.2.1 and shows good agreement:

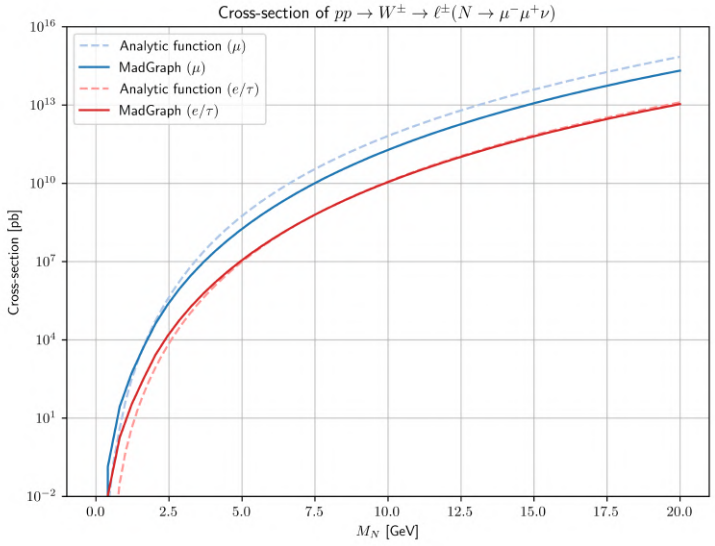

Figure 8.17: Comparison between the analytically estimated cross-section of the $W^\pm$-process and the cross-section generated from MadGraph. The analytic results were normalized to match the values from MG. The shape of the analytic decay functions of (4.2.2) are thus in very good agreement with data supplied by MG.

Chapter 9

Data analysis and post-processing

In this chapter the general architecture of data generation and subsequent data handling processes i.e post-processing will be presented. It will be described how data from the three sub-processed S_0, S_1 and S_2 described in chapter 8 were joined by consecutive boosts, and how a multiple selection criteria was be applied to the events in the resulting data. These selection criteria will collectively be referred to as cuts, of which three were used for the present analysis; pseudorapidity-cut (η-cut), displaced vertex cut (DV-cut) and transverse momentum cut (p_T cut).

9.1 Post-processing architecture

To simulate the complete charged meson processes of Fig. 4.2 each of the sub-processes (S_0), (S_1) and (S_2) were handled respectively by PYTHIA, EFFECTIVE_HEAVYN and SM_HEAVYN as described in Chapter 8. These events were produced independent of each other, and subsequently joined by Lorentz boosts between mother and daughter particles[1], adopting PYTHIA's frame of reference as lab-frame. After this initial step was done, creating one coherent data set with the same inertial frame, the various cuts were applied. A schematic representation of the the overall post-processing architecture can be seen in Fig. 9.1.

[1]This could be achieved because the decay processes of (S_1) and (S_2) can be studied from the rest-frame of the mother particle, and Lorentz boosted into the lab frame of (S_0).

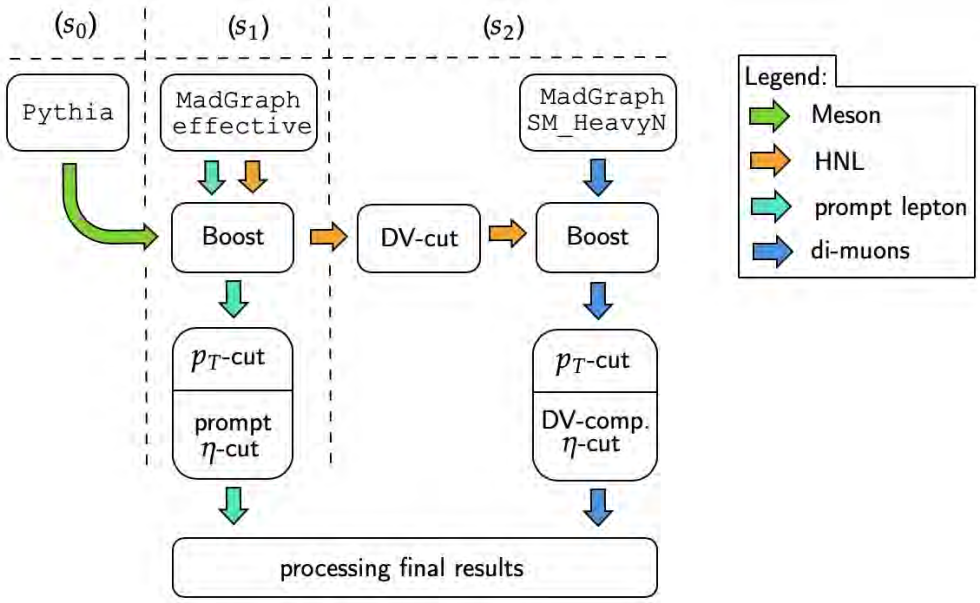

Figure 9.1: Flowchart of the data generation and post-processing for the charged meson processes. Arrows flowing into a boost from the right are in lab-frame, arrows flowing downwards into a boost are boosted into lab-frame. The labeling (S_0),(S_1) and (S_2) is consistent with the Feynman diagram in Fig. 4.2

9.1.1 Lorentz stitching

The mesons generated in PYTHIA are in the proton-proton centre-of-mass frame, and can be understood to be the ATLAS rest-frame. The subsequent decay processes in MG are done in the rest-frame of the mother particle. The daughter particles can then subsequently be boosted into the lab-frame, effectively joining the independent data sets into one. In the case of a multiple decay chains, a Lorentz transformation must be done multiple times, in e.g. the decay of $pp \to B^+ \to e^+N, N \to \mu^+\mu^-\nu_e$, a boost must first take the decay products of N into the frame in which N was produced, and then once more into the reference-frame in which the B^+-meson was produced, i.e. the lab-frame. This procedure could be though of as *stitching* the data sets together through successive boosts, hence the choice of phrasing.

The Lorentz transformation of a relativistic four-vector X^μ into a frame with arbitrary relative velocity $\mathbf{v}$ is given by

$$X'^\mu = B(\mathbf{v})^\mu{}_\nu X^\nu, \tag{9.1.1}$$

where $B(\mathbf{v})^\mu{}_\nu$ is the Lorentz transformation relating the two frames, and X'^μ is the transformed four-vector. To give this expression an explicit form [122] was followed, yielding

$$X'^0 = \gamma(X^0 + \beta\hat{\mathbf{b}} \cdot \mathbf{X}) \tag{9.1.2}$$

$$\mathbf{X}' = \mathbf{X} + \hat{\mathbf{b}}(\hat{\mathbf{b}} \cdot \mathbf{X})(\gamma - 1) + \gamma\beta\hat{\mathbf{b}}X^0, \tag{9.1.3}$$

where $\hat{\mathbf{b}}$ is the unit vector pointing in the direction of $\mathbf{v}$, and $\mathbf{X}, \mathbf{X}'$ are the spacial components of the original and boosted four-momentum respectively. The definitions of γ and β (in natural units) are the usual

$$\beta = |\mathbf{v}|, \quad \gamma = \frac{1}{\sqrt{1-\beta^2}}. \tag{9.1.4}$$

The boosts were done without taking into account effects of spin-polarization, which however does not influence the transformations joining together (S_0) and (S_1) because the mesons considered $(D^{\pm}, B^{\pm}, B_c^{\pm})$ are all pseudo-scalar particles. However, for the second Lorentz *stitching* (i.e. the joining of a rest frame decay with the laboratory frame), transforming (S_2) into the lab frame, an inaccuracy was introduced since the HNL is fermionic and thus spin-correlation effects are present. The inaccuracy introduced is equivalent to averaging over initial spin-states of the lab-frame HNL and summing over the final states of the (S_2)-frame HNL.

It should be noted here, that this inaccuracy is only relevant for the charged meson processes, as there is necessarily no Lorentz transformations between frames in the on-shell $W^{\pm}$-boson process.

9.1.2 Validation of boost implementation

As the Lorentz transformation between frames was a key ingredient to joining otherwise independent events, this method was validated with the following approaches:

- On the level of single events, the transformed four-vectors $\mathbf{X}'$ were checked against the python based Pylorentz package[2], and perfect agreement between the two was found.
- On the level of an ensemble, the transformed momentum distributions were also checked by comparison to the Pylorentz package, and yet again perfect agreement was found.
- The distributions of invariant masses before and after boosts were compared and found to be in satisfactory agreement, as one would expect from a correctly implemented boost. One such comparison is shown in Fig. 9.2. Small deviation were present but could be due to the numerical computations involved when calculating the transformation.
- Three dimensional momentum-space histograms were used to sanity check that the spacial momentum components behaved as expected. Concretely this meant that 3D histograms of momenta of the frame that was boosted into, was compared before and after boost. One such comparison can be seen in Fig 9.3.

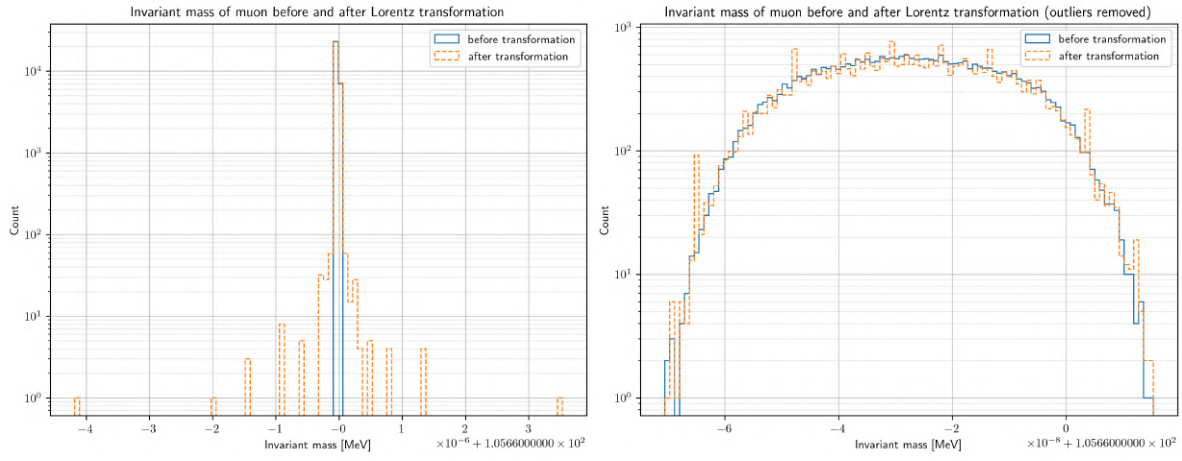

Figure 9.2: The invariant mass distributions of the muon sample, before and after boosts. The plot on the right zooms in at the non-boosted ensemble, emphasizing the good fit but ignoring approximately$\sim 2\%$ of the data points from the boosted ensemble. Even with these outliers included the agreement is satisfactory.

[2]Source code available here.

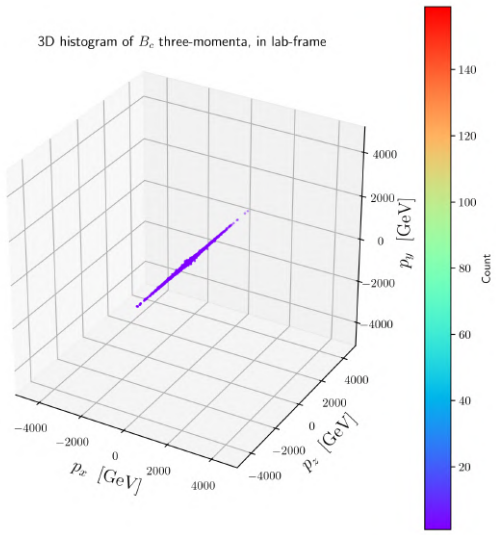

(a) Momentum of mother (B_c) in lab frame

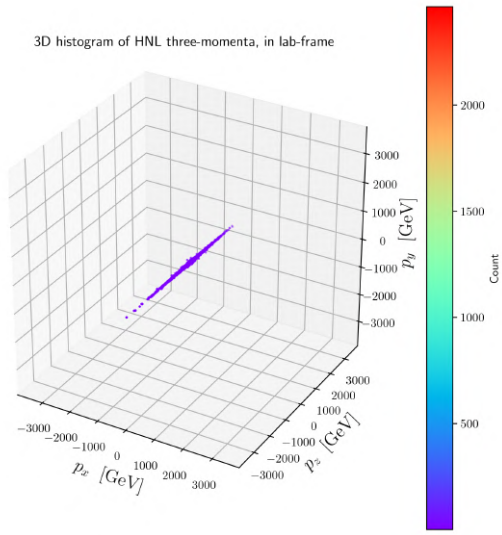

(b) Momentum of daughter (HNL) in lab frame

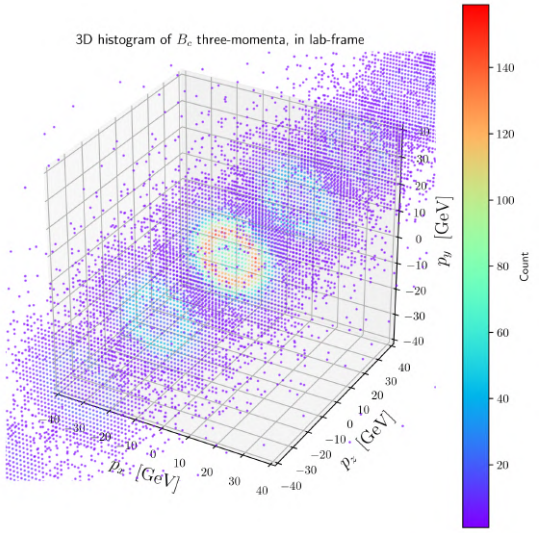

(c) Zoom of mother momenta in lab frame

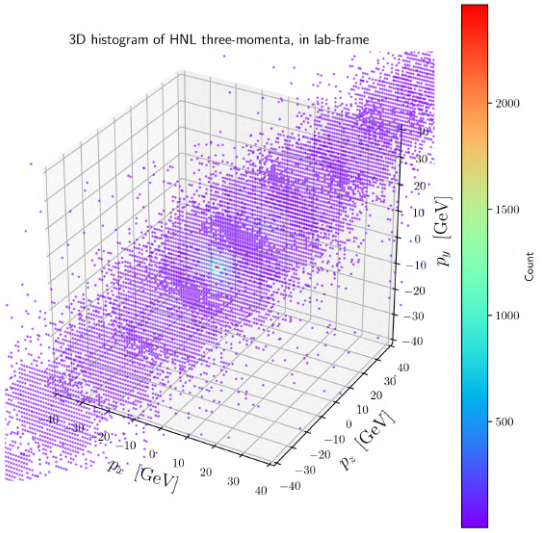

(d) Zoom of daughter momenta in lab frame

Figure 9.3: Three-dimensional momentum-space histograms showing the momentum distributions of mother (**(a)** and **(c)**) and daughter (**(b)** and **(d)**) particles in lab-frame. Analogues histograms of daughter particles in the rest-frame of the mother (i.e. before boost into lab-frame) can be seen in Fig. 8.14. Triangulation of the three was used for validation. For plots **(a)** and **(c)** bins along the p_z-axis has a ∼32 GeV and separation and for plots **(b)** and **(d)** the separation is ∼45 GeV separation. The specific process shown here is $B_c^{\pm} \to N\tau^{\pm}$ (for $M_N = 0.5$ GeV). Notice the strong concentration of events with relatively low p_T seen in the slices of **(c)** and **(d)**. This is in agreement with the general shape of the p_T histograms in of section 8.1.1

9.2 Event selection

The data generated by the event generators is agnostic to detector environment. Therefore a coherent set of selection criteria is required to emulate the detector geometry and produce the signal estimation.

9.2.1 Pseudorapidity

The pseudorapidity, η, of a given momentum-vector can be obtained from p_T and p_z by solving (7.1.12) for the angle θ and substituting into (7.1.11). Following this procedure, any particles with pseudorapidity outside of a range determined by the detector geometry are then to be discarded. In the case of the

MS at the ATLAS detector, this range is $|\eta| \leq 2.4$ and the quoted range for SND is $7.2 \leq \eta \leq 8.6$ (see [123]), however as mentioned in Sec. 7.2.2, the precise geometry of the detector position is instead taken into account, and thus *pseudorapidity* (in contrast to generalised *geometry*) cuts are only taken into consideration for the ATLAS detector.

There is a small caveat however; as mentioned in section 7.1.3 , this procedure works *only* for particles produced at the *interaction point*. For particles produced a macroscopic distance away, such as in the case of visible decay modes of long lived particles, this procedure does not hold. This is indeed the case of an HNL decaying into a displaced lepton pair a macroscopic distance away from the IP, see Fig. 9.5 **(a)**. Thus, a more sophisticated approach was developed, taking into consideration the exact trajectory of the displaced leptons, this approach will henceforth be referred to as the *DV-compatible* η-cut.

To arrive at a crude procedure[3] for performing the η-cut that takes into account the displaced vertex, a simple ray-plane intersection algorithm was developed and utilised. This novel procedure discriminates events based on the criteria that only particles whose trajectory[4] intersects the end planes of the ATLAS detector inside the cone swept out by the blind η-range (depicted in red in Fig. 9.5a), will be discarded. This allows otherwise discarded events such as the one shown in Fig. 9.5b to be retained, in accordance with the geometry of the ATLAS muon detection system. The exact computational procedure of the η-cut is presented in Appendix A.4.2.

To get an intuition of the effect of the DV η-cut, a parameter space plot of its efficiency can be found in Fig. 9.4. The plot was generated based on the μ flavoured $D^{\pm}$ process, but represents the general trend with higher efficiency for small masses and lower mixing. Note that the figure clearly shows how the DV introduces a mixing dependence otherwise absent in the regular prompt η-cut.

9.2.2 Validation of DV compatible η-cut

The DV compatible η-cut procedure was validated at the level of individual events. For this purpose an *event display* was developed, visualising geometric and kinematic information associated with the event. Specifically it plots a projection of the event onto the xz- and yz-planes, as well as a 3D plot of the entire decay chain for a specific event. Examples of the event display output can be seen in Fig. 9.5, where both an event that passes and one that fails the η-cut are displayed. The visualizations produced by the event display allowed for validation of the η-cut and acting as a sanity check that the general geometric and kinematic structure of the events looked reasonable e.g. had displaced vertex of expected displacement and a momentum vector of reasonable direction and magnitude.

An alternative procedure for calculating the DV compatible η-cut was also developed and tested against the one used for the present study (described in Appendix A.4.2). The alternative procedure is given in Appendix A.6.

[3]The procedure can be called crude as it does not account for particle curvature due to the magnetic field, nor exact detector geometry - but based rather on a homogeneous cylindrical geometry absent of magnetic field.

[4]This trajectory is extended ad infinitum, and solved for where on the detector *shell* it intersects.

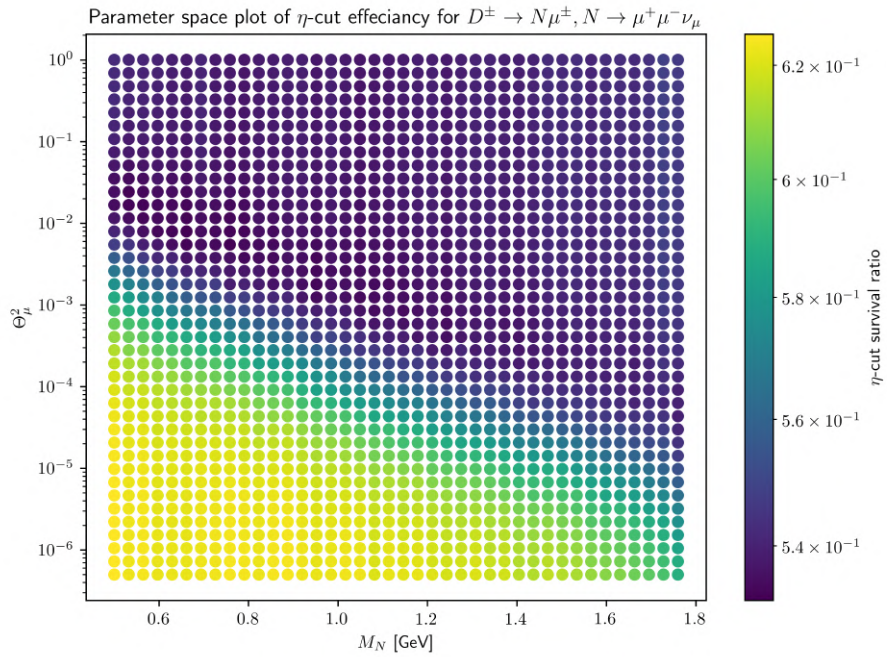

Figure 9.4: Parameters space plot of the efficiency of the DV compatible η-cut. The process is shown in the plot title. This specific process represents the general trend, where clear angular dependence is seenm favoring survival of HNLs with small masses and low mixing.

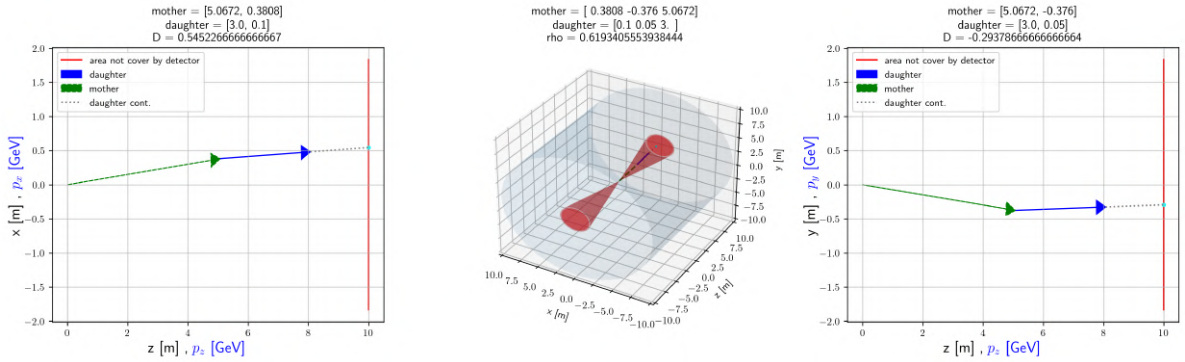

(a)

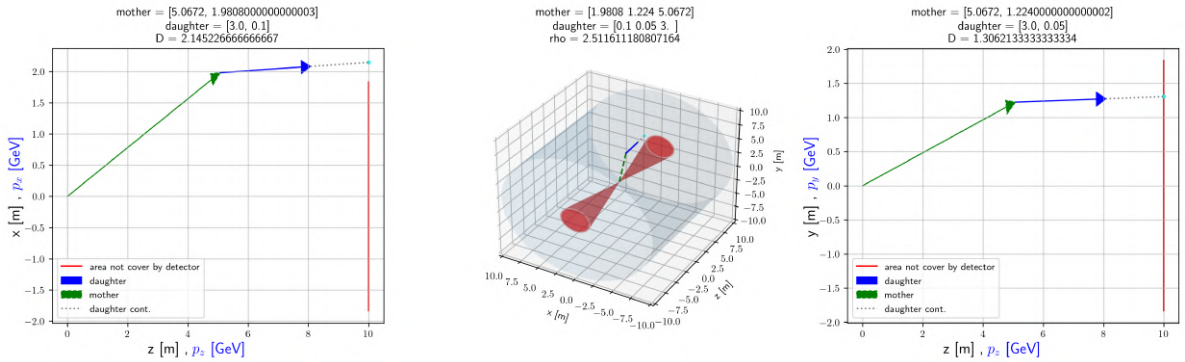

(b)

Figure 9.5: Two examples of events plotted with the event display. The transparent cylinder is a demarcation of the outer edge of the ATLAS detector and the red cones represents the blind volume swept out by the disallowed η-range (represented by a red line on the 2D plots). The green arrow represents the position vector of the production vertex of the particle whose directional momentum vector is represented by the blue arrow. The magnitude of the blue arrow has dimensions of GeV, while all other elements are plotted in meters. The dotted line represents the trajectory and the cyan dot is indicates the exit-point. Above each plot the relevant vectors are printed along with distance to the z-axis labelled as D and rho for the 2D and 3D plots respectively. **(a)** Event that fails both the naïve and DV-compatible DV-cuts. **(b)** Event that fail the naïve DV-cut but pass the DV-compatible DV-cut.

9.2.3 Validation of transverse momentum cut

In contrast to the added complexity of displaced pseudorapidity cuts, the relatively simple nature of the p_T cut makes its implementation less prone to errors because it follows directly from (7.1.9).

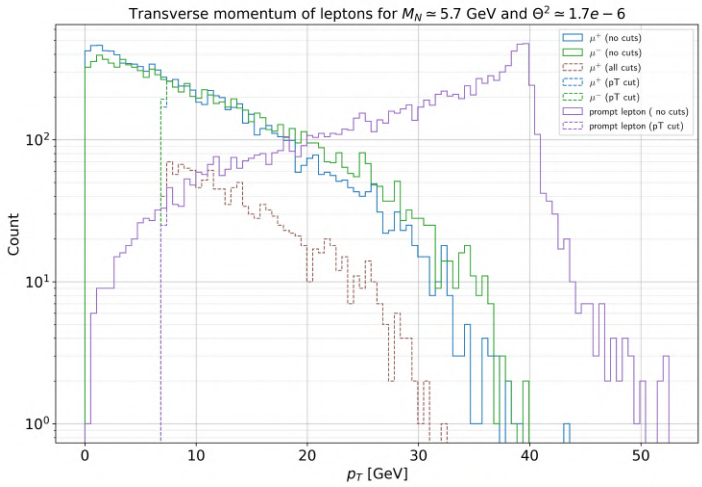

Figure 9.6: The transverse momenta of charged leptons in the process $pp \to W^{\pm} \to N\mu^{\pm}, N \to \mu^+\mu^-\nu_\mu$ where a selection criteria of $p_T > 7$ GeV for each charged lepton was placed. The dotted line represents the transverse momentum of the leptons *after* the cut, and the full lines represent *before* the cut. A clear line at 7 GeV is enough to validate the effect of this procedure. The brown dotted line represents the p_T of a μ^+-lepton after *all* cuts.

Special care was taken to include the option of combining multiple triggers on di-muons such that events which satisfied at least one of two requirements would pass selection, specifically.

- Displaced muons with $p_T > 15$ GeV each
- A single displaced muon with $p_T > 9$ GeV, and the other with $p_T > 23$ GeV.

As validation that the cut was implemented correctly Fig. 9.7 shows a p_T distribution before and after the the trigger cut above, including a cut on prompt lepton selecting those with $p_T > 43$ GeV. It should be noted here that the 10 GeV b- or c-jet cut is taken purely for event selection, to ensure that the quark jet is not *too soft* as to not appear in later, offline, data analysis. It is therefore the assumption that a 10 GeV quark jet criteria is enough so that under offline analysis, a jet can be reconstructed, however the jet is not to be understood as the *trigger*.

9.2.4 Displaced vertex

Similarly to how the η-cut ensured events whose trajectory evaded the detection system were discarded, a criteria must also be in place to ensure the displaced vertex occurs inside the detector volume, and not beyond some *maximum* distance. Furthermore, to reduce the relatively short lived Standard Model background in the ATLAS experiment, it is advantageous to require the displaced vertex to have a *minimum* distance from the interaction point. Collectively these selection criteria will be referred to as the *displaced vertex cut* (DV-cut).

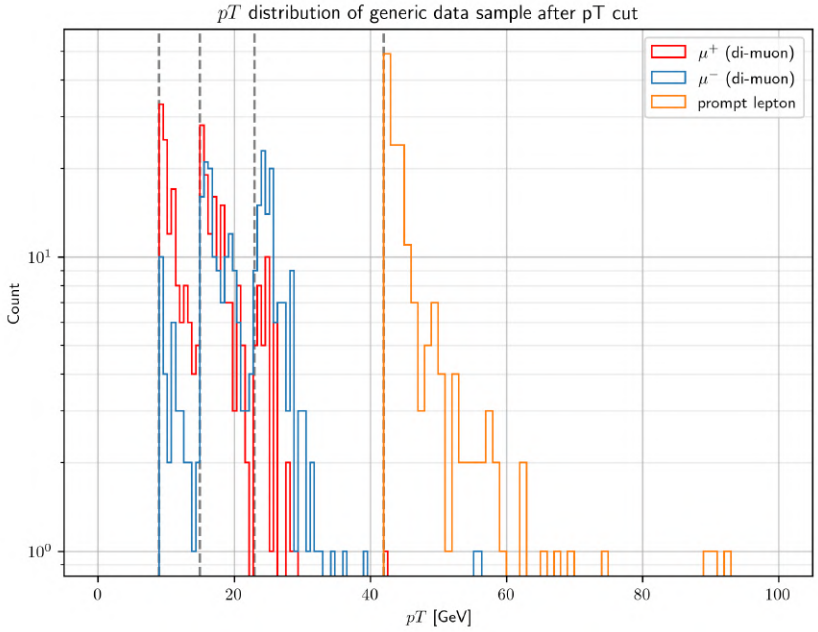

Figure 9.7: Validation of p_T cut implementation on generic p_T distribution. Dotted vertical lines coincides with cuts: prompt lepton $p_T > 43$ GeV, di-muons $p_T > 15$ GeV, 15 GeV or > 9 GeV, 23 GeV

To perform the DV-cut, particle decays were simulated individually by drawing stochastic samples from an exponential distribution [5] with probability density function

$$P(x) = \tau^{-1} e^{x/\tau}, \tag{9.2.1}$$

where the scale parameter τ, the proper *mean* lifetime of the the HNL, is dependent on the mixing angles and mass of the HNL. This gives the *actual* simulated proper lifetime τ_X which will vary between individual HNLs. The mean-lifetime follows from (3.2.20) and the exact computational method is placed in A.4.3.

9.2.5 Validation of DV-cut

The displaced vertex, and the subsequent event selection criteria are one of the most central aspects of this thesis. Therefore, a lot of care is put in to ensure the physics as well as post-processing and data handling is correctly validated. The validation will occur through the following points:

- The analytically expected form of the displaced vertex is compared with data.
- The mass dependence of the HNL lifetime is checked with analysis.
- The form and behavior of the subsequent parameter space exclusion region is probed and verified to behave as expected.
- The underlying *landscape* of the DV cut is used to validate the form of the exclusion region on the parameter space plot for two luminosities.
- 3D-histograms of the DV positions of simulated HNLs were plottet before and after the DV-cut, allowing for qualitatively validation of the resultant distributions as seen in Fig. 9.10 and 9.9.

[5] Specifically the `random.exponential` function from Numpy's `random` module was used to generate the sample.

9.2.5.1 Comparison with analytic prediction

Perhaps the strongest indicator that the DV-cut procedure is correct, is in it's agreement with analysis. Starting with the analytic expression, derived from (4.0.1), one can plot this expression with the events that survived the cut shown in Fig. 9.8 and demonstrates good agreement. [6] The plot was produced

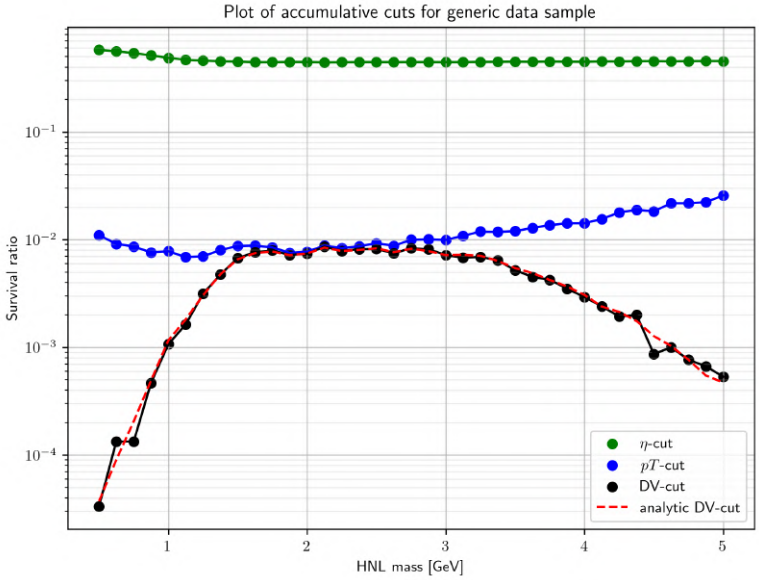

Figure 9.8: Validation of DV-cut implementation on generic data sample. The dashed red line is calculated based on (4.0.1) and for a spherical detector geometry

for a spherical detector geometry. The DV-cut function can be reduced to a spherical geometry, or extended to a cylindrical volume with minor changes. In the case of a spherical geometry, the analytic line is in good agreement. In the case of a cylindrical geometry, an analytic line is more involved, and outside the scope of the current thesis, but as nothing else but the geometry changes, the agreement can be extrapolated to the case of the cylinder.

9.2.5.2 Position space 3D histograms

To qualitatively validate the DV-cut was implemented correctly, probes using three dimensional position space histograms were made, examplesof which are shown in Fig. 9.9 and 9.9. These histograms also served to strengthen the intuition with respect to the actual physical structure of the DV distribution, as they change dramatically with HNL mass and mixing, which also can be seen comparing the scales involved in the two figures.

[6] For regions of the parameter space with low survival, the analytically expected line and the computationally implemented DV-cut deviate from as strong of agreement, due to low statistics.

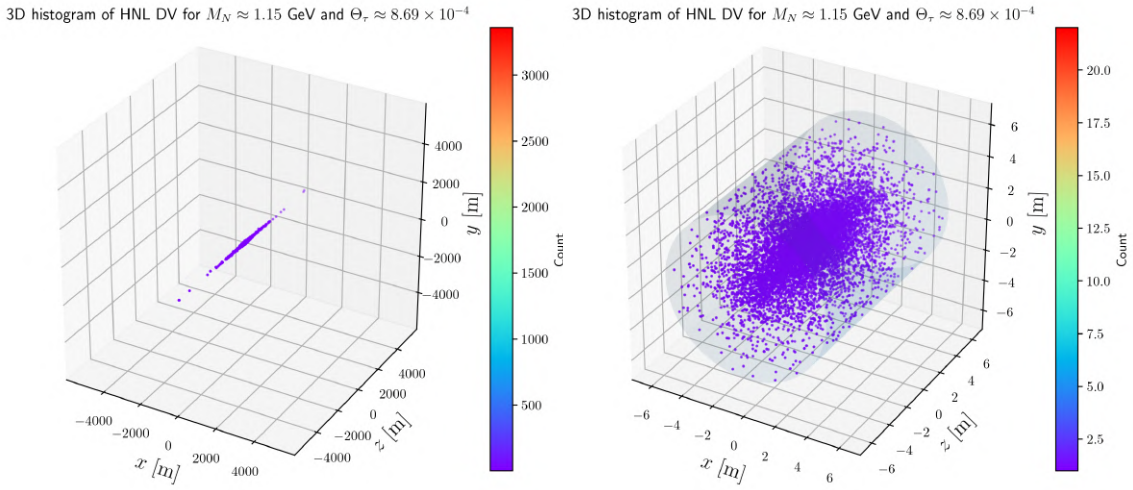

(a) DV positions before DV-cut **(b)** DV positions after DV-cut

Figure 9.9: Three-dimensional position-space histograms showing the DV distributions a single ensembles of 30.000 HNLs before (**(a)**) and after (**(b)**) DV-cut. The specific process generating the HNLs in the plots is $B_c^\pm \to N\tau^\pm$ and the parameters for the ensemble ($M_N \approx 1.15$ GeV, $\Theta_\tau \approx 8.69$ and $\Theta_e = \Theta_\mu = 0$) were chosen such that it would serve to represent the maximum DV distance cut, modelled as a cylinder of radius 5 m and length 14 m. Both plots are *faithful representations of the exact same ensemble before and after the DV-cut* i.e. all particles that survived the cut has been included, validating that the implementation of the maximal distance DV-cut indeed results in an expected distribution (e.g. the z-axis before and after suggest a change in range from ∼8.000 m to ∼14 m as expected).

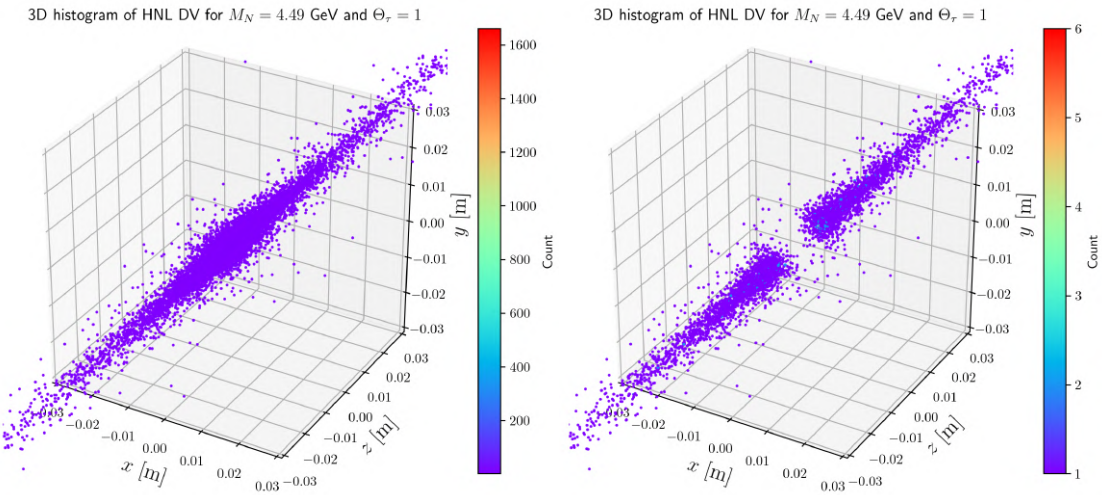

(a) DV positions before DV-cut **(b)** DV positions after DV-cut

Figure 9.10: Three-dimensional position-space histograms showing the DV distributions a single ensembles of 30.000 HNLs before (**(a)**) and after (**(b)**) DV-cut. The specific process generating the HNLs in the plots is $B_c^\pm \to N\tau^\pm$ and the parameters for the ensemble ($M_N = 4.49$ GeV, $\Theta_\tau = 1$ and $\Theta_e = \Theta_\mu = 0$) were chosen such that it would serve to represent the minimum DV distance cut, here modelled as a sphere of radius 2 cm. Axes of both plots are fixed to the same values, excluding part of the ensemble, but effectively zooming in on the relevant region for the minimal distance DV-cut. The absence of particles at the center of **(b)** qualitatively validates that the implementation of the DV-cut indeed results in an expected distribution.

9.2.5.3 Validation of HNL lifetime

A key part of the displaced vertex (and the DV compatible η cut), lies in the lifetime of the HNL. A validated script was used to generate the lifetimes needed, but to validate that we implemented it correctly it was used that the HNL lifetimes, τ_N, obeys the following approximate proportionality with with Θ_α and M_N

$$\tau_N \approx \frac{96\pi^3}{11.9 G_F^2} \Theta_\alpha^{-2} M_N^{-5}, \tag{9.2.2}$$

in the mass range $5 \ll M_N \ll 80$ GeV, where G_F is Fermi's constant. Comparison between the lifetimes used and the above approximation can be seen in Fig. 9.12 for the mass range $5 < M_N < 20$ GeV.

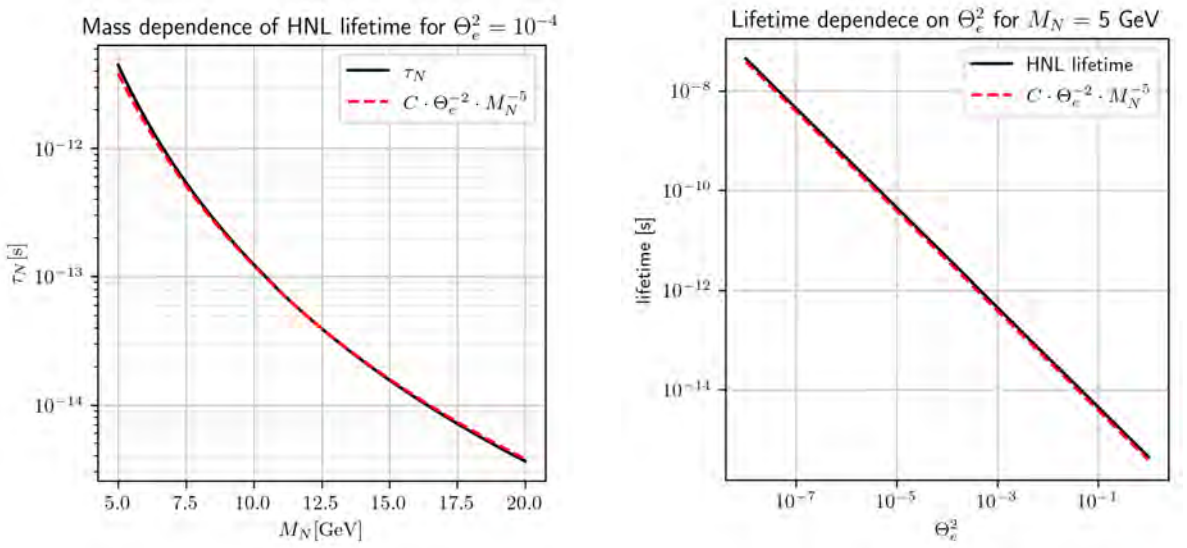

(a) Mass dependence

(b) Mixing dependence

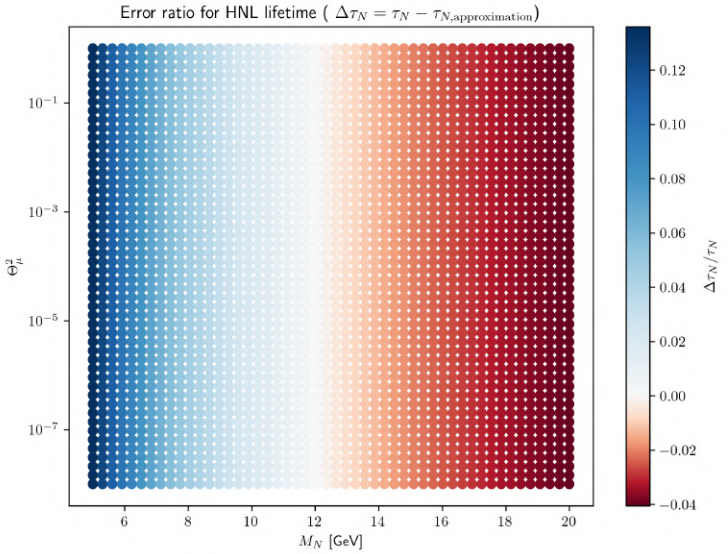

Figure 9.12: Validation of HNL lifetimes, τ_N used in the current study, by comparison to the approximation given in equation (9.2.2). The approximation is valid in the mass range 5 [GeV] $\ll M_N \ll$ 80 [GeV], thus deviation for $M_N \approx 5$ [GeV] is acceptable. **(a)** Shows mass dependence for a representative mixing angle, **(b)** shows mixing dependence for a representative mass and **(c)** shows a parameter space plot over the mass and mixing dependence of the discrepancy ratio $(\tau_N - \tau_{N,\text{approximation}})/\tau_N$.

9.2.5.4 Validation with parameter space plot

As derived in section 7.2.1 and shown in Fig. 5.1, one can predict regions of exponential decrease, constant behaviour and linear decrease (see (5.3.2)) of the DV-cut efficiency analytically. This leads to parameter space of plots the event rate in HNL DV searches to follow a distinct pattern shown in Fig. 9.13. The start of the exponential region is marked by a green line, the linear by a blue line and the constant fertile region is in between the two lines. Two effects are at play giving the characteristic shape:

- Smaller mixing means longer lifetime and visa versa, thus HNLs with small mixing tends to travel further before decaying, and on the contrary HNLs with larger mixing tend to travel shorter before decaying;
- Smaller masses leads to higher velocities causing the DV distance to increase. Additionally higher speeds cause time dilation, effectively extending the lifetime which also contributes to the DV distance as per the point above.

The combination of these two effects result in the exponential region being associated with particles of larger masses and higher mixing, which tend to decay promptly within the region excluded by the minimum DV distance. Likewise, HNLs with smaller masses and lower mixing tend to travel farther situating their DV outside the detector in the linear region.

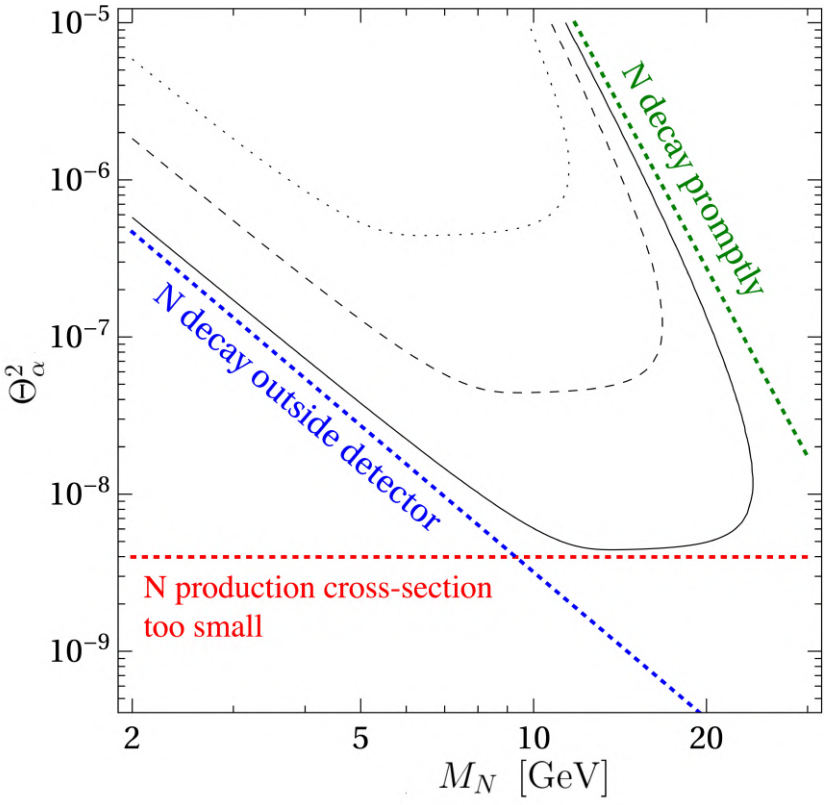

Figure 9.13: The theoretical form of the exclusion region on the parameter space plot, determined by three boundaries: a minimum DV criteria (green), a maximum DV criteria (blue) and bounded from below by production rate.

In Fig. 9.13 the boundary in green is determined by the minimum distance DV criteria, the boundary in blue is determined by the maximum distance DV criteria, and the red line demarcates the region

where the product of the cross-section and luminosity do not give rise to sufficient production, i.e. too small of a production rate to be detectable within the course of the experiment.

This form is in good agreement with the results show for the $W^{\pm}$-boson mediated processes in Sec. 6. For the meson processes, the shape of Fig. 9.13 is not so obvious, but can be seen when studying the underlying data using efficiency plots such as presented in Fig.9.19. In fact the kink seen in some of the exclusion region plots in Chapter 6 (e.g. the e flavored mixing processes in Fig. 6.8 and 6.14) are caused by the mechanism depicted in Fig. 9.13. Most notably the shape of Fig. 9.13 can be seen in the stability plot in Fig. 6.24 where the minimal DV distance is increased to 5 cm.

To further demonstrate the point, below in Fig. 9.14 the exclusion region for the μ-flavored on-shell $W^{\pm}$-boson mediated process is presented for varying minimum and maximum DV cut distances. It can be seen that exclusion regions are sensitive in the expected areas with respect to Fig. 9.13.

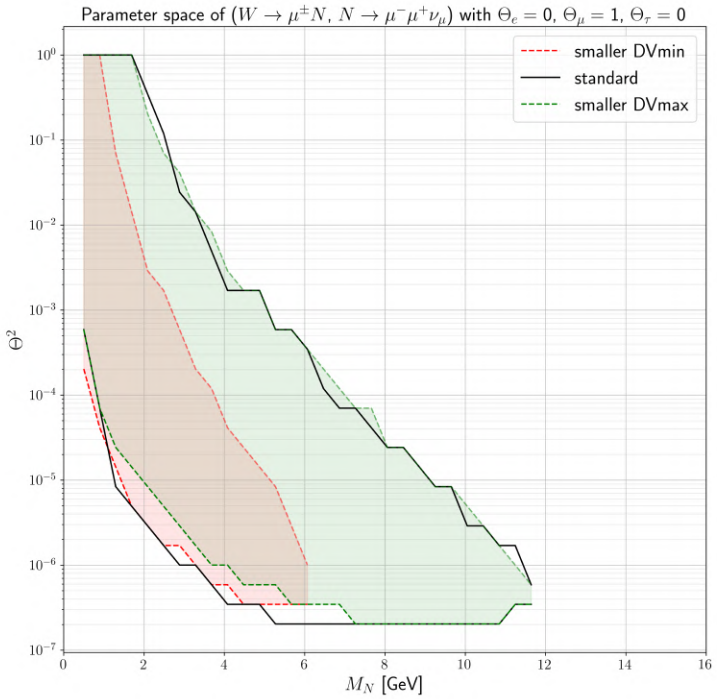

Figure 9.14: The exclusion region of the parameter space plot for the process of $pp \to W^{\pm} \to \mu^{\pm} N \to \mu^{+}\mu^{-}\nu_{\mu}$ with $p_T \geq 7$ GeV for all charged leptons. The exclusion region labeled *standard* is with a maximum displaced vertex position of 7 m (longitudinal) and 5 m (transverse) with a minimum displaced vertex position of 2 cm. The exclusion region (*red*) labeled *smaller DVmin* is with a maximum displaced vertex position of 7 m (longitudinal) and 5 m (transverse) however with a minimum displaced vertex position of 1 m. The exclusion region (*green*) labeled *smaller DVmax* is with a maximum displaced vertex position of 1 m (longitudinal) and 1 m (transverse) with a minimum displaced vertex position of 2 cm. It is clear, that the changes in the contour agree with the expected behavior from Fig. 9.13. Another observation lies in the fact that the parameter space exclusion region is more sensitive to a change in the minimum displaced vertex criteria, rather than the maximum.

9.2.5.5 Validation with parameter space cut flow-diagrams

One can further validate the behavior of the parameter space plot, by close analysis of key points, comparing points on the parameter space plot, e.g. shown below in Fig. 9.15, with points on an event selection flow-diagram for the same point, e.g. Fig. 9.16 (left).

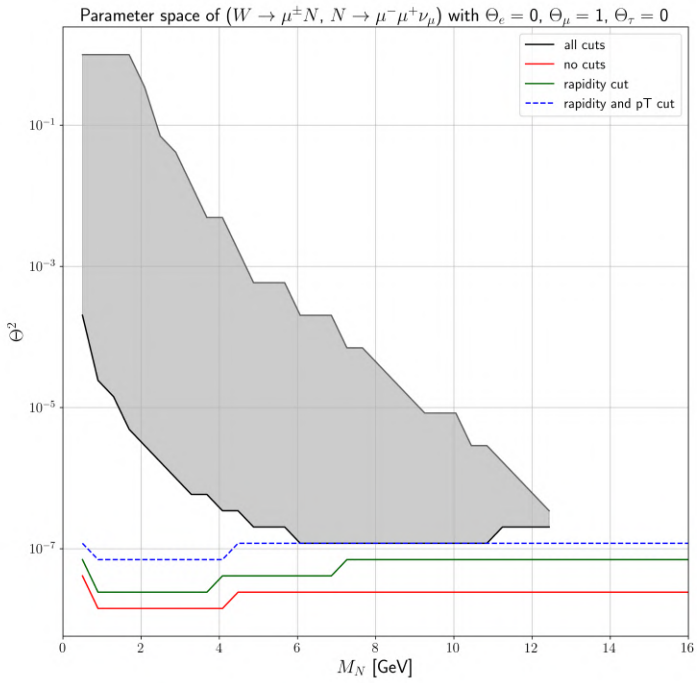

Figure 9.15: Parameter space of the $pp \to W^{\pm} \to \mu^{\pm} N, N \to \mu^{+}\mu^{-}\nu_{\mu}$ process with contour lines representing event selection criteria for p_T-, η- and DV-cut efficiencies. The shaded exclusion region represent a region of $N_{\text{events}} \geq 3$ from (5.1.1).

The lowest line (in black) of the exclusion region of Fig. 9.15, corresponds to a mixing angle of $\Theta_\mu^2 \simeq 1.2 \times 10^{-7}$ between the masses of $6 \lesssim M_N \gtrsim 11$ GeV. Referring then to the flow-chart of Fig. 9.16 (left), which displays the efficiency functions for a single mixing angle, one can qualitatively validate that the displaced vertex cut (black) meets the $p_T + \eta$ cut (blue) between approximately the same mass range as for the parameter space plot.

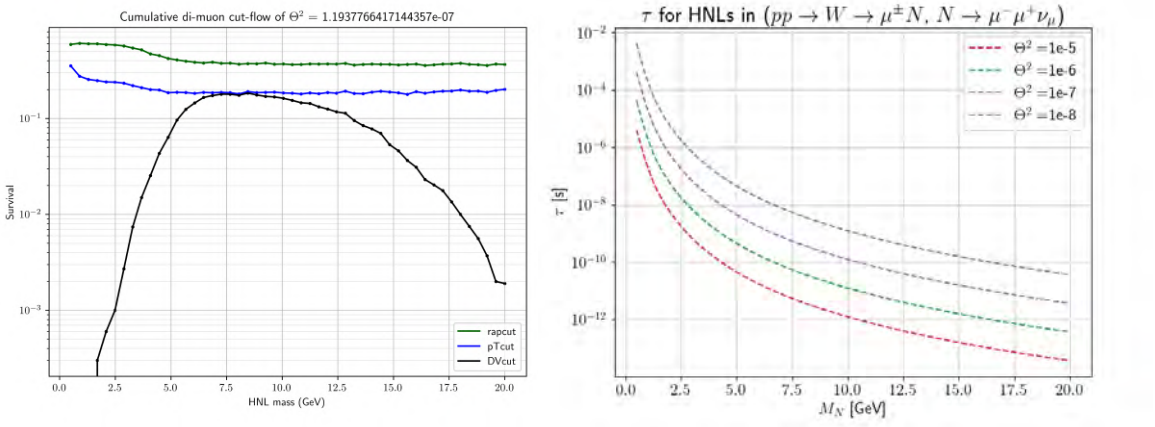

Figure 9.16: A plot cut flow-diagram (left) and mean lifetimes (right) of HNLs, to be used in validation with Fig. 9.15

This agreement can further be validated on the level of single points, by computing the decay positions of the HNLs for a given mass, e.g. $M_N = 8$ and mixing 1×10^{-7}, corresponding to a point in Fig. 9.15

where every HNL that passes the prior selection criteria of p_T and η, passes the DV cut[7], and verifying that the product of the γ-factor, velocity, v and the lifetime τ lies within the range of the DV cut.

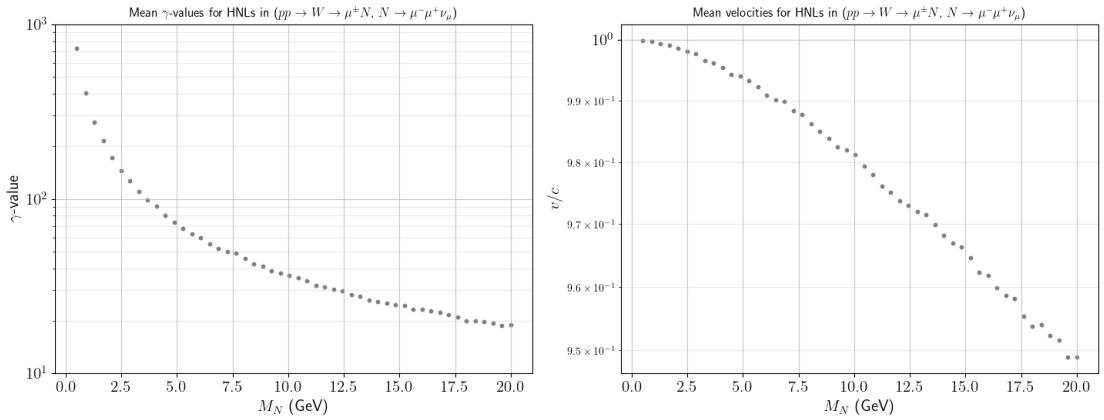

(a) Mean HNL γ-factor **(b)** Mean HNL velocity

Figure 9.17: A plot of mean γ-values (left) and mean velocities (right) of HNLs, to be used in validation with Fig. 9.15 and Fig. 9.16.

Referring then to Fig. 9.16 (b) where it can be seen that an HNL of mass $M_N = 8$ GeV with mixing angle $\Theta^2 = 1 \times 10^{-7}$ corresponds to a lifetime of $\tau \simeq 5 \times 10^{-10}$ sec. As seen from Fig. 9.17 (a) and (b), these HNLs will have a mean γ-factor of 40 and velocity of 0.985c, respectively. Thus, the mean distance traveled within the detector of these HNLs is

$$v\tau\gamma \simeq 6 \text{ m}, \tag{9.2.3}$$

which fits with the observed behavior, that the DV cut efficiency is effectively 1. [8]

9.3 Event rate and efficiency landscapes

The production rates and total efficiencies of surviving events can be drawn on the parameter space plot as well, and it is illustrative in giving reason to why the exclusion region has the form that it does, as well as conveying how the form *changes* after increasing the luminosity tenfold. Naïvely, one may assume that multiplying the $\mathcal{L} = 300$ fb^{-1} exclusion region by a factor ten would simply increase the volume in all directions by one order of magnitude.

However, as shown in Fig. 9.18, a region highly sensitive to change exists, and thus multiplying the luminosity by a factor ten does *not* lead to uniform growth, but rather an increase along the most sensitive regions of the efficiency plot shown below in Fig. 9.18.

[7] This can be seen from the fact that the line representing the p_T cut and the DV cut *touch*, which is only possible if the efficiency of the DV cut is 1.

[8] As seen from Fig. 9.10, the HNLs decay primarily along the beamline, thus as the maximum transverse distance they can have, as enforced by the DV cut, is only 5 m, the maximum longitudinal displacement is 7 m.

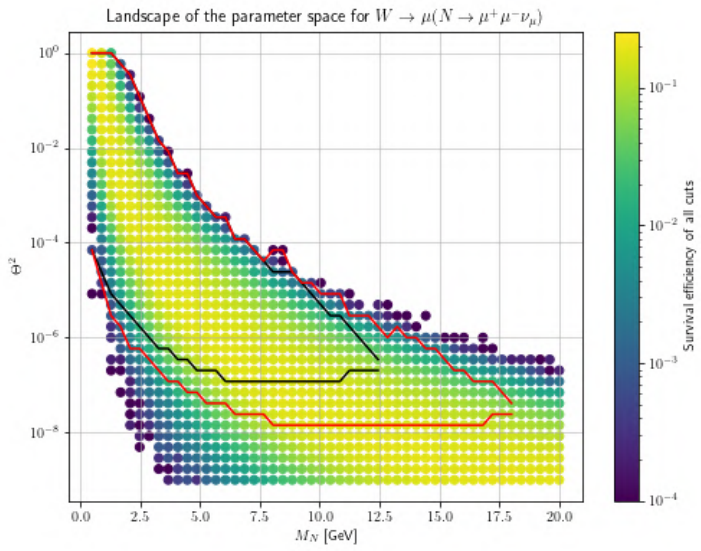

Figure 9.18: A figure demonstrating the underlying *landscape* shaped by considering the total efficiencies of the events for coordinates on the parameter space.

The form of the diagonal slope is produced due to the DV-cut, as particles that decay too promptly, or too displaced will simply not survive the cut, and thus a region forms along the diagonal in which survival efficiency is greatest. On the next page, three diagrams are presented showing the cumulative formation of the landscape below, as each successive selection criteria is applied.

The *analytic* landscape shown in (a) is the product of $\mathcal{L} \cdot \sigma$ without any other cuts. The subsequent landscapes of (b)-(d) display only *efficiencies*, i.e. the efficiency of surviving the event selection criteria named in the caption without multiplying luminosity or cross-section.

The subsequent exclusion contour is then computed from (5.1.1), with the landscape of (a) in Fig. 9.19 , containing $\mathcal{L} \cdot \sigma$, multiplied with the efficiencies, $\epsilon_{\text{detector}}$ taken from (d) in Fig. 9.19 to give the red contour of Fig. 9.18. As discussed in Sec. 9.2.5.4, the exclusion contour follows the form predicted in Fig. 9.13 and bounded from below due to low production rates, otherwise the contour could simply continue ad infinitum[9], following the shape of the efficiency landscape of Fig. 9.18

It is clear that the displaced vertex selection criteria is the main force behind the shape of the exclusion contour. The final exclusion region can be arrived at by multiplying the landscape of (a) with that of (d).

Similarly to Fig. 9.19 **(a)**, the production landscapes of the meson processes can also be plotted. Unlike the for the $W^{\pm}$-boson mediated processes which were handled in entirety by MG, the total cross-section for the for the meson processes was pieced together using the branching fractions of the involved decays. As an example, a collage of the ingredients used to create combined branching $Br(B^{\pm} \to N\mu^{\pm}) \cdot Br(N \to \mu^+\mu^-\nu_\mu)$ can be seen Fig. 9.20.

[9]Not quite, as the mass is bounded by the W-boson, however for other processes, e.g. $pp \to XN$, the upper bound in mass would be approximately the center-of-mass energy.

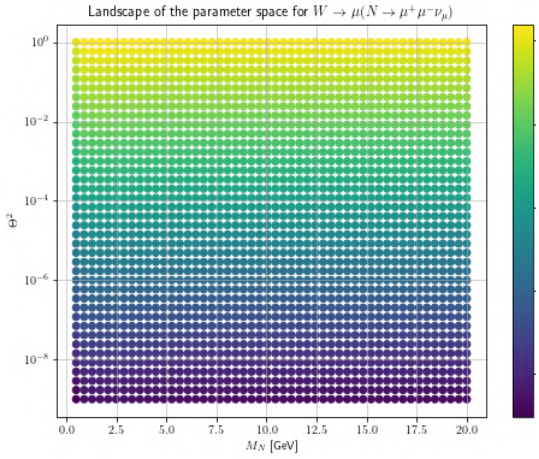

(a) No cuts

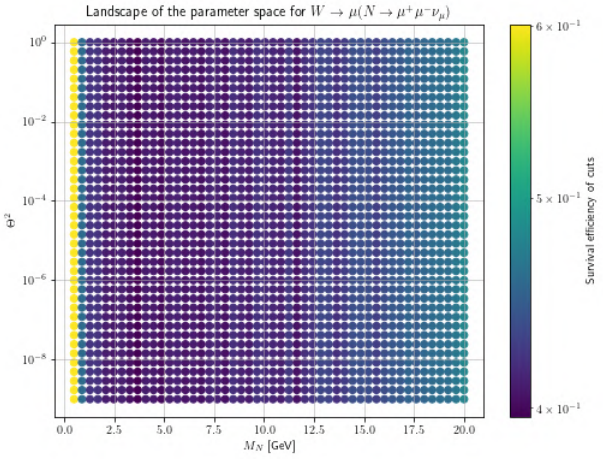

(b) p_T cut

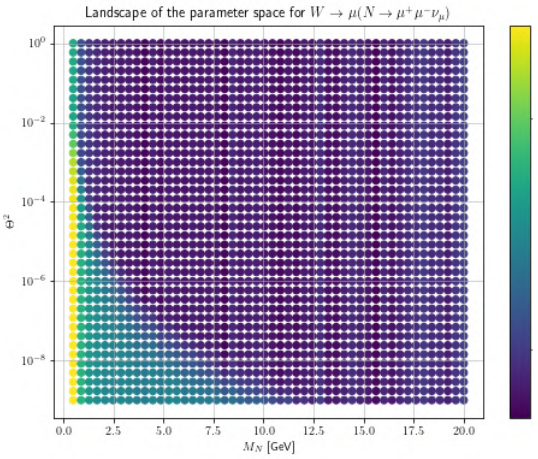

(c) $p_T + \eta$ cut

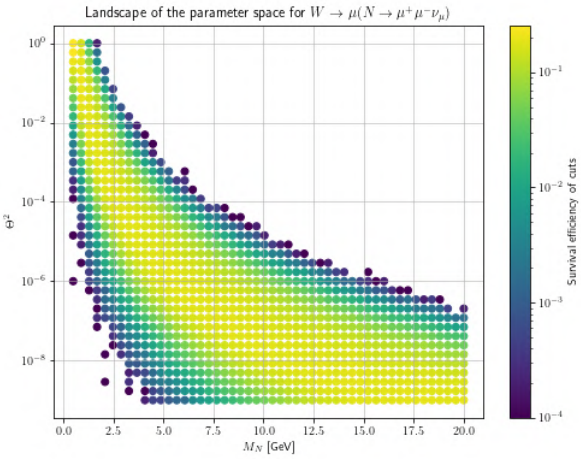

(d) $p_T + \eta$+DV cut

Figure 9.19: Figure showing the formation of the efficiency landscape after successive event selection criteria is applied. Figure (a) is the product of luminosity and cross-section, $\mathcal{L} \cdot \sigma$ without any event selection criteria applied. Figures (b)-(d) are *only* efficiencies, without any luminosity or cross-section.

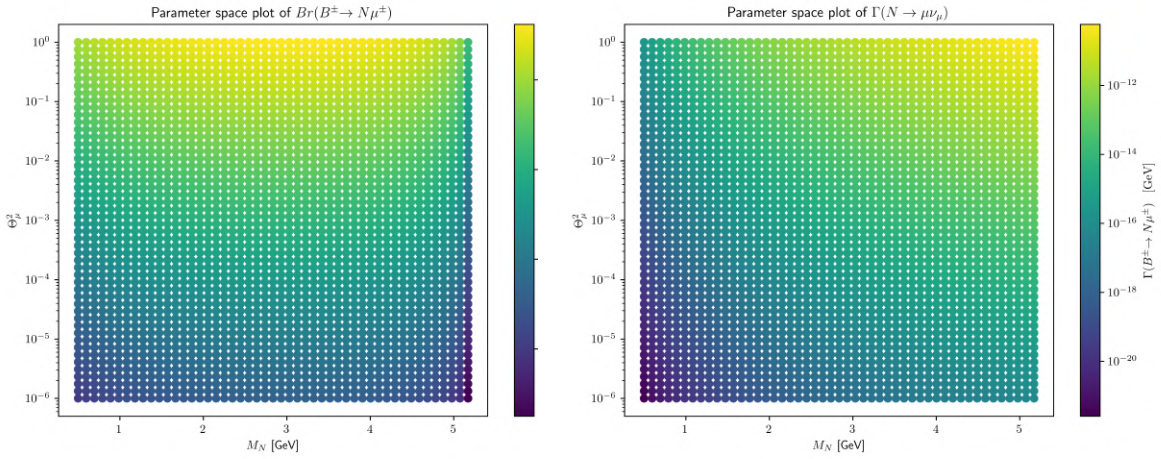

(a) $Br(B^{\pm} \to N\mu)$ **(b)** $\Gamma(N \to \mu^{+}\mu^{-}\nu_{\mu})$

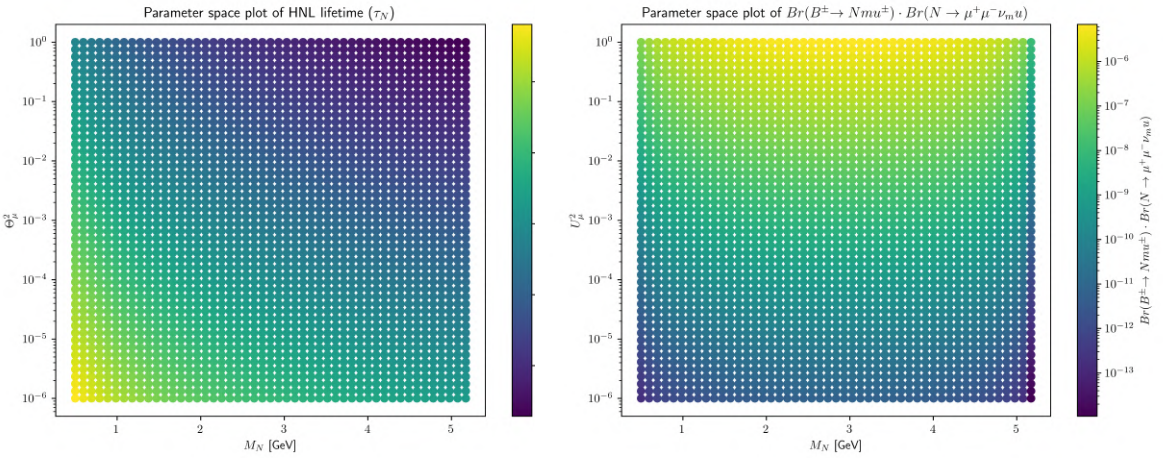

(c) τ_N **(d)** $Br(B^{\pm} \to N\mu) \cdot \tau_N \cdot \Gamma(N \to \mu^{+}\mu^{-}\nu_{\mu})$

Figure 9.20: Figure showing the formation of the landscape of the cross-section for charged meson processes. Neglecting the initial meson production cross-section, which is assumed constant, diagram (a) is the branching ratio of the leptonic decay mode of the $B^{\pm}$ meson to an HNL and muon. Diagram (b) is the width of the leptonic decay mode of the HNL to a di-muon final state. Diagram (c) is the lifetimes, and (d) is the product of (a), (b) and (c), that when multiplied by the initial meson production cross-section and luminosity, yields the landscape for $\mathcal{L} \cdot \sigma$ for the charged meson process.

9.4 Invariant mass

The invariant mass of the displaced muons is computed, and will depend on the mass of the HNL as seen in Fig. 9.21.

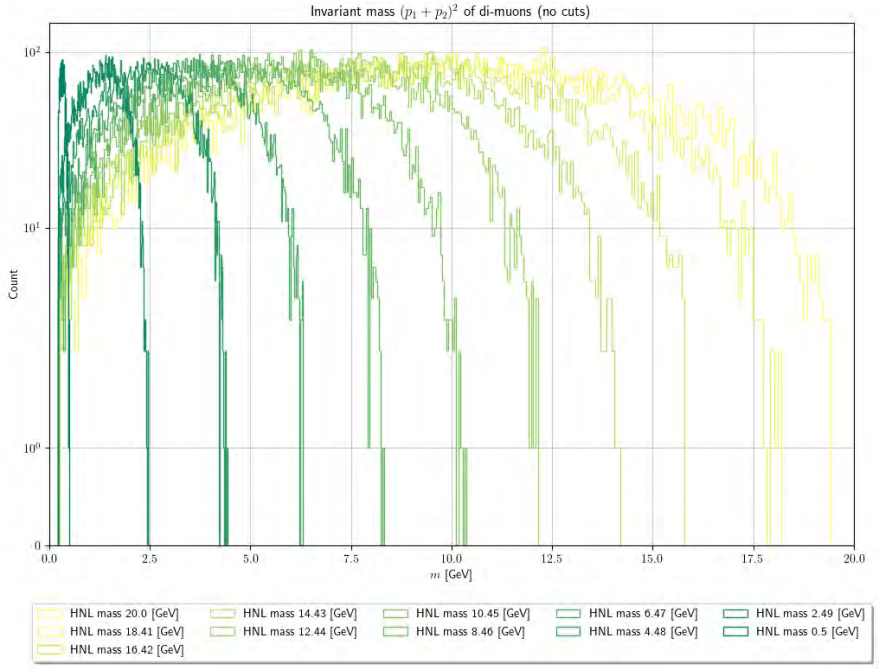

Figure 9.21: Invariant mass distributions of the displaced muons of $pp \to W^{\pm} \to \mu^{+}N \to \mu^{+}\mu^{-}$ as a function of HNL masses are presented without cuts of any kind.

The distributions in Fig. 9.21 do *not* account for cuts of any kind, and as the displaced vertex cuts will in general depend on the HNLs mixing angle and mass, it no longer becomes possible to present a single plot of the invariant mass distributions after cuts, and, rather, can be shown after selecting an HNL mass and mixing. An example can be seen below in Fig. 9.22

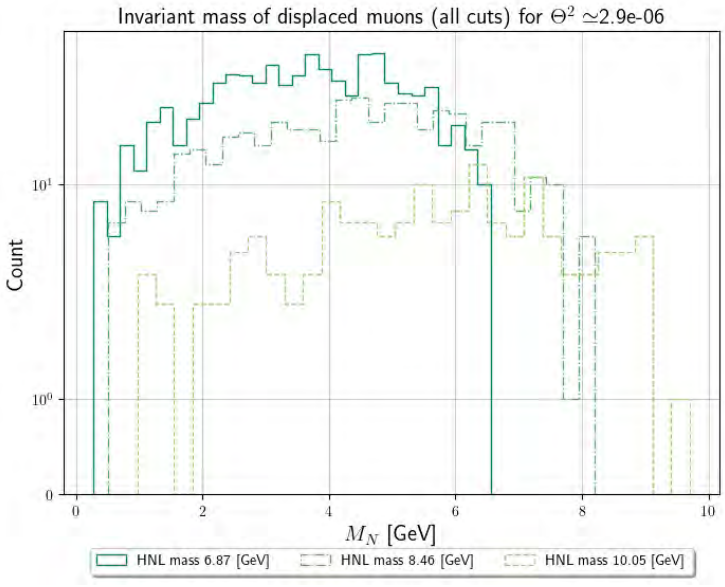

Figure 9.22: Invariant mass distributions of the displaced muons of $pp \to W^{\pm} \to \mu^{+}N \to \mu^{+}\mu^{-}$ as a function of HNL masses are presented after taking all cuts: (p_T, η and DV.

9.5 Summary of trigger and cut parameters

The upper distance limit on the displacement of the displaced vertex was set to coincide with a cylinder of length 7 m and radius 5 m, modelling the ATLAS detector. The lower limit was modelled as a sphere of radius $r_{min} = 1$ mm (2mm for the W-processes), such that particles with a lifetime of less than $\gamma \cdot r_{min}/c$ will tend to be excluded from the background [124].

With respect to triggers, the SND experiment is extremely simple in the sense that it operates in a trigger-less fashion [125].

For ATLAS, the trigger for the DV search scheme 1 is events with two muons of opposite sign, with $p_T \geq 5$ GeV each, originating from a displaced vertex with minimum distance to the IP of 1 cm (2cm for the W-processes). Triggering on di-muon invariant mass could also be considered. Triggers for DV search scheme 2 was described in 5.4.2.

Cut type	ATLAS	SND[10]
DV compatible η-cut	based on $\lvert\eta\rvert \leq 2.4$	pass through veto-plate at the rear end of SND
DV-cut	$R_{\text{DVmin}} \geq 1$ cm (spherical) **and** decay within $R_{\text{MS}} = 5$ m, $L_{\text{MS}} = 14$ m (cylindrical)	decay within detector: x-axis: 80 - 120 mm y-axis: 155 - 195 mm z-axis: 480 - 482.4 m

Table 9.1: Cuts implemented on the data to emulate the geometry of the detectors (only R_{DVmin} is applied to reduce background). R_{DVmin} is the displacement of the DV and R_{MS}, L_{MS} are the radius and total length of the inner ATLAS MS volume. Specifications of the SND dimensions and position can be found in detector can be found in Section 7.2.2.

	Process	ATLAS	SND
Scheme 1	W-boson *and* heavy meson [11] processes	two μ's with shared displaced vertex and opposite charge, both with $p_T \geq 5$ GeV	none
Scheme 2	W-boson processes	two μ's , both with $p_T \geq 15$ GeV **or** two μ's , one with $p_T \geq 23$ GeV and one with $p_T \geq 9$ GeV	none
	W and B, B_c Tri-μ processes	three μ's, all with with $p_T > 7$ GeV	none

Table 9.2: Triggers used for the different processes on the the ATLAS and SND detectors for both DV search scheme 1 and 2.

[10] The SND rear end lays 482.4 m down stream of ATLAS collision point, with transversal area 0.16 m^2, slightly of center with respect to collision axis. For details and coordinate system see Section 7.2.2.

[11] For the ATLAS results a redundant p_T cut was imposed on the b and c quarks requiring them to have $p_T \geq 10$ GeV. This is not intended as a trigger and therefore not listed in the table. From the stability plot in Fig. 6.24 the negligible effect of this cut can be seen. Note that this p_T cut was not imposed for the SND experiment since it would have been detrimental for due to the lack of p_T threshold and forward position of the SND experiment.

Part III

Conclusions & Outlook

Chapter 10

Conclusion and outlook

In the following chapter, the conclusive comments of the current work are elaborated, with focus on discussing the most interesting processes, as well as current and future experimental details and assumptions.

10.1 Conclusion

The exclusion regions with the most favourable sensitivity are those for the processes from the leptonic decay of the $W^{\pm}$-boson, i.e. $W^{\pm} \to \ell^{\pm} N, N \to \mu^{+}\mu^{-}\nu_{\ell}$ with the triple muon flavoured process being the *most* favorable. The reason the triple muon process dominates is because in the case of $W^{\pm} \to \mu^{\pm} N, N \to \mu\mu\nu_{\mu}$, the charged current process, mediated by an off-shell $W^{\pm}$-boson gives rise to a factor ~ 10 increase in branching ratio (see Fig. 8.17), necessarily leading to greater sensitivity. Thus, with the search scheme proposed for the triple muon process the following sensitivities can be achieved:

- For $\mathcal{L} = 300$ fb^{-1}: The search scheme proposed is sensitive to a mass range of $0.5 \leq M_N \lesssim 12.5\,\text{GeV}$ for $10^{-7} \lesssim \Theta^2 \leq 1$
- For $\mathcal{L} = 3000$ fb^{-1}: The search scheme proposed is sensitive to a mass range of $0.5 \geq M_N \lesssim 20$ GeV for $10^{-8} \lesssim \Theta^2 \leq 1$

For the sensitivities of the di-muon channels, one should refer to Fig. 6.1 and Fig. 6.2. Further, it should be stated that the tri-muon channels, for the currently proposed search strategies, are universally dominating due to the contribution of a charged-current mediated process, thus the results commented upon here will be for the tri-muon channels only, as they provide the greatest sensitivities.

Thereafter, it is the tri-muon process of the $B_c^{\pm}$-meson which showed higher sensitivity. Specifically for HNLs mixed with τ-flavour, HNLs, high-luminosity bounds can improve existing limits by more than an order of magnitude (still less significant than the improvement from W-boson production).

- For $\mathcal{L} = 300$ fb^{-1}: The search scheme proposed is sensitive to a mass range of $0.5 \leq M_N \lesssim 6$ GeV for $10^{-5} \lesssim \Theta^2 \leq 1$
- For $\mathcal{L} = 3000$ fb^{-1}: The search scheme proposed is sensitive to a mass range of $0.5 \leq M_N \lesssim 6$ GeV for $10^{-6} \lesssim \Theta^2 \leq 1$

The exclusion region for the tri-muon channel with the $B^{\pm}$-meson is very similar to that of the $B_c^{\pm}$, however with a slightly smaller mass range, as the meson is less massive (by ~ 1 GeV) than its charming cousin. The $D^{\pm}$ showed negligible sensitivity, as due the mesons relatively light mass, the search scheme is strongly restricted in this domain, and thus the exclusion region of the parameter space is entirely engulfed by the BEBC [126] and other previous experiments.

With respect to HNL searches at the SND via the meson processes investigated in the current study, not a single process across all mesons and all mixing schemes were found to produce any signal after cuts were applied. Most processes retained some signal after the η cut, but none was retained after applying the DV cut. Of all the processes, the tri-muon $D^{\pm}$ process saw most events surviving the cuts.

10.2 Outlook

The current thesis proposes optimistic search strategies for displaced vertex searches at the LHC, however as the methods used are novel, or otherwise niche, there have been assumed or ignored effects to do with experimental precision.

The most obvious such assumption is in the geometries and triggers of the detectors. The current study is intended as a *first-approach* in exploring the possibilities for the proposed search schemes, and to bridge the gap to experimentally realistic results, one must consider the *exact* detector geometry in combination with *exact* trigger requirements of both the L1 hardware trigger and the high-level software trigger (HLT). As the field is developing, and the experimental design is constantly being upgraded, the computational pipe-line produced during our research is designed for flexibility with respect to such changes. Once a coherent detector model can be established for a given run (e.g. Run 3 at ATLAS), with coherent trigger settings, the pipeline can be run to generate results closer to a realistic prediction. With this being said, the dedicated b-physics trigger of $p_T \geq 6$ GeV on two muons could be implemented if the combined total final state leptons of the associated HNL mediated process was taken into consideration, as further elaborated in Sec. 7.1.2.

Further, in consideration with the trigger settings used, one must allow for further parameters such as the transverse and longitudinal impact parameters, d_0 and z_0 respectively[1], as well as the opening angle between the displaced muons. Track reconstruction efficiencies must also be accounted for, and most probably, must be defined as a function taking into consideration the weakening precision at large distances.

The present study does also not consider spin-polarisation when boosting the HNLs to join the two MadGraph models used for the charged meson processes. This shortcoming could be remedied either by overcoming the malfunctions[2] found when running the entire process within the effective_HeavyN model (letting MadGraph handle the boost internally), or by extending the external boost script to including spin-polarisation. Note that spin-correlation was taken-into account for the W-processes, and thus no further work is need on this front for those results.

With respect to the SND experiment, despite the dim prospects our results predict for HNL searches, there is still a some hope. For LHC's Run4, scheduled to start 2030, an upgrade of the SND experiment, Advanced SND, has been planned to be operational. It consists of two detectors; a new at distance 55m downstream from the ATLAS IP with a transversal surface of 1.2m $\times$ 1.2m and a redesign of the current SND detector, increasing its transversal surface to 0.4m $\times$ 1m. This opens for searches in new

[1] The transverse impact parameter, d_0 is defined as the shortest distance between a track and the beamline in the transverse plane, where the longitudinal impact parameter, z_0, is the shortest distance between the primary vertex and the point on the track used to define d_0 as per the description in [127].

[2] For some reason we could not get the effective_HeavyN model to handle decay chains with two decays as was necessary. This seemed to be a bug in the model, but maybe one could find a way to make it work.

$v\tau\gamma$ regions with up to a 9 times increase in transversal surface area. This could possibly improve the otherwise not so promising prospects for DV HNLs searches at SND found in the present study, and merits further study.

Also regarding the SND experiment; inspired by the fact that the $D^{\pm}$ meson beat the heavier mesons at SND, it would be interesting to look into some of the other light mesons supported by the EFFECTIVE_HEAVYN model such as e.g. charged kaon, eta and rho mesons. Although their small masses limit the HNL mass range considerably, the absence of p_T cut at SND gives them a chance as long as they are produced in abundance.

Moving on to the trigger settings, multiple outlooks could be considered:

1. For the prompts muon processes specifically, all three muons (one prompt and two displaced) could be pooled into one group and the event kept if the group as a whole satisfied any of the the triggers of Search Scheme 2 (either the T_3 trigger of $p_T > 7, 7, 7$ GeV or the T_2 trigger of $p_T > 15, 15$ GeV or $p_T > 9, 23$ GeV), whereas the present study only considered T_2 and T_3 separately. Furthermore, the T_3 were only applied on the displaced muons, excluding the prompt muon. As the tri-muon processes already yield promising results without these contributions, including them may prove an especially interesting avenue to explore!
2. The trigger menu used for the present study [75] included tagging on *loose*, *medium*, *tight*[3] and *single* particle, options that may be fruitful to consider.
3. The present study was based on an excerpt of the ATLAS trigger menu of 2018 from [75], however, as the precise trigger menu is inaccessible, new triggers may be available. Further, the trigger menu for the high-luminosity phase of the LHC is still in development, the settings of which are therefore currently unknown. Further study of currently available and future triggers may reveal new options that could improve the results achieved by this analysis.

When it comes to decay modes, the present study only considered leptonic decay modes, but several semi-leptonic decay modes are also available for the charged-meson processes. Of these, especially the $B^{\pm} \to D^{0*}\ell^{\pm}N$ and $B^0 \to D^{\pm *}\ell^{\mp}N$, looks favorable with $\Theta_e = 1$, $\Theta_\mu = \Theta_\tau = 0$ branching ratios of $\sim 6 \times 10^{-2}$, which is on par with the $B_c^{\pm} \to \ell^{\pm}N$ processes, which contributed with some of the best results of the meson processes considered. The $B_s^{\pm} \to D_s^{*}\ell^{\pm}N$ processes have similarly high branching ratios, however $B_s^{\pm}$ production is suppressed with about a a factor of $\sim \frac{1}{4}$ (see Fig. 8.3), bringing its HNL production on level with other channels of secondary interest $B^{\pm} \to D^{0}\ell^{\pm}N$ and $B^0 \to D^{\pm}\ell^{\mp}N$ and $B_s \to D_s^{\pm}\ell^{\mp}N$, which all also have favorable branchings at $\sim 2 \times 10^{-2}$ for similar choice of mixing. Note that $B^{\pm}$ and B^0 are produced at same abundance (again see Fig. 8.3).

Incidentally a package including HNLs for PYTHIA is actually available, which encompasses both the charged meson processes and W processes. However the reason for not using this package, and instead developing our own pipeline, is due to its lack of validation and documentation – there could be no guarantee that the HNL sample produced from PYTHIA is physically reasonable,[4] and thus PYTHIA was only used to generate a meson sample, which was then cross-checked and verified with data from ATLAS as well. Despite the convenience of not having to externally stitch separate simulations together, use of the PYTHIA package faces a further problem, namely that by it's construction, it cannot support accounting for spin polarisation between e.g. the prompt and displaced leptons, extending the inaccuracy already found in the meson processes in present study to also include the $W^{\pm}$-processes otherwise handled with spin polarisation by MADGRAPH.

[3] *Loose*, *medium* and *tight* referring to the certainty with which the particle type is identified. Loosening the identification criteria will introduce more miss identifications. The other way around if they are tightened

[4] For example, this package did not include neutral current-mediated decay processes that constitute a significant part of our analysis.

At a more fundamental level, the limitations and flaws of HNL searches based on single-flavour mixing described in Sec. 3.3 is of obvious relevance to the present study, as the models used fall within this category. Work is being done to reveal the possible misleading conclusions such searches may be subject to, and is an underlying crucial theme for all such HNL searches, bridging the gap between theoretical models and experimental feasibility.

In conclusion, there are experimental concerns that need addressing, namely more precise modelling of the detector geometry, track reconstruction and precise trigger settings. As well as more fundamental work needed on accounting for spin-polarization in the charged-meson processes. Finally, there is an underlying theoretical misalignment by using the *single-flavour mixing* model, which should be addressed by e.g. considering *democratic* mixing such that $\Theta_\alpha = \Theta_\beta = 0.5 \cdot \Theta_{\text{tot}}$ in processes with two flavours, where in processes of single flavours, one could use the previously elaborated *single-flavour mixing* model, and rescale to fit points on the unitarity triangle of Fig. 3.8, to fit with the experimental constraints[5].

[5]Ideally, there should be scientific consensus around which set of mixing parameters are the most physically reasonable, and all subsequent studies using a set of an agreed upon set of parameters, in some way like defining the use of the inverted or normal hierarchy. This requires further work in both the theoretical and extensively in the experimental realms however.

Appendix A

Appendices

A.1 HNL Theory

A.1.1 Narrow width approximation

Consider amplitude α in Fig. A.1, where, in the limit where $\Gamma \ll M$, the intermediate particle can be approximated to be *on-shell* for $\Gamma \neq 0$, and thus, for $\Gamma \to 0$, the respective term in the lagrangian approaches a delta-function,

$$\frac{1}{(q^2 - m^2) + m^2\Gamma^2} \to \frac{\pi}{m\Gamma}\delta(q^2 - m^2),$$

and thus, dropping off-shell contributions and spin correlation, one can obtain the physical cross-section under the NWA, by

$$\sigma^{\text{NWA}} = \sigma \frac{\Gamma_N^{\text{channel}}}{\Gamma_N}.$$

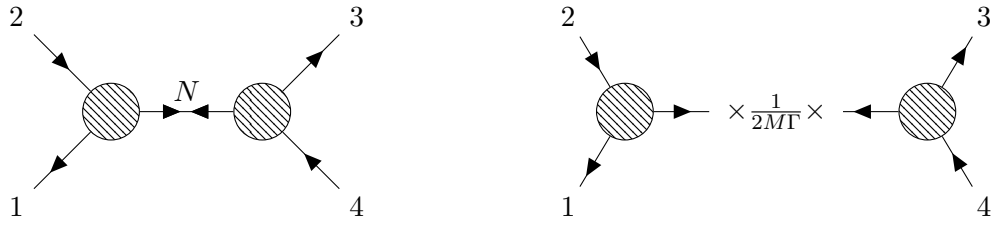

Amplitude (α) Amplitude (β)

Figure A.1: Narrow width approximation

A.2 A Realistic choice of mixing angles

Under a realistic choice of mixing, as presented in Fig. 3.8, one can chose the mixing angles to be $\Theta_\mu^2 = \Theta_\tau^2 = 0.5$ and $\Theta_e = 0$ such that for the $pp \to W^\pm \to N\mu^\pm \to \mu^\pm\mu^\mp\nu_\mu$ process, the exclusion region of the parameter space, under a specific choice of event selection criteria, may look like the one presented below in Fig. A.2

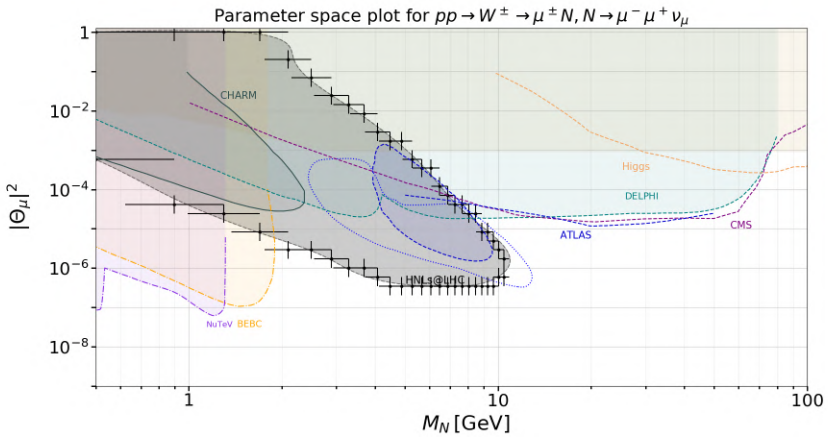

Figure A.2: Projected 95% CL exclusion region for HNLs with $\Theta_e = 0, \Theta_\mu = \Theta_\tau = 0.5$ for integrated luminosities $300\,\text{fb}^{-1}$ (black crosses). The top label shows the analysed process. All 3 muons pass transverse momentum cut of $p_T > 7\,\text{GeV}$ according to the tri-muon trigger [73] and are in the pseudo-rapidity range $|\eta| < 2.4$. The DV cuts are described in the Section 5.3.1. Color shaded regions are exclusions from the previous experiments, see Section 6.1.

A.3 QCD

A.3.1 Deep inelastic scattering (DIS)

Considering the following DIS process occuring at the high energy regime, where an incoming lepton, ℓ scatters off a quark within a proton's wavefunction,

$$\ell + p \to \ell' + X \tag{A.3.1}$$

through exchange of a virtual photon, γ^*, as shown below following closely the notation of [10] Here

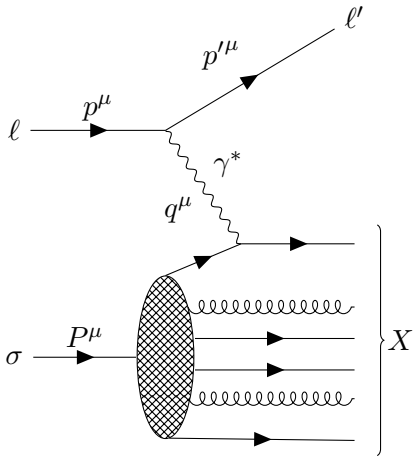

Figure A.3: Feynman diagram of the deep inelastic scattering process $\ell p \to \ell' X$.

ℓ' represents the outgoing lepton, p is the proton, which is denoted σ to avoid confusion between the momentum label p^μ. Considering the rest frame of the proton the associated momentum is thus $P^\mu = (m_p, \vec{0})$ where the incoming and outgoing leptons momenta are respectively $p^\mu = (E, p^\mu)$ and $p'^\mu = (E', p'^\mu)$. The virtual photon's momenta can therefore be expressed as the difference between the incoming and outgoing leptons four-momenta $q^\mu = p^\mu - p'^\mu$ where the following three invariants are usually defined for DIS processes [10]:

$$\begin{aligned} Q^2 =& - q^2, \\ x_{Bj} =& \frac{Q^2}{2P \cdot q}, \\ y =& \frac{P \cdot q}{P \cdot p}, \end{aligned}$$

where Q^2 is the *virtuality* of the photon, x_{Bj} is the *Bjorken-x* variable. In the rest frame of the proton, one can show that

$$Q^2 = 4EE' \sin \tfrac{\theta}{2} \tag{A.3.2}$$

where θ is the scattering angle between the two leptons,and further,

$$y = \frac{E - E'}{E}. \tag{A.3.3}$$

In the proton's rest frame, y can be understood to be the fraction of the incoming leptons energy that is delivered to the proton [128, 10]. From the measured cross-section of the above process, one can extract the standard hadronic tensor $W^{\mu\nu}(q^\mu, p^\mu)$, which we generalize for arbitrary hadrons and quarks, defined as [129]

$$W^{\mu\nu} = \frac{1}{4\pi} \int \mathrm{d}^4 y e^{iq-y} \sum_X \langle A \left| j^\mu(y) \right| X \rangle \langle X \left| j^\nu(0) \right| A \rangle \tag{A.3.4}$$

$$= F_1\left(x, Q^2\right) \left(-g^{\mu\nu} + \frac{q^\mu q^\nu}{q^2} \right) \tag{A.3.5}$$

$$+ F_2\left(x, Q^2\right) \frac{\left(P^\mu - q^\mu P \cdot q/q^2\right)\left(P^\nu - q^\nu P \cdot q/q^2\right)}{P \cdot q} \tag{A.3.6}$$

where $F_1(x, Q^2)$ and $F_2(x, Q^2)$ are the two scalar structure functions[1]. In the limit with large Q at fixed x, called the *Bjorken limit*, factorization theorem leads to

$$W^{\mu\nu}(q^\mu, P^\mu) = \sum_a \int_x^1 \frac{\mathrm{d}\xi}{\xi} f_{a/A}(\xi, \mu) H_a^{\mu\nu}\left(q^\mu, \xi p^\mu, \mu, \alpha_s(\mu)\right) + \text{ remainder} \tag{A.3.7}$$

where $f_{a/A}(\xi, \mu)$ is a parton distribution function such that $f_{a/A}(\xi, \mu)\mathrm{d}\xi$ has physical interpretation as the probability of finding a parton of type $a \in \{q, \overline{q}, g\}$ in a hadron of type A carrying a fraction ξ to $\xi + \mathrm{d}\xi$ of the hadron's momentum [129].

[1] Referring to the treatment of structure functions given in [5].

A.4 Geometry

A.4.1 Intersection of a line and a cylinder

A cylinder in $\mathbb{R}^3$ is centered around $(x, y, z) = (0, 0, 0)$ along the z-axis is given with

$$x^2 + y^2 = r^2 \tag{A.4.1}$$

and is intersected by a line, parameterised as follows

$$\begin{pmatrix} x \\ y \\ z \end{pmatrix} = \begin{pmatrix} x_0 \\ y_0 \\ z_0 \end{pmatrix} + t \begin{pmatrix} \alpha \\ \beta \\ \gamma \end{pmatrix}, \tag{A.4.2}$$

leading to the following three coupled equations

$$x = x_0 + \alpha t \tag{A.4.3}$$
$$y = y_0 + \beta t \tag{A.4.4}$$
$$z = z_0 + \gamma t. \tag{A.4.5}$$

Inserting the solutions for x and y into the equation of a cylinder, eq. 2.1.1,

$$(x_0 + \alpha t)^2 + (y_0 + \beta t)^2 = r^2, \tag{A.4.6}$$
$$x_0^2 + y_0^2 + 2x_0\alpha t + \alpha t^2 + 2y_0\beta t + \beta t^2 = r^2 \tag{A.4.7}$$
$$t^2(\alpha^2 + \beta^2) + t(2\alpha x_0 + 2\beta y_0) + x_0^2 + y_0^2 = r^2 \tag{A.4.8}$$

leading to the second order equation in t,

$$t^2(\alpha + \beta) + t(2\alpha x_0 + 2\beta y_0) + x_0^2 + y_0^2 - r^2 = 0 \tag{A.4.9}$$

which can be recast using χ_1, χ_2, χ_3 so that eq. 2.1.9 becomes

$$\chi_1 t^2 + \chi_2 t + \chi_3 = 0 \tag{A.4.10}$$

where $\chi_1 = \alpha^2 + \beta^2$, $\chi_2 = 2(\alpha x_0 + \beta y_0)$ and $\chi_3 = x_0^2 + y_0^2 - r^2$, to which one can solve the second order equation for t using the quadratic equation

$$t_\pm = \frac{-\chi_2 \pm \sqrt{\chi_2^2 - 4\chi_1\chi_3}}{2\chi_1} \tag{A.4.11}$$

which has two solutions t_+ and t_-, where the intersection to the cylinder occurs at

$$x_+ = x_0 + \alpha t_+ \quad \text{and} \quad x_- = x_0 + \alpha t_- \tag{A.4.12}$$
$$y_+ = y_0 + \beta t_+ \quad \text{and} \quad y_- = y_0 + \alpha t_- \tag{A.4.13}$$
$$z_+ = z_0 + \gamma t_+ \quad \text{and} \quad z_- = z_0 + \gamma t_- \tag{A.4.14}$$

A.4.2 Pseudorapidity event selection for macroscopically displaced particles

Starting from the parameterisation of a ray, as demonstrated in Section A.4.1

$$\vec{r} = \vec{r}_o + s\vec{u}, \tag{A.4.15}$$

defined by the production vertex position vector, $\vec{r}_o$, and directional vector ,$\vec{u}$, belonging to a particle whose η-cut is to be evaluated. The value of the parametrisation parameter s at the intersection point with a plane spanned by the x- and y-axis at z_0, is found by separately solving the equation for the z-component of $\vec{r} = (r_x, r_y, r_z)$ as given by the parametrisation in (A.4.15) for s, with $r_z = z_0$. This yields

$$z_0 = r_{o,z} + s' u_z \implies s' = \frac{z_0 - r_{o,z}}{u_z}, \tag{A.4.16}$$

where s' is the specific value of s where the intersection occurs. Knowing s' one can then construct the intersection point with the plane simply by inserting s' into the parametrisation in (A.4.15). Note that to distinguish which end-cap of the ATLAS detector through which the trajectory exits, we need to add the condition that

$$z_0 = \begin{cases} L & \text{if} \quad p_z > 0 \\ -L & \text{if} \quad p_z < 0 \end{cases}, \tag{A.4.17}$$

where $2L$ is the total length of the detector along the z-axis (beam axis) and p_z is the z-component of the particles momentum. This ensure that we are evaluating the η-cut based on intersection with the plane coinciding with the end-cap through which the particle exits.

Now we have the exit-point of the trajectory, but to judge whether or not is lies within the cone defined by the disallowed η-range we need to know the radius, B, of the disc defined by the cone's intersection with the plane at $z = z_0$. This radius can be obtain by combining the expressions

$$B = L \cdot \tan(\theta_\eta) \tag{A.4.18}$$

$$\theta_\eta = 2 \cdot \arctan(e^{-\eta_{max}}), \tag{A.4.19}$$

where η_{max} is the maximum absolute pseudorapidity tolerable for the detector and ϕ_η is its corresponding angle.

For the final computation of the algorithm we can switch from Cartesian coordinates to cylindrical coordinates (as in figure 7.2 **(a)**) and calculate ρ_D, the radial distance from the z-axis at which the trajectory will exit the detector. We will then discard the event if

$$\rho_D = \sqrt{{r'_x}^2 + {r'_y}^2} < B, \tag{A.4.20}$$

where r'_x and r'_y are the x- and y-components of the exit-point, respectively.

The above has all pertained to the ATLAS experiment, for SND it is a bit simpler, but the same algorithm can be applied. The SND requires the di-muon trajectories to exit through the back-end of the detector (its veto plates). Because it is modelled as an elongated box aligned with the z-axis, this simply means finding the intersection between the trajectory and the xy-plane at $z = z_0$, where z_0 is the z-coordinate of the back-end of the SND detector. This as done exactly as described above, but because the SND detector is located only to one side of the ATLAS experiment, the condition in (A.4.17) is replaced with one that simply discards the event if the particle has $p_z < 0$. Because the SND detection system is simpler than the ATLAS Muon Spectrometer, this η-cut procedure is deemed to be less crude and possibly quite accurate.

A.4.3 Displaced vertex event selection

In order to transfer to lab-frame time, the γ-factor of the individual HNLs, γ_X, were calculated using

$$\gamma_X = \frac{1}{\sqrt{1 - |\mathbf{v}_X^{\text{lab}}|^2}}, \quad \mathbf{v}_X^{\text{lab}} = \frac{\mathbf{p}_X^{\text{lab}}}{E_X^{\text{lab}}}, \tag{A.4.21}$$

where $p_X = (E_X^{\text{lab}}, \mathbf{p}_X^{\text{lab}})$ is the four-momenta of the individual HNLs in the lab-frame. Knowing γ_X, one simply scales the proper actual lifetime to get the lab-fame actual lifetime, τ_X^{lab}, such that

$$\tau_X^{\text{lab}} = \tau_X \gamma_X. \tag{A.4.22}$$

From here, the lab-frame position of the individual HNLs decay vertices, $\vec{r}_X^{\,\text{lab}}$, can be calculated by making use of the relativistic relation between a generic four-momentum, $p = (E, p_x, p_y, p_z)$, and its associated four-velocity, v,

$$p = \gamma m_0 v = Ev \implies v = \frac{p}{E}, \tag{A.4.23}$$

such that

$$\vec{r}_X^{\,\text{lab}} = \vec{v}_X^{\,\text{lab}} \tau_X^{\text{lab}} = \frac{\vec{p}_X^{\,\text{lab}}}{E_X^{\text{lab}}} \tau_X^{\text{lab}}, \tag{A.4.24}$$

where $\vec{v}_X^{\,\text{lab}}$ are the spacial components of the individual HNLs lab-frame four-velocities. Note that the fraction on the right hand side of (A.4.24) is available to us from the four-momentum. Having obtained $\vec{r}_X^{\,\text{lab}}$ one is then ready to apply the DV-cut.

For the purpose of the analysis in present thesis the detector volumes of the ATLAS and SND experiments were modelled as a cylinder and a box respectively.

To evaluate the DV-cut in the SND geometry, each of the three components of the $\vec{r}_X^{\,\text{lab}}$ vector was simply individually checked against the interval defining the sides of the SND box model, such that events with

$$SND_i \leq r_{i,X}^{\text{lab}} \leq SND_i + SND_{\text{sides},i} \tag{A.4.25}$$

passes the cut, where $r_{i,X}^{\text{lab}}$ is the i'th component of $\vec{r}_X^{\,\text{lab}}$, SND_i denotes the i'th component of the position vector defining the corner of the box model closest to the origin and $SND_{\text{sides},i}$ are the length of the box's sides along the i'th axis. The condition in (A.4.25) is of cause understood to be true for all i's in order for the decay vertex to be positioned inside the box.

For the ATLAS experiment, the DV-cut is more easily evaluated by shifting to cylindrical coordinates, of which only

$$\rho = \sqrt{(r_{x,X}^{\text{lab}})^2 + (r_{y,X}^{\text{lab}})^2} \quad \text{and} \quad z = r_{z,X}^{\text{lab}}, \tag{A.4.26}$$

are relevant. The maximal distance DV-cut can then be applied by requiring

$$\rho \leq \rho_{max} \quad \text{and} \quad z \leq z_{max}, \tag{A.4.27}$$

where ρ_{max} and z_{max} defines the decay volume of the model. The spherically modelled minimal distance DV-cut for the ATLAS detector can simply be evaluated by taking the norm of $\vec{r}_X^{\,\text{lab}}$and require that it

be longer than the minimal distance, r_{min}, defining the cut. This excludes all displaced vertices located within a sphere centered around the IP with radius r_{min}.

As a little detail it should be mentioned the displaced vertex of the mesons (yes, though almost insignificant, they too have a DV!) was also taken into account when calculating the displaced vertex of the HNLs. This was done simply by harvesting the position vectors of the meson decay vertices from Pythia and adding them to the decay vertex position vectors of the calculated for the HNLs. This effectively shifted the frame back exactly to the IP.

A.5 The Abelian & non-Abelian Higgs models

A.5.1 The Abelian case

Following the same treatment as [6], one can consider a complex scalar field, ϕ, coupled to itself and an electromagnetic field, A^μ with field strength $F^{\mu\nu}$,

$$\mathscr{L} = -\tfrac{1}{4}(F_{\mu\nu})^2 + |D_\mu\phi|^2 - V(\phi) \tag{A.5.1}$$

with the covariant derivative given as the usual

$$D_\mu = \partial_\mu + ieA_\mu. \tag{A.5.2}$$

Under a gauge transformation, namely, a $U(1)$ transformation such that

$$\phi(x) \to e^{i\alpha(x)}\phi(x) \quad \text{and} \quad A_\mu(x) \to A_\mu(x) - \frac{1}{e}\partial_\mu\alpha(x), \tag{A.5.3}$$

the Lagrangian is invariant. One can choose a potential, $V(\phi)$, such that

$$V(\phi) = -\mu^2\phi^*\phi + \frac{\lambda}{2}(\phi^*\phi)^2 \tag{A.5.4}$$

with $\mu^2 > 0$. The scalar field, ϕ, will then acquire a vacuum expectation value and the $U(1)$ global symmetry will be *spontaneously broken* with a minimum at

$$\langle\phi\rangle = \phi_0 = \left(\frac{\mu}{\sqrt{\lambda}}\right). \tag{A.5.5}$$

Expanding the Lagrangian in (A.5.1) around the vacuum state minimum, ϕ_0, one can decompose the field, ϕ as

$$\phi(x) = \tfrac{1}{\sqrt{2}}\phi_0(x) + \phi_1(x) + i\phi_2(x) \tag{A.5.6}$$

where the complex conjugate is simply

$$\phi^*(x) = \sqrt{2}\phi_0(x) + \phi_1(x) - i\phi_2(x) \tag{A.5.7}$$

and so one can reformulate the potential in (A.5.4) to

$$V(\phi) = -\tfrac{1}{2}\left(\lambda^{-1}\mu^4 - 2\mu^2\phi_1^2\right) + \mathcal{O}(\phi_i^3) \tag{A.5.8}$$

so that $\phi_1(x)$, the Higgs field, acquires a mass $m = \sqrt{2}\mu$ and ϕ_2 corresponds to a massless Goldstone boson. Further, the kinetic energy term of ϕ can be expanded for ϕ given in (A.5.6) so that

$$\begin{aligned}
|D_\mu\phi|^2 =& 2\left(\partial_\mu\phi_0\right)^2 + \sqrt{2}_\mu\phi_0\partial^\mu\phi_1 + i\sqrt{2}\partial_\mu\phi_0\partial^\mu\phi_2 + ie\partial_\mu\phi_0 A^\mu\phi_0 \\
&+ 2ie\partial_\mu\phi_0 A^\mu\phi_0 + \sqrt{2}ie\partial_\mu\phi_0 A^\mu\phi_1 + \sqrt{2}e\partial_\mu\phi_0 A^\mu\phi_2 \\
&+ \sqrt{2}\partial_\mu\phi_1\partial^\mu\phi_0 + \left(\partial_\mu\phi_1\right)^2 + i\partial_\mu\phi_1\partial^\mu\phi_2 + ie\sqrt{2}\partial_\mu\phi_1 A^\mu\phi_0 \\
&+ ie\partial_\mu\phi_1 A^\mu\phi_1 + e\partial_\mu\phi_1 A^\mu\phi_2 + i\sqrt{2}\partial_\mu\phi_2\partial^r\phi_0 + i\partial_\mu\phi_2\partial^r\phi_1 \\
&+ \left(\partial_\mu\phi_2\right)^2 + e\sqrt{2}\partial_\mu\phi_2 A^\mu\phi_0 + e\partial_\mu\phi_2 A^\mu\phi_1 + e_\mu\partial_2 A^\mu\phi_2 \\
&+ 2ieA_\mu\phi_0\partial^\mu\phi_0 + ie\sqrt{2}A_\mu\phi_0\partial_\mu\phi_1 + e\sqrt{2}A_\mu\phi_0\partial^\mu\phi_2 + \boxed{2e^2\left(A_\mu\phi_0\right)^2} \\
&+ \sqrt{2}e^2 A_\mu A^\mu\phi_0\phi_1 + \sqrt{2}^2 A_\mu\phi_0 A^\mu\phi_2 + ie\sqrt{2}A_\mu\phi_1\partial^\mu\phi_0 \\
&+ ieA_\mu\phi_1\partial^\mu\phi_1 + e^2 A_\mu\phi_1\partial^\mu\phi_2 + \boxed{e^2\sqrt{2}A_\mu\phi_1 A^\mu\phi_0} + \boxed{e^2\left(A_\mu\phi_1\right)^2} \\
&+ ie^2 A_\mu\phi_1 A^\mu\phi_2 + e\sqrt{2}_\mu\phi_2\partial^\mu\phi_0 + eA_\mu\phi_2\partial^\mu\phi_1 + ieA_\mu\phi_2\partial^\mu\phi_2 \\
&+ \boxed{ie^2\sqrt{2}A_\mu\phi_2 A^\mu\phi_0} + \boxed{ie^2 A_\mu\phi_2 A^\mu\phi_1} + \boxed{e^2\left(A_\mu\phi_2\right)^2}.
\end{aligned} \tag{A.5.9}$$

In the above derivation, there are a few notable terms which have been highlighted, amongst them is the $2e^2(A_\mu\phi_0)^2$ term which is formally the mass term of the *photon*. Further, four-point vertex terms arise, such as the ones presented below, and three point vertices, all of which are highlighted. Two-point

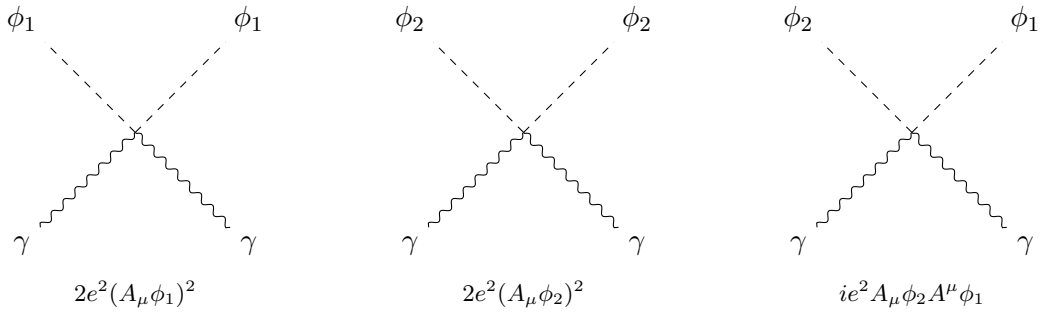

vertices deriving from terms such as $\sqrt{2}\phi_0\partial^\mu\phi_2$ arises where a Goldstone boson couples directly to the gauge boson,

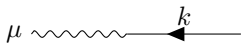

$$= i\sqrt{2}e\phi_0(-ik^\mu) = m_A k^\mu \tag{A.5.10}$$

these however have not been highlighted [6].

A.5.2 The non-Abelian case

The Higgs mechanism can be extended to the non-Abelian case by introducing a system of scalar fields ϕ_i which is invariant under a local gauge symmetry, one can promote the covariant derivative of (A.5.2) to

$$D_\mu \phi_i = (\partial_\mu + g A_\mu^a T^a)\phi \tag{A.5.11}$$

so that the kinetic energy term expands to

$$(D_\mu \phi_i)^2 = (\partial_\mu \phi_i)^2 + 2gA_\mu^a(\partial_\mu \phi_i T_{ij} \phi_j) + g^2 A_\mu^a A^{b\mu}(T^a\phi)_i(T^b\phi)_i \tag{A.5.12}$$

whereby the field acquires a vacuum expectation value $\langle \phi_i \rangle = (\phi_0)_i$ and the gauge field, A_μ, acquires a mass derived from the above highlighted term.

A.6 Alternative rapidity cut computation

To arrive at a procedure for performing the η-cut that takes into account the displaced vertex, it is convenient to split the problem in two, and first deal with the xz-plane and the yz-plane separately. For each plane we want to know D_x and D_y, the respective distance from the z-axis at which the particle will exit the detector. Knowing these, we can then switch from Cartesian coordinates to cylindrical coordinates (as in figure 7.2 **(a)**) and calculate ρ_D, the radial distance from the z-axis at which the particle will exit the detector. We will then discard the event if

$$\rho_D = \sqrt{D_x^2 + D_y^2} < B, \tag{A.6.1}$$

where B is the radius of the blind discs at either end of the detector, defined by its η-range and its total length $2L$ along the z-axis through the expressions

$$B = L \cdot \tan(\theta_\eta) \tag{A.6.2}$$

$$\theta_\eta = 2 \cdot \arctan(e^{-\eta_{max}}), \tag{A.6.3}$$

where η_{max} is the maximum absolute pseudorapidity tolerable for the detector and ϕ_η is its corresponding angle. The relevant quantities are schematically represented in figure A.6, to which one can also refer for the naming conventions in the following.

The only task left is then to determine D_x and D_y, for which we need the distance L' along the z-axis from the displaced vertex to the end plane of the detector at $z = \pm L$ (sign depending on the direction of the trajectory). Expressed through the longitudinal element of the displacement vector $\vec{r}$ and the particle momentum $\vec{p}$ we have

$$L' = \begin{cases} L - |r_z| & \text{if} \quad \text{sgn}(p_z) = \text{sgn}(r_z) \\ L + |r_z| & \text{if} \quad \text{sgn}(p_z) \neq \text{sgn}(r_z) \end{cases}, \tag{A.6.4}$$

where sgn denotes the sign function. This expression also takes into account the case where the daughter particle travels in the opposite longitudinal direction of the mother particle, formally encoded by $\text{sgn}(p_z) \neq \text{sgn}(r_z)$. The displaced vertex cut introduced in section 9.2.4 makes sure that $|r_z| \leq L$ and thus $L' \geq 0$ as required for a length.

If we define $\xi \in \{x, y\}$, we then also need A_ξ, the side coinciding with the ξ-axis of the triangle formed by the detector exit plane, the straight line running from the displaced vertex to the detector exit plane

and the line coinciding with $\vec{p}$ going from the displaced vertex to the detector exit plane. For this triangle, elementary trigonometry gives us

$$\left.\begin{aligned}\tan(\theta_\xi) &= \tfrac{A_\xi}{L'} \\ \tan(\theta_\xi) &= \left|\tfrac{p_\xi}{p_z}\right|\end{aligned}\right\} \implies A_\xi = L' \cdot \left|\frac{p_\xi}{p_z}\right|, \tag{A.6.5}$$

where we take the absolute value of the momentum components since the length A_ξ is required to be positive. We can then get the expressions for D_x and D_y by

$$D_\xi = \begin{cases} A_\xi + |r_\xi| & \text{if} \quad \text{sgn}(p_\xi) = \text{sgn}(r_\xi) \\ |(A - |r_\xi|)| & \text{if} \quad \text{sgn}(p_\xi) \neq \text{sgn}(r_\xi), \end{cases} \tag{A.6.6}$$

where the conditional definition this time takes into account the case where the daughter particle travels in the opposite ξ-direction of the mother particle.

After performing the procedure above for both $\xi = x$ and $\xi = y$, we are then ready to return back to equation A.4.20 and judge whether or not the event fulfills the η-cut criteria or needs to be discarded.

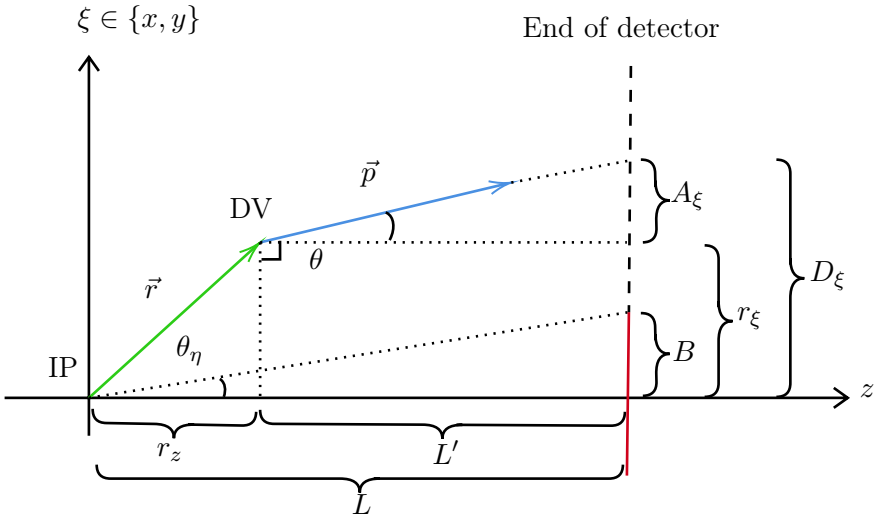

Figure A.6: Schematic representation of the quantities involved in the alternative DV compatible η cut computation.

A.7 $B_c^{\pm}$ meson sample validation

In the computation of the exclusion region of the $B_c^{\pm}$ meson on the parameter space plot, the kinematics was assumed to be equivalent to that of the $B^{\pm}$-meson, for which data is much more plentiful due to the higher fragmentation ratio of the $B^{\pm}$ meson. The assumption of equivalent kinematics was based on the following comparison of their four-momenta:[2]

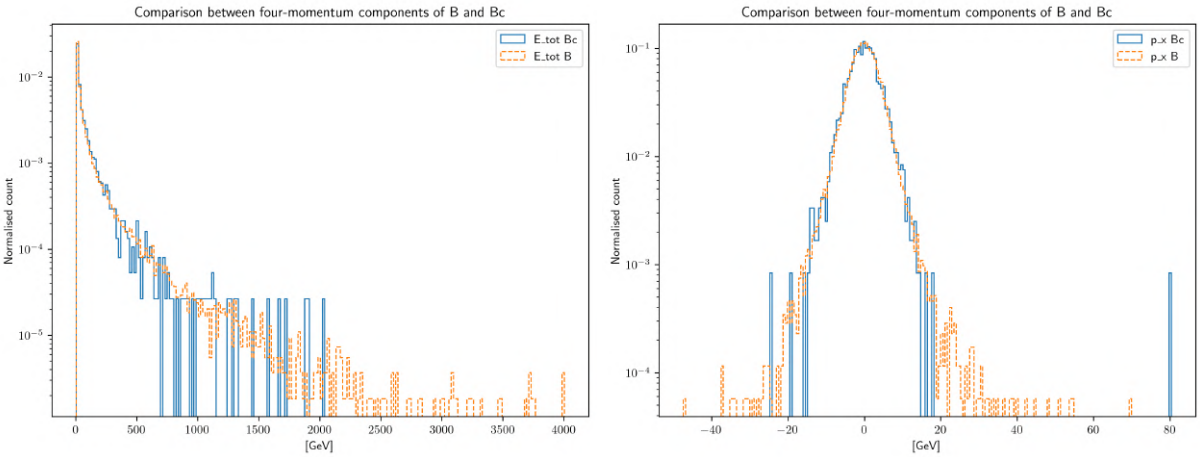

Figure A.7: A comparison between the normalised distributions of total energy (left) and momentum in the x-axis (right) between the $B^{\pm}$ (orange) and $B_c^{\pm}$ (blue) mesons. The comparison is between a sample size of ~ 30 thousand $B^{\pm}$ and ~ 2000 $B_c^{\pm}$ mesons.

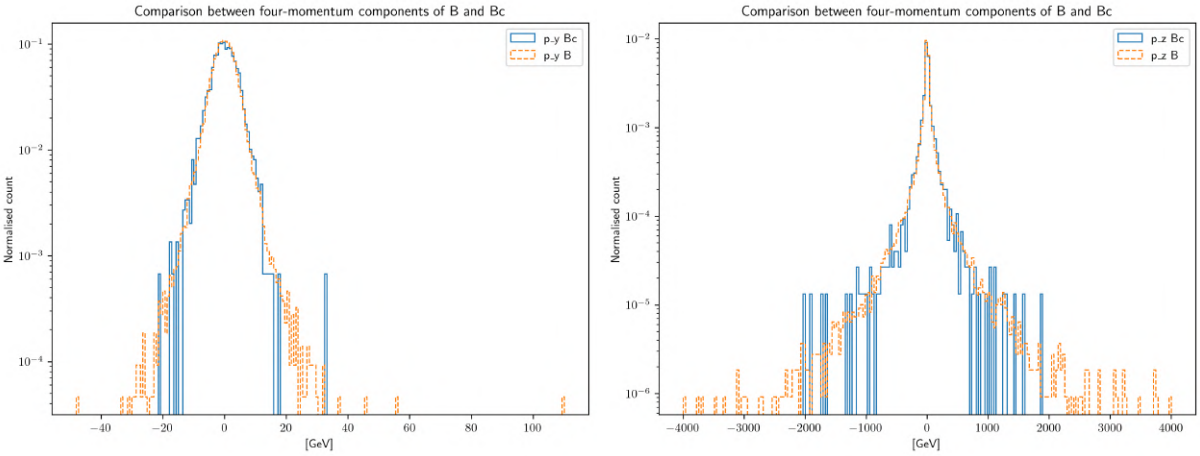

Figure A.8: A comparison between the normalised distributions of momentum in the y-axis (left) and momentum in the z-axis (right) between the $B^{\pm}$ (orange) and $B_c^{\pm}$ (blue) mesons.The comparison is between a sample size of ~ 30 thousand $B^{\pm}$ and ~ 2000 $B_c^{\pm}$ mesons.

where it can be seen that there is good agreement between the normalised distributions of their four-momenta, regardless of respective sample size.

[2]The comparison is made without applying any event selection criteria.

Appendix B

Notation & Conventions

Here we introduce the notation and conventions used throughout the thesis, starting with conventions

B.1 Convention

We use the *mostly-minus* prescription for the metric tensor, such that

$$\eta^{\mu\nu} = \begin{pmatrix} 1 & 0 & 0 & 0 \\ 0 & -1 & 0 & 0 \\ 0 & 0 & -1 & 0 \\ 0 & 0 & 0 & -1 \end{pmatrix} \tag{B.1.1}$$

B.2 Notation

Commuting and anti-commuting upper/lower indices are defined as [130]:

$$\partial_{[\mu} A_{\nu]} = \partial_\mu A_\nu - \partial_\nu A_\mu \tag{B.2.1}$$
$$\partial_{\{\mu} A_{\nu\}} = \partial_\mu A_\nu + \partial_\nu A_\mu \tag{B.2.2}$$

The three Pauli matrices are defined as

$$\sigma^1 = \begin{pmatrix} 0 & 1 \\ 1 & 0 \end{pmatrix}, \quad \sigma^2 = \begin{pmatrix} 0 & -i \\ i & 0 \end{pmatrix}, \quad \sigma^3 = \begin{pmatrix} 1 & 0 \\ 0 & -1 \end{pmatrix} \tag{B.2.3}$$

The eight Gell-Mann matrices are defined as

$$\lambda_1 = \begin{pmatrix} 0 & 1 & 0 \\ 0 & 0 & 0 \\ 0 & 0 & 0 \end{pmatrix}, \quad \lambda_2 = \begin{pmatrix} 0 & -i & 0 \\ i & 0 & 0 \\ 0 & 0 & 0 \end{pmatrix}, \quad \lambda_3 = \begin{pmatrix} 1 & 0 & 0 \\ 0 & -1 & 0 \\ 0 & 0 & 0 \end{pmatrix}, \quad \lambda_4 = \begin{pmatrix} 0 & 0 & 1 \\ 0 & 0 & 0 \\ 1 & 0 & 0 \end{pmatrix} \tag{B.2.4}$$

$$\lambda_5 = \begin{pmatrix} 0 & 0 & -i \\ 0 & 0 & 0 \\ i & 0 & 0 \end{pmatrix}, \quad \lambda_6 = \begin{pmatrix} 0 & 0 & 0 \\ 0 & 0 & 1 \\ 0 & 1 & 0 \end{pmatrix}, \quad \lambda_7 = \begin{pmatrix} 0 & 0 & 0 \\ 0 & 0 & -i \\ 0 & i & 0 \end{pmatrix}, \quad \lambda_8 = \begin{pmatrix} \frac{1}{\sqrt{3}} & 0 & 0 \\ 0 & \frac{1}{\sqrt{3}} & 0 \\ 0 & 0 & \frac{-2}{\sqrt{3}} \end{pmatrix} \tag{B.2.5}$$

with $t^a = \frac{\lambda^a}{2}$.

The Gamma matrices, under the Dirac basis, is given as

$$\gamma^0 = \begin{pmatrix} \mathbb{I}_2 & 0 \\ 0 & \text{-}\mathbb{I}_2 \end{pmatrix}, \qquad \gamma^k = \begin{pmatrix} 0 & \sigma^k \\ \text{-}\sigma^k & 0 \end{pmatrix}, \qquad \gamma^5 = \begin{pmatrix} 0 & \mathbb{I}_2 \\ \mathbb{I}_2 & 0 \end{pmatrix}, \tag{B.2.6}$$

for $0 \notin k$. The charge conjugation operator, $\mathcal{C}$ can therefore be defined as

$$\mathcal{C} = i\gamma^2\gamma^0 = \begin{pmatrix} 0 & \text{-}i\sigma^2 \\ \text{-}i\sigma^2 & 0 \end{pmatrix} \tag{B.2.7}$$

The Gamma matrices, under the Weyl basis, is given as

$$\gamma^0 = \begin{pmatrix} 0 & \mathbb{I}_2 \\ \mathbb{I}_2 & 0 \end{pmatrix}, \qquad \gamma^k = \begin{pmatrix} 0 & \sigma^k \\ \text{-}\sigma^k & 0 \end{pmatrix}, \qquad \gamma^5 = \begin{pmatrix} \text{-}\mathbb{I}_2 & 0 \\ 0 & \mathbb{I}_2 \end{pmatrix}, \tag{B.2.8}$$

for $0 \notin k$. The charge conjugation operator, $\mathcal{C}$ can therefore be defined as

$$\mathcal{C} = i\gamma^2\gamma^0 = \begin{pmatrix} i\sigma^2 & 0 \\ 0 & \text{-}i\sigma^2 \end{pmatrix} \tag{B.2.9}$$

The Feynman-slash notation is defined as

$$\not{\partial} = \gamma^\mu \partial_\mu \qquad \not{D} = \gamma^\mu D_\mu \tag{B.2.10}$$

The charge conjugation matrix, $\mathcal{C}$, has following properties

$$\mathcal{C}^\dagger = \mathcal{C}^{\text{-}1} \quad \text{and} \quad \mathcal{C}^T = -\mathcal{C} \tag{B.2.11}$$

so that for any spinor, the charge conjugate is

$$\nu^c = \mathcal{C}\bar{\nu}^T = -\gamma^0\mathcal{C}\nu^{\dagger T} \tag{B.2.12}$$

Bibliography

[1] J.-L. Tastet, *Searching for Heavy Neutral Leptons at CERN*. PhD thesis, Copenhagen University, feb, 2021.

[2] C. Giunti and C. W. Kim, *Fundamentals of neutrino physics and astrophysics*. Oxford University Press, 2016.

[3] L. Meredith, *Helicity, chirality, and the Dirac equation in the non-relativistic limit*. 2018.

[4] E. Majorana, *Teoria simmetrica dell'elettrone e del positrone*, *Nuovo Cim.* **14** (1937) 171–184.

[5] M. D. Schwartz, *Quantum Field Theory and the standard model*. Cambridge University Press, 2021.

[6] M. E. Peskin and D. V. Schroeder, *An Introduction to Quantum Field Theory*. Westview Press, 1995.

[7] M. Thomson, *Modern particle physics*. Cambridge University Press, 2015.

[8] G. P. Salam, *Elements of qcd for hadron colliders*, .

[9] Particle Data Group collaboration, R. L. Workman and Others, *Review of Particle Physics*, *PTEP* **2022** (2022) 083C01.

[10] Y. V. Kovchegov and E. Levin, *Quantum Chromodynamics at High Energy*. Cambridge Monographs on Particle Physics, Nuclear Physics and Cosmology. Cambridge University Press, 2012, 10.1017/CBO9781139022187.

[11] C. Davies, *Lattice qcd - a guide for people who want results*, 2005. 10.48550/ARXIV.HEP-LAT/0509046.

[12] Y. Bi, Y. Xiao, W. Guo, G. Ming, P. Sun, S. Xu et al., *Lattice qcd gpu inverters on rocm platform*, *EPJ Web of Conferences* **245** (01, 2020) 09008.

[13] J. Erdmenger, *Introduction to Gauge/Gravity Duality*, *PoS* **TASI2017** (2018) 001, [1807.09872].

[14] S. J. Brodsky and G. F. de Téramond, *ADS/CFT and QCD*, in *The Origin of Mass and Strong Coupling Gauge Theories*, WORLD SCIENTIFIC, jan, 2008. DOI.

[15] S. J. Brodsky and G. F. de Té ramond, *Applications of AdS/CFT duality to QCD*, *International Journal of Modern Physics A* **21** (feb, 2006) 762–768.

[16] J. Erlich, *How Well Does AdS/QCD Describe QCD?*, *Int. J. Mod. Phys. A* **25** (2010) 411–421, [0908.0312].

[17] J. Erlich, *An introduction to holographic qcd for nonspecialists*, 2014. 10.48550/ARXIV.1407.5002.

[18] A. Deur, S. J. Brodsky and G. F. de Téramond, *The QCD running coupling*, *Progress in Particle and Nuclear Physics* **90** (sep, 2016) 1–74.

[19] Y. L. Dokshitzer, *Basics of Perturbative QCD*. Editions Frontières, 1991.

[20] J. M. Campbell, J. W. Huston and W. J. Stirling, *Hard interactions of quarks and gluons: a primer for LHC physics*, *Reports on Progress in Physics* **70** (dec, 2006) 89–193.

[21] L. Di Giustino, *The renormalization scale setting problem in qcd [ph.d. thesis]*, 2022. 10.48550/ARXIV.2205.03689.

[22] C. Giganti, S. Lavignac and M. Zito, *Neutrino oscillations: The rise of the PMNS paradigm*, *Progress in Particle and Nuclear Physics* **98** (jan, 2018) 1–54.

[23] P. A. M. Dirac and R. H. Fowler, *The quantum theory of the electron*, *Proceedings of the Royal Society of London. Series A, Containing Papers of a Mathematical and Physical Character* **117** (1928) 610–624, [https://royalsocietypublishing.org/doi/pdf/10.1098/rspa.1928.0023].

[24] L. Canetti, M. Drewes and M. Shaposhnikov, *Matter and antimatter in the universe*, *New Journal of Physics* **14** (sep, 2012) 095012.

[25] *On anomalous electroweak baryon-number non-conservation in the early universe*, *Physics Letters B* **155** (1985) 36–42.

[26] K. Freese, *Review of observational evidence for dark matter in the universe and in upcoming searches for dark stars*, *EAS Publications Series* **36** (2009) 113–126.

[27] A. Einstein, *Lens-like action of a star by the deviation of light in the gravitational field*, Dec, 1936. 10.1126/science.84.2188.506.

[28] A. Arbey and F. Mahmoudi, *Dark matter and the early universe: A review*, *Progress in Particle and Nuclear Physics* (apr, 2021) 103865.

[29] R. Barbieri and D. V. Nanopoulos, *An Exceptional Model for Grand Unification*, *Phys. Lett. B* **91** (1980) 369–375.

[30] M. Pernow, *Phenomenology of SO(10) Grand Unified Theories*. PhD thesis, Royal Inst. Tech., Stockholm, 2019.

[31] S. P. Martin, *A Supersymmetry primer*, *Adv. Ser. Direct. High Energy Phys.* **18** (1998) 1–98, [hep-ph/9709356].

[32] E. Ponton, *TASI 2011: Four Lectures on TeV Scale Extra Dimensions*, in *Theoretical Advanced Study Institute in Elementary Particle Physics: The Dark Secrets of the Terascale*, pp. 283–374, 2013. 1207.3827. DOI.

[33] K. D. Lane, *Technicolor 2000*, *Frascati Phys. Ser.* **18** (2000) 235–280, [hep-ph/0007304].

[34] M. Shaposhnikov, *Is there a new physics between electroweak and Planck scales?*, in *Astroparticle Physics: Current Issues, 2007 (APCI07)*, 8, 2007. 0708.3550.

[35] M. Farina, D. Pappadopulo and A. Strumia, *A modified naturalness principle and its experimental tests*, *JHEP* **08** (2013) 022, [1303.7244].

[36] G. F. Giudice, *Naturalness after LHC8*, *PoS* **EPS-HEP2013** (2013) 163, [1307.7879].

[37] G. F. Giudice, *The Dawn of the Post-Naturalness Era*, pp. 267–292. 2019. 1710.07663. 10.1142/9789813238053_0013.

[38] T. M. Nieuwenhuizen, *The standard model of particle physics with diracian neutrino sector*, .

[39] S. Zhou, *Neutrino masses, leptonic flavor mixing, and muon (g-2) in the seesaw model with the gauge symmetry **, .

[40] V. Tello, *Connections between the high and low energy violation of Lepton and Flavor numbers in the minimal left-right symmetric model*. PhD thesis, SISSA, Trieste, 2012.

[41] R. N. Mohapatra, *Seesaw mechanism and its implications*, in *SEESAW25: International Conference on the Seesaw Mechanism and the Neutrino Mass*, pp. 29–44, 12, 2004. hep-ph/0412379. DOI.

[42] K. Bondarenko, A. Boyarsky, D. Gorbunov and O. Ruchayskiy, *Phenomenology of gev-scale heavy neutral leptons*, *Journal of High Energy Physics* **2018** (Nov, 2018) .

[43] M. Drewes and J. Hajer, *Heavy Neutrinos in displaced vertex searches at the LHC and HL-LHC*, *JHEP* **02** (2020) 070, [1903.06100].

[44] H. Fulbright, *A search for the double beta decay of 124 tin and 96 zirconium*, *Physica* **18** (1952) 1026–1031.

[45] H. E. Haber and G. L. Kane, *The Search for Supersymmetry: Probing Physics Beyond the Standard Model*, *Phys. Rept.* **117** (1985) 75–263.

[46] K. A. U. Calderón, I. Timiryasov and O. Ruchayskiy, *Improved constraints and the prospects of detecting TeV to PeV scale Heavy Neutral Leptons*, 2206.04540.

[47] J. Klaric, M. Shaposhnikov and I. Timiryasov, *Reconciling resonant leptogenesis and baryogenesis via neutrino oscillations*, *Physical Review D* **104** (sep, 2021) .

[48] M. Fukugita and T. Yanagida, *Baryogenesis Without Grand Unification*, *Phys. Lett. B* **174** (1986) 45–47.

[49] A. Pilaftsis, *CP violation and baryogenesis due to heavy Majorana neutrinos*, *Physical Review D* **56** (nov, 1997) 5431–5451.

[50] A. Boyarsky, M. Drewes, T. Lasserre, S. Mertens and O. Ruchayskiy, *Sterile Neutrino Dark Matter*, *Prog. Part. Nucl. Phys.* **104** (2019) 1–45, [1807.07938].

[51] T. Asaka and M. Shaposhnikov, *The νMSM, dark matter and baryon asymmetry of the universe*, *Phys. Lett. B* **620** (2005) 17–26, [hep-ph/0505013].

[52] T. Asaka, S. Blanchet and M. Shaposhnikov, *The nuMSM, dark matter and neutrino masses*, *Phys. Lett. B* **631** (2005) 151–156, [hep-ph/0503065].

[53] A. Boyarsky, O. Ruchayskiy and M. Shaposhnikov, *The Role of sterile neutrinos in cosmology and astrophysics*, *Ann. Rev. Nucl. Part. Sci.* **59** (2009) 191–214, [0901.0011].

[54] Z.-z. Xing, *Casas-Ibarra Parametrization and Unflavored Leptogenesis*, *Chin. Phys. C* **34** (2010) 1–6, [0902.2469].

[55] I. Esteban, M. C. Gonzalez-Garcia, M. Maltoni, T. Schwetz and A. Zhou, *The fate of hints: updated global analysis of three-flavor neutrino oscillations*, *JHEP* **09** (2020) 178, [2007.14792].

[56] J. Beacham et al., *Physics Beyond Colliders at CERN: Beyond the Standard Model Working Group Report*, *J. Phys. G* **47** (2020) 010501, [1901.09966].

[57] A. M. Abdullahi et al., *The Present and Future Status of Heavy Neutral Leptons*, in *2022 Snowmass Summer Study*, 3, 2022. 2203.08039.

[58] J. Alimena et al., *Searching for long-lived particles beyond the Standard Model at the Large Hadron Collider*, *J. Phys. G* **47** (2020) 090501, [1903.04497].

[59] K. Bondarenko, A. Boyarsky, M. Ovchynnikov, O. Ruchayskiy and L. Shchutska, *Probing new physics with displaced vertices: Muon tracker at cms*, *Physical Review D* **100** (Oct, 2019) .

[60] ATLAS collaboration, G. Aad et al., *Search for heavy neutral leptons in decays of W bosons produced in 13 TeV pp collisions using prompt and displaced signatures with the ATLAS detector*, *JHEP* **10** (2019) 265, [1905.09787].

[61] ATLAS collaboration, *Search for heavy neutral leptons in decays of W bosons using a dilepton displaced vertex in $\sqrt{s} = 13$ TeV pp collisions with the ATLAS detector*, 2204.11988.

[62] CMS collaboration, A. Tumasyan et al., *Search for long-lived heavy neutral leptons with displaced vertices in proton-proton collisions at* $\sqrt{\text{s}}$ *=13 TeV*, *JHEP* **07** (2022) 081, [2201.05578].

[63] L. Kaldamäe and S. Groote, *Virtual and real processes, the källé n function, and the relation to dilogarithms*, *Journal of Physics G: Nuclear and Particle Physics* **42** (jul, 2015) 085003.

[64] P. Coloma, E. Fernández-Martínez, M. González-López, J. Hernández-García and Z. Pavlovic, *GeV-scale neutrinos: interactions with mesons and DUNE sensitivity*, *The European Physical Journal C* **81** (jan, 2021) .

[65] C. Degrande, O. Mattelaer, R. Ruiz and J. Turner, *Fully automated precision predictions for heavy neutrino production mechanisms at hadron colliders*, *Physical Review D* **94** (sep, 2016) .

[66] A. V. Kurilin, *Leptonic decays of the W boson in a strong electromagnetic field*, *Physics of Atomic Nuclei* **67** (nov, 2004) 2095–2100.

[67] K. Bondarenko, A. Boyarsky, M. Ovchynnikov and O. Ruchayskiy, *Sensitivity of the intensity frontier experiments for neutrino and scalar portals: analytic estimates*, *JHEP* **08** (2019) 061, [1902.06240].

[68] ATLAS collaboration, G. Aad et al., *Search for displaced vertices arising from decays of new heavy particles in 7 TeV pp collisions at ATLAS*, *Phys. Lett. B* **707** (2012) 478–496, [1109.2242].

[69] ATLAS collaboration, G. Aad et al., *Search for long-lived, heavy particles in final states with a muon and multi-track displaced vertex in proton-proton collisions at $\sqrt{s} = 7$ TeV with the ATLAS detector*, *Phys. Lett. B* **719** (2013) 280–298, [1210.7451].

[70] S. Kazama, *Search for Charginos Nearly Mass-Degenerate with the Lightest Neutralino: Based on a Disappearing-Track Signature in pp Collisions at $\sqrt{s} = 8$ TeV*. PhD thesis, Tokyo U. of Sci., 2013. 10.1007/978-4-431-55657-2.

[71] ATLAS collaboration, *Performance of the reconstruction of large impact parameter tracks in the ATLAS inner detector*, .

[72] ATLAS collaboration, M. S. Lutz, *Large Radius Tracking at the ATLAS Experiment*, *PoS* **EPS-HEP2017** (2018) 708.

[73] E. Piccaro, *Measurement of the atlas di-muon trigger efficiency in proton-proton collisions at 7 tev*, 2011. 10.48550/ARXIV.1111.4329.

[74] T. Lagouri, N. Kanaya and A. Krasznahorkay, *B-physics and LVL1 di-muon trigger in the ATLAS experiment at the LHC*, *Journal of Physics: Conference Series* **53** (nov, 2006) 255–278.

[75] ATLAS Collaboration collaboration, *Trigger menu in 2018*, tech. rep., CERN, Geneva, Oct, 2019.

[76] P. Agrawal et al., *Feebly-interacting particles: FIPs 2020 workshop report*, *Eur. Phys. J. C* **81** (2021) 1015, [2102.12143].

[77] CHARM collaboration, F. Bergsma et al., *A Search for Decays of Heavy Neutrinos in the Mass Range 0.5-GeV to 2.8-GeV*, *Phys. Lett. B* **166** (1986) 473–478.

[78] NuTeV, E815 collaboration, A. Vaitaitis et al., *Search for neutral heavy leptons in a high-energy neutrino beam*, *Phys. Rev. Lett.* **83** (1999) 4943–4946, [hep-ex/9908011].

[79] I. Boiarska, A. Boyarsky, O. Mikulenko and M. Ovchynnikov, *Constraints from the CHARM experiment on heavy neutral leptons with tau mixing*, *Phys. Rev. D* **104** (2021) 095019, [2107.14685].

[80] DELPHI collaboration, P. Abreu et al., *Search for neutral heavy leptons produced in Z decays*, *Z. Phys. C* **74** (1997) 57–71.

[81] CMS collaboration, A. M. Sirunyan et al., *Search for heavy Majorana neutrinos in same-sign dilepton channels in proton-proton collisions at* $\sqrt{s} = 13$ *TeV*, *JHEP* **01** (2019) 122, [1806.10905].

[82] CMS collaboration, *Search for heavy neutral leptons in events with three charged leptons in proton-proton collisions at* $\sqrt{s} = 13$ *TeV*, *Phys. Rev. Lett.* **120** (2018) 221801, [1802.02965].

[83] V. Lüth, *A Challenge to Lepton Universality in B Meson Decays*, *Hyperfine Interact.* **239** (2018) 59, [1808.02587].

[84] T. Pierzchala, E. Richter-Was, Z. Was and M. Worek, *Spin effects in tau-lepton pair production at lhc*, .

[85] M.-L. Riis, *Piggyback riding the higgs searches: A hunt for heavy neutral leptons with tau triggers.*, Master's thesis, Copenhagen University, 2022.

[86] M. D. Schwartz, *Tasi lectures on collider physics*, in *Proceedings, Theoretical Advanced Study Institute in Elementary Particle Physics : Anticipating the Next Discoveries in Particle Physics (TASI 2016): Boulder, CO, USA, June 6-July 1, 2016* (R. Essig and I. Low, eds.), 2018. 1709.04533. DOI.

[87] M. PERELSTEIN, *INTRODUCTION TO COLLIDER PHYSICS*, in *Physics of the Large and the Small*, WORLD SCIENTIFIC, mar, 2011. DOI.

[88] L. Rossi and O. Brüning, *Progress with the High Luminosity LHC project at CERN*, .

[89] ATLAS collaboration, Y. Okumura, *Triggering in ATLAS in Run 2 and Run 3*, *PoS* **EPS-HEP2021** (2022) 788.

[90] B. A. Petersen and C. Schwick, *Experiment Requests and Constraints for Run 3*, .

[91] The TOTEM Collaboration, . Antchev, P. Aspell, I. Atanassov, V. Avati, J. Baechler et al., *First measurement of elastic, inelastic and total cross-section at* $\sqrt{s} = 13$ *tev by totem and overview of cross-section data at lhc energies*, 2017. 10.48550/ARXIV.1712.06153.

[92] S. Akatsuka, *The phase-1 upgrade of the atlas level-1 endcap muon trigger*, 2018. 10.48550/ARXIV.1806.09234.

[93] G. Apollinari, I. Béjar Alonso, O. Brüning, M. Lamont and L. Rossi, *High-Luminosity Large Hadron Collider (HL-LHC): Preliminary Design Report*. CERN Yellow Reports: Monographs. CERN, Geneva, 2015, 10.5170/CERN-2015-005.

[94] I. Neutelings, *CMS coordinate system*, 2022.

[95] https://tikz.net/axis2d_pseudorapidity/.

[96] J. Thomason, R. Garoby, S. Gilardoni, L. Jenner and J. Pasternak, *Proton driver scenarios at cern and rutherford appleton laboratory*, *Physical Review Special Topics - Accelerators and Beams* **16** (05, 2013) .

[97] "Detector & technology."

[98] ATLAS collaboration, D. E. Boumediene, *ATLAS Calorimeter: Run 2 performance and Phase-II upgrades*, *PoS* **EPS-HEP2017** (2017) 485.

[99] D. Attree, B. Anderson, E. Anderssen, V. Akhnazarov, R. Apsimon, P. Barclay et al., *The evaporative cooling system for the atlas inner detector*, *Journal of Instrumentation* **3** (07, 2008) .

[100] ATLAS collaboration, E. Stanecka, *ATLAS Inner Tracker Performance at the Beginning of the LHC Run 2*, *Acta Phys. Polon. B* **47** (2016) 1739–1744.

[101] "Atlas calorimetry: Hadronic calibration studies." `https://tikz.net/axis2d_pseudorapidity/`.

[102] `https://cds.cern.ch/record/1095924`.

[103] ATLAS Collaboration collaboration, *Search prospects for dark-photons decaying to displaced collimated jets of muons at HL-LHC*, tech. rep., CERN, Geneva, Jan, 2019.

[104] G. Aielli, *Cavern background measurement with the ATLAS RPC system*, tech. rep., CERN, Geneva, Jun, 2012.

[105] A. Di Crescenzo, *2022. 4th forward physics facility meeting*, 2022.

[106] L. A. Anchordoqui, A. Ariga, T. Ariga, W. Bai, K. Balazs, B. Batell et al., *The forward physics facility: Sites, experiments, and physics potential*, *Physics Reports* **968** (jul, 2022) 1–50.

[107] F.-L. Navarria, *The scattering and neutrino detector at the lhc*, 2022. 10.48550/ARXIV.2201.09291.

[108] M. H. Seymour and M. Marx, *Monte carlo event generators*, 2013. 10.48550/ARXIV.1304.6677.

[109] T. Sjöstrand, S. Ask, J. R. Christiansen, R. Corke, N. Desai, P. Ilten et al., *An introduction to pythia 8.2*, *Computer Physics Communications* **191** (Jun, 2015) .

[110] P. M. Nadolsky, H.-L. Lai, Q.-H. Cao, J. Huston, J. Pumplin, D. Stump et al., *Implications of CTEQ global analysis for collider observables*, *Physical Review D* **78** (jul, 2008) .

[111] R. D. Ball, V. Bertone, S. Carrazza, L. D. Debbio, S. Forte, P. Groth-Merrild et al., *Parton distributions from high-precision collider data*, *The European Physical Journal C* **77** (oct, 2017) .

[112] A. collaboration, *Measurement of the differential cross-section of B^+ meson production in pp collisions at $\sqrt{s}$ = 7 TeV at ATLAS*, *Journal of High Energy Physics* **2013** (oct, 2013) .

[113] M. Cacciari, M. Greco and P. Nason, *The p_t spectrum in heavy-flavour hadroproduction*, *Journal of High Energy Physics* **1998** (May, 1998) .

[114] A. Collaboration, *Measurement of $D^{*\pm}$, $D^{\pm}$ and $D_s^{\pm}$ meson production cross sections in pp collisions at $\sqrt{s} = 7$ TeV with the ATLAS detector*, *Nuclear Physics B* **907** (jun, 2016) 717–763.

[115] K. Bondarenko, A. Boyarsky, M. Ovchynnikov and O. Ruchayskiy, *Sensitivity of the intensity frontier experiments for neutrino and scalar portals: analytic estimates*, *Journal of High Energy Physics* **2019** (aug, 2019) .

[116] J. Alwall, R. Frederix, S. Frixione, V. Hirschi, F. Maltoni, O. Mattelaer et al., *The automated computation of tree-level and next-to-leading order differential cross sections, and their matching to parton shower simulations*, *JHEP* **07** (2014) 079, [1405.0301].

[117] A. Alloul, N. D. Christensen, C. Degrande, C. Duhr and B. Fuks, *Feynrules 2.0 — a complete toolbox for tree-level phenomenology*, *Computer Physics Communications* **185** (Aug, 2014) 2250–2300.

[118] J. Alwall, A. Ballestrero, P. Bartalini, S. Belov, E. Boos, A. Buckley et al., *A standard format for les houches event files*, *Computer Physics Communications* **176** (feb, 2007) 300–304.

[119] E. Boos, M. Dobbs, W. Giele, I. Hinchliffe, J. Huston, V. Ilyin et al., *Generic user process interface for event generators*, 2001. 10.48550/ARXIV.HEP-PH/0109068.

[120] P. Coloma, E. Fernández-Martínez, M. González-López, J. Hernández-García and Z. Pavlovic, *GeV-scale neutrinos: interactions with mesons and DUNE sensitivity*, *Eur. Phys. J. C* **81** (2021) 78, [2007.03701].

[121] D. Gorbunov and M. Shaposhnikov, *How to find neutral leptons of the νMSM?*, *Journal of High Energy Physics* **2007** (oct, 2007) 015–015.

[122] R. G. Littlejohn, *Physics 221b spring 2020 notes 46 - university of california, berkeley*, 2019.

[123] SND@LHC collaboration, E. Van Herwijnen, *Status of SND@LHC (Scattering and Neutrino Detector at the LHC)*, *PoS* **NuFact2021** (2022) 158.

[124] A. M. Sirunyan, , A. Tumasyan, W. Adam, F. Ambrogi, E. Asilar et al., *Measurement of b hadron lifetimes in pp collisions at* $\sqrt{s} = 8$ *TeV*, *The European Physical Journal C* **78** (jun, 2018) .

[125] C. C. Ahdida, R. Albanese, A. Alexandrov, M. Andreini, A. Anokhina, A. Bay et al., *Scattering and neutrino detector at the lhc letter of intent*, 2020.

[126] R. Barouki, G. Marocco and S. Sarkar, *Blast from the past ii: Constraints on heavy neutral leptons from the bebc wa66 beam dump experiment*, 2022. 10.48550/ARXIV.2208.00416.

[127] A. Collaboration, *Study of the material of the ATLAS inner detector for run 2 of the LHC*, *Journal of Instrumentation* **12** (dec, 2017) P12009–P12009.

[128] M. Thomson, *Modern particle physics*. Cambridge University Press, 2015.

[129] J. C. Collins, D. E. Soper and G. Sterman, *Factorization of hard processes in qcd*, .

[130] E. Tireli, *Quantum field theory on curved space and blackhole thermodynamics*, 2020. 10.13140/RG.2.2.30069.60642.